A dissertation submitted to the

Faculty of Biology, Chemistry and Geosciences
University of Bayreuth

to attain the academic degree of
Dr. rer. nat.

Measuring and understanding site-specific wind and turbulence characteristics for wind energy applications

Lukas Pauscher
Dipl.-Geoökol.

born 22 April, 1983
in Singen (Hohentwiel), Germany

Bayreuth, August 23, 2017

supervised by Prof. Dr. Thomas Foken

This doctoral thesis was prepared at the Department of Micrometeorology at the University of Bayreuth from November 2013 until April 2017 and was supervised by Prof. Dr. Thomas Foken.

This is a full reprint of the dissertation submitted to obtain the academic degree of Doctor of Natural Sciences (Dr. rer. nat) and approved by the Faculty of Biology, Chemistry and Geosciences of the University of Bayreuth.

Date of submission: 19.04.2017

Date of defence: 30.06.2017

Acting dean: Prof. Dr. Stefan Schuster

Doctoral committee:

Prof. Dr. Thomas Foken (1st reviewer)
Prof. Dr. Stefan Emeis (2nd reviewer)
Prof. Dr. Andreas Held (chairman)
Prof. Dr. Christoph Thomas

Contents

List of manuscripts

This dissertation is presented in cumulative form. The manuscripts listed in this section form its basis.

Published peer-reviewed publications

Klaas, T., Pauscher, L. and Callies, D.: LiDAR-mast deviations in complex terrain and their simulation using CFD, Meteorologische Zeitschrift, 24(6), 591–603, doi:10.1127/metz/2015/0637, 2015.

Pauscher, L., Vasiljevic, N., Callies, D., Lea, G., Mann, J., Klaas, T., Hieronimus, J., Gottschall, J., Schwesig, A., Kühn, M. and Courtney, M.: An inter-comparison study of multi- and DBS-lidar measurements in complex terrain, Remote Sensing, 8(9),782, doi:10.3390/rs8090782 [Erratum: Remote Sens. 2017, 9(7), 667; doi:10.3390/rs9070667], 2016.

Manuscripts accepted for publication

Pauscher, L., Callies, D., Klaas T. and Foken, T.: Wind observations from a forested hill: Relating turbulence statistics to surface characteristics in hilly and patchy terrain, Meteorologische Zeitschrift, accepted for publication.

Manuscripts to be submitted for peer review

Pauscher, L., Mann, J., Vasiljevic and Lea, G.: Estimation of the dissipation rate of TKE from a single staring lidar, to be submitted to Journal of Atmospheric and Oceanic Technology.

List of additional peer-reviewed publications

This section lists peer-reviewed publications to which I contributed with content, which is linked to the topics covered in this dissertation, but are not part of the dissertation.

Mann, J., Angelou, N., Arnqvist, J., Callies, D., Cantero, E., Arroyo, R. C., Courtney, M., Cuxart, J., Dellwik, E., Gottschall, J., Ivanell, S., Kühn, P., Lea, G., Matos, J. C., Palma, J. M. L. M., Pauscher, L., Peña, A., Rodrigo, J. S., S, S., Vasiljeviç, N., and Rodrigues, C. V.: Complex terrain experiments in the New European

Wind Atlas, Philosophical Transactions of the Royal Society of London A: Mathematical, Physical and Engineering Sciences, 375, doi:10.1098/rsta.2016.0101, 2017.

Sathe, A., Banta, R., Pauscher, L., Vogstad, K., Schlipf, D., and Wylie, S.: Estimating turbulence statistics and parameters from ground- and nacelle-based lidar measurements: IEA Wind Expert Report, ISBN 978-87-93278-35-6, Roskilde, Denmark, 2015.

Wood, C. R., Pauscher, L., Ward, H. C., Kotthaus, S., Barlow, J. F., Gouvea, M., Lane, S. E., and Grimmond, C. S. B.: Wind observations above an urban river using a new lidar technique, scintillometry and anemometry, The Science of the Total Environment, 442, 527-533, 2013.

Acknowledgments

I am grateful to many people, who supported me during the preparation of this dissertation:

- Thomas Foken for the excellent supervision and guidance at all stages of this dissertation. I am thankful for his valuable and critical input to and revision of my work. I would also like to express my gratitude for his patience and pointing me towards the right direction, when I was about to get lost in details.
- Jakob Mann for hosting me at DTU, for his support and for sharing his knowledge about turbulence with me. He greatly helped me in choosing and developing the theoretical framework for analysing and evaluating the lidar measurements.
- Doron Callies for supporting me with critical discussions and the possibility to work with the data from the Kassel 2014 Experiment.
- Tobias Klaas for all the interesting work and discussions on lidar measurements in complex terrain.
- Paul Kühn for all the support to pursue my research interests and the freedom to allocate the time that was necessary to prepare this dissertation.
- Richard Döpfer and Klaus Otto for their invaluable support concerning the technical aspects of the measurement campaigns.
- Guillaume Lea and Nicola Vasiljevic for their help when working with the WindScanner technology.
- Alexander Basse for proofreading the manuscript.
- Steffen Rettig, Thomas Schwander, Nicole Eigenmann, Mai Tu, Joscha Rohrig and Alexander Basse, who helped to perform the field work.

Most of all, I would like to thank my wife Kristina and my family, who have always supported me on the long journey of writing this dissertation.

Summary

Onshore wind energy has become the most important source of renewable energy in Germany. This success also lead to rapid developments in turbine technology. The strongly increased turbine size creates a need for the application of new measurement technologies to replace tall, expensive and inflexible measurement masts. For this reason, Doppler-lidar measurements have become increasingly popular in the wind energy community. Yet, for measurements in complex terrain and for turbulence measurements, conically scanning lidars still suffer from systematic errors. However, especially in complex terrain accurate measurements of the mean wind speed and turbulence intensity are key for resource and site suitability assessment, as modelling is often associated with high uncertainties. Also, the relation of observed turbulence quantities to surface characteristics and the atmospheric stability regime is often difficult for the experimentalist. This dissertation focuses on the aforementioned problems and presents different approaches to resolve them.

The complex terrain error of conically scanning lidars is analysed experimentally and using flow modelling. The simulations revealed a high sensitivity to land cover, especially forest generally reduces the error. Among the investigated models, the linear flow model showed the worst performance in predicting the observed error. The RANS-models could reproduce the right pattern and magnitude of the lidar error.

As an alternative the multi-lidar (ML) approach is investigated. The value of the ML-approach, when compared to a single conically scanning lidar, is demonstrated experimentally in complex terrain for the first time. Given an appropriate setup, measuring with two or three lidars in the same point significantly improved the agreement with a high quality reference measurement. This can greatly reduce the uncertainties of lidar measurements in complex flow regimes.

The multi-lidar approach was also experimentally demonstrated to be a promising approach to measure turbulence statistics in complex terrain. In contrast, the conically scanning lidar showed a strong overestimation, when compared to the reference measurements. One of the problems which remains unsolved in the ML-approach is the attenuation of small scale turbulence by the spatial averaging of the lidar. This was also clearly visible in the spectral analysis of the ML-experiment.

This dissertation approaches the problem by investigating the capability of a pulsed lidar to measure the dissipation rate of turbulent kinetic energy (TKE) using three different methods: A previously described method based on short term variances is corrected to remove significant systematic errors which were present. Moreover, a theoretically suggested method based on the structure function of the radial velocity fluctuations is experimentally evaluated for the first time. The third approach uses the power-spectral density in the inertial sub-range. It is shown that, given the knowledge about the spatial averaging function of the lidar and a careful removal of the noise, the dissipation rate of TKE can be estimated with a reasonable accuracy. However, the experimentally determined form of the spatial averaging function and the one derived

from theoretical considerations showed significant differences. The differences between the investigated methods to derive the dissipation rate of TKE are mainly found in their applicability to different experimental setups with the structure-function approach providing the most flexible option.

Finally, the dissertation investigates observed turbulence quantities and their relation to surface characteristics and stability at a 200-m-mast at a forested hilltop site. A simple approach based on footprint modelling is developed to characterise the surface ruggedness and roughness in the area of effect of the measurement. It is shown that especially the normalised standard deviation of the wind along the stream lines exhibits a high correlation to the surface characteristics within the footprint. Atmospheric stability also had a strong influence on the representative turbulence intensity at the investigated hilltop site. The prevalence of stable conditions for wind speeds between $6 - 12$ m s^{-1} lead to a significantly reduced turbulence intensity in this wind speed range, which is in the order of the difference between standard turbulence classes for wind turbines.

Zusammenfassung

Die Windenergie an Land ist der wichtigste Energieträger unter den erneuerbaren Energien in Deutschland. Dieser Erfolg ging mit einer schnellen Entwicklung in der verwendeten Technologie einher. Mit den stark gewachsenen Anlagenhöhen werden klassische mastbasierte Messungen teuer und sind zudem unflexibel. Durch diesen Trend sind Lidar-Messungen in den vergangen Jahren im Bereich Windenergie immer populärer geworden. Allerdings sind diese im komplexen Gelände mit systematischen Fehlern behaftet und weisen bei der Messung von Turbulenz erhebliche Ungenauigkeiten auf. Demgegenüber sind besonders im komplexen Gelände Messungen der Windgeschwindigkeit und Turbulenzeigenschaften wichtig, da die Modellierung hier mit großen Unsicherheiten verbunden ist. Allgemein erweist sich auch die Interpretation experimentell bestimmter turbulenter Windbedingungen im komplexen und heterogenen Gelände als schwierig. Ebenso ist die Abschätzung des Einflusses der atmosphärischen Stabilität auf die repräsentative Turbulenzintensität, die zur Bestimmung der Eignung einer Windenergieanlage wichtig ist, oft schwierig. Die vorgelegte Dissertation befasst sich mit den beschriebenen Problemen und entwickelt dazu verschiedene Lösungsansätze.

Zuerst wurde der Fehler eines konisch scannenden Lidars experimentell und mittels Strömungssimulation untersucht. In den Ergebnissen der Modellierung zeigte sich eine große Abhängigkeit des Lidar-Fehlers von der Oberflächenbedeckung. Bei einem bewaldeten Hügel war der Fehler gegenüber einer unbewaldeten Oberfläche deutlich reduziert. Auch zwischen den verwendeten Modellen zeigten sich große Unterschiede. So war die Übereinstimmung zwischen den RANS-Modellen und den experimentell bestimmten Fehlern deutlich besser als für das untersuchte lineare Model.

Als Alternative zu konisch scannenden Lidars wurde die Multi-Lidar (ML) Methode für den Einsatz im komplexen Gelände untersucht. Dabei konnte erstmals experimentell gezeigt werden, dass die Messfehler in der mittleren Windgeschwindigkeit gegenüber konisch scannenden Lidars deutlich reduziert werden können, wenn zwei oder drei Lidars im gleichen Punkt messen. Dies bietet die Möglichkeit die Unsicherheiten in Lidar-Messungen im komplexen Gelände deutlich zu reduzieren.

Auch bei den Turbulenzmessungen zeigte sich die ML-Methode als vielversprechend. Im Gegensatz dazu wurde bei der Messung des konisch scannenden Lidars eine deutliche Überschätzung der Referenzmessung beobachtet. Eines der ungelösten Probleme mit dem ML-Ansatz ist jedoch die Dämpfung kleiner Turbulenzskalen durch die räumliche Mittelung der Lidar-Messung. Dies konnte deutlich in der Analyse der Spektren aus dem ML-Experiment beobachtet werden. Die vorgelegte Dissertation untersucht in diesem Kontext die Möglichkeit aus Lidar-Messungen die Dissipationsrate turbulenter kinetischer Energie (TKE) abzuleiten. Dazu wurden drei Ansätze verglichen. Die erste Methode ist eine Weiterentwicklung und Korrektur eines zuvor veröffentlichten Ansatzes, der auf der Varianz der radialen Windgeschwindigkeit innerhalb kurzer Messperioden beruht. Gegenüber dem ursprünglichen Ansatz können durch die Weiterentwicklung erhebliche systematische Fehler vermieden werden. Der zweite Ansatz basiert auf der

Strukturfunktion der radialen Windgeschwindigkeit und wurde bisher nur theoretisch beschrieben. In dieser Arbeit wird er zum ersten Mal experimentell überprüft. Der dritte Ansatz führt die Bestimmung der Dissipationsrate der TKE basierend auf einer Analyse der Powerspektren im Trägheitsbereich durch. Die Arbeit zeigt, dass es möglich ist die Dissipationsrate der TKE aus Lidar-Messungen mit zufriedenstellender Genauigkeit zu schätzen. Allerdings muss dazu die räumliche Mittelungsfunktion des Lidars bekannt sein. Bei der experimentellen Untersuchung der räumlichen Mittelungsfunktion zeigten sich jedoch signifikante Unterschiede zu den vorher durchgeführten theoretischen Überlegungen. Der Unterschied zwischen den Methoden zur Bestimmung der Dissipationsrate der TKE liegt vor allem in ihrer Anwendbarkeit auf verschiedene Messkonfigurationen. Hier zeigt die Methode basiernd auf der Strukturfunktion die größte Flexibilität.

Neben der Entwicklung von Methoden im Bereich der Lidar-Messungen präsentiert die Arbeit auch Messungen verschiedener Turbulenzgrößen vom 200-m-Mast des Fraunhofer IWES am Rödeser Berg. Zur Interpretation des Zusammenhangs zwischen den Eigenschaften der Oberfläche im Einflussbereich der Messung und den Beobachtungen wurde ein einfaches Tool basierend auf dem Footprintansatz entwickelt. Besonders für die normalisierte Standardabweichung entlang der Strömungslinien zeigten sich hohe Korrelationen mit der Rauigkeit und dem Zerklüftungsgrad der Oberfläche im modellierten Footprint. Neben den Oberflächeneigenschaften hatte auch die atmosphärische Stabilität einen großen Einfluss auf die Turbulenzeigenschaften. Besonders im für die Ermüdungslasten wichtigen Bereich zwischen 6-12 m s^{-1} war die Turbulenzintensität aufgrund des häufigen Auftretens stabiler Schichtung signifikant reduziert.

1. Introduction

1.1. Motivation and background

One of the major challenges for our society is the anthropogenically induced climate change and the associated risks (IPCC, 2014). More than half of the anthropogenic greenhouse gas emissions stem from the combustion of fossil fuel to extract primary energy (IPCC, 2011). The transformation of the energy system - away from fossil fuels towards renewable energies - is, thus, one of the central pillars for the reduction of the emission of greenhouse gases. Wind energy has seen a rapid development over the past decades and plays a key role in this context (Wiser et al., 2011).

In Germany, onshore wind energy has already become the biggest renewable energy source. In 2014, its share on the total gross energy consumption was approx. 9.4 % (Berkhout et al., 2015). Despite this development, further extension is required to meet the ambitious goals of the German government (§1 Abs. 2 of the Erneuerbare-Energien-Gesetz - EEG 2017). Several studies have shown, that onshore wind energy still offers large unused potentials in Europe and in Germany (EEA, 2011; Bofinger et al., 2011; Lütkehus et al., 2013; Callies, 2015). While the coastal regions in Germany are already extensively used for wind energy, a lot of the unused wind energy potential is found further onshore (Callies, 2015) and current development of wind park projects is also moving towards this direction (Berkhout et al., 2015). Much of the wind energy potential in the middle and south of Germany is located in orographically complex terrain and/or forested areas. This has lead to new technical developments. To make onshore sites with generally lower wind speeds and often higher turbulence environments economically viable, hub heights and rotor diameters have grown significantly.

These developments also pose significant challenges to resource and site assessment methods in wind energy projects. Modelling and understanding of the wind conditions in complex terrains and up to great heights remains one of the challenges in wind energy science (van Kuik et al., 2016). The topic is also still subject of intensive experimental research in the wind energy community (e.g. Mann et al., 2017).

The move towards more complex areas has also triggered an increased need for measurements in commercial wind energy developments. Due to the high sensitivity of the power output of a wind turbine to the wind speed, the estimation of the wind resource is one of the major uncertainty factors in the economical assessment of a wind park development. For this reason, the wind energy community has established a comprehensive framework to ensure the quality of traditional mast based anemometry (IEC,

2005b, 2016; FGW, 2014; Measnet, 2016). However, measurements at the hub height of a modern wind turbine (up to 160 m by the time of writing this dissertation) are not economically feasible using a traditional measurement mast and cup or sonic anemometers. Therefore, remote sensing - especially lidar technology - has become a popular alternative and quickly penetrated several wind energy applications. Much of the research in the wind energy community has gone into evaluating lidar measurements against classical mast based anemometry (point measurements) (e.g. Antoniou et al., 2004; Smith et al., 2006; Kindler et al., 2007; Gottschall et al., 2012) to establish the technology in a relatively conservative industrial community. The main motivation for this is the need of a validation against traceable reference to estimate the uncertainties associated with the application of a measurement device. By the time of writing this dissertation lidar measurements in flat terrain were well established in resource assessment (e.g. FGW, 2014; Measnet, 2016) and power performance measurements (IEC, 2016).

In orographically complex terrain, however, measurements with classical profiling lidars can be associated with systematic errors (Bingöl et al., 2009; Bradley et al., 2015). One of the approaches to deal with this problem is to simulate and correct the complex terrain errors of lidars using flow models of different complexities (Bingöl et al., 2009; Bradley, 2012; Bradley et al., 2012; Behrens et al., 2012). However, validation from lidar-mast inter-comparisons is scarce. Also, the performance difference among models of different complexity has not been evaluated, yet. Moreover, the sensitivity of the modelled complex terrain error to parameters like roughness length or forest cover remains largely unknown. The experimental investigations and modelling results presented in Klaas et al. (2015, Appendix B) aim at closing this gap.

One of the downsides of the lack of experience is the largely unknown uncertainty of lidar measurements in complex terrain and their corrections. In practical applications the restrictions on the application of lidars in complex terrain vary among different standards. The German guideline on resource assessment (FGW, 2014) is relatively progressive and allows the use of corrected lidar measurements in moderately complex terrain. The more international Measnet standard (Measnet, 2016) only allows the application of a lidar in complex terrain in conjunction with a measurement mast on site. The standard of the International Electrical Commission on power curve measurements (IEC, 2016) is even more restricted and prohibits the application of lidars in complex terrain.

An alternative to the correction of classical profiling lidar measurements for their complex terrain errors is the reconstruction of the wind vector from multiple measurements within a single confined location. This technique avoids the measurement errors in complex terrain by using the beams of multiple lidars which cross in a single measurement point to reconstruct the wind vector. This multi-lidar (ML) technique has shown promising results in flat and homogeneous terrain for comparisons of short time series with measurement masts (Fuertes et al., 2014; Vasiljevic, 2014; Berg et al., 2015). The use of a multi-static lidar with one lidar source and multiple receivers is

also possible (e.g. Harris et al., 2001), but its technical development in wind energy applications is still in the prototype phase (Eggert et al., 2014) and many technical issues like eye safety and reliability remain unsolved.

Despite the simplicity of the idea, no experimental results demonstrating the potentials of the ML technique to improve measurement accuracy of the mean wind speed in complex terrain have been published previous to this work. One of the reasons might be the absence of sophisticated methods and protocols to precisely align and synchronise multiple lidar devices. With the recent development of the WindScanner technology (Vasiljevic, 2014; Vasiljevic et al., 2016) such a system has recently become available. Some results of bi-static sodar measurements, which rely on a similar principle, have been published in Bradley et al. (2015). However, due to the relatively large scatter in the data the results can only serve as limited evidence in this context. The measurements presented in Pauscher et al. (2016, Appendix C), thus, are the first experimental results demonstrating the improvements in accuracy which can be achieved with the ML technique in complex terrain.

Besides the errors in complex terrain, the largest drawback of the currently available commercial lidar technology for the wind energy community is its inability to accurately measure turbulence (Sathe and Mann, 2013; Sathe et al., 2015). For this reason the question of turbulence measurements with ground based lidars is a very active research topic within the wind energy community. For a current overview of its status in wind energy applications see e.g. the review report by Sathe et al. (2015), which is listed as one of the additional publications at the beginning of this dissertation.

For the site suitability analysis of a wind turbine the turbulence environment needs to be known to simulate the loads which will occur during the lifetime of a wind turbine at the selected site (IEC, 2005a). Usually, this is done by feeding the measured variance of the horizontal wind speed or the wind vector components into a stochastic wind field model which is based on Fourier simulation (Veers, 1988; Mann, 1994, 1998). Especially classical, conically scanning lidars suffer from significant errors measuring turbulence (Sathe et al., 2011). A promising way forward in this context is again the ML technique. However, experimental results evaluating the ML-technique are scarce and the few existing studies, which have a reliable reference measurement, only cover a few half-hour periods (Mann et al., 2009; Fuertes et al., 2014). The second part of the analysis presented in Pauscher et al. (2016, Appendix C) focuses on this topic and experimentally evaluates the potentials of the ML technique to improve the measurements of the variance of the wind vector components.

An alternative to the variance of the wind vector components in the simulation of turbulent wind fields is the dissipation rate of turbulent kinetic energy (ϵ). Due to its well-known relation to the spectral density in the inertial sub-range (Kolmogorov, 1941), ϵ makes an excellent parameter to model turbulence spectra. In fact, the description of spectral models in boundary layer meteorology is usually done using ϵ rather than the variance of the wind component (e.g. Kaimal and Finnigan, 1994). The original formulation of the model in Mann (1994) is also based on ϵ. It was later adapted

to use the variance of the wind velocity in the direction of the mean stream-lines σ_u^2 for load simulations in the respective IEC standard (IEC, 2005a), as this is easier to measure with a cup anemometer.

Due to its importance for turbulence modelling, several publications have proposed methods to estimate ϵ from lidar measurements (Kunkel et al., 1980; Banakh et al., 1995, 1999, 2010; Frehlich et al., 1998; Dobrinski et al., 2000; Frehlich, 2001; Frehlich and Cornman, 2002; Smalikho et al., 2005; Frehlich et al., 2006; Kristensen et al., 2011, 2012; O'Connor et al., 2010; Smalikho and Banakh, 2013; Borque et al., 2016). Considering this abundance of studies using lidars to derive ϵ, it is surprising that robust validations of the suggested methods over longer periods or covering a wider range of atmospheric conditions are rather scarce. Some studies are purely theoretical (Kristensen et al., 2011, 2012) or only use modelling results to evaluate the proposed methods (Frehlich and Cornman, 2002). Other studies include experimental results, but miss a reference to evaluate the quality of the estimates of ϵ estimated from the lidar measurements (Davies et al., 2004, 2005; Smalikho et al., 2005; Frehlich and Kelley, 2008; Chan, 2011). Some studies use reference measurements which are themselves prone to measurement errors such as sodars (Smalikho and Rahm, 2010), radars (Borque et al., 2016) or sonic anemometry in conjuction with Monin-Obukhov similarity theory (Kunkel et al., 1980). In studies, in which high quality reference measurements are available from balloon or tower based measurements, the experimental evidence presented is limited to a few individual profiles (Banakh et al., 1999; Frehlich et al., 1998; Frehlich, 2001; Frehlich et al., 2006, 2008; O'Connor et al., 2010) or a few selected periods of comparisons with sonic anemometry (Banakh et al., 2010; Dobrinski et al., 2000; Smalikho et al., 2013).

While some of the results were promising, also relatively large deviations from the references have been reported. The quality of estimates of ϵ from pulsed lidar measurements remains unclear. The study in Pauscher et al. (2017b, Appendix D) picks up this point. The manuscript evaluates three different methods to estimate ϵ from pulsed lidar measurements using theoretical considerations and experimental results. For one of the methods a correction is developed to remove significant systematic errors.

If no turbulence measurements at a potential wind turbine site are available (e.g. in the early project phase), the turbulence conditions have to be estimated using modelling approaches and/or empirical values. Unfortunately, published measurements in complex and/or forested areas reaching to the height of a modern wind turbine are limited to a few studies (Bradley, 1980; Arnqvist et al., 2015). Our understanding of wind flows in complex and forested terrain, therefore, still largely stems from modelling exercises (e.g. Brown et al., 2001; Allen and Brown, 2002; Finnigan and Belcher, 2004; Ross and Vosper, 2005; Patton and Katul, 2009), wind tunnel studies (Ruck and Adams, 1991; Kaimal and Finnigan, 1994; Neff and Meroney, 1998) or flume experiments (Poggi and Katul, 2007, 2008). Especially for heterogeneous orography and patchy land cover, as found in real world cases, experimental data is missing.

In this scenario one of the main influences on the turbulence environment are varying surface characteristics within the fetch of a wind turbine. However, it is not straight forward to identify the area influencing the turbulence statistics experienced by a wind turbine. Recently, Foken (2013) suggested to use footprint models to improve roughness estimations for resource estimation in wind energy applications. Footprint models were originally developed and are now widely used in the flux community (for recent reviews see Vesala et al., 2008; Leclerc and Foken, 2014). Due to the simplicity of many approaches, they are an appealing approach to relate observed measurements to the surface surrounding a site or to identify wind sectors within which turbulence levels might become critical for the site suitability of a wind turbine. The last manuscript in this dissertation (Pauscher et al., 2017a, Appendix E) presents measurements from a complex forested hill reaching well above the hub height of a modern wind turbine. It also employs the footprint approach to investigate the influence of surface characteristics on turbulence statistics and evaluates its potential suitability for wind energy applications.

1.2. Objectives of the dissertation

Motivated by the needs of the wind energy community this thesis aims at improving and developing experimental and modelling tools to more accurately estimate the wind and turbulence conditions for wind energy applications. The focus in this context is put on wind energy applications in complex and heterogeneous terrain, although many of the approaches are also transferable to areas with simpler surface characteristics and one of the experiments is carried out in flat terrain.

The first focus topic of this dissertation is the investigation of the lidar technology in the context of resource assessments. As the measurement of 'classical' conically scanning lidars in complex orography can be associated with systematic errors (Bingöl et al., 2009), this dissertation evaluates two different methods to mitigate and overcome this problem. The main questions addressed in this dissertation are:

- How large is the lidar error found at a complex and forested site in central Germany?
- How do different flow models perform in reproducing and correcting this error and what are the model sensitivities in this context?
- Can the complex terrain error be overcome by using a ML approach rather than a conically scanning lidar?

The estimation of the turbulence characteristics is an important step in the site assessment process for a wind farm project (IEC, 2005a; Measnet, 2016). The second focus of the dissertation, therefore, is the estimation of turbulence quantities from lidar measurements. Here the major points of investigation are:

- Can errors in measurements of the variance of the wind speed be improved using the multi-lidar approach?
- The experimental assessment of different methods to estimate dissipation rate of turbulent kinetic energy (ϵ) from lidar measurements.

There is a lack of published experimental observations of turbulence statistics from complex and forested terrain covering the height range of a modern wind turbine. Also it is difficult for the experimentalist to relate such observations to the surrounding terrain. In the third part of this dissertation turbulence measurements from a tall mast at a forested hill are presented. The main questions underlying this analysis are:

- What are the turbulence charcteristics at a forested hill over a wide range of measurements heights and what are the main influence factors on the observed turbulence?
- Can we use the footprint-model approach, which was originally developed in the surface flux community, in wind energy applications to relate the observed turbulence statistics to surface characteristics?

2. Methods

2.1. Lidar measurements

2.1.1. The principles of Doppler wind lidars

Doppler wind lidars use the optical Doppler effect to derive the wind velocity along a laser beam emitted by the lidar device. In atmospheric measurement applications, wavelengths which scatter at aerosols are the most popular. For typical wavelengths used in aerosol Doppler lidars, most of the back scatter in the atmosphere is caused by aerosol particles small enough (a few μm) to be advected with the wind speed. These particles are, thus, an effective tracer for wind speed measurements (Huffaker and Hardesty, 1996). The radial wind velocity v_r from a Doppler lidar can be derived using the following equation:

$$f = f_0(1 + 2v_r/c), \tag{2.1}$$

where f_0 is the emitted frequency, f is the frequency of the back-scattered signal and c is the speed of light. To spatially confine the region where the received back scatter is coming from, currently two techniques are available. One is based on pulsed laser technology and the other one on a continuous wave (cw) laser. For the first one the distance follows from the time of flight as

$$d = \frac{c \cdot t}{2}, \tag{2.2}$$

where t is the time between the pulse emission and the measurement of the back scattered signal. This allows multiple measurements in multiple distances along a single measurement beam. For a cw lidar the laser beam is focused in a certain distance to confine the measurement volume and the laser is emitted continuously. Therefore, only one measurement distance is possible. In this dissertation only pulsed lidars were used and, thus, the further discussion will be confined to this technology.

To derive the three dimensional wind vector from a single lidar, usually measurements in multiple locations have to be combined. The radial velocity v_r can be expressed as:

$$v_{r,i} = sin(\phi_i)cos(\theta_i)u_i + sin(\phi_i)sin(\theta_i)v + cos(\phi_i)w_i, \tag{2.3}$$

where the index i denotes the individual measurement location, ϕ is the elevation angle and θ is the angle between the mean wind direction and the beam pointing

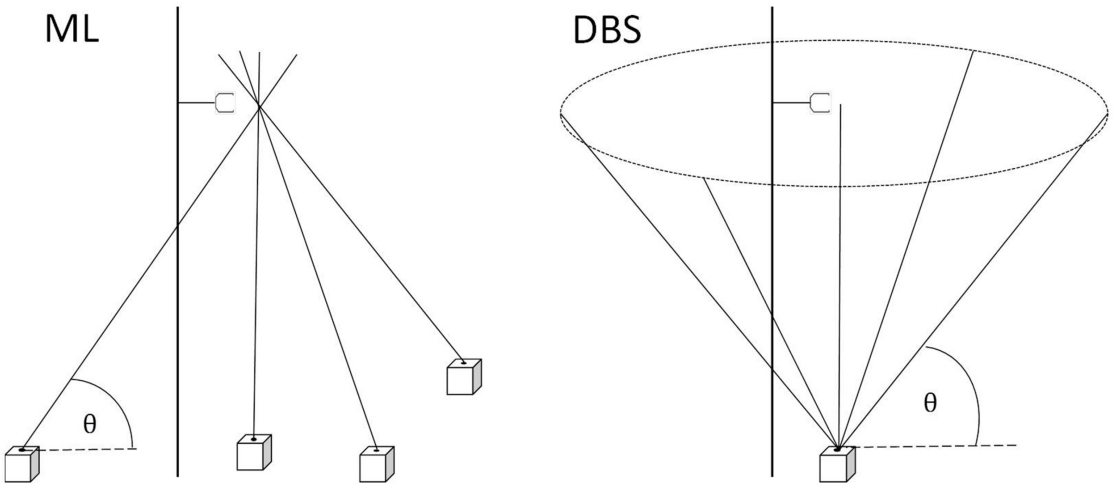

Figure 2.1. Schematic comparing the multi-lidar (ML) and the Doppler-beam-swinging (DBS) techniques; figure taken from Pauscher et al. (2016, Appendix C).

direction of the lidar. u, v and w are the along wind, lateral and vertical components of the wind vector. If the wind field is assumed to be constant across the different measurement points, i.e. u, v and w are independent of i, a combination of at least three beams can be used to derive the wind vector. This restricts measurements with a single profiling lidar to homogeneous flows and in turbulent conditions also to long enough averaging periods. If multiple lidars are used and focused in a single point (ML technique), obviously this limitation does not apply. There are multiple ways to derive the wind speed from a measurement using a single lidar. In this dissertation the so-called Doppler-beam-swinging (DBS) technique is used, which scans the wind field in multiple locations and then directly solves Equation 2.3. A comparison of the ML and DBS techniques is shown in Figure 2.1.

2.1.2. Lidar measurements in complex terrain

As discussed in section 2.1.1, the perquisite to solving Equation 2.3 is flow homogeneity across the different sampling locations which are scanned. In complex terrain, however, the flow can vary across the different sampling points. This can introduce considerable errors in conically scanning lidars (Bingöl et al., 2009; Bradley et al., 2015) such as the DBS lidar.

The most important factor for the deviations from a co-located point measurement in complex terrain is the variation of the flow angle across the different scanning locations which can be induced by the shape of the terrain (Bingöl et al., 2009). To better understand the phenomenon the problem is simplified to the two dimensional case - i.e. a lidar measurement of a two dimensional flow with two beams. Moreover, the beams are assumed to have the same elevation angle and the flow angles from the horizontal at

Table 2.1. Overview of the differnt models used to estimate the complex terrain error of the DBS lidar.

Name	Model type	Forest model	Reference
Meteodyn WT	RANS	porous medium	METEODYN (2014)
WindSim	RANS	porous medium	Castro (2007)
WAsP Engineering	linear	displacement height	Mann et al. (2002)

beam one and beam two are related as $\beta_1 = -\beta_2$ - i.e. the flow is symmetric above the lidar. The influence of the flow angle on the lidar measurement can then be simplified to (Bradley et al., 2015):

$$\breve{u} = u\Big(cos(\beta) + \frac{tan(\beta)}{tan(90 - \Phi)}\Big), \tag{2.4}$$

where β is the angle between the flow and the horizontal at the beam locations, Φ is the angle between the lidar beam and the horizontal plane and $\breve{u}$ is the wind speed measured by the vector reconstruction from the lidar; positive β indicate downwards flows and negative β upwards flows at the first beam location. Equation 2.4 implies, that concave flow regimes such as at a hill top cause an underestimation of u and convex flow as e.g. found in an escarpment causes an overestimation of u.

A potential flow model in conjunction with Equation 2.4 can provide a first estimation of the expected lidar error (Bradley, 2012; Bradley et al., 2012). However, in most real world situations the flow will be much more complex. Therefore, a more complex approach to model the lidar error in complex terrain is chosen for the work in this dissertation (Klaas et al., 2015, Appendix B).

Rather than making simplification about the flow geometry the investigations in this dissertation use terrain data obtained from overflights in conjunction with three-dimensional flow models of varying complexity. The different components of the wind vector at each measurement location of the lidar scan u_i, v_i and w_i are derived from the flow simulations. They are then inserted into Equation 2.3 directly to compute $\breve{u}$. Three different flow models were used to simulate the lidar error. One is a linear model. The other two are simulations based on the Reynolds-averaged Navier-Stokes equations (RANS). All models are commercially available software packages and widely used in the wind energy community. Table 2.1 summarises the key features of the different models. For more details about the flow models and their parametrisation the reader is referred to Klaas et al. (2015, Appendix B).

The following lidar error definition is used in Klaas et al. (2015, Appendix B) and Pauscher et al. (2016, Appendix C):

$$e_{lidar} = \frac{V_L - V_M}{V_M}, \tag{2.5}$$

where V_L is the horizontal wind speed measured by the lidar and V_M is the horizontal wind speed measured by an anemometer mounted on a mast placed on top of the lidar location. This comparison against a point measurement is done as the point measurement provides the well established reference in the wind energy industry. The result of this modelling exercise can then be used to correct for unwanted biases in the wind speed measured by the lidar.

The second approach taken in this work to deal with the difficulties of lidar measurements in complex terrain is to avoid them a priory using a modified scanning approach (Pauscher et al., 2016, Appendix C). As pointed out in Section 2.1.1, crossing multiple lidar beams (Figure 2.1) in the same measurement point does not need the homogeneous flow assumption across a large scanning volume. The averaging volume of the lidar along the beam (compare also Section 2.1.3) can usually be neglected in this context.

2.1.3. Turbulence measurements using lidars

Two of the articles in this dissertation (Pauscher et al. (2016, Appendix C) and Pauscher et al. (2017b, Appendix D)) investigate turbulence measurements with lidars. They both use the same theoretical framework, which is shortly summarised here.

The design of pulsed lidars as used in this work makes spatial averaging inherent in the measurement of the radial velocity v_r. In this context, the width of the beam is usually much smaller than the averaging in the along beam direction and can be neglected. The spatial averaging of the lidar can then be written as (Mann et al., 2009):

$$v_r(\mathbf{x}) = \int_{-\infty}^{\infty} \varphi(s)\mathbf{n} \cdot \mathbf{V}(\mathbf{n}s + \mathbf{x})ds, \tag{2.6}$$

where $\mathbf{x}$ is the location of the measurement beam, $\mathbf{n}$ is the unit vector in the direction of the lidar beam and $\mathbf{V}$ is the three dimensional velocity field. The spatial averaging $\varphi(s)$ is caused by the pulse length and the internal signal processing. The length (full-width-half-max) of the pulse is usually in the order of a few hundred ns. The internal signal processing often uses some kind of tapering window before performing the Fourier transform of the received back scatter signal. In case of the Leosphere lidars (used in this study) a Gaussian window with adjustable length is used (Carriou, 2016). The spatial averaging can then be described by the convolution of the pulse intensity and the tapering window sometimes also called gating function. Figure 2.2 displays the measured pulse intensity and its convolution with the Gaussian gating function with a standard deviation of $\sigma_g = 9.5$ m. Also shown is the convolution of a Gaussian pulse shape with the same gating function, as this is sometimes also given as an approximation (Carriou, 2016) and easier to treat analytically. Note that when transforming from the pulse length to the spatial extend of the averaging window the

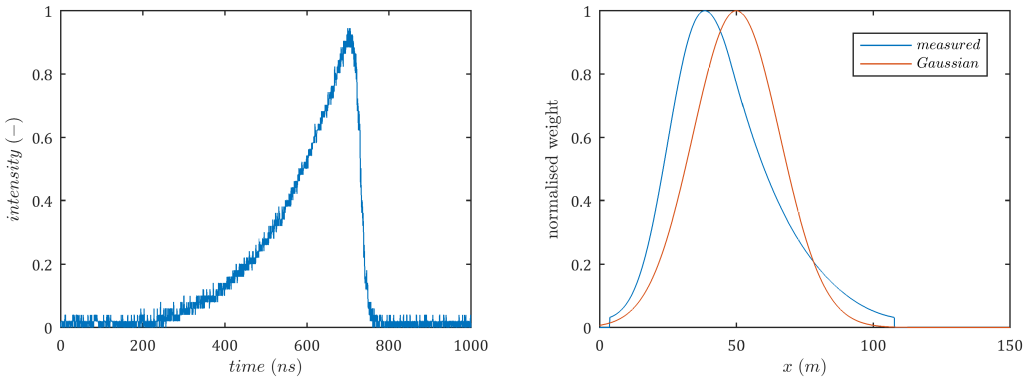

Figure 2.2. Left: Measurement of the pulse intensity for one of the WindScanner devices which was used during the ϵ-Experiment (Section 2.3.3) for a pulse setting of 200 ns; **right:** comparison of the convolution between the pulse intensity and a Gaussian tapering window with $\sigma_g = 9.5$ m and the convolution of a Gaussian pulse intensity with $\sigma_p = 12.8$ m; during the Kassel Experiment 2014 (Section 2.3.2) pulse length and gating function were twice as long; figures taken from Pauscher et al. (2017b, Appendix D)

factor 1/2 needs to be applied, as the light travels from the lidar to the measurement point and back. The spatial averaging as displayed in Figure 2.2 was used in the ϵ-Experiment (Section 2.3.3). For the Kassel 2014 Experiment (Section 2.3.2) $\sigma_g = 19.1$ m and the pulse length was twice of that shown in Figure 2.2. Another measure, which is often given to characterise the spatial averaging, is the full width at half maximum ($FWHM$) of the window function. This is more intuitive as it is a good measure for the physical length of the pulse. The $FWHM$ is related to the standard deviations the windowing functions as:

$$FWHM = 2\sqrt{2\ln 2}\sqrt{\sigma_g^2 + \sigma_p^2}. \tag{2.7}$$

For the ϵ-experiment (Pauscher et al., 2017b, Appendix D) the $FWHM$ is 37.5 m; for the Kassel-Experiment (Pauscher et al., 2016, Appendix C) the $FWHM$ is 75.2 m.

The Fourier transform of Equation 2.6 can be written as:

$$\hat{v}_r(\mathbf{k}) = \varphi(\mathbf{n}\cdot\mathbf{k})\hat{\mathbf{V}}(\mathbf{k}), \tag{2.8}$$

where $\hat{}$ denotes the Fourier transform. If the turbulence field is assumed to be homogeneous, e.g. the one point spectrum of the radial velocity can be expressed as Mann et al. (2009)

$$S_{v_r}(k_1) = n_i n_j \int_{-\infty}^{\infty}\int_{-\infty}^{\infty} |\varphi(\mathbf{n}\cdot\mathbf{k})|^2 \Phi_{ij}(\mathbf{k}) dk_2 dk_3, \tag{2.9}$$

where Φ is the spectral velocity tensor of turbulence and repeated summation of i and j is assumed. If one is interested in deriving statistics from multiple points such as in the DBS measurement (Section 2.1.1) or for the derivation of structure function, the location of the measurement points also becomes important and a phase shift needs to be added to Equation 2.8:

$$\hat{v}_{r,m}(\mathbf{k}) = e^{-i\mathbf{k}\cdot\mathbf{d}_m}\varphi(\mathbf{n}\cdot\mathbf{k})\hat{\mathbf{V}}(\mathbf{k}), \tag{2.10}$$

where $\mathbf{d}$ denotes the location of the measurement and m is the index for the measurement location. The detailed implications for the variance and spectral estimates of the wind vector components for the DBS and the ML method are discussed in Pauscher et al. (2016, Appendix C).

Since small scale turbulence is most strongly affected by the spatial averaging of the lidar, Pauscher et al. (2017b, Appendix D) investigate the measurement of fine-scale turbulence with lidars. For this purpose three approaches to estimate the dissipation rate of turbulent kinetic energy ϵ are evaluated experimentally, which are based on the theoretical framework in Equations 2.6 - 2.10.

The first relies on the power spectral density in the inertial sub-range (Champagne et al., 1977; Smalikho, 1997; Banakh et al., 2010). The second one is based on the approach presented by Bouniol et al. (2003) and O'Connor et al. (2010), which relies on the calculation of short-term variances by cutting a longer time series into shorter pieces. A correction is developed to this method in this dissertation to remove significant systematic errors, which were present before. Both approaches use temporal statistics at a single measurement location. The third approach relies on the relationship between the spatial structure function and ϵ in the inertial sub-range. In contrast to the first two methods the spatial statistics rather than the temporal ones are used. It is the first experimental evaluation of an approach theoretically derived by Kristensen et al. (2011). For a definition of the structure function and a discussion of its relationship to the power spectral density see e.g. Monin and Yaglom (1975). The derivation of the individual methods is quite lengthy and the reader is therefore referred to Pauscher et al. (2017b, Appendix D) for a detailed explanation.

2.2. Fetch characterisation for wind turbines

2.2.1. Footprint modelling

Turbulence characteristics are strongly influenced by surface characteristics. To identify the area which influences the observed turbulence statistics a footprint modelling approach is used in this dissertation (Pauscher et al., 2017a, Appendix E). One of the biggest advantages of this approach over more complex flow models is its simplicity. Therefore, footprint approaches based on complex flow models using e.g. large eddy simulations (e.g. Steinfeld et al., 2008) do not seem reasonable in this context. If an

LES of the site is done, the turbulence statistics from the flow simulation can be used directly.

For this work the footprint model proposed by Kljun et al. (2015) is used as it is easy to apply and is also valid for elevated measurements heights and shows good agreement with more complex models. In general, the footprint is the transfer function between the source of passive scalar at the surface and its flux (or concentration) at a point in the atmosphere. The footprint equation can be formulated as (Horst and Weil, 1992):

$$F(x_m, y_m, z_m) = \int_{-\infty}^{-\infty} \int_{-\infty}^{-\infty} Q(x_m - x', y_m - y', z = z_0) f(x_m - x', y_m - y', z_m - z_0) dx dy, \tag{2.11}$$

where F is the flux, Q is the source function and f is the footprint function. The index m indicates the measurement location.

When transferring this approach to turbulence quantities, it can be seen that the formulation in Equation 2.11 is a rather crude simplification as turbulence is not 'released' within a source area and not conserved during its transport through the atmosphere. Sink and source terms (production and dissipation of turbulent kinetic energy) are distributed in 3D-space and turbulence does not behave as a passive/conservative quantity. Nevertheless, surface roughness and surface ruggedness (the most important turbulence creating surface properties) can be be related to a surface area. The footprint model concept is thus seen as a proxy to the area of influence for the turbulence statistics measured at the measurement location. This assumption has also been been made for the estimation of the effective roughness for footprint modelling of flux measurements (Göckede et al., 2004, 2006) and wind turbines (Foken, 2013).

Some evidence for the appropriateness of the assumption that the footprint of a scalar and that of turbulence quantities are similar can be found in the fact that the vertical length scales of the footprint concept and the blending height concept as well as the internal boundary-layer concept are very similar (Horst, 2000). Moreover, a convection-diffusion equation for shear stress in analogy to passive scalars can be derived and assuming the equality eddy diffusivity and eddy viscosity, the blending height of scalar fluxes and shear stress are very similar (Philip, 1997).

2.2.2. Terrain classification

While widely used in the wind energy community, a standard definition the term 'complex terrain' or a measure for terrain complexity is still missing. One of the reasons might be the different needs for different applications. In the IEC standards for power performance (IEC, 2016) and turbine design terrain (IEC, 2005a) complexity is classified by fitting planes through the base of the turbine tower and the terrain. The first is more conservative and defines critical slopes between 0.03 and 0.1, the latter one as approx. 0.17. The German technical guideline TR6 (FGW, 2014) adopts the second approach. The international Measnet standard (Measnet, 2016) uses a photograph of

a sample site and the hint that slopes exceeding 0.3 are indicative for the definition of complex sites.

Here, also a critical slope is used as a measure for terrain complexity. The method is a slight modification of the ruggedness index as originally defined for resource assessment purposes (Bowen and Mortensen, 1996; Mortensen and Petersen, 1997). Areas exhibiting a slope greater than 0.3 are classified as rugged. This roughly corresponds to the slope at which flow separation occurs (Wood, 1995). In contrast to the definition by Bowen and Mortensen (1996) this includes any direction and not only the flow direction towards the mast/turbine. The ruggedness r_s is then defined as the percentage of the footprint area exhibiting a slope greater than 0.3 (Pauscher et al., 2017a, Appendix E):

$$r_s = \frac{A_{r_s}}{A_{effect}}, \tag{2.12}$$

where A_{r_s} is the area with slopes greater than 0.3 and A_{effect} is the area influencing the measurement location. In Pauscher et al. (2017a, Appendix E) the 80-%-effect area of the footprint is used in this context.

The concept of describing roughness using the roughness lengths is one of the key principles of boundary-layer meteorology and thus much better investigated. For purposes of roughness averaging in the footprint area a simple logarithmic averaging (Taylor, 1987) is used in the work for this dissertation.

2.3. Experiments

Since this dissertation is heavily based on experimental data, the experiments play a key role. For the work presented here two different experimental sites were used. The first is the measurement site at Rödeser Berg, which is run by Fraunhofer IWES and, within the institute, the central experimental facility to investigate wind conditions and measurement technology in complex terrain. The second one is the wind turbine test station at Høvsøre which is operated by the Technical University of Denmark (Peña et al., 2016).

2.3.1. The 200-m-mast at Rödeser Berg

The complex terrain test station at Rödeser Berg is located close to Kassel in the center of Germany (51° 21' 46" N, 9° 11' 43"E). The area around the site is typical for low mountain ranges in Germany. It is characterised by a hilly orography and a patchy landscape. The hill tops are often covered by forests while the lower elevations are mainly used for agricultural purposes. The region surrounding Rödeser Berg has seen substantial wind energy developments in recent years. Detailed information on the terrain surrounding the area can be found in Pauscher et al. (2017a, Appendix E). On

top of the ridge of Rödeser Berg a 200 m tall measurement mast was erected in 2012 and forms the core piece of the experimental infrastructure.

The mast is heavily equipped with sensors between heights of 2 m and 200 m. To accurately sense the wind profile, cup and sonic anemometers are installed between 10 m and 200 m. All cup anemometers were calibrated according to Measnet standards (Measnet, 2009) on a yearly cycle and classified according to (IEC, 2005b). Cup anemometers used in this study are of type Thies first class advanced. Sonic anemometers are of the type Gill HS50 and Thies 3D. To ensure minimal flow disturbance by the mast structure the anemometers were mounted on booms with a length of 5.4 m. Booms were additionally guyed to the mast and stabilised with a metal tube to ensure minimal boom vibration effects. The sensors, which were used in the analysis in Klaas et al. (2015, Appendix B), Pauscher et al. (2016, Appendix C) and Pauscher et al. (2017a, Appendix E), are listed in Table 2.2

2.3.2. Kassel 2014 Experiment

The measurement mast at Rödeser Berg also forms the reference measurement for the evaluation of the mutli-lidar measurements presented in Pauscher et al. (2016, Appendix C) during the Kassel Experiment 2014. The measurement campaign in 2014 served as a preparatory experiment to the extensive use of multi-lidar measurements during the complex terrain experiment in the New European Wind Atlas (Mann et al., 2017).

To successfully and accurately perform the multi-lidar measurements the experiment relied on the WindScanner technology (Vasiljevic, 2014; Vasiljevic et al., 2016). The WindScanner technology is basically a software package which allows the operation of multiple scanning lidars from a master computer and permits temporally and spatially synchronised measurements.

Table 2.2. Overview of the anemometers used in the analysis in Klaas et al. (2015, Appendix B), Pauscher et al. (2016, Appendix C) and Pauscher et al. (2017a, Appendix E); * indicates sensors used in Klaas et al. (2015, Appendix B); $^{\cup}$ indicates sensors used in Pauscher et al. (2016, Appendix C); † indicates sensors used in Pauscher et al. (2017a, Appendix E).

height (m)	sensor type	sampling frequency (Hz)	orientation (°)
$60^{\dagger\star}$	Thies First Class Advanced Cup Anemometer	1	321
$80^{\star}$	Thies First Class Advanced Cup Anemometer	1	140
$80^{\dagger\star}$	Thies Ultrasonic Anemometer 3D	20	320
$120^{\star}$	Thies First Class Advanced Cup Anemometer	1	139
$120^{\dagger\star}$	Thies First Class Advanced Cup Anemometer	1	319
$135^{\dagger}$	Gill HS50 Ultrasonic Anemometer	50	319
$160^{\star}$	Thies First Class Advanced Cup Anemometer	1	136
$160^{\star}$	Thies First Class Advanced Cup Anemometer	1	317
$188^{\cup\dagger}$	Gill HS50 Ultrasonic Anemometer	50	316
$191^{\dagger}$	Thies First Class Advanced Cup Anemometer	1	316
$200^{\star}$	Thies First Class Advanced Cup Anemometer	1	mast top

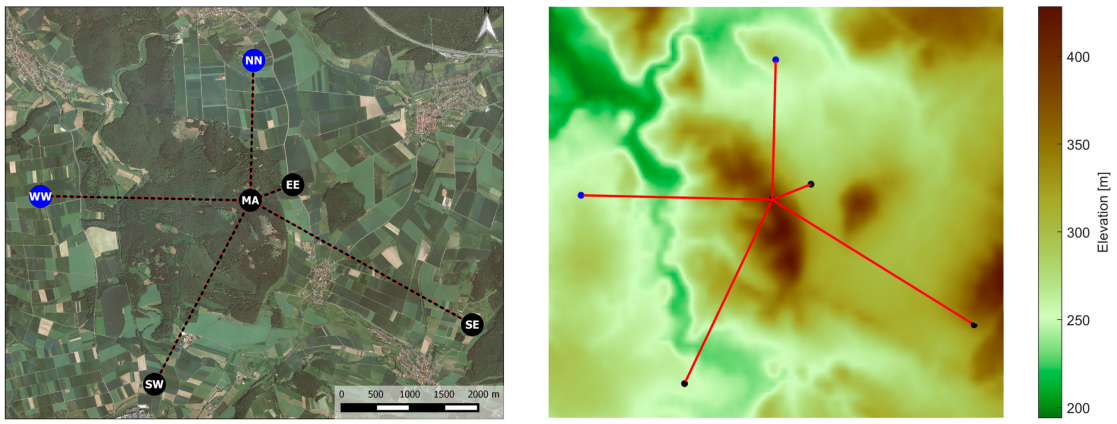

Figure 2.3. Left: locations of the WindScanner devices during the Kassel 2014 Experiment; the black dots indicate positions of WindScanners which were analysed; **right:** terrain (data source: Shuttle Radar Topography Mission version 2.1) and trajectories of the intersecting lidar beams for the ML measurement. The windcube v2 is also located at the MA position; figure taken from Pauscher et al. (2016, Appendix C).

As Doppler lidars rely on the back scatter of light, a clear line of sight to the target location needs to be ensured. In complex terrain, however, vision can often be obstructed by terrain or vegetation. During the planing phase of the experiment, maps of the area were derived from geographical data to identify regions from which the reference mast could be seen. The WindScanners were then set up using differential GPS and hard target returns to ensure a high pointing accuracy (Vasiljevic, 2014). Positions and angles were validated using hard target returns from the mast.

2.3.3. The ϵ-Experiment at Høvsøre test station

Like the Kassel Experiment 2014 the ϵ-Experiment was relying on the WindScanner technology. However, it only uses a single lidar staring at a reference sonic anemometer (Metek USA1 F2901A) mounted at a height of 100 m at a measurement mast (Figure 2.4). The lidar beam during the measurement only had an elevation angle of 3.58° and, thus, is almost horizontal. This ensures that multiple measurement distances at almost the same height could be probed.

The configuration of the lidar was chosen to suit the needs for turbulence measurements. With an accumulation time of approx. 0.5 s the sampling rate is chosen at the upper limit to have a reliable operation of the WindScanner system (Lea, 2016). Also the spatial separation of the individual range gate was chosen very small (1 m). In fact, the physically possible resolution of the range gates is limited to 0.6 m, due to the internal signal processing (Carriou, 2016). The pulse duration was set to 200 ns and the internal signal processing used a gating function with $\sigma_g = 9.5$ m which corresponds to using 64 points in the Fourier transform when analysing the Doppler spectrum. For

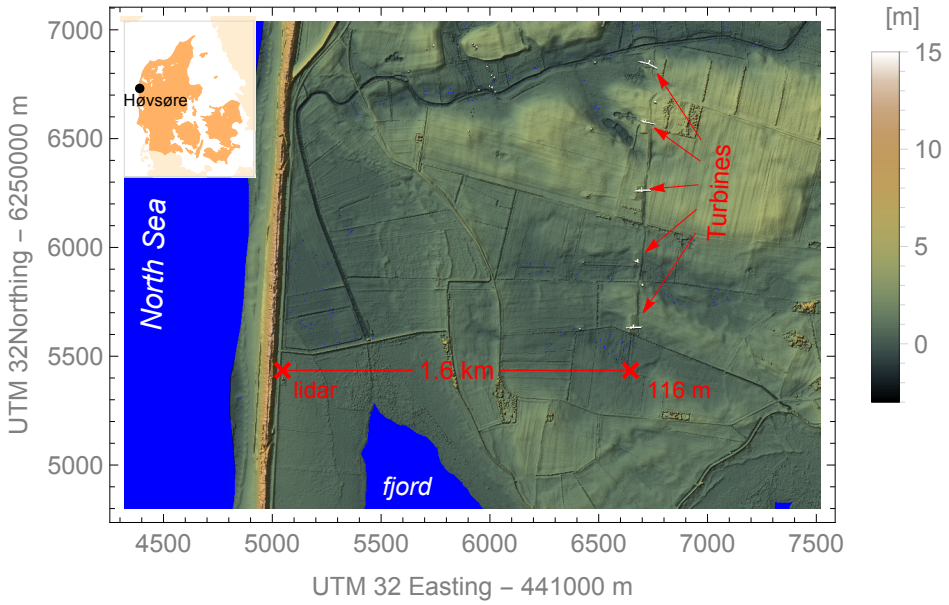

Figure 2.4. Satellite image of the measurement site during the ϵ-Experiment; red crosses indicate the positions of the lidar and the mast; the distance between the two is approx 1.6 km; figure taken from Pauscher et al. (2017b, Appendix D).

this configuration the WindScanners provide good measurements. If both the size of the gating window or the pulse lengths are further reduced, previous experience has shown worse measurement quality (Lea, 2016).

3. Results

3.1. Lidar measurements of the mean wind speed in complex terrain

The first part of this work evaluates different approaches towards improving measurements of the mean wind speed in complex terrain using lidar technology. The first step was the quantification of the error of a conically scanning DBS lidar at a typical complex site for wind energy developments in the German lower mountain ranges (Klaas et al., 2015, Appendix B). The observed deviation (Figure 3.1) clearly reflects the shape of the orography of the terrain at Rödeser Berg. Flow which is directed perpendicular to the ridge of the hill (30° - 90° and 210° - 270°) exhibits a clear underestimation of the mast-based cup anemometer measurement. These directions are associated with convex terrain profile and most likely convex flow. As outlined in Section 2.1.2 a negative bias would also be expected in the horizontal wind speed in this situation from theoretical considerations. In contrast, the mean wind speed of the lidar for flow along the ridge (140° - 180° and 300° - 20°) of the hill is similar and for the second sector slightly higher than the reference mast. The interpretation of the observations for these sectors is more difficult but might correspond to the fact that the mast and lidar are placed a few hundred meters from the highest point of the ridge and the ridge shows a slightly concave shape.

While all investigated flow models seem to be able to reproduce the general pattern of the lidar-mast deviations, there are large differences in the magnitude of the modelled deviations (Figure 3.1a). Interestingly, the linear model (WAsP Engineering) significantly overestimates the lidar-mast deviations. In contrast, given the right parametrisation, the two more complex RANS models show a good agreement with the observations.

In addition to the more complex model type both RANS models also have a forest model implemented. In the linear model forest can only be represented by using a displacement height approach. A sensitivity analysis of one of the RANS models is shown in Figure 3.1b. In general, the most complex forest model (dissipative) gives the best results. Adding 'more' forest (higher trees and higher density) also reduces the error and improves the model estimations. In fact, turning the forest model off during the simulations produces some of the worst results (blue line in Figure 3.1b). The real forest is in many places relatively dense and with tree heights of apporox. 30 m relatively high.

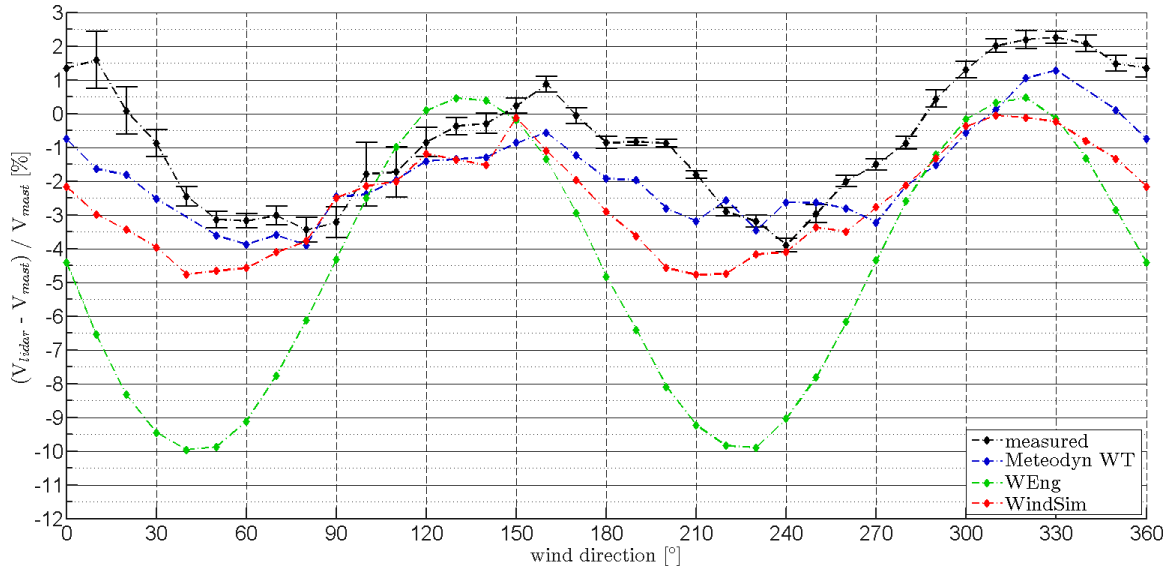

(a)

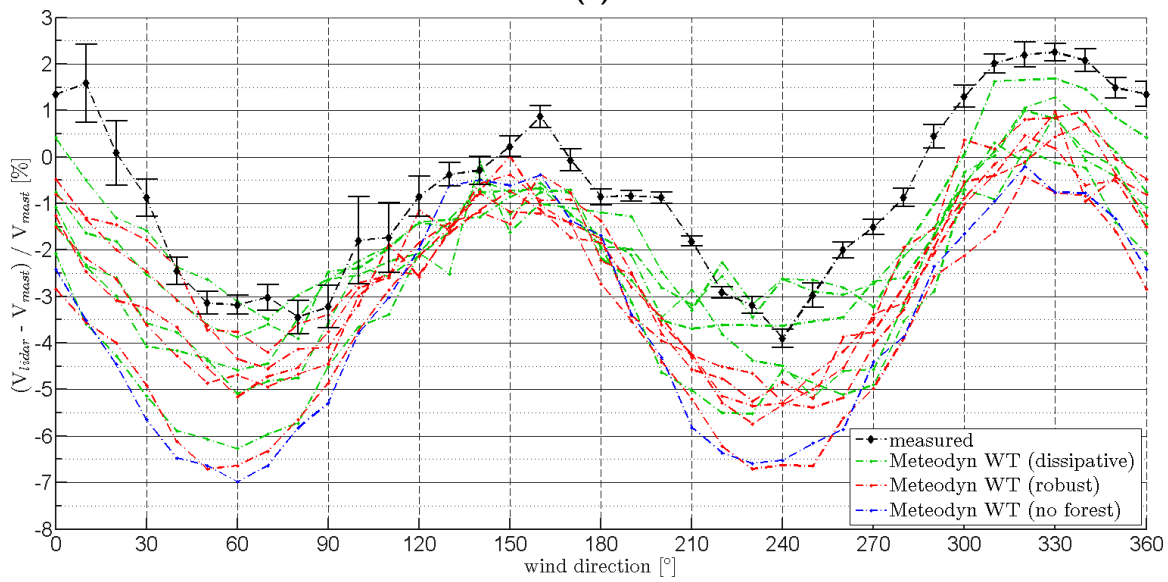

(b)

Figure 3.1. **(a)** Measured lidar-mast deviation of the horizontal wind speed V at Rödeser Berg for a measurement height of 120 m in comparison to the complex terrain error as simulated using different models; **(b)** sensitivity of the modelled complex terrain error of the lidar for different forest parametrisations in one of the RANS models (Meteodyn WT); note that the scales on the y-axis are different between the two figures; the error bars indicate the confidence intervals; only wind speeds $\geq$4 m s^{-1} are considered; figures taken from Klaas et al. (2015, Appendix B).

A likely explanation for this observation is that over forested hills flow separation will generally occur earlier and be stronger (Finnigan and Belcher, 2004). The occurrence of flow separation will in turn also reduce the flow inclination angles of the stream lines and will, thus, reduce the complex terrain error of the lidar. WAsP Engineering does not have a forest model (Mann et al., 2002) and therefore cannot reproduce this effect. An introduction of a forest model might improve the results for WAsP engineering. However, it should also be noted that linear models generally perform worse than more complex RANS models in reproducing the flow in complex situations, where flow separation occurs (Palma et al., 2008).

A key point when modelling the lidar error in complex terrain seems to be the accurate representation of the surface cover - especially forest. Existing studies so far only focused on proving the existence of the complex terrain error and to some degree on quantifying its magnitude using experimental results and modelling (e.g. Bingöl et al., 2009; Bradley, 2012; Bradley et al., 2012, 2015). This study, in contrast, demonstrates the sensitivity of the complex terrain error to surface cover. Moreover, it provides a comparison of different modelling approaches of different degrees of sophistication and, gives a first indication of the range of their applicability. Creating an error map from the flow model as done in Klaas et al. (2015, Appendix B) during the experiment design can provide useful guidance on where to place the the conically scanning lidar to minimise the error.

An alternative to the application of flow models is to avoid the complex terrain error in the experimental setup. If multiple lidar devices are available their beams can be crossed in a single point (Section 2.1.1). The advantage is that the homogeneous flow assumption over a large scan volume is not necessary. The first experimental evaluation of this ML approach in complex terrain is performed in Pauscher et al. (2016, Appendix C). Figure 3.2 shows the comparison between a reference Sonic (Gill HS50) and the triple- (Figure 3.2a) and dual-Doppler (Figure 3.2b) lidar as well as a DBS lidar (Figure 3.2c). The agreement is excellent for both multi-lidar systems. The DBS-system shows a slightly worse agreement to the reference sonic. Especially for smaller wind speeds the scatter is larger.

The comparison between the dual- and triple-Doppler lidar shows no significant difference. A dual-Doppler system, thus, seems to be an appropriate tool to accurately measure the horizontal wind speed at a complex site. It should be noted, however, that the elevation angles of the lidars were relatively small (3.5° and 6°) and the angle between the two lidar beams was close to 90°, which is ideal for this setup. Investigation of other WindScanner combinations (not shown here) indicated slightly worse results for smaller angles between the lidars. For a full comparison of the different multi-lidar setups see Pauscher et al. (2016, Appendix C).

A directional analysis reveals that also the directional variation of the mean deviation from the mast measurements is reduced for the multi-lidar approach (Figure 3.3). The DBS lidar again shows the typical terrain-following pattern as in Figure 3.1. The DBS lidar shows slightly higher values when compared to the reference. The reasons for this

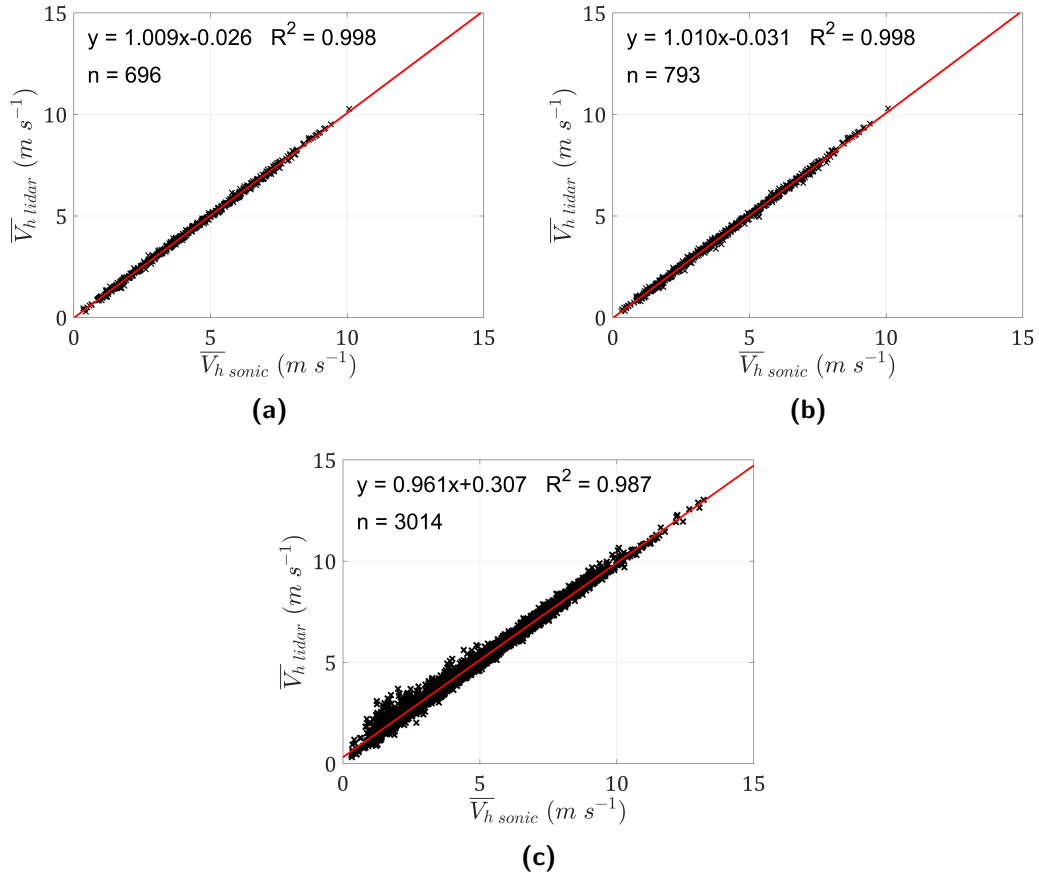

Figure 3.2. Scatter plots of the comparison between the sonic at 188 m and the **(a)** multi-lidar measurements using three WindScanners (SE, SW and EE in Figure 2.3); **(b)** multi-lidar measurements using two WindScanners (SE and SW in Figure 2.3); $w = 0$ m s^{-1} is assumed; **(c)** windcube v2 measuring in DBS mode (WC in Figure 2.3); the red line indicates the linear regression; figures taken from Pauscher et al. (2016, Appendix C).

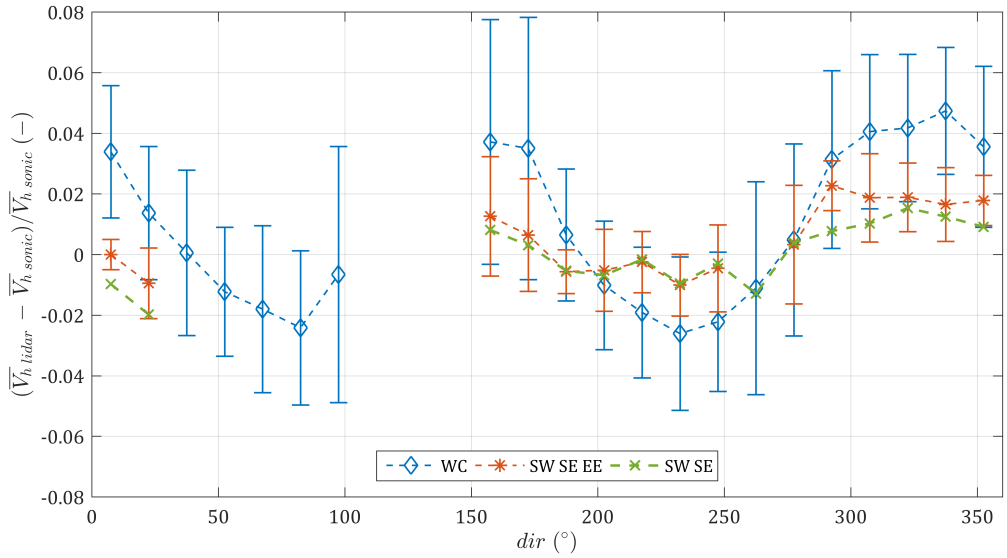

Figure 3.3. Comparison of the directional deviation of the horizontal wind speed $\overline{V}_h$ of different lidar measurements from the reference sonic (Gill HS50) at 188 m; SW SE indicates the dual-Doppler, SW SE EE the triple-Doppler and WC the DBS measurement; only wind speeds $\geq$4 m s^{-1} are considered; figure modified after Pauscher et al. (2016, Appendix C).

behaviour are not entirely clear. Some of the difference to the experiment shown in Figure 3.1 might be caused by the lower wind speeds during the ML experiment. Also two different DBS lidars were used in the two experiments. The reference was a sonic while in Figure 3.1 a cup anemometer provides the reference.

Some directional variation still remains for the ML-measurements, but is to be expected. An analysis of cup anemometers mounted on opposing booms at 191 m (not shown) revealed a directional dependence of the difference of up to 1.5 % between the two cup anemometers even outside of the direct mast shadow. This is slightly higher as the estimation according to IEC (2016) would suggest (less than 0.5 %; compare also Klaas et al. (2015, Appendix B)). In fact, the directional pattern in Figure 3.3 is in line with the observed differences between the cups, where smaller wind speeds are observed if the anemometer is in front of the mast. This direction corresponds to the sector around 320°, where the ML measurements are higher than the reference sonic. Also, differences in the accuracy which might be present between the different WindScanners can cause direction-dependent deviations between the ML measurements and the reference sonic.

3.2. Turbulence measurements using lidars

3.2.1. Variance measurements from ML-measurements

Pauscher et al. (2016, Appendix C) report on an experimental comparison of different lidar measurement techniques to estimate turbulence quantities in complex terrain. The first focus of the analysis is put on the evaluation of the variances of the radial wind velocity measured $\overline{v_r'^2}$ by the WindScanner systems. In comparison to the respective wind component derived from the sonic anemometer by coordinate rotation a clear underestimation can be observed for the WindScanners surrounding the measurement mast. Most of this can be attributed to a relatively large probe volume (the pulse length was set to 400 ns and $\sigma_p = 19.5$ m) and to a lesser degree the temporal averaging (2 s). In contrast,a vertically pointing WindScanner, which was placed next to the mast showed no significant underestimation of $\overline{v_r'^2}$, when compared to the reference sonic. For this WindScanner the pulse length was chosen as 100 ns and $\sigma_g = 6.4$ m.

Scatter plots comparing the variance of the u-component ($\overline{u'^2}$) between different lidar setups and the reference sonic are shown in Figure 3.4. For ML combinations with favourable angles (SW/SE/EE and SW/SE in Figure 2.3) the reduced variances are also propagated into the variances of the horizontal components of the wind vector (Figure 3.4a&b). The dual-Doppler combination SW/EE shows a worse correlation and increased scatter (Figure 3.4c). Here, also the slope of the linear regression is higher. A very similar behaviour can be observed for SE/EE (not shown here, see Pauscher et al. (2016, Appendix C)). One of the possible reasons is a contamination of the observed horizontal component by the vertical component, caused by the relatively large elevation angle of the EE-scanner (22.3°). The assumption that w does not contribute to the observed radial variance in EE is a rather crude approximation. Another reason might be the smaller angle between the lidar beams, which can lead to a stronger error propagation of errors in the radial variances (Stawiarski et al., 2013). The angles for the SW/EE and SE/EE combinations are significantly smaller than for SW/SE (Figure 2.3). The DBS lidar shows the worst agreement with the sonic (Figure 3.4d). The likely reason for this is a cross-contamination of $\overline{u'^2}$ by the other components of the Reynolds-stress tensor (Sathe et al., 2011; Sathe and Mann, 2012). The results for $\overline{v'^2}$ are very similar for those of $\overline{u'^2}$ (for details see Pauscher et al. (2016, Appendix C)).

The processes influencing $\overline{u'^2}$ are also clearly reflected in the spectra of the different lidar setups. For the ML measurements a clear underestimation for the high wave-number range can be observed (Figure 3.5a&b). This reflects the spatial averaging caused by the relatively large probe volume of the WindScanners. The spectra of the DBS lidar show a much more complex pattern. The effects of the cross-contamination (Sathe and Mann, 2012) are reflected in the bumpy shape of the spectra (Figure 3.5c). The flat section at the high wave number end corresponds to the fact that the DBS only generates a new independent value every approx 5-6 s (Canadillas et al., 2010).

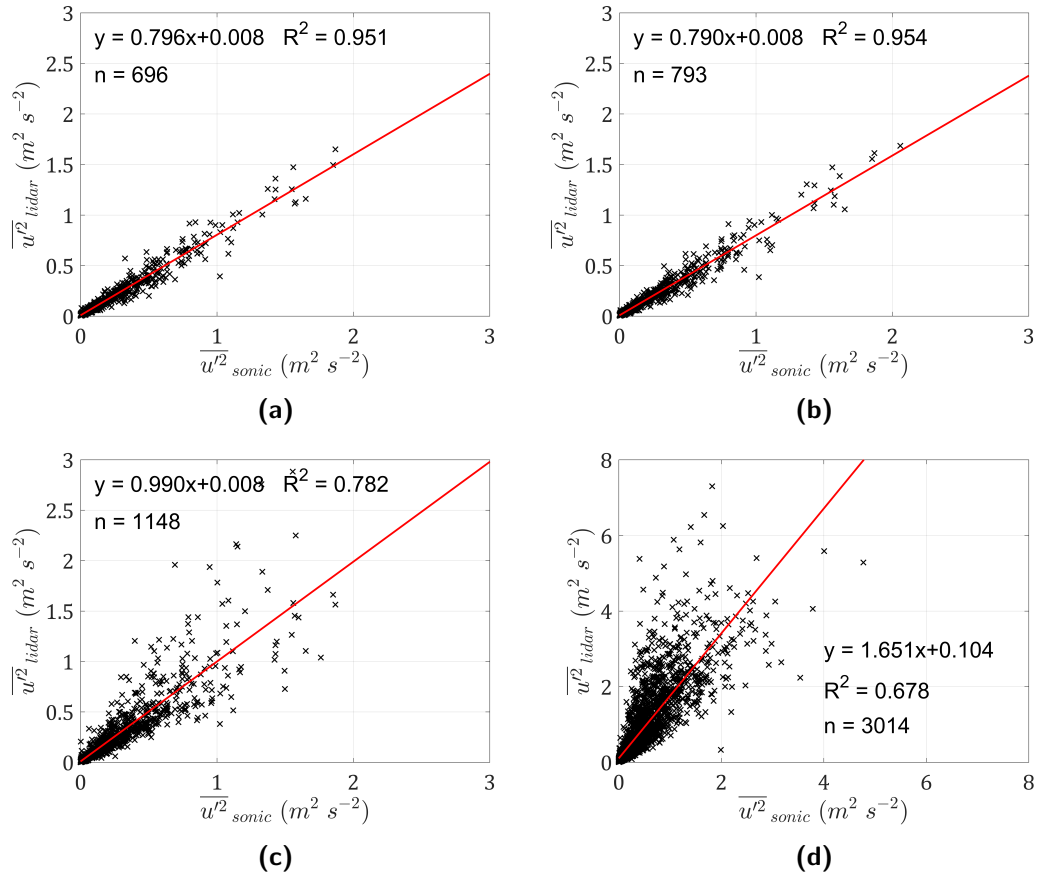

Figure 3.4. Scatter plots for $\overline{u'^2}$ of the comparison between the sonic at 188 m and the **(a)** multi-lidar measurements using three WindScanners (SE, SW and EE in Figure 2.3); **(b)** ML measurements using two WindScanners (SE and SW in Figure 2.3); $w = 0$ m s^{-1} is assumed; **(c)** ML measurements using two WindScanners (SW and EE in Figure 2.3); $w = 0$ m s^{-1} is assumed; **(d)** the windcube v2 measuring in DBS mode (MA in Figure 2.3); the red line indicates the linear regression; figures taken from Pauscher et al. (2016, Appendix C).

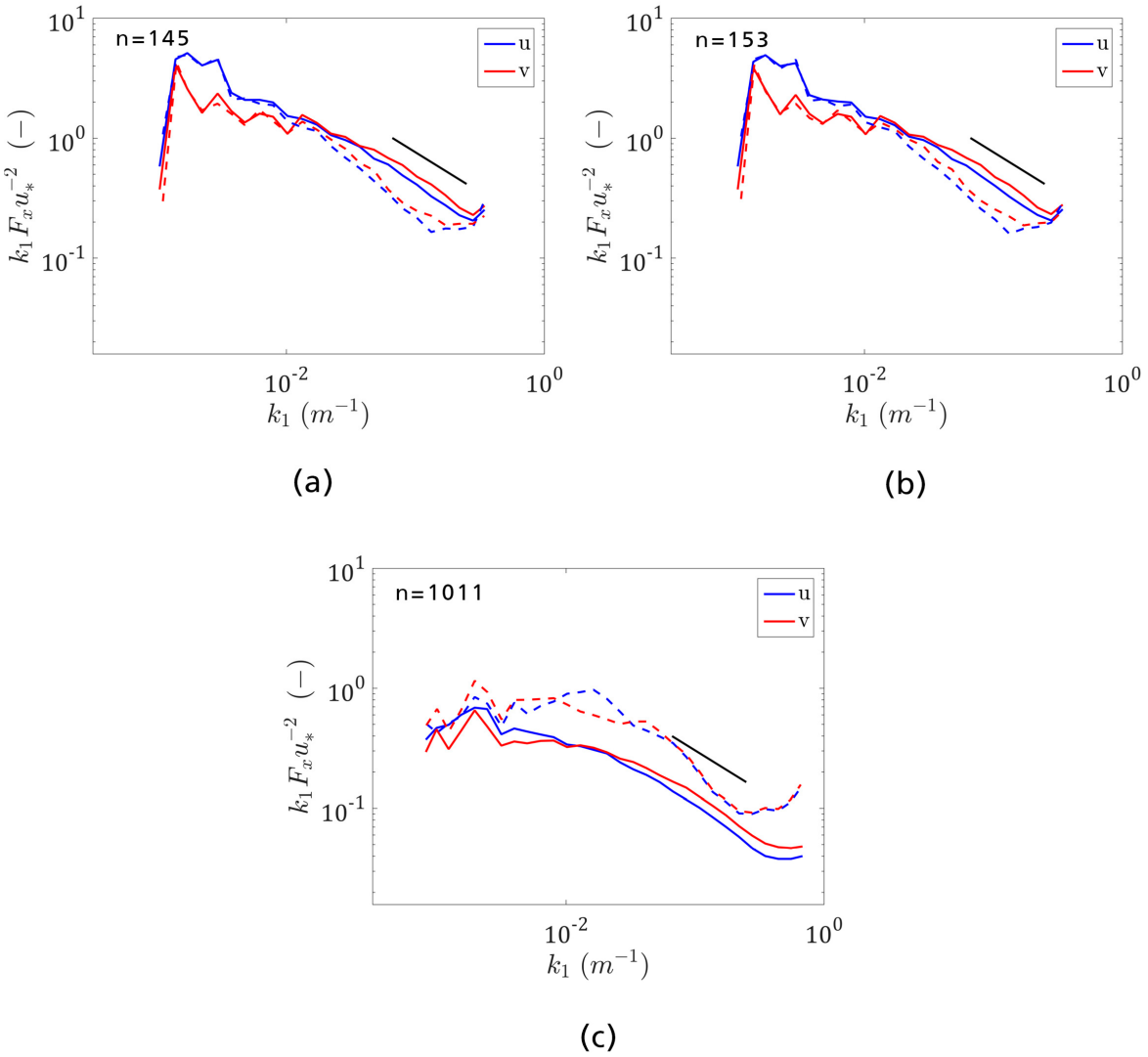

Figure 3.5. Composite spectra **(a)** multi-lidar measurements using three WindScanners (SE, SW and EE in Figure 2.3); **(b)** multi-lidar measurements using two WindScanners (SE, SW in Figure 2.3); **(c)** the windcube v2 measuring in DBS mode (WC in Figure 2.3); solid lines are the sonic spectra; dashed lines are the lidar spectra; sonic time series have been aggregated to 0.5 Hz (**a** & **b**) and 0.89 Hz (**c**); before calculation of the spectra; only periods with $u_{sonic} > 4$ m s^{-1} and $\overline{u'^2}_{sonic} > 0.2$ m^2 s^{-2} were used in the spectral averaging; u_* is the friction velocity computed from the sonic anemometer measurements; the black line indicates the theoretical -2/3-slope in the inertial sub-range; figures taken from Pauscher et al. (2016, Appendix C).

The findings in Pauscher et al. (2016, Appendix C) reiterate the complexity of measuring turbulence using lidars. The DBS lidar is prone to errors when measuring the variance of the wind vector components. Other studies have reported overestimation (Sathe et al., 2011; Newman et al., 2016) and underestimations (Sathe et al., 2011) of $\overline{u'^2}$ and $\overline{v'^2}$ by DBS lidar depending on measurement setup and atmospheric conditions.

The results from the ML measurements indicate that, given a careful setup, the ML approach is a promising way forward for measuring turbulence with lidars. The unsolved problem which remains is the attenuation of the turbulent fluctuations at high wave numbers - i.e. the fine-scale turbulence. Some investigations concerning this topic were conducted in Pauscher et al. (2017b, Appendix D) and to a lesser extend also in Pauscher et al. (2016, Appendix C) and are presented in the following section.

3.2.2. Fine-scale turbulence measurements with a pulsed lidar

The observations in Pauscher et al. (2016, Appendix C) motivate a more detailed investigation of fine-scale turbulence measurements using lidars. This analysis is presented in Pauscher et al. (2017b, Appendix D) and Pauscher et al. (2016, Appendix C). As outlined in Section 2.1.3, knowledge of the spatial averaging is key to a derivation of small-scale turbulence from lidar measurements. Figure 3.6 compares the spectral transfer function $\varphi^2(k)$ derived from theoretical consideration to the observations obtained from measurements.

The theoretical averaging functions in Figure 2.2a show a good agreement with the experimentally determined $\varphi^2(k)$ from the cross-spectral method (for details on the method see Pauscher et al. (2017b, Appendix D)). The difference between the measured pulse and the assumption of a Gaussian pulse shape is rather small, if $\sigma_l = 15.8$ m is chosen. In contrast, $\varphi^2(k)$ obtained from the spectral method shows a much slower drop-off. It roughly corresponds to $\sigma_l = 9$ m, which is significantly smaller than the theoretical considerations. An observation which was also made by Angelou et al. (2012) for a continuous wave lidar and is consistent with the observations in Pauscher et al. (2016, Appendix C) (see Erratum).

Due to its relation to the spectral density in the inertial sub-range, the dissipation rate of turbulent kinetic energy ϵ is well suited to model and characterise small scale turbulence. Pauscher et al. (2017b, Appendix D), therefore, focus on the estimation of ϵ from a pulsed lidar. Three methods are investigated in detail. First and as a baseline scenario, the 'classical' spectral method exploiting the -5/3-slope of the spectrum in the inertial sub-range is applied. For the second method an approach originally proposed by Bouniol et al. (2003) and O'Connor et al. (2010) based on short term variances was improved and corrected for the contribution of larger turbulence scales. Compared to the original formulation a significant bias towards an overestimation of ϵ could be removed. The third method is based on the spatial structure function (Kristensen et al., 2011) and is the first experimental evaluation of this method. For details of the individual approaches the reader is referred to Pauscher et al. (2017b, Appendix D).

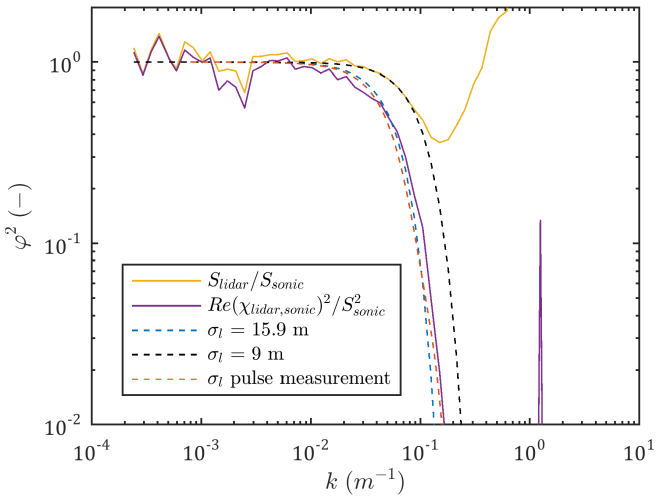

Figure 3.6. Comparison of $\varphi^2(k)$ obtained from theory in comparison to the experimentally determined values during the ϵ-Experiment; only wind directions $\pm 5°$ the beam direction of the lidar were used; the theoretical functions (dashed blue and orange lines) correspond to the spatial averaging functions in Figure 2.2.

In general, all methods produce acceptable results and ϵ_{lidar} shows a good correlation to the measurements from the reference sonic (Figure 3.7). The analysis of the statistical error in Pauscher et al. (2017b, Appendix D) showed that the statistical random errors in the different methods are also similar and is between approx. 10-30 %. The majority of the scatter in the comparison in Figure 3.7 is thus likely to stem from the noise in the measurements. For all methods an average underestimation of the ϵ_{sonic} by ϵ_{lidar} which is in the order of magnitude of the random error can be observed. For the spectral method this underestimation a first order correction using $|\varphi(k)|^3$ (see also Equation 2.9) can be applied. For the wave-number interval k = 0.0454 - 0.1 m^{-1} the median underestimation can be reduced from 39 % to 2 % applying this correction. For the short term variance method the underestimation is likely to be caused by the fact that scales outside the inertial sub-range contribute to the short term variances. In case of the structure function method the underestimation (19 %) might be related to uncertainties in $\varphi(k)$ and correlated noise along the measurement beam. For the structure-function and the short-term variance method a removal of the noise for small ϵ, which are connected to week turbulence, is important.

From Figure 3.7 it is difficult to make a judgement, which of the methods is the best to estimate ϵ from lidar measurements. The differences between the individual methods rather lie in their applicability to different measurement scenarios. The spectral as well as the short term variance method require a fast sampling rate at the same point to allow for the calculation of the temporal statistics at wave number intervals which lie within the inertial sub-range. Currently available pulsed lidar technology requires

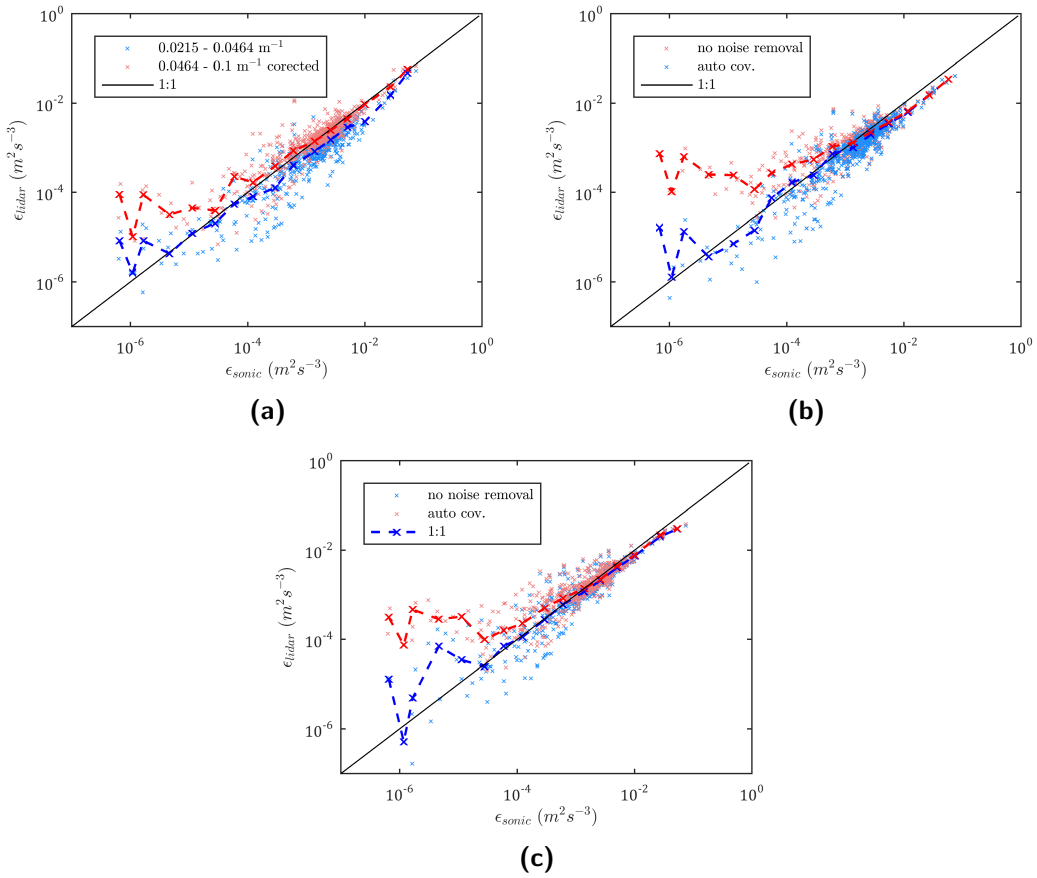

Figure 3.7. Comparison of ϵ as estimated from the reference sonic and the lidar measurements for **(a)** the spectral method; the colors indicate two different wave number intervals (given in the legend) which were used for the estimation of ϵ_{lidar}; for the red line ϵ_{lidar} is corrected using $|\varphi(k)|^3$ **(b)** ϵ_{lidar} based on short term variances; blue: noise was removed using the auto covariance method (Frehlich, 2001); red: no noise removal; **(c)** ϵ_{lidar} based on the structure function method; color code see **(b)**; darker markers and dashed line indicate the binned median values.

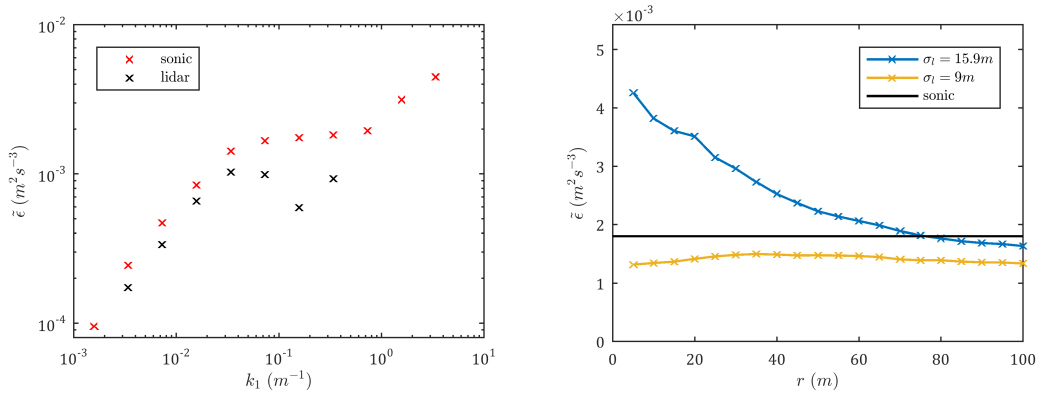

Figure 3.8. **(a)** median ϵ derived from the reference sonic and the lidar during the ϵ-Experiment using the spectral method for different wave-number intervals; **(b)** influence of the choice of the separation distances (r) on the median ϵ_{lidar} derived from the structure-function method for the theoretically derived $\varphi(k)$ ($\sigma_l = 15.8$ m) and the experimentally determined $\varphi(k)$ ($\sigma_l = 9$ m); the black line indicates the median value derived from the sonic measurements using the spectral method; figures taken from Pauscher et al. (2017b, Appendix D).

accumulation times of at least in the order of 0.5 - 1 s. Moreover, currently available scanner heads usually have a maximum speed of approx 30° s^{-1}. The spectral and short-term variance method are mainly suitable for staring configurations and, thus, primarily interesting for research applications. The short-term variance method should only be applied in the corrected version presented in Pauscher et al. (2017b, Appendix D). The downside of the corrected method is, that the equations become more complex and it looses some of the previous appeal, which was its simplicity.

One of the advantages of the spectral method is, that the spectral analysis of the measurement data allows a better judgement, whether the scales used to derive ϵ are contained within the inertial sub-range and at which scale noise will become dominant. An example of such an analysis is shown in Figure 3.8a. The first minimum in lidar measurements (black crosses) is reassuring that the signal at high wave numbers is not dominated by noise.

The structure function method exploits the capability of a pulsed lidar to sample multiple points of the atmosphere along the measurement beam quasi-simultaneously. This reduces the need for a high sampling rate at the same point. It is, thus, more suitable for more complex scan patterns like DBS, plane-position indicator or range-height indicator scans and presents the most flexible option. One thing to keep in mind when applying the structure function method is the increased sensitivity of the estimate of ϵ to uncertainties in $\varphi(k)$ with decreasing r (Figure 3.8b). This consideration needs

to be balanced against the need to measure at scales which are small enough to lie in the inertial sub-range.

It should be noted here, that the experimental results in Pauscher et al. (2017b, Appendix D) were obtained at a height of 100 m above ground. At lower heights the results might get worse as turbulent scales get smaller. For the short-term variance this might lead to the situation that at high wind speeds the time interval gets too small to reliably calculate the variance. Here again the structure function method is advantageous as pulsed lidars allow for a relatively fine resolution of the measurement distances. Moreover, Figure 3.8a indicates that the measurement of ϵ is still possible at small separation distances. Given an appropriate noise removal the scatter for $r =$ 5 m (not shown) is similar as for $r = 35$ m.

Generally, the methods are also transferable to more complex sites. It should be noted, however, that the spatial heterogeneity can affect the performance of the structure function method. In this context small separation distances are again advantageous. Also the distance along the beam over which the structure function is averaged is limited in this situation.

3.3. Turbulence characteristics at Rödeser Berg

While the work in Sections 3.1 and 3.2 focused on different methods to improve measurements of wind statistics, the last part of this dissertation deals with the interpretation of measured wind statistics. For this purpose a detailed investigation of the turbulence statistics at the 200-m-mast at Rödeser Berg (Section 2.3.1) is presented. The experimental results in Pauscher et al. (2017a, Appendix E) are the first published field observations of high quality turbulence statistics from a forested hill covering the height range of a modern wind turbine.

Figure 3.9 displays the directional behaviour of turbulence statistics for the u- component of the wind vector by wind direction. This wind component is chosen here as it is the most important for load calculations in wind turbine design. Details for the other wind-vector components can be found in Pauscher et al. (2017a, Appendix E). The observed values of σ_u/u_* are smaller than $\sigma_u/u_* = 2.4$, which is usually assumed for flat and homogeneous terrain (Panofsky and Dutton, 1984), but for most sectors slightly higher than those observed at a tall mast over a homogeneous forest in Sweden (Arnqvist et al., 2015). It should be pointed out that the statistics in 3.9 were derived using 10-minute intervals, which is common practice in wind energy applications. In many other micrometeorological applications a 30-minute interval is the standard interval (Aubinet et al., 2012). The average σ_u/u_* (and σ_u/u_*) increases by approx. 7 - 13 % depending measurement on height. The shorter interval can thus explain some of the deviations from flat terrain.

A clear directional dependence of I_u is visible with the strongest variation found at the lowest investigated height (80 m). As only neutral conditions are considered, the

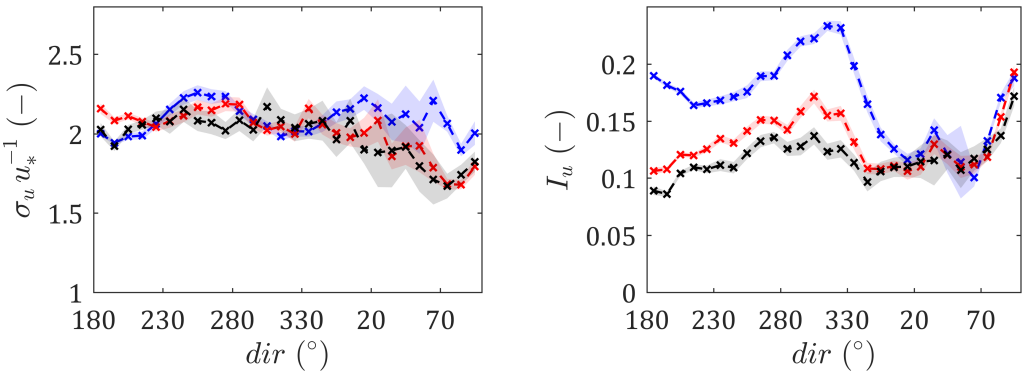

Figure 3.9. Turbulence statistics under neutral conditions as measured by sonic anemometers at different heights of the mast at Rödeser Berg; blue 80 m, red 135 m and black 188 m; **(a)** integral turbulence statistic of of the wind along the mean stream lines σ_u/u_*; **(b)** turbulence intensity of the wind along the mean stream lines $I_u = \sigma_u/u$; the schaded areas denote the 95-%-confidence-intervals derived using student's t-statistics; figures taken from Pauscher et al. (2017a, Appendix E).

patterns are likely to stem from the surface characteristics in the upstream area of the measurement. Indeed, the observed patterns correlate with the terrain characteristics of the surrounding terrain. All heights show the maximum turbulence intensity for wind directions between approx. 280° and 340°. A forested ridge with a relatively high terrain ruggedness forms the first few km in this direction. For the sector 360° to 60° the terrain is much more open and also turbulence intensities are lower.

This (intuitive) qualitative observation motivated a further investigation of the relation between terrain characteristics and the observed turbulence statistics in Pauscher et al. (2017a, Appendix E). The analysis requires two steps to be taken. Firstly, the area of effect (i.e. the area of the surface which is influencing the measurement) has to be identified. Secondly, the surface characteristics have to be quantified. Especially for orography effects, there is a lack of established simple methods for the second task.

The work in Pauscher et al. (2017a, Appendix E) proposes a new combination of different existing methods to tackle these problems. Footprint modelling, which is usually used to model the source area for scalar fluxes, is applied to identify the relevant surface area. The transfer of the footprint modelling approach has been suggested for resource estimation problems before (Foken, 2013), but has not been evaluated to interpret turbulence statistics in a wind energy context. For the quantification of the terrain ruggedness a variation of a method originally developed for resource estimation (Bowen and Mortensen, 1996; Mortensen and Petersen, 1997) is used (see also Section 2.2.2).

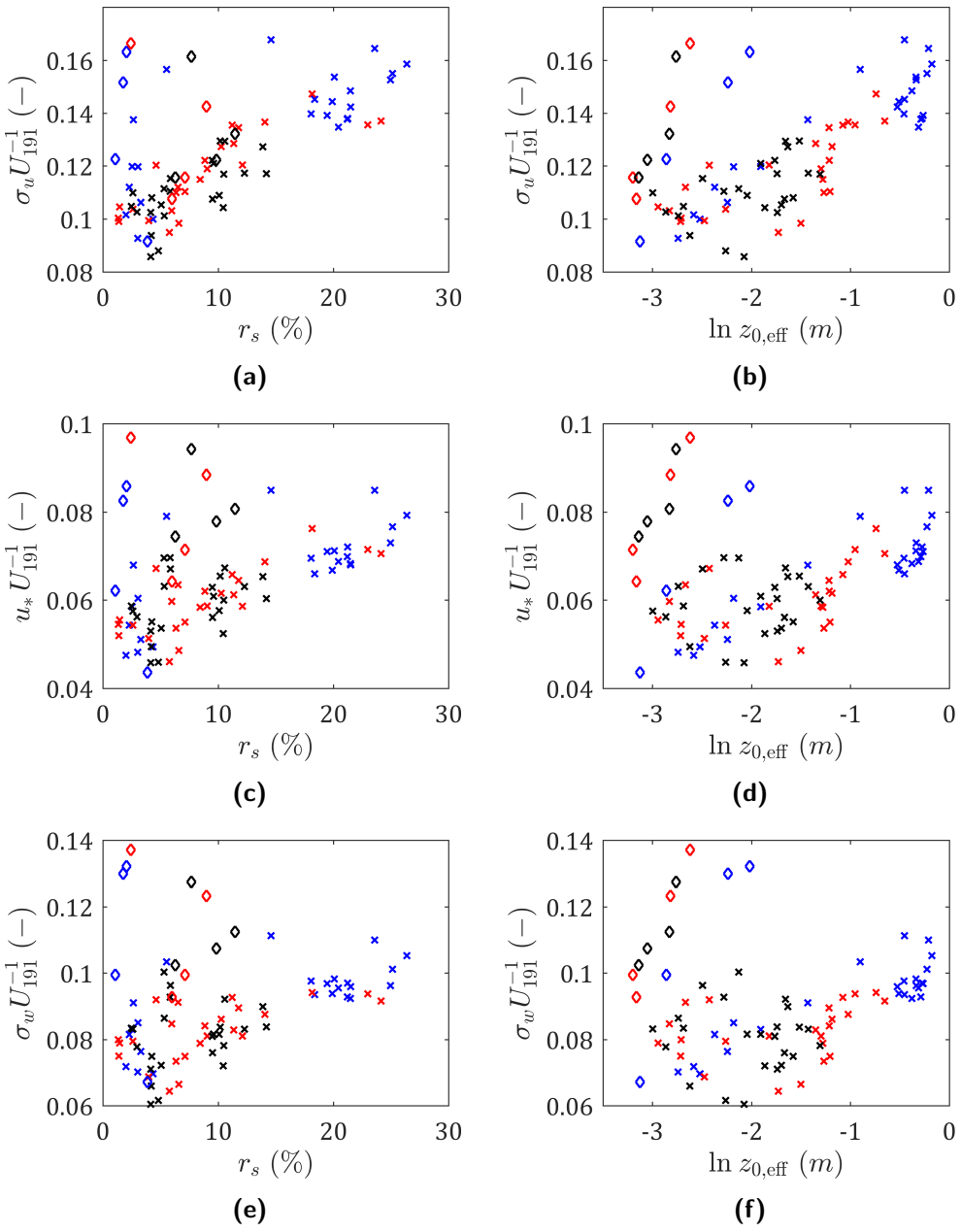

Figure 3.10. Scatter plots of second-order turbulence statistics in relation to surface properties within the 80-%-effect-area of the footprint climatologies for neutral conditions ($|L|$ >500 m); **left column:** normalised turbulence quantities vs the index for ruggedness r_s; **right column:** normalised turbulence quantities vs the effective roughness $z_{0,eff}$; **(a,b)** $\sigma_u U_{191}^{-1}$ **(c,d)** $u_* U_{191}^{-1}$ and **(e,f)** $\sigma_w U_{191}^{-1}$; calculations are based on 10° bins; diamonds indicate bins which lie within $60 - 100°$; periods when $U_{120} > 4$ m s^{-1} are excluded from the analysis; for colour coding see Figure 3.9; figures taken from Pauscher et al. (2017a, Appendix E).

Figure 3.10 shows the relation of the normalised second order turbulence statistics with the ruggedness (left) and roughness (right) within the modelled footprint of the measurement. The normalisation of the turbulence statistics is done with a common measurement height (191 m) to improve the comparability among the different heights. For $\sigma_u U_{191}^{-1}$ (Figure 3.10a) a good correlation to the surface characteristics within the footprint can be found and observations more or less cluster around a linear relationship. This applies for the ruggedness of the terrain as well as for the logarithm of the effective roughness derived from the land cover inside the footprint area $z_{0,eff}$. The linear correlation coefficient is $r = 0.62$ for r_s and $r = 0.60$ for $ln(z_{0,eff})$. However, for the sector between $60 - 100°$ some outliers can be observed. It is interesting to note that these outliers are directed towards high turbulence and low values of r_s and $z_{0,eff}$, respectively. In the aforementioned direction several hills which are higher than Rödeser Berg are found in a few km distance. These terrain features might not be appropriately captured by the footprint modeling and/or the definition of r_s.

For $u_* U_{191}^{-1}$ the correlation is worse than for $\sigma_u U_{191}^{-1}$. r is 0.43 and 0.26 for r_s and $ln(z_{0,eff})$, respectively. For $\sigma_w U_{191}^{-1}$ r further drops to 0.28 and 0.12, respectively. This indicates that the predictive power of the modelled footprint is better for the turbulence statistics of the u-component than for the w-component.

In particular for the u-component, the footprint modelling approach in combination with the terrain classification scheme seems to be a promising way forward when relating surface characteristics to observed turbulence intensities. For the site at Rödeser Berg terrain ruggedness and forest cover (high roughness) are closely related as the hill tops are mainly forested and the lower areas are primarily used for agriculture. Therefore, it is difficult to differentiate between the effect of the two..

In wind energy siting applications, turbulence intensity is usually described as a function of wind speed. For turbine design according to standard turbulence classes this is done using the empirical normal turbulence model (NTM) (IEC, 2005a). The NTM is then compared against the representative turbulence intensity (90-%-percentile) measured on site. Figure 3.11 shows the comparison of the representative turbulence intensity and the NTM for the three standard turbulence classes defined in IEC (2005a). To make the different heights comparable among each other they are all normalised on the wind speed at 120 m (U_{120}), which is a typical hub height of a modern wind turbine. The observation which catches the eye is the large difference in σ_u accross the different heights. Especially the difference between 60 m and 180 m is exceeding the difference between the different turbine classes. This is likely to be related to the heterogeneity of the terrain. In the investigated sector the closer surroundings are characterised by forested and orographically complex terrain. The further distance is comparatively flat and homogeneous (compare also Figure 1 in Pauscher et al. (2017a, Appendix E)).

When compared to the shape of the NTM, the representative turbulence shows a trough-like behaviour for wind speeds between approx. 6-12 m s^{-1} with a minimum at approx. 9 m s^{-1}. The occurrence of stable atmospheric stratification shows a maximum within this wind speed range as well suggesting that the damping effect of

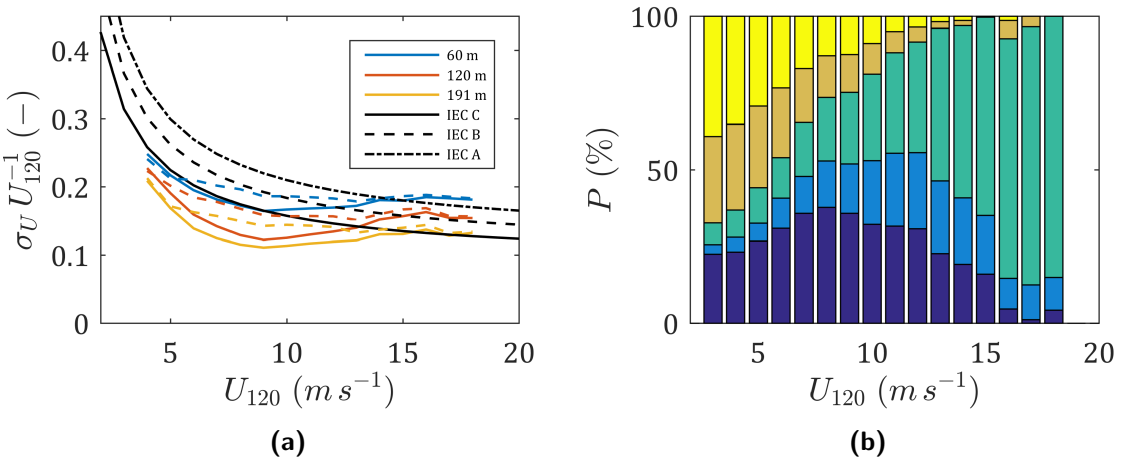

Figure 3.11. **(a)** 90-%-percentile of $\sigma_{u_x} U_{120}^{-1}$ for the sector 180-210° in comparison to the normal turbulence model for different turbulence classes as defined in IEC (2005a); solid lines indicate all wind speeds; dashed lines are only neutral conditions; **(b)** stability distribution as measured by the sonic at 135 m; dark blue: very stable, light blue: stable, green: neutral; orange: unstable, yellow: very unstable; figure taken from Pauscher et al. (2017a, Appendix E).

the stable stratification reduces the turbulence intensity. In fact, if only neutral cases are considered, the trough-like behaviour disappears.

The stable stratification can induce different processes which explain the occurrence of relatively high wind speeds during stable conditions. One is the reduction of the frictional forces in stable stratification, which causes a speed up of the wind at elevated heights and can result in the formation of a low level jet (LLJ) (Blackadar, 1957). The LLJ has also been suggested to influence the wind resource in northern Germany (Emeis, 2014; Lampert et al., 2016) and has been shown to frequently occur in forested low mountain ranges in Germany (Serafimovich et al., 2017). Atmospheric stability also influences the interaction of the flow with the terrain. The speed-up over hills can be significantly increased in stable conditions (Carruthers and Choularton, 1982; Bradley, 1983). Moreover, streamlines can be diverged around the hill (Snyder et al., 1985). This can elevate the hilltop measurements in the atmospheric boundary-layer or even place them above the atmospheric boundary-layer. A combination of these effects at Rödeser Berg is likely.

From the perspective of wind energy the observations are important because in a wind climate as found at Rödeser Berg the wind turbine will produce most of its power output between 6-12 m s^{-1}. Therefore, the majority of the fatigue loads will occur within this wind-speed interval. Fatigue loads, in turn, are strongly influenced by turbulence intensity. Lower turbulence intensity is usually related to lower fatigue loads.

4. Conclusions

The work in this dissertation was motivated by the demand for refined measurement techniques for resource and site assessment applications in wind energy and the need for an improved understanding of these measurements in complex and heterogeneous terrain. The presented dissertation addresses these issues in three steps: First, the investigations focus on improving pulsed Doppler-lidar measurements in complex terrain. Second, methods are developed and experimentally investigated to perform turbulence measurements using Doppler-lidar. Third, measured turbulence characteristics are analysed and their relation to surface properties is investigated. Progress has been made in all three points and the main conclusions are summarised in the following.

The first part of the dissertation focuses on errors, which can be induced in conically scanning Doppler-lidar measurements in complex terrain due to the inhomogeneous flow across the scanning volume. The simulation of the problem shows that the surface cover has a significant influence on the errors. Forest cover reduced the error in the simulations. The reason for this result is thought to lie in the stronger flow separation, which is present in the forest case. These findings are also supported by the experimental results presented in this dissertation. Given the choice of an appropriate model and parametrisation, flow modelling can provide a good estimation of the effects of complex flow on conically scanning lidar measurements. In practical applications, like wind resource estimation, it can also serve as a first correction to the measured horizontal wind speed and are valuable in the experiment design. An inappropriate model can lead to a gross overcorrection of the lidar measurements.

The modelling exercise is, however, associated with additional uncertainties. The ML-technique provides an alternative and allows to overcome the complex terrain error by changing the measurement design. While previously suggested theoretically (e.g. Bradley et al., 2015), the work in this dissertation for the first time demonstrates experimentally the improved accuracy of the ML-technique when measuring in complex terrain. Given an appropriate setup, two scanning lidars are enough to make accurate measurements of the horizontal wind speed. These findings are especially valuable as scanning lidars can also be used to probe the flow at multiple locations. This untaps the full potential of the flexibility of the instruments. ML-measurements also form a corner stone of the complex terrain experiments in the New European Wind Atlas (Mann et al., 2017), which is one of the key research projects in site and resource assessment in Europe at the moment.

One of the largest drawbacks of the lidar technology in wind energy applications is its current inability to measure turbulence accurately enough for site assessment

applications. The experimental results in this dissertation confirm this for a conically scanning DBS-lidar. The evaluation of the ML-measurements clearly demonstrates the advantages of the ML-technique to measure the variance of the horizontal wind vector components and suggests that they are a promising way forward to solve this problem. The spectral analysis, however, shows, that at small scales turbulence is attenuated by the probe volume averaging. This leads to an underestimation of the variances of the reference by the ML-method.

Motivated by these observations, the capability of lidar measurements to capture fine-scale turbulence was investigated. Analysis of the spectral transfer function revealed that a theoretical derivation from instrument parameters overestimated the experimentally determined effect of the spectral averaging on the lidar spectra. When evaluating the radial velocity spectra of the lidar against the sonic measurements, the attenuation of the turbulence signal only started at wave numbers higher than the theoretical prediction. Interestingly, this effect could not be found for the cross-spectral method, which agreed well with the theoretical prediction. While a similar observation has been made before for continuous wave lidars (Angelou et al., 2012), the reasons remain unclear and should be further investigated.

The analysis of three methods to derive the dissipation rate of turbulent kinetic energy ϵ from lidar measurements demonstrated that pulsed lidars can be used to measure this parameter over a wide range of values spanning several decades. A prerequisite, however, is, that the spatial averaging characteristics of the lidar are known from e.g. a measurement using a reference sonic as done here. For the short-term variance method it should be stressed again that the corrected method developed in Pauscher et al. (2017b, Appendix D) needs to be applied. Otherwise, a large overestimation of ϵ can result.

All three approaches yielded similar results when compared to the sonic anemometer measurements and are generally suitable to derive ϵ from lidar measurements. The difference between the methods lies in their range of applications. The spectral and the short-term variance method rely on temporal statistics and thus need a high sampling frequency. In contrast, the structure-function method exploits the capability of a pulsed lidar to sample multiple distances along the laser beam quasi-synchronously and uses spatial statistics. This makes it more suitable for more complex scan patterns such as DBS, PPI or RHI scans, where the same locations are probed more intermittently. Also the fact that good results could be achieved at very small scales makes it potentially suitable at lower measurement heights. While the experiment was carried out in flat terrain, the findings are transferable to complex terrain as well. For the structure-function method, it should be noted that the spatial heterogeneity will introduce some additional uncertainty in the method. Small separation distances become even more important in this context.

Besides the methodological work on lidar measurements, also turbulence statistics from a tall mast at a complex and forested site were analysed. An approach to relate observed turbulence characteristics to surface characteristics was developed. It is

based on a simple footprint model combined with a description of the area within the footprint by ruggedness and roughness. Especially the turbulence intensity of the horizontal wind speed, which is the most important in wind energy applications, showed a good correlation with the surface characteristics inside the modelled footprints. The results indicated that, despite the simplicity of the approach, it can provide a useful tool to interpret turbulence measurements in complex terrain. Further experimental validations and comparison with more complex models - e.g. large eddy simulations - could also develop the footprint modelling approach into a tool to perform a first site characterisation in site assessment applications.

When compared to the currently used standards for wind turbine design (IEC, 2005a), the observed turbulence characteristics at Rödeser Berg showed some distinctive differences to the assumptions which are usually made. The turbulence intensity was significantly reduced in the wind speed range between 6 - 12 m s^{-1}. This is especially interesting, because the majority of the energy output from a wind turbine, which would be typically installed at the investigated site, would stem from this wind speed range. The reduced turbulence intensity could be related to the frequent occurrence of stable conditions between 6 - 12 m s^{-1}. In site assessment usually neutral conditions are assumed. The results indicate that the inclusion of stability can improve turbine design and potentially save costs. Besides the stability effects, the variance of the wind components normalised on a common height were strongly dependent on height. This suggests that the assumption of a constant variance across the whole rotor area, as usually done in load modelling for wind turbines, might not be adequate for a complex site. The discrepancy between the observed turbulence characteristics and the current standard for turbine design also reiterate the advantage the wind energy community gains from improvements in turbulence measurements using lidars - especially for complex terrain sites.

References

Allen, T. and Brown, A. R.: Large-eddy simulation of turbulent separated flow over rough hills, Boundary-Layer Meteorology, 102, 177–198, doi:10.1023/A:1013155712154, 2002.

Angelou, N., Mann, J., Sjöholm, M., and Courtney, M.: Direct measurement of the spectral transfer function of a laser based anemometer, Review of Scientific Instruments, 83, 033 111, doi:10.1063/1.3697728, 2012.

Antoniou, I., Ejsing Jørgensen, H., Mikkelsen, T., Friis Pedersen, T., Warmbier, G., and Smith, D.: Comparison of wind speed and power curve measurements using a cup anemometer, a LIDAR and a SODAR, in: Scientific proceedings of the European Wind Energy Conference and Exhibition 22.11.2004 - 25.11.2004 - London, United Kingdom, pp. 47–51, European Wind Energy Association, 2004.

Arnqvist, J., Segalini, A., Dellwik, E., and Bergström, H.: Wind statistics from a forested landscape, Boundary-Layer Meteorology, pp. 1–19, doi:10.1007/s10546-015-0016-x, 2015.

Aubinet, M., Vesala, T., and Papale, D., eds.: Eddy Covariance, Springer, Dordrecht, doi:10.1007/978-94-007-2351-1, 2012.

Banakh, V. A., Smalikho, I. N., Köpp, F., and Werner, C.: Representativeness of wind measurements with a cw Doppler lidar in the atmospheric boundary layer, Appl. Opt., 34, 2055–2067, doi:10.1364/AO.34.002055, 1995.

Banakh, V. A., Smalikho, I., Köpp, F., and Werner, C.: Measurements of turbulent energy dissipation rate with a cw Doppler lidar in the atmospheric boundary layer, Journal of Atmospheric and Oceanic Technology, 16, 1044–1061, doi:10.1175/1520-0426(1999)016⟨1044:MOTEDR⟩2.0.CO;2, 1999.

Banakh, V. A., Smalikho, I. N., Pichugina, E. L., and Brewer, W. A.: Representativeness of measurements of the dissipation rate of turbulence energy by scanning Doppler lidar, Atmospheric and Oceanic Optics, 23, 48–54, doi:10.1134/S1024856010010100, 2010.

Behrens, P., O'Sullivan, J., Archer, R., and Bradley, S.: Underestimation of monostatic sodar measurements in complex terrain, Boundary-Layer Meteorology, 143, 97–106, doi:10.1007/s10546-011-9665-6, 2012.

Berg, J., Vasiljevíc, N., Kelly, M., Lea, G., and Courtney, M.: Addressing spatial variability of surface-layer wind with long-range WindScanners, Journal of Atmospheric and Oceanic Technology, 32, 518–527, doi:10.1175/JTECH-D-14-00123.1, 2015.

Berkhout, V., Faulstich, S., Hahn, B., Hirsch, J., Linke, K., Neuschäfer, M., Pfaffel, S., Rafik, K., Rohrig, K., Sack, A., Stark, E., Schuldt, L., and Zieße, M.: Wind energy report Germany 2014, Kassel, 2015.

Bingöl, F., Mann, J., and Foussekis, D.: Conically scanning lidar error in complex terrain, Meteorologische Zeitschrift, 18, 189–195, doi:10.1127/0941-2948/2009/0368, 2009.

Blackadar, A. K.: Boundary layer wind maxima and their significance for the growth of nocturnal inversions, Bulletin of the American Meteorological Society, 38, 283–290, 1957.

Bofinger, S., Callies, D., Scheibe, M., Saint-Drenan, Y.-M., and Rohrig, K.: Potenzial der Windenergienutzung an Land - Kurzfassung, Bundesverband WindEnergie e.V., Berlin, Germany, 22 pp., 2011.

Borque, P., Luke, E., and Kollias, P.: On the unified estimation of turbulence eddy dissipation rate using Doppler cloud radars and lidars, Journal of Geophysical Research: Atmospheres, 121, 5972–5989, doi:10.1002/2015JD024543, 2016.

Bouniol, D., Illingworth, A. J., and Hogan, R. J.: Deriving turbulent kinetic energy dissipation rate within clouds using ground based 94 GHz radar, Preprints 31st Conference on Radar Meteorology, pp. 193–196, 2003.

Bowen, A. J. and Mortensen, N. G.: Exploring the limits of WAsP the wind atlas analysis and application program, in: European Wind Energy Conference and Exhibition 20.05.1996 - 24.05.1996 - Göteborg, Sweden, pp. 584–587, 1996.

Bradley, E.: The influence of thermal stability and angle of incidence on the acceleration of wind up a slope, Journal of Wind Engineering and Industrial Aerodynamics, 15, 231 – 242, doi:10.1016/0167-6105(83)90193-9, 1983.

Bradley, E. F.: An experimental study of the profiles of wind speed, shearing stress and turbulence at the crest of a large hill, Quarterly Journal of the Royal Meteorological Society, 106, 101–123, doi:10.1002/qj.49710644708, 1980.

Bradley, S.: A simple model for correcting sodar and lidar errors in complex terrain, Journal of Atmospheric and Oceanic Technology, 29, 1717–1722, doi:10.1175/JTECH-D-12-00106.1, 2012.

Bradley, S., Perrott, Y., Behrens, P., and Oldroyd, A.: Corrections for wind-speed errors from sodar and lidar in complex terrain, Boundary-Layer Meteorology, 143, 37–48, doi:10.1007/s10546-012-9702-0, 2012.

Bradley, S., Strehz, A., and Emeis, S.: Remote sensing winds in complex terrain - a review, Meteorologische Zeitschrift, 24, 547–555, doi:10.1127/metz/2015/0640, 2015.

Brown, A. R., Hobson, J. M., and Wood, N.: Large-eddy simulation of neutral turbulent flow over rough sinusoidal ridges, Boundary-Layer Meteorology, 98, 411–441, doi:10.1023/A:1018703209408, 2001.

Callies, D.: Analyse des Potenzials der Onshore-Windenergie in Deutschland unter Berücksichtigung von technischen und planerischen Randbedingungen, Ph.D. thesis, Universität Kassel, Hessen, 170 pp., 2015.

Canadillas, B., Bégué, A., and Neumann, T.: Comparison of turbulence spectra derived from LiDAR and sonic measurements at the offshore platform FINO1, in: 10th German Wind Energy Conference (DEWEK 2010) Bremen, Germany, November 17-18, 2010, p. 4, 2010.

Carriou, J.-P.: personal communication, affiliation Leosphere, France, 2016.

Carruthers, D. J. and Choularton, T. W.: Airflow over hills of moderate slope, Quarterly Journal of the Royal Meteorological Society, 108, 603–624, doi:10.1002/qj.49710845708, 1982.

Castro, G.: Numerical simulations of the atmospheric boundary layer, Ph.D. thesis, 183 pp., 2007.

Champagne, F. H., Friehe, C. A., LaRue, J. C., and Wyngaard, J. C.: Flux measurements, flux estimation techniques, and fine-scale turbulence measurements in the unstable surface layer over land, Journal of the Atmospheric Sciences, 34, 515–530, doi:10.1175/1520-0469(1977)034⟨0515:FMFETA⟩2.0.CO;2, 1977.

Chan, P. W.: Generation of an eddy dissipation rate map at the Hong Kong International Airport based on Doppler lidar data, Journal of Atmospheric and Oceanic Technology, 28, 37–49, doi:10.1175/2010JTECHA1458.1, 2011.

Davies, F., Collier, C. G., Pearson, G. N., and Bozier, K. E.: Doppler lidar measurements of turbulent structure function over an urban area, Journal of Atmospheric and Oceanic Technology, 21, 753–761, doi:10.1175/1520-0426(2004)021⟨0753:DLMOTS⟩2.0.CO;2, 2004.

Davies, F., Collier, C. G., and Bozier, K. E.: Errors associated with dual-Doppler-lidar turbulence measurements, Journal of Optics A: Pure and Applied Optics, 7, S280, doi:10.1088/1464-4258/7/6/005, 2005.

Dobrinski, P., Dabas, A., and Flamant, P.: Remote measurement of turbulent wind spectra by heterodyne Doppler-lidar technique, Journal of Applied Meteorology, 39, 2434–2451, doi:10.1175/1520-0450(2000)039⟨2434:RMOTWS⟩2.0.CO;2, 2000.

EEA: Europe's onshore and offshore wind energy potential, European Environment Agency, Copenhagen, Denmark, doi:10.2800/11373, 2011.

Eggert, M., Gutsmuths, c., Müller, H., and Többen, H.: Zeitaufgelöste, vektorielle Vergleichsmessungen zwischen dem Doppler-Lidar-Transfernormal der PTB und einem Referenz-Ultraschallanemometer, in: Fachtagung "Lasermethoden in der Strömungsmesstechnik", 09.09.2014 - 11.09.2014, Karlsruhe, Germany, 11 pp., 2014.

Emeis, S.: Wind speed and shear associated with low-level jets over Northern Germany, Meteorologische Zeitschrift, 23, 295–304, doi:10.1127/0941-2948/2014/0551, 2014.

Erneuerbare-Energien-Gesetz - EEG 2017: Gesetz für den Ausbau erneuerbarer Energien (Erneuerbare-Energien-Gesetz - EEG 2017) of 21.07.2014.

FGW: TR6 Bestimmung von Windpotenzial und Energieerträgen: Revision 9 22.09.2014 - Fördergesellschaft Windenergie und andere Erneuerbare Energien e.V., 23 pp., 2014.

Finnigan, J. J. and Belcher, S. E.: Flow over a hill covered with a plant canopy, Quarterly Journal of the Royal Meteorological Society, 130, 1–29, doi:10.1256/qj.02.177, 2004.

Foken, T.: Application of footprint models for wind turbine locations, Meteorologische Zeitschrift, 22, 111–115, doi:10.1127/0941-2948/2012/0390, 2013.

Frehlich, R.: Estimation of velocity error for Doppler lidar measurements, Journal of Atmospheric and Oceanic Technology, 18, 1628–1639, doi:10.1175/1520-0426(2001)018⟨1628:EOVEFD⟩2.0.CO;2, 2001.

Frehlich, R. and Cornman, L.: Estimating spatial velocity statistics with coherent Doppler lidar, Journal of Atmospheric and Oceanic Technology, 19, 355–366, doi:10.1175/1520-0426-19.3.355, 2002.

Frehlich, R. and Kelley, N.: Measurements of wind and turbulence profiles with scanning Doppler lidar for wind energy applications, IEEE Journal of Selected Topics in Applied Earth Observations and Remote Sensing, 1, 42–47, doi:10.1109/JSTARS.2008.2001758, 2008.

Frehlich, R., Hannon, S. M., and Henderson, S. W.: Coherent Doppler lidar measurements of wind field statistics, Boundary-Layer Meteorology, 86, 233–256, doi:10.1023/A:1000676021745, 1998.

Frehlich, R., Meillier, Y., Jensen, M. L., Balsley, B., and Sharman, R.: Measurements of boundary layer profiles in an urban environment, Journal of Applied Meteorology and Climatology, 45, 821–837, doi:10.1175/JAM2368.1, 2006.

Frehlich, R., Meillier, Y., and Jensen, M. L.: Measurements of boundary layer profiles with in situ sensors and Doppler lidar, Journal of Atmospheric and Oceanic Technology, 25, 1328–1340, doi:10.1175/2007JTECHA963.1, 2008.

Fuertes, F. C., Iungo, G. V., and Porté-Agel, F.: 3D turbulence measurements using three synchronous wind lidars: Validation against sonic anemometry, Journal of Atmospheric and Oceanic Technology, 31, 1549–1556, 2014.

Göckede, M., Rebmann, C., and Foken, T.: A combination of quality assessment tools for eddy covariance measurements with footprint modelling for the characterisation of complex sites, Agricultural and Forest Meteorology, 127, 175–188, doi:10.1016/j.agrformet.2004.07.012, 2004.

Göckede, M., Markkanen, T., Hasager, C. B., and Foken, T.: Update of a footprint-based approach for the characterisation of complex measurement sites, Boundary-Layer Meteorology, 118, 635–655, doi:10.1007/s10546-005-6435-3, 2006.

Gottschall, J., Courtney, M. S., Wagner, R., Jørgensen, H. E., and Antoniou, I.: Lidar profilers in the context of wind energy - a verification procedure for traceable measurements, Wind Energy, 15, 147–159, doi:10.1002/we.518, 2012.

Harris, M., Constant, G., and Ward, C.: Continuous-wave bistatic laser Doppler wind sensor, Applied Optics, 40, 1501–1506, doi:10.1364/AO.40.001501, 2001.

Horst, T.: An intercomparison of measures of spatial inhomogeneity for surface fluxes of passive scalars, in: Proceedings of the 14th Symposium on Boundary Layer and Turbulence, Aspen, CO. American Meteorological Society, Boston, MA, pp. 11–14, 2000.

Horst, T. W. and Weil, J. C.: Footprint estimation for scalar flux measurements in the atmospheric surface layer, Boundary-Layer Meteorology, 59, 279–296, doi:10.1007/BF00119817, 1992.

Huffaker, R. M. and Hardesty, R. M.: Remote sensing of atmospheric wind velocities using solid-state and CO_2 coherent laser systems, Proceedings of the IEEE, 84, 181–204, 1996.

IEC: IEC 61400-1 Wind turbines – Part 1: Design requirements., 2005a.

IEC: IEC 61400-12-1 Wind turbines – Part 12-1: Power performance measurements of electricity producing wind turbines, 2005b.

IEC: IEC 61400-12-1 Wind turbines - Part 12-1: Power performance measurements of electricity producing wind turbines Draft FDIS 2nd ed., 2016.

IPCC: Special Report on Renewable Energy Sources and Climate Change Mitigation, Cambridge University Press, United Kingdom and New York, NY, USA, 1076, 2011.

IPCC: Climate Change 2014: Synthesis report. Contribution of working groups I, II and III to the fifth assessment report of the intergovernmental panel on climate change [Core Writing Team, R.K. Pachauri and L.A. Meyer (eds.)], IPCC, Geneva, Switzerland, 151 pp., 2014.

Kaimal, J. C. and Finnigan, J. J.: Atmospheric boundary layer flows: Their structure and measurement, Oxford University Press, New York, 289 pp., 1994.

Kindler, D., Oldroyd, A., MacAskill, A., and Finch, D.: An eight month test campaign of the Qinetiq ZephIR system: Preliminary results, Meteorologische Zeitschrift, 16, 479–489, doi:10.1127/0941-2948/2007/0226, 2007.

Klaas, T., Pauscher, L., and Callies, D.: LiDAR-mast deviations in complex terrain and their simulation using CFD, Meteorologische Zeitschrift, 24, 591–603, doi:10.1127/metz/2015/0637, 2015.

Kljun, N., Calanca, P., Rotach, M. W., and Schmid, H. P.: A simple two-dimensional parameterisation for Flux Footprint Prediction (FFP), Geoscientific Model Development, 8, 3695–3713, doi:10.5194/gmd-8-3695-2015, 2015.

Kolmogorov, A.: The Local structure of turbulence in incompressible viscous fluid for very large Reynolds numbers, Akademiia Nauk SSSR Doklady, 30, 301–305, 1941.

Kristensen, L., Kirkegaard, P., and Mikkelsen, T.: Determining the velocity fine structure by a laser anemometer with fixed orientation, Danmarks Tekniske Universitet, Risø Nationallaboratoriet for Bæredygtig Energi, risø-R-1762, 2011.

Kristensen, L., Kirkegaard, P., and Mikkelsen, T.: Determining the velocity fine structure by a laser anemometer in VAD operation, DTU Wind Energy, Denmark, 40 pp., 2012.

Kunkel, K. E., Eloranta, E., and Weinman, J.: Remote determination of winds, turbulence spectra and energy dissipation rates in the boundary layer from lidar measurements, Journal of the Atmospheric Sciences, 37, 978–985, doi:10.1175/1520-0469(1980)037⟨0978:RDOWTS⟩2.0.CO;2, 1980.

Lampert, A., Bernalte Jimenez, B., Gross, G., Wulff, D., and Kenull, T.: One-year observations of the wind distribution and low-level jet occurrence at Braunschweig, North German Plain, Wind Energy, 19, 1807–1817, doi:10.1002/we.1951, 2016.

Lea, G.: personal communication, affiliation DTU, Denmark, 2016.

Leclerc, M. Y. and Foken, T.: Footprints in micrometeorology and ecology, Springer Berlin Heidelberg, Berlin, Heidelberg, doi:10.1007/978-3-642-54545-0, 2014.

Lütkehus, I., Salecker, H., and Kristen, A.: Potenzial der Windenergie an Land - Studie zur Ermittlung des bundesweiten Flächen- und Leistungspotenzials der Windenergienutzung an Land, Umweltbundesamt, Berlin, Germany, 2013.

Mann, J.: The spatial structure of neutral atmospheric surface-layer turbulence, Journal of Fluid Mechanics, 273, 141, 1994.

Mann, J.: Wind field simulation, Probabilistic Engineering Mechanics, 13, 269–282, 1998.

Mann, J., Ott, S., Jørgensen, B., and Frank, H.: WAsP engineering 2000, 90 pp., 2002.

Mann, J., Cariou, J.-P., Courtney, M. S., Parmentier, R., Mikkelsen, T., Wagner, R., Lindelöw, P., Sjöholm, M., and Enevoldsen, K.: Comparison of 3D turbulence measurements using three staring wind lidars and a sonic anemometer, Meteorologische Zeitschrift, 18, 135–140, 2009.

Mann, J., Angelou, N., Arnqvist, J., Callies, D., Cantero, E., Arroyo, R. C., Courtney, M., Cuxart, J., Dellwik, E., Gottschall, J., Ivanell, S., Kühn, P., Lea, G., Matos, J. C., Palma, J. M. L. M., Pauscher, L., Peña, A., Rodrigo, J. S., Söderberg, S., Vasiljevic, N., and Rodrigues, C. V.: Complex terrain experiments in the New European Wind Atlas, Philosophical Transactions of the Royal Society of London A: Mathematical, Physical and Engineering Sciences, 375, doi:10.1098/rsta.2016.0101, 2017.

Measnet: MEASNET Procedure: Anemometer calibration procedure - Version 2, October 2009, 2009.

Measnet: MEASNET Procedure: Evaluation of site-specific wind conditions - Version 2, April 2016, 2016.

METEODYN: Manual. – meteodyn WT, Meteodyn, Nantes, France, 2014.

Monin, A. S. and Yaglom, A. M.: Statistical fluid mechanics, volume II: Mechanics of turbulence, MIT Press, Cambridge, Massachusetts, 769 pp., 1975.

Mortensen, N. G. and Petersen, E. L.: Influence of topographical input data on the accuracy of wind flow modelling in complex terrain, in: European Wind Energy Conference, Dublin, Ireland, 06.10.1997 - 09.10.1997, pp. 317–320, 1997.

Neff, D. E. and Meroney, R. N.: Wind-tunnel modeling of hill and vegetation influence on wind power availability, Journal of Wind Engineering and Industrial Aerodynamics, 74-76, 335–343, doi:10.1016/S0167-6105(98)00030-0, 1998.

Newman, J. F., Klein, P. M., Wharton, S., Sathe, A., Bonin, T. A., Chilson, P. B., and Muschinski, A.: Evaluation of three lidar scanning strategies for turbulence measurements, Atmospheric Measurement Techniques, 9, 1993–2013, 2016.

O'Connor, E. J., Illingworth, A. J., Brooks, I. M., Westbrook, C. D., Hogan, R. J., Davies, F., and Brooks, B. J.: A method for estimating the turbulent kinetic energy dissipation rate from a vertically pointing Doppler lidar, and independent evaluation from balloon-borne in situ measurements, Journal of Atmospheric and Oceanic Technology, 27, 1652–1664, doi:10.1175/2010JTECHA1455.1, 2010.

Palma, J., Castro, F. A., Ribeiro, L. F., Rodrigues, A. H., and Pinto, A. P.: Linear and nonlinear models in wind resource assessment and wind turbine micro-siting in complex terrain, Journal of Wind Engineering and Industrial Aerodynamics, 96, 2308–2326, doi:10.1016/j.jweia.2008.03.012, 2008.

Panofsky, H. A. and Dutton, J. A.: Atmospheric turbulence: Models and methods for engineering applications, Wiley, New York and Chichester, 397 pp., 1984.

Patton, E. G. and Katul, G. G.: Turbulent pressure and velocity perturbations induced by gentle hills covered with sparse and dense canopies, Boundary-Layer Meteorology, 133, 189–217, doi:10.1007/s10546-009-9427-x, 2009.

Pauscher, L., Vasiljevic, N., Callies, D., Lea, G., Mann, J., Klaas, T., Hieronimus, J., Gottschall, J., Schwesig, A., Kühn, M., and Courtney, M.: An intercomparison study of multi- and DBS lidar measurements in complex terrain, Remote Sensing, 8, 782, doi:10.3390/rs8090782, [Erratum: Remote Sens. 2017, 9(7), 667; doi:10.3390/rs9070667], 2016.

Pauscher, L., Klaas, T., Callies, D., and Foken, T.: Wind obsevations from a forested hill: Relating turbulence statistics to surface characteristics in hilly and patchy terrain, accepted for publication in Meteorologische Zeitschrift, 2017, 2017a.

Pauscher, L., Mann, J., Vasiljevic, and Lea, G.: Estimation of the dissipation rate of TKE from a single staring lidar, to be submitted to Journal of Atmospheric and Oceanic Technology, 2017, 2017b.

Peña, A., Floors, R., Sathe, A., Gryning, S.-E., Wagner, R., Courtney, M. S., Larsén, X. G., Hahmann, A. N., and Hasager, C. B.: Ten years of boundary-layer and windpower meteorology at Høvsøre, Denmark, Boundary-Layer Meteorology, 158, 1–26, doi:10.1007/s10546-015-0079-8, 2016.

Philip, J.: Blending and internal boundary-layer heights, and shear stress, Boundary-Layer Meteorology, 84, 85–98, doi:10.1023/A:1000345015838, 1997.

Poggi, D. and Katul, G. G.: Turbulent flows on forested hilly terrain: The recirculation region, Quarterly Journal of the Royal Meteorological Society, 133, 1027–1039, doi: 10.1002/qj.73, 2007.

Poggi, D. and Katul, G. G.: Turbulent intensities and velocity spectra for bare and forested gentle hills: Flume experiments, Boundary-Layer Meteorology, 129, 25–46, doi:10.1007/s10546-008-9308-8, 2008.

Ross, A. N. and Vosper, S. B.: Neutral turbulent flow over forested hills, Quarterly Journal of the Royal Meteorological Society, 131, 1841–1862, doi:10.1256/qj.04.129, 2005.

Ruck, B. and Adams, E.: Fluid mechanical aspects of the pollutant transport to coniferous trees, Boundary-Layer Meteorology, 56, 163–195, doi:10.1007/BF00119966, 1991.

Sathe, A. and Mann, J.: Measurement of turbulence spectra using scanning pulsed wind lidars, Journal of Geophysical Research, 117, doi:10.1029/2011JD016786, 2012.

Sathe, A. and Mann, J.: A review of turbulence measurements using ground-based wind lidars, Atmospheric Measurement Techniques, 6, 3147–3167, 2013.

Sathe, A., Mann, J., Gottschall, J., and Courtney, M. S.: Can Wind lidars measure turbulence?, Journal of Atmospheric and Oceanic Technology, 28, 853–868, doi:10.1175/JTECH-D-10-05004.1, 2011.

Sathe, A., Banta, R., Pauscher, L., Vogstad, K., Schlipf, D., and Wylie, S.: Estimating turbulence statistics and parameters from ground- and nacelle-based lidar measurements: IEA Wind Expert Report, Roskilde, Denmark, 2015.

Serafimovich, A., Hübner, J., Leclerc, M. Y., Duarte, H. F., and Foken, T.: Influence of low-level jets and gravity waves on turbulent fluxes, in: Energy and Matter Fluxes of a Spruce Forest Ecosystem, edited by Foken, T., pp. 247–276, Springer International Publishing, Cham, Switzerland, doi:10.1007/978-3-319-49389-3_11, 2017.

Smalikho, I., Köpp, F., and Rahm, S.: Measurement of atmospheric turbulence by 2-m doppler lidar, Journal of Atmospheric and Oceanic Technology, 22, 1733–1747, doi:10.1175/JTECH1815.1, 2005.

Smalikho, I. N. and Banakh, V. A.: Accuracy of estimation of the turbulent energy dissipation rate from wind measurements with a conically scanning pulsed coherent Doppler lidar. Part I. Algorithm of data processing, Atmospheric and Oceanic Optics, 26, 404–410, doi:10.1134/S102485601305014X, 2013.

Smalikho, I. N. and Rahm, S.: Lidar investigations of the effects of wind and atmospheric turbulence on an aircraft wake vortex, Atmospheric and Oceanic Optics, 23, 137–146, doi:10.1134/S1024856010020107, 2010.

Smalikho, I. N., Banakh, V. A., Pichugina, E. L., and Brewer, A.: Accuracy of estimation of the turbulent energy dissipation rate from wind measurements with a conically scanning pulsed coherent Doppler lidar. Part II. Numerical and atmospheric experiments, Atmospheric and Oceanic Optics, 26, 411–416, doi:10.1134/S1024856013050151, 2013.

Smalikho, J.: Accuracy of the turbulent energy dissipation rate estimation from the temporal spectrum of wind velocity fluctuations, Atmospheric and Oceanic Optics C/C of Optika Atmosphery i Okeana, 10, 559–563, 1997.

Smith, D. A., Harris, M., and Coffey, A. S.: Wind lidar evaluation at the danish wind test site in Høvsøre, Wind Energy, 9, 87–93, doi:10.1002/we.193, 2006.

Snyder, W. H., Thompson, R. S., Eskridge, R. E., Lawson, R. E., Castro, I. P., Lee, J. T., Hunt, J. C. R., and Ogawa, Y.: The structure of strongly stratified flow over hills: dividing-streamline concept, Journal of Fluid Mechanics, 152, 249–288, doi:10.1017/S0022112085000684, 1985.

Stawiarski, C., Träumner, K., Knigge, C., and Calhoun, R.: Scopes and challenges of dual-Doppler lidar wind measurements - an error analysis, Journal of Atmospheric and Oceanic Technology, 30, 2044–2062, doi:10.1175/JTECH-D-12-00244.1, 2013.

Steinfeld, G., Raasch, S., and Markkanen, T.: Footprints in homogeneously and heterogeneously driven boundary layers derived from a Lagrangian stochastic particle model embedded into large-eddy simulation, Boundary-Layer Meteorology, 129, 225–248, doi:10.1007/s10546-008-9317-7, 2008.

Taylor, P. A.: Comments and further analysis on effective roughness lengths for use in numerical three-dimensional models, Boundary-Layer Meteorology, 39, 403–418, doi:10.1007/BF00125144, 1987.

van Kuik, G. A. M., Peinke, J., Nijssen, R., Lekou, D., Mann, J., Sørensen, J. N., Ferreira, C., van Wingerden, J. W., Schlipf, D., Gebraad, P., Polinder, H., Abrahamsen, A., van Bussel, G. J. W., Sørensen, J. D., Tavner, P., Bottasso, C. L., Muskulus, M., Matha, D., Lindeboom, H. J., Degraer, S., Kramer, O., Lehnhoff, S., Sonnenschein, M., Sørensen, P. E., Künneke, R. W., Morthorst, P. E., and Skytte, K.: Long-term research challenges in wind energy – a research agenda by the European Academy of Wind Energy, Wind Energy Science, 1, 1–39, doi:10.5194/wes-1-1-2016, 2016.

Vasiljevic, N.: A time-space synchronization of coherent Doppler scanning lidars for 3D measurements of wind fields, vol. 0027 of *DTU Wind Energy PhD*, DTU Wind Energy PhD - 0027, Roskilde, Denmark, 2014.

Vasiljevic, N., Lea, G., Courtney, M., Cariou, J.-P., Mann, J., and Mikkelsen, T.: Long-range WindScanner system, Remote Sensing, 8, doi:10.3390/rs8110896, 176 pp., 2016.

Veers, P. S.: Three-dimensional wind simulation, Sandia National Labs. Albuquerque, NM (USA), 36 pp., 1988.

Vesala, T., Kljun, N., Rannik, U., Rinne, J., Sogachev, A., Markkanen, T., Sabelfeld, K., Foken, T., and Leclerc, M. Y.: Flux and concentration footprint modelling: state of the art, Environmental Pollution, 152, 653–666, doi:10.1016/j.envpol.2007.06.070, 2008.

Wiser, R., Yang, Z., Hand, M., Hohmeyer, O., Infield, D., Jensen, P. H., Nikolaev, V., O'Malley, M., Sinden, G., and Zervos, A.: Wind Energy, in: IPCC special report on renewable energy sources and climate change mitigation, edited by Edenhofer, O., Pichs-Madruga, R., Sokona, Y., Seyboth, K., Matschoss, P., Kadner, S., Zwickel, T., Eickemeier, P., Hansen, G., Schlömer, S., and von Stechow, C., pp. 535–608, Cambridge University Press, Cambridge, United Kingdom and New York, NY, USA, 2011.

Wood, N.: The onset of separation in neutral, turbulent flow over hills, Boundary-Layer Meteorology, 76, 137–164, doi:10.1007/BF00710894, 1995.

A. Individual contributions to the joint publications

A.1. Appendix B

Klaas, T., Pauscher, L. and Callies, D.: LiDAR-mast deviations in complex terrain and their simulation using CFD, Meteorologische Zeitschrift, 24(6), 591–603, doi:10.1127/metz/2015/0637, 2015.

The following contributions were made by the individual authors to the content of this article:

- Tobias Klaas performed the data analysis and the simulations. He participated in performing the lidar and mast measurements at Rödeser Berg. He also had the lead in writing the manuscript.

- It was my idea to analyse the sensitivity of the complex terrain error of the lidar to the forest parametrisation and I initiated the modelling exercise. Together with Tobias Klaas, I defined the modelling setup for Meteodym and WAsP engineering. During the analysis of the measurement data and the simulations I had a supervisory role for Tobias Klaas. I also had a supervisory role during the writing of this manuscript. In addition, I contributed text during the writing of the manuscript to Sections 1, 2, 3.1, 4.1, 4.2 and 5.

- Doron Callies initiated the measurement campaign comparing the mast and lidar measurements at Rödeser Berg. During the analysis of the simulations and the measurement data he helped with valuable discussions and suggestions. He critically reviewed the final manuscript and provided useful input.

A.2. Appendix C

Pauscher, L., Vasiljevic, N., Callies, D., Lea, G., Mann, J., Klaas, T., Hieronimus, J., Gottschall, J., Schwesig, A., Kühn, M. and Courtney, M.: An inter-comparison study of multi- and DBS-lidar measurements in complex terrain, Remote Sensing, 8(9),782, doi:10.3390/rs8090782, [Erratum: Remote Sens. 2017, 9(7), 667; doi:10.3390/rs9070667], 2016.

The following contributions were made by the individual authors to the content of this article:

- I performed all analysis in the form as it is presented in the manuscript. This includes the development of the quality control scheme for the lidars, the post-processing of the lidar and sonic data, all statistical analysis and writing the matlab code used in this process. I also developed the concept for the presentation of the results and wrote the entire manuscript except from a paragraph concerning the WindScanners in the methods section. Moreover, I participated in the planing and design of the experiment, helped to set up the WindScanner devices and together with our technical staff was responsible for the mast measurements during the campaign. I acted as the corresponding author.

- Nicola Vasiljevic was the main person in charge of operating the WindScanners during the experiment and provided a paragraph in the methods section about the WindScanners. He also participated in the planing of the experiment.

- Doron Callies initiated the measurement campaign and took the lead in planing the measurement campaign.

- Guillaume Lea performed a first analysis of the WindScanner data to ensure useful data had been captured during the experiment. This included horizontal wind speed as well as radial wind velocities. While providing some guidance for further investigations none of this analysis directly went into the manuscript. He also provided useful input to the definition of the quality control scheme.

- Jakob Mann provided supervision and useful discussions for the spectral analysis in the paper.

- Julian Hieronimus and Tobias Klaas helped in identifying useful measurement periods during the initial phase of the analysis. They also helped with the field work.

- Julia Gottschall participated in planing the experiment and provided measurement equipment.

- Annedore Schwesig wrote a master's thesis about an initial analysis of the WindScanner data and a comparison to a cup anemometer, which was supervised by me. The thesis led into the detailed analysis of the experiment in the manuscript. However, none of the results presented in the manuscript directly stem from this work.

- Martin Kühn participated in the initial planing of the experiment and provided measurement equipment.

- Michael Courtney participated in the planing of the experiment. He also provided valuable feedback to the discussion of the complex terrain errors.

- All authors read, reviewed and approved the final manuscript and provided valuable editorial and critical input and feedback for the document.

A.3. Appendix D

Pauscher, L., Mann, J., Vasiljevic and Lea, G.: Estimation of the dissipation rate of TKE from a single staring lidar, to be submitted to Journal of Atmospheric and Oceanic Technology.

The following contributions were made by the individual authors to the content of this article:

- During and after a research stay at DTU I performed all the analysis presented in this paper. This includes the post-processing of the measurement data, all statistical analysis and writing the matlab code used in this process. Moreover, I had the idea of comparing several different methods to derive the dissipation rate from the lidar data and suggested and developed the corrections to the short-term variance method after O'Connor et al. (2010). Under the supervision of Jacob Mann I performed the numerical calculations to estimate the theoretical effects of the lidar on the turbulence measurements and developed the statistical error estimation scheme. I also developed the concept for the presentation of the results and wrote the entire manuscript.

- Nicola Vasiljevic and Guillaume Lea performed the measurements and Nicola Vasiljevic provided the measurements of the laser pulse of the WindScanner.

- Jakob Mann had the initial idea for the experiment and designed the experiment layout. He also suggested the use of the method after Kristensen et al. (2011). During my stay at DTU he closely supervised my work and provided critical input and help with the interpretation of the results. He also critically reviewed the manuscript.

A.4. Appendix E

Pauscher, L., Callies, D., Klaas T. and Foken, T.: Wind obsevations from a forested hill: Relating turbulence statistics to surface characteristics in hilly and patchy terrain, Meteorologische Zeitschrift, accepted for publication.

The following contributions were made by the individual authors to the content of this article:

- I performed all analysis presented in the manuscript. This includes the post-processing of the measurement data, all statistical analysis and writing the matlab code used in this process. I also performed the footprint modelling and the definition and calculation of the surface characteristics. I developed the concept for the presentation of the results and wrote the entire manuscript. During the measurements I was the responsible scientist for the operation of the 200-m-mast at Rödeser Berg.

- Doron Callies planed and supervised the installation of the 200-m-mast and the scientific instrumentation at Rödeser Berg. He provided the GIS-Data and helped to convert it so that it could be used in the footprint modelling. Moreover, he provided useful discussions in the interpretation of the observed turbulence statistics.

- Tobias Klaas led the project which provided the framework of the operation of the 200-m-mast. He also provided useful advice during the data analysis.

- Thomas Foken supervised the analysis and helped to choose the appropriate tools for the interpretation of the results. He critically reviewed the manuscript several times and helped to destil the core results presented in the paper.

- All authors approved the final manuscript and provided valuable editorial and critical input and feedback for the final document.

B. Klaas et al. (2015)

Klaas, T., Pauscher, L. and Callies, D.: LiDAR-mast deviations in complex terrain and their simulation using CFD, Meteorologische Zeitschrift, 24(6), 591–603, doi:10.1127/metz/2015/0637, 2015.

Meteorologische Zeitschrift, Vol. **24**, No. 6, 591–603 (published online July 16, 2015)

ISARS 17

LiDAR-mast deviations in complex terrain and their simulation using CFD

Tobias Klaas*, Lukas Pauscher and Doron Callies

Fraunhofer IWES

(Manuscript received July 30, 2014; in revised form March 23, 2015; accepted March 23, 2015)

Abstract

LiDARs (Light Detection and Ranging) are becoming important tools for wind resource assessments in all kinds of terrain. Compared to mast measurements, mobility and flexibility are their greatest benefits. However, care needs to be taken when setting up a measurement campaign. The influence of complex terrain on the wind leads to inhomogeneous flow. This can cause considerable errors in ground based mono-static LiDAR measurements due to their measurement principle and simplifying assumptions.Within this work, wind measurements from Fraunhofer IWES's 200 m research mast in complex terrain at "Rödeser Berg" in Kassel, Germany, and a pulsed Doppler LiDAR (Leosphere windcube), located at the mast, are compared. The relative deviation between the measurements of the horizontal wind speed by the LiDAR and the mast (LiDAR-mast deviations) varies with wind direction and height. It ranges from about −4 % underestimation to +2.5 % overestimation by the LiDAR - for heights between 120 and 200 m. Two steady-state Reynolds-Averaged-Navier-Stokes (RANS) Computational Fluid Dynamics (CFD)-models and a model based on linearized Navier-Stokes Equations were used to estimate the LiDAR error from a flow simulation. Model results were evaluated depending on model parameterisation such as forest height and density. Given the right parameterisations – especially for the forest model – the CFD-models showed a good performance when compared to the observed LiDAR-mast deviations. These simulations can thus be used to correct the LiDAR error induced by the complex flow.

To demonstrate variations of LiDAR errors due to choice of measurement location, one of the models was run to calculate the wind flow in an area of $2 \times 2\,\mathrm{km}^2$ around the 200 m measurement mast. This allows the visualization of the estimated LiDAR errors to characterize measurement locations. Results showed the significant variation of measurement errors due to the location.

Keywords: lidar, wind measurements, complex terrain, flow modelling, forest, remote sensing, wind energy

1 Introduction

Over recent years, there has been significant progress towards accurate and reliable wind profile measurements using LiDAR (Light Detection And Ranging) technology (Emeis et al., 2007, Courtney et al. 2008; Gottschall et al., 2011). This progress in the development of LiDAR systems is predicated on the need for high quality wind measurements for resource assessments and power performance tests. Wind turbine size has considerably increased within the last years, with hub heights of up to 150 m and large rotor diameters of more than 130 m. For many wind energy applications it is desirable or even mandatory to measure wind speed at hub height. The ability to measure up to great heights, their flexibility, mobility and ease of deployment has made LiDARs an appealing alternative to expensive and immobile met masts.

In the past, several studies showed the high accuracy of commercially available LiDARs in comparison to meteorological masts equipped with cup anemometers in flat terrain (e.g. Antoniou, 2004; Smith et al., 2006; Kindler, 2007; Albers and Janssen, 2008), qualifying these devices for real world applications. As a consequence, their use in wind energy applications will be standardised in the new revision of the International Electrotechnical Commission (IEC) standard for power performance measurements of wind turbines (IEC, 2013).

Ground based mono-static remote sensing measurements of the horizontal wind speed can suffer from considerable errors in complex terrain due to their measurement principle and simplifying assumptions. For conically scanning LiDARs the most important simplification in the wind speed retrieval algorithm is that flow conditions across the different sampling volumes are homogeneous (Clive, 2008). In complex terrain this assumption is often violated and systematic errors in the derived wind speeds can occur (Emeis, 2007; Bradley, 2008; Bingöl et al., 2009).

Bingöl et al. (2009) uses a simplified model of two dimensional flow over an idealized hill to describe the influence of a linear variation of the vertical wind speed on the LiDAR error, respectively. In most real world measurement applications the terrain is more complex and different models of different complexities have been used to estimate the LiDAR error (Bingöl et al. (2009); Bradley et al., 2012). Since recently, also commer-

*Corresponding author: Tobias Klaas, Fraunhofer IWES, Königstor 59, 34119 Kassel, Germany, Tobias.Klaas@iwes.fraunhofer.de

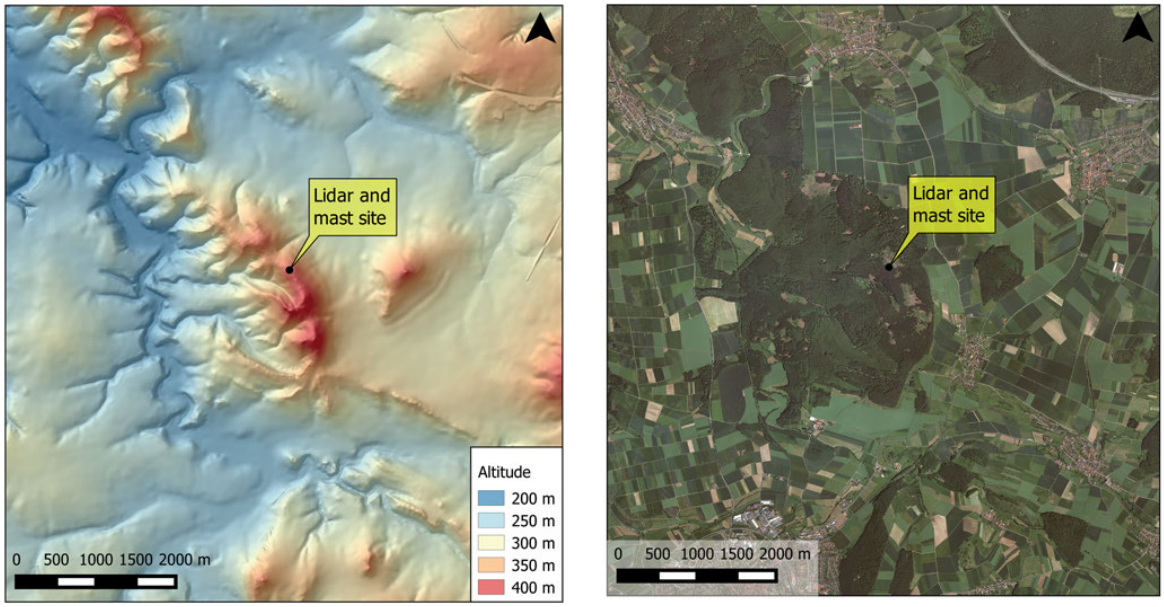

Figure 1: Orography (left) and satellite picture (right) of the location of the mast-LiDAR inter-comparison (marked with black dot) (geographical data from (HVGB 2010), modified by T. Klaas). LiDAR and mast measurements are located on top of a ridge that is oriented from north-west to south-east. Most significant inclinations are to the west and south-west (10–15 °) (approx. main wind direction) and the north-east (10 °). In terms of roughness, the measurements are located within a small clearing surrounded by forest. To the west and south-west the ground is covered with mixed forest up to approx. 2 km distance.

cially available Computational Fluid Dynamics (CFD) tools offer a 'LiDAR-correction module' (e.g. Meteodyn WT and WindSim) for complex terrain. Leosphere also developed an on-board real-time correction algorithm for their windcube v2. As the underlying algorithm is proprietary and thus secret, an objective evaluation is difficult (Wagner and Bejdic, 2014). A current review over the most relevant correction approaches for LiDAR measurements in complex terrain can also be found in Bradley et al. (2015).

However, experimental data remains scarce and typical magnitudes of the LiDAR-mast deviations and their dependency on e.g. surface cover and atmospheric conditions remain unclear. Also, the performance and limitations of different modelling approaches are not well understood. For a successful application and acceptance of LiDAR technology in complex terrain (including a correction) in applications where high precision horizontal wind speed measurements are needed (e.g. wind engineering) there is a need for independent assessments.

This paper gives a detailed analysis of LiDAR-mast deviations at a complex, forested site at "Rödeser Berg" close to Kassel in central Germany. LiDAR measurements are compared to cup anemometry at a high quality 200 m mast measurement. Subsequently, three different flow models are used to estimate the LiDAR error. The aim of this paper is to evaluate the performance of different flow models in reproducing the LiDAR error due to complex terrain and reveal their sensitivities to parameterisation. It is also sketched out how the simulations can be used in pre-campaign modelling to assess different locations for the LiDAR measurement. This information can be used to optimise a measurement campaign and reduce the LiDAR error.

2 Measurement sites, instrumentation and experiments

The data presented in this paper was collected at the Fraunhofer IWES complex terrain test site at Rödeser Berg about 30 km north-west of Kassel in central Germany (51 ° 21 ′ 46 ″ N, 9 ° 11 ′ 43 ″ E). A Leosphere windcube v1 LiDAR was placed next (distance ~ 4 m) to the 200 m tall met mast on the crest of a forested hill (Fig. 1). The mast and the LiDAR were located on a small clearing, which is surrounded by trees with an approximate height of 20–30 m. While the closer surroundings of the measurement site are forested with varying tree heights and small clearings, the wider surroundings of Rödeser Berg are characterised by a patchy landscape with a mixture of agricultural land use, small villages and patches of forests (mainly on the hill tops). Within the main wind direction (210 °) the forest extends about 2 km. The most significant inclinations (approx. 10–15 °) are in the west/south-west sectors (210–270 °) and in east/north-east sectors (60–90 °). For these sectors inclinations are larger for the closer proximity of the measurement site (approx. 15 °). The hill then flattens out in the wider area.

Table 1: Overview of the wind sensors used within this work. All cup anemometers are Thies Clima "first class" advanced. For 60 m there is only one cup anemometer. For 80 m there is an Ultrasonic anemometer at one side of the mast. The top anemometer at 200 m height is placed on a vertical pole and is only influenced by a lightning rod in the south-eastern sector.

Height [m]	Sensor 1	Orientation [°]	Sensor 2	Orientation [°]
60	–	–	Cup anemometer – "first class" advanced, Thies Clima	321
80	Cup anemometer "first class" advanced, Thies Clima	140	Ultrasonic Anemometer 3D, Thies Clima	320
120	Cup anemometer "first class" advanced, Thies Clima	139	Cup anemometer "first class" advanced, Thies Clima	319
160	Cup anemometer "first class" advanced, Thies Clima	136	Cup anemometer "first class" advanced, Thies Clima	317
200	Cup anemometer "first class" advanced, Thies Clima	Mast top	–	–

The measurement mast is a rectangular lattice tower with a side length of 1.05 m and a solidity of 0.220 and 0.204 below and above 100 m, respectively. The mast is equipped with opposing boom pairs with a length of 5.40 m (diameter 50 mm). The sensors are mounted on a pole at a height of 1 m above the end of the boom. These mountings result in a wind speed deficit of approx. 99.5 % (i.e. effects due to flow distortion are 0.5 %) according to IEC 61400–12–1 (IEC 2013) for the anemometer being directly upwind of the mast. For all other wind directions in the 180 ° upwind sector the influence of the mast can be assumed to be smaller as stated in IEC 61400-12-1 (IEC 2013). The mast LiDAR comparison was then carried out using data from the 180 ° upstream sectors of the two opposite anemometers at each height.

The mast is equipped with a dense array of anemometers and meteorological sensors. An overview of the sonic and cup anemometers that were used for the inter-comparison can be found in Table 1. In addition to the sensors mentioned in Table 1, there are several temperature, humidity, pressure sensors mounted at different heights on the mast. Also, several Gill HS-50 sonic anemometers and fully heated Vaisala Cup anemometers are installed on the mast. However, due to technical problems with the Gill HS-50 sonics, they were not used in the data analysis. The fully heated Vaisala Cups are used for the detection of icing in the unheated/bearing-heated cup anemometers. Their wind speed measurements are not part of the instrument-inter-comparison as their measurement behaviour differed from the unheated/bearing-heated cup anemometers and the sonic anemometers. Also, fully heated cup anemometers are reported to be less accurate in literature (Fikke et al., 2007; Ronsten et al., 2012). All mast mounted anemometers used in this study were calibrated according to IEC61400-12-1:2005 and MEASNET guidelines (IEC 2013; MEASNET, 2009).

The analysis in this paper is based on 10 minute intervals. The collected mast data was filtered for periods of icing by visually comparing the time series to the fully heated cup sensors. In addition to that, periods with sensor failures and malfunction were removed. For the measurement at the mast top (200 m) the sector with an influence of the lightning rod was excluded. At 60 m height only one Thies cup anemometer is available for the sector 60–220°. The opposing sensor is a fully heated Vaisala cup (see above). For the comparison the wind speed data was binned by wind direction (10 degree bins). For most wind direction bins there are more than 50 data points available for all presented heights. Bins from 10–40 ° and from 90–120 ° contain less than 50 data points for at least one height. At the height used in the simulations (120 m) there are still 26 to 146 within these sectors – except for the 100 ° sector with only 13 data points (Fig. 2).

The LiDAR (Leosphere windcube v1) used in this experiment is a pulsed Doppler LiDAR. It uses a conically scanning laser and relies on the Doppler beam swinging technique. For more detailed information about LiDARs in general the reader is referred to e.g. (Emeis, 2007). Four beam directions with angles of 90 ° between them and a fixed half cone angle of about 28 ° are emitted (Fig. 3). The three components of the wind vector are then reconstructed from trigonometric relations using the radial beam directions of the individual scans. In case of the windcube v1, they read:

$$u_L = \frac{v_{r4} - v_{r2}}{2 \sin\varphi \sin\theta} \tag{2.1}$$

$$v_L = \frac{v_{r3} - v_{r1}}{2 \sin\varphi \cos\theta} \tag{2.2}$$

$$w_L = \frac{-v_{r1} + v_{r2} - v_{r3} + v_{r4}}{4 \cos\varphi} \tag{2.3}$$

With u_L, v_L and w_L being the x, y, and z vector components of the wind speed, φ the half cone angle, θ the azimuth angle (from north), v_{r1}, v_{r2}, v_{r3}, v_{r4} the north, east, south and west measured radial wind speeds. This study uses the following convention for the three components of the wind vector: u, v and w as u positive from west to east, v positive from south to north and w positive upwards. Radial wind speeds are defined positive, if oriented towards, and negative, if oriented away from the LiDAR.

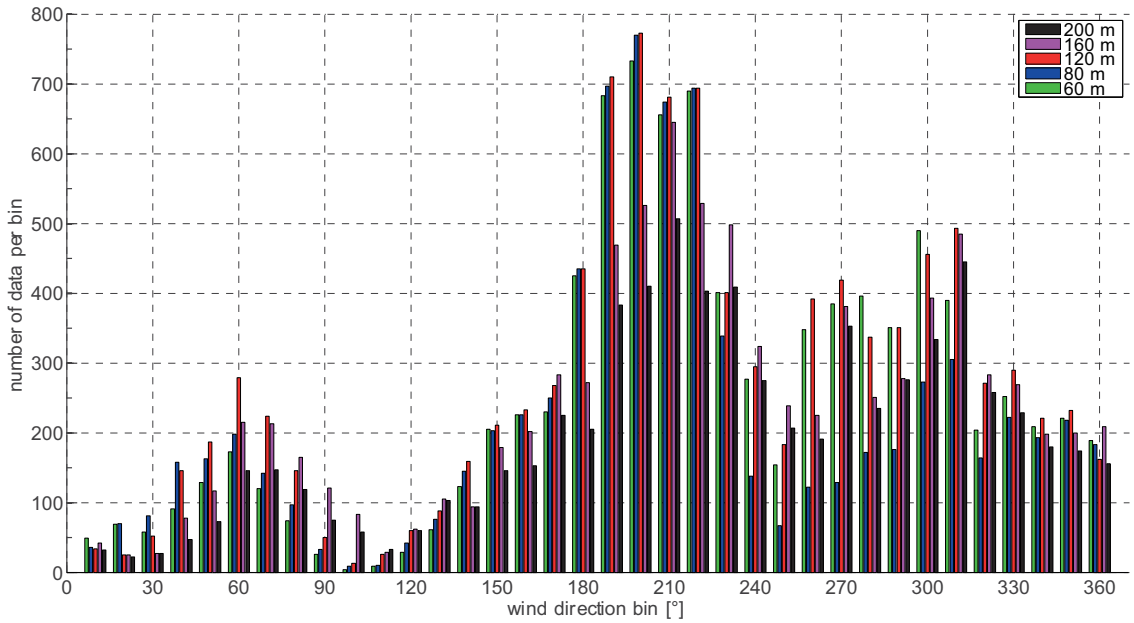

Figure 2: Number of data points per wind direction bin for different heights. The values indicate the number of 10 min periods for which both LiDAR and mast data was available after the filter criteria described in the text were applied.

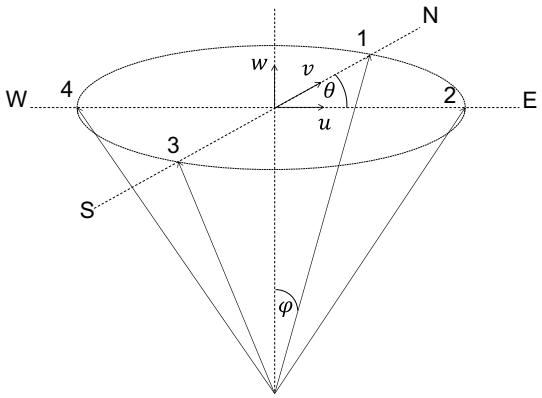

Figure 3: Beam directions (1–4) of the LiDAR and definition of the half cone angle φ as well as the azimuth angle θ. The wind vector components u, v, and w are also shown with regards to their orientation to North (N), East (E), South (S) and West (W) directions.

After that, the horizontal wind speed is derived and averaged to 10 minutes. The windcube v1 allows measurements at up to 10 different heights that are taken simultaneously. The constant pulse length of the laser results in a measurement volume of about ±10 m around the individual height (Pauliac, 2009). LiDAR data was filtered for an availability of 80 % – i.e. 80 % of the individual scans had to be available in specific 10 minute interval. Moreover, periods when the wiper of the LiDAR was active, were removed since this indicates rain which might influence the measurement accuracy of the LiDAR.

3 Theory and method

3.1 LiDAR errors in complex terrain

Equations (2.1) to (2.3) underlie the assumption that the flow among all beams is homogeneous (constant u, v, w). While this is true in flat terrain over sufficiently long measurement periods, the wind flow in complex terrain is considerably influenced by local orography and vegetation (e.g. forests). Hence, the homogeneous flow assumption is violated – i.e. components of the wind vector become dependent on the position of the LiDAR beam:

$$v_{\mathrm{ri}} = u_i \sin(\varphi)\sin(\theta) + v_i \sin(\varphi)\cos(\theta) + w_i \cos(\varphi) \quad (3.1)$$

with u_i, v_i and w_i being the wind vector components at the measurement locations $i = 1$ to 4.

Following (Bingöl et al., 2009), especially the influence of the w component/the flow angle is important in this context. A concave shape of the flow (e.g. valleys) results in an overestimation in the LiDAR wind speed when compared to the 'true' wind speed. A convex shape (e.g. hills) in contrast causes an underestimation. Bingöl et al. (2009) also demonstrates that the LiDAR errors are independent of half cone angle if the w component is assumed to change linearly with distance.

Here, the LiDAR error is presented as the relative deviation of the horizontal wind speed V_L from the LiDAR in comparison to the wind speed from a co-located reference mast V_M.

3.2 Estimation of LiDAR error

The method used here to estimate the LiDAR error is based on flow model results. It is generally applicable to all kinds of three dimensional wind fields, regardless of the flow model. A LiDAR measurement is virtually placed at the measurement site. The different LiDAR measurement points (radial measurements) are calculated in a global coordinate system following simple trigonometric functions:

$$\begin{pmatrix} x_i \\ y_i \\ z_i \end{pmatrix} = \begin{pmatrix} x_L \\ y_L \\ z_L \end{pmatrix} + \begin{pmatrix} \sin(\theta + \frac{1}{2}\pi(i-1)) \tan\varphi h_j \\ \cos(\theta + \frac{1}{2}\pi(i-1)) \tan\varphi h_j \\ h_j \end{pmatrix} \quad (3.2)$$

with x_i, y_i, z_i denoting the individual measurement location coordinates, x_L, y_L, z_L the LiDAR location, h_j the measurement height above ground and i the beam number (1 to 4).

For each simulated wind direction, the wind vector components for each beam (u_i, v_i and w_i) are extracted from the model results using linear interpolation within the three dimensional grid. They are then projected on the particular beam direction:

$$v_{ri} = -\vec{e_0} \cdot \begin{pmatrix} u_i \\ v_i \\ w_i \end{pmatrix} \quad (3.3)$$

$$\text{with} \quad \vec{e_0} = \begin{pmatrix} \sin(\theta + \frac{1}{2}\pi(i-1)) \sin\varphi \\ \cos(\theta + \frac{1}{2}\pi(i-1)) \sin\varphi \\ \cos\varphi \end{pmatrix}$$

Following equations (2.1) to (2.2) the wind vector components as measured by a LiDAR are then computed. The 'true' wind speed from a mast measurement (u_M and v_M) is extracted from the model results as well. The estimated LiDAR error for the individual wind direction is defined as follows:

$$E_{\text{lidar}} = \frac{\sqrt{u_L^2 + v_L^2} - \sqrt{u_M^2 + v_M^2}}{\sqrt{u_M^2 + v_M^2}} = \frac{V_L - V_M}{V_M} \quad (3.4)$$

All estimated LiDAR errors in this paper have been calculated using this approach. Built-in approaches of the flow models are not included in this paper as (unknown) methodological differences might lead to unwanted differences in the results.

By extending this method to multiple LiDAR locations, a map of LiDAR errors at a pre-defined area of interest can by generated.

3.3 Flow models

To account for the complexity of real world terrain, three dimensional flow models can be used to simulate the flow between the different LiDAR beams at the site of interest. The modelled wind vectors in the different beams can then be used to simulate the LiDAR error as described above. A comparison to the simulated wind speed at the mast position (equation (3.4)) then allows a calculation of a direction dependent LiDAR error. The models used within the study are briefly presented in the following.

A commonly used model for wind energy applications is WAsP Engineering (Mann et al., 2002). The flow model underlying the flow simulations is based on LINCOM. It is based on the Linearized Navier Stokes Equations and was initially published by (Jackson and Hunt, 1975). Since then there have been several further developments (e.g. Troen, 1990; Mann et al., 2000). The influences of the terrain on the boundary-layer flow are treated as perturbations on a constant horizontal flow. The developers define the range of application as flat and moderately complex terrain without steep inclinations causing flow separation (Mann et al., 2000). WAsP Engineering (WEng) does not have a dedicated forest model. In this study the forest is therefore parameterised using a displacement height of $z_d = 20\,\text{m}$ and increased roughness length (Dellwik et al., 2006). For details about the model, refer to (Mann et al., 2002).

Originally, the model was intended for site assessment applications in wind energy. However, Bingöl et al. (2009) developed a method to extract the modelled radial velocities and estimate the LiDAR error in complex flow. For this paper the Visual Basic Script provided with the publication was adapted to match the method described above.

In recent times, models based on the Reynolds averaged Navier-Stokes equations (RANS models) have become more and more popular in engineering applications that require modelling atmospheric boundary layer flows. In contrast to the linearized model, they are capable of resolving e.g. flow separation that often occurs in complex terrain (Landberg et al., 2003). With current computer technology they can now be run on desktop PCs within a reasonable time (Landberg et al., 2003; Palma et al., 2008). For this study, the two commercially available RANS codes Meteodyn WT and WindSim were used. Both models are used to perform steady-state simulations.

WindSim is based on the CFD Code "PHOENICS" (Open-Source) using standard steady-state RANS equations for incompressible flow. Details on the parameters of the used k-ε turbulence closure can be found in (Gravdahl, 1998).

For Meteodyn WT all relevant model equations and additional information can be found in a technical note on the developers' website (METEODYN, 2007). Meteodyn WT also uses standard steady-state RANS equations for incompressible flow. For turbulence closure a K closure scheme is used (Hurley, 1997).

Since the RANS codes are commercial products, the degrees of freedom in the parameterisation are limited. In this study only the influence of the forest model

settings is investigated. Both RANS models allow a variation of the forest density (respectively porosity) and height, which are the most important parameters to vary in terms of the forest model. The model is also offering the possibility to include atmospheric stability in its simulations. This was not done in this study as it caused numerical instabilities and simulations often did not converge.

The presented results mainly focus on the parameterisation of the forest model of Meteodyn WT. Therefore a short summary of the Meteodyn WT forest model and its parameterisation is presented below.

In Meteodyn WT the local roughness length is directly related to the tree-height-to-roughness-length-ratio A:

$$A = \frac{h_t}{z_0} \tag{3.5}$$

Meteodyn WT suggests a value of $A = 20$, but it can be changed by the user in order to increase the tree height resulting from local roughness values (METEODYN, 2014).

The forest model then changes several parameters of the turbulence model below the canopy's height. For calculation of the dissipation term ε the following equation is used (Wilson et al., 1998):

$$\varepsilon = \max(\varepsilon_{cc}, \varepsilon_{fd}) \text{ with } \begin{cases} \varepsilon_{cc} = C_\mu \frac{v_T}{L_T^2} k \\ \varepsilon_{fd} = C_d |\boldsymbol{U}| k \end{cases} \tag{3.6}$$

with U being the wind vector, v_T the turbulent viscosity, L_T the turbulent length scale and k the turbulent kinetic energy. C_μ is a term, which is dependent on the Richardson number, while the drag force coefficient C_d was empirically determined by the software developer based on a field study (METEODYN, 2007). For more detailed information on the two different definitions for the dissipation rate of the turbulent kinetic energy ε_{cc} and ε_{fd} refer to (Wilson et al., 1998).

There are two choices in forest models for Meteodyn WT, the "robust" and the "dissipative" model. According to the developer, the latter gives better results on turbulence intensity caused by the forest, while the former is more stable in terms of convergence (METEODYN, 2014).

For the robust forest model, the mixing length l is kept constant within the canopy, following (Ross and Vosper, 2005):

$$\frac{1}{l} = \begin{cases} \frac{1}{l_0} + \frac{1}{\kappa z} \text{ for } z > h_t \\ \frac{1}{l_0} + \frac{1}{\kappa h_t} \text{ for } z \leq h_t \end{cases} \tag{3.7}$$

with h_t being the canopy's height (tree height) and z the height above ground, κ the von-Karman constant and $l_0 = 100\,\text{m}$ an empirical coefficient chosen after Arritt 1987 (METEODYN, 2007).

The dissipative forest model additionally introduces a dissipative zone above the forest, and the mixing length becomes (METEODYN, 2014):

$$\frac{1}{l} = \begin{cases} \frac{1}{2} \text{ for } z < h_t \\ (1 - \propto) \frac{1}{2} + \propto (\frac{1}{l_0} + \frac{1}{\kappa z}) \quad \text{for } h_t < z \leq h_t + 15\,\text{m} \\ \qquad\qquad \text{with} \propto = \frac{z - h_t}{15\,\text{m}} \\ \frac{1}{l_0} + \frac{1}{\kappa d} \text{ for } z > h_t + 15\,\text{m} \end{cases} \tag{3.8}$$

For the RANS equations, an additional volumetric sink term is applied for the computational cells that are located within the canopy:

$$F_V = -\rho C_d \boldsymbol{U} |\boldsymbol{U}| \tag{3.9}$$

The drag force coefficient C_d can be changed by the user as the forest density from the default setting "normal" to either "low" or "high", which means decreasing or increasing the drag force coefficient for the model (METEODYN, 2014, Ross and Vosper, 2005).

WindSim uses a slightly different forest model with five parameters to describe the canopy layer as a porous medium. The model is triggered by a user-defined roughness length within the roughness map. The forest is then modelled by adding an additional sink term to the RANS equations. Porosity and tree height can be changed by the user. For details of the WindSim forest model, refer to (Crasto, 2007).

Both, Meteodyn WT and WindSim, have Add-On modules to estimate the LiDAR error for a given measurement site. As these are commercial tools, the underlying equations are not published. For this paper these built-in options were not used. Instead the flow fields were extracted from the model runs and the LiDAR error was calculated according to the method presented in Section 3.2.

4 Results and discussion

4.1 Observed LiDAR-mast deviations

To analyse overall accuracy of the LiDAR measurement versus the mast, a two parametric linear regression was fitted to the results, exemplarily shown for 80 and 200 m height (Fig. 4). At both heights, the correlation is very good with a slope and R^2 close to 1 and only small offset values. The mean wind speed is slightly underestimated by the LiDAR by about 1.5 and 1.1 % for 80 and 200 m height (Table 2). In comparison to a flat terrain case, the scatter is higher (compare e.g. Gottschall et al., 2011). Detailed results for other heights are presented in Table 2.

When looking at the direction dependent deviations between the LiDAR measurement and the reference mast (Fig. 5) a clear double sine wave pattern, with maxima/minima at 150 and 330/60 and 240 ° wind direction,

Table 2: Results of the linear regression at measurement heights 80, 120, 160 and 200 m. R^2 denotes the coefficient of determination of the linear fit. Only wind speeds $V \geq 4\,\mathrm{ms}^{-1}$ were considered for the fit. No. valid data points and data availability refer to the number of data pairs used to compare LiDAR and mast measurements after filtering the total time series of 22,752 data points.

Height [m]	Slope	Offset	R^2	Mean relative error [%]	Mean absolute error [m/s]	No. valid data points	Data availability [%]
80	0,973	0,091	0,989	−1,49	−0,095	8026	35,4
120	0,976	0,104	0,992	−0,84	−0,058	9938	43,9
160	0,982	0,075	0,992	−0,88	−0,058	8895	39,5
200	0,974	0,118	0,992	−1,12	−0,076	7097	31,6

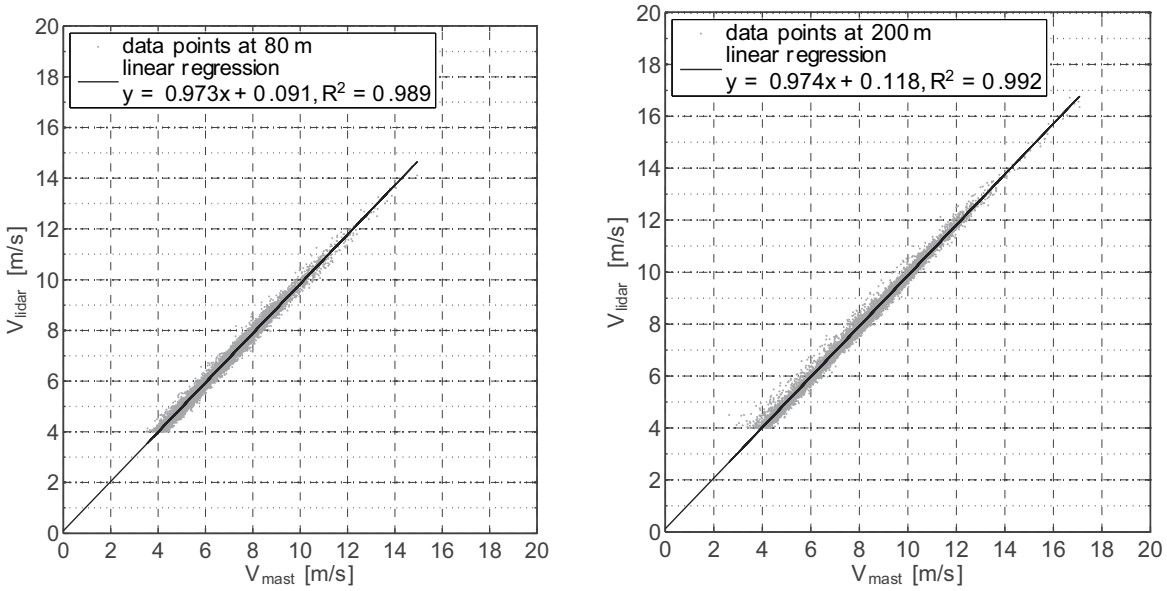

Figure 4: Scatter plot and linear regression between the horizontal wind speed V at the mast and the LiDAR at 80 m (left) and 200 m (right) measurement height; R^2 denotes the coefficient of determination of the linear fit.

can be observed. This behaviour is present for all analysed heights. For heights between 120 and 200 m there is neither significant difference in pattern nor magnitude in the LiDAR-mast deviations. To put this into context it is helpful to remember that Rödeser Berg has an altitude of about 100–170 m above the surrounding terrain.

The maximum underestimation for 240 ° wind direction – which is very close to the main wind direction at this site – reaches about 4.0 %. Similar values occur for the opposing wind direction (60 °). For wind directions orthogonal to these there is an overestimation of the LiDAR versus the mast of about 2 % for northern and north-western (300–10 °) winds and about 1 % for a small sector of the opposing wind direction (130–170 °).

At 60 and 80 m the LiDAR-mast deviations differ slightly from those observed at higher altitudes. This might be caused by a stronger influence of the proximity of the ground and the canopy. Especially for the south-western sector (240–270 °) it does significantly increase at 80 m height up to −5 %. At 60 m height, LiDAR-mast deviations are also increased for 150–220 ° and the observed pattern slightly changes.

The shape of these curves resembles the orography at Rödeser Berg: For the two sectors 240 and 60 ° the maximum slopes are comparable and reach values of 10–15 °. The terrain has a clearly convex shape in the directions of the flow. In this situation the observed underestimation of the mean horizontal wind speed can be expected. For wind directions along the ridge the LiDAR-mast deviations are smaller. While for flows from the sector of approx. 120–200 °, the LiDAR and the mast measurements are very similar for heights between 80 and 200 m, an overestimation of the mast measurements by the LiDAR can be observed for northerly and north-westerly (320–10 °) flows. The sector of the overestimation is somewhat smaller for the measurement height of 80 m. This behaviour might be connected to the slightly concave shape of the ridge at the mast location. However, the flow is very complex in this situation and it is difficult to identify the dominating terrain or flow features. When averaging LiDAR-mast deviations over all wind directions, some of these positive and negative deviations cancel out (Table 3). No dependence of LiDAR-mast deviations on the wind speed was observed.

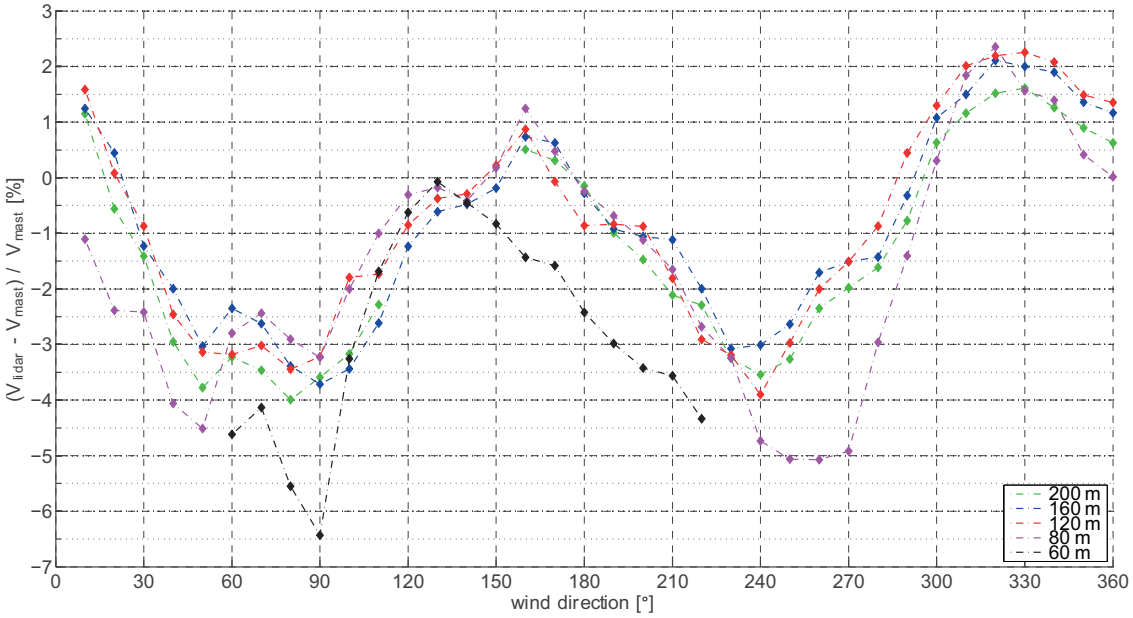

Figure 5: Mean relative deviation in the horizontal wind speed V between LiDAR and mast measurements versus wind direction at five different heights (60, 80, 120, 160, 200 m). For 60 m height only the sectors from 60 to 220 ° (upwind direction for the Thies Cup Anemometer) are shown. Deviations are binned in sectors of 10 °. Confidence intervals are not shown for reasons of readability. Only $V \geq 4\,\mathrm{ms}^{-1}$ were used.

Table 3: Statistics for LiDAR error estimation by different models and parameterisations. The error of the model is defined as the mean of the absolute deviations between modelled and measured complex terrain error of the LiDAR. All statistics were calculated from 10 ° bins of the wind directions and are given in percent. *1) For WindSim, forest porosity and tree height are constant 0.3 (standard value) and 30 m. *2) Ratio of Forest Height to Roughness.

	Meteodyn WT											**WindSim**	**WEng**
Forest Model	dissipative					robust					none	standard	none
Forest density	low	normal		high		low	normal		high		–	*1)	–
A–ratio *2)	30	30	20	30	40	30	30	20	30	40	–	*1)	–
Mean deviation [%]	2,46	1,46	1,69	1,16	0,88	2,81	1,96	1,89	1,61	1,33	3,54	2,33	4,35
Maximum deviation [%]	5,18	3,91	3,94	3,23	2,14	5,14	3,77	4,06	3,03	2,89	5,89	4,08	8,35
Minimum deviation [%]	0,41	0,03	0,18	0,23	0,02	0,21	0,73	0,30	0,15	0,09	0,38	0,22	0,31
Standard deviation [%]	1,12	0,86	0,86	0,66	0,60	1,12	0,67	0,84	0,78	0,66	1,37	1,28	2,70

LiDAR-mast deviations found in this study are relatively small when compared to experimental results from other studies in more complex terrain. (Bingöl et al., 2009) found deviations of 4–7 % between a LiDAR and a co-located mast, dependent on wind direction. However, terrain slopes at the two investigated sites were significantly higher. (Bradley et al., 2012) analysed LiDAR-mast deviations for a Scottish Site (Myres Hill) of moderate complexity. In relation to the co-located met mast there also was a slight underestimation that decreased with increasing measurement height. Regarding the magnitude of the mean deviations, the errors found there are comparable to those at Rödeser Berg. Yet, there is no significant decrease in regression slope with increasing measurement height for the 200 m met mast site as it was found at Myres Hill (Bradley et al., 2012).

4.2 Modelling the LiDAR error

As described in Section 3.2 and 3.3 the LiDAR error was estimated using three different flow models. The results for 120 m measurement height in comparison to the observed LiDAR-mast deviations are shown in Fig. 6 (upper plot). In general, all models capture the pattern of the double sine wave in the observations. However, WEng strongly over-estimates the LiDAR error for directions with steep terrain inclinations.

In contrast both RANS-models perform better and capture the magnitude as well as the pattern of the LiDAR error. The RANS results are especially promising when compared to typical uncertainties assumed for mast based cup anemometer measurements of about 1–2 %. Fig. 6 (upper plot) model runs were performed using parameterisations estimated based on the observa-

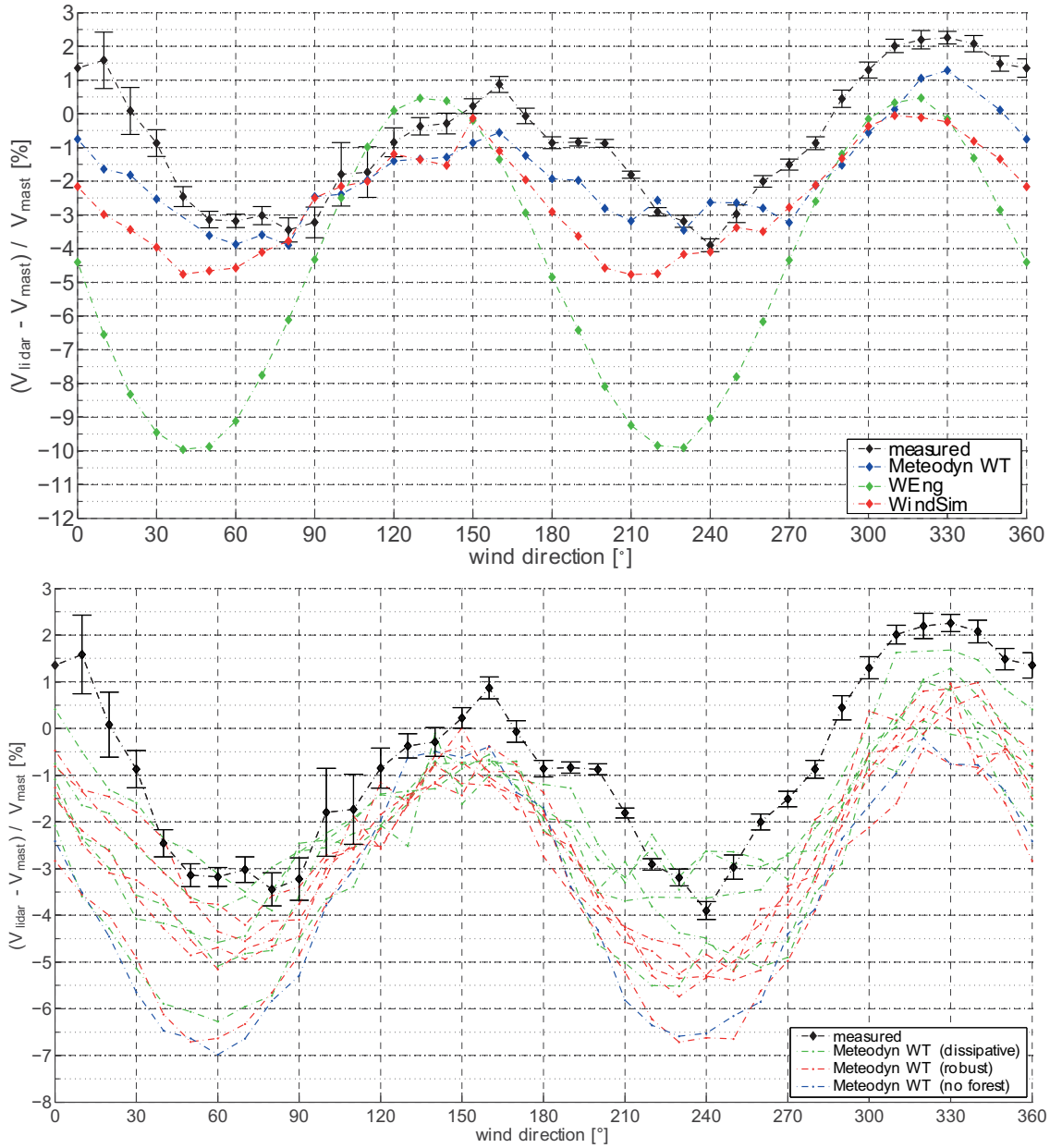

Figure 6: Mean relative deviation between LiDAR and mast measurements versus wind direction at 120 m height compared to estimated LiDAR error for different models (upper plot) and model spread caused by different parameterisations of Meteodyn WT (lower plot). For both, the dissipative and the robust forest model, the forest density and forest-height-to-roughness-ratio are varied. Only wind speeds $V \geq 4\,\mathrm{ms}^{-1}$ are considered. For this height, the number of data points per wind direction bin varies from 17 to 773. The errors bars indicate the confidence intervals.

tions during site visits and on the recommendations from the software manuals of Meteodyn WT and WindSim.

It is interesting to note that for sectors with steep terrain inclination angles and long forest fetch the differences between WEng and the RANS models is largest. For flow along the ridge the results from all three models are similar.

By extending the methodology to compute the LiDAR error, the effect of different terrain features on the measurement behaviour of the LiDAR can be illustrated. Fig. 7 shows an example for the spatial distribution of the simulated LiDAR error in the hilly landscape of Rödeser Berg for the wind direction of 240 °.

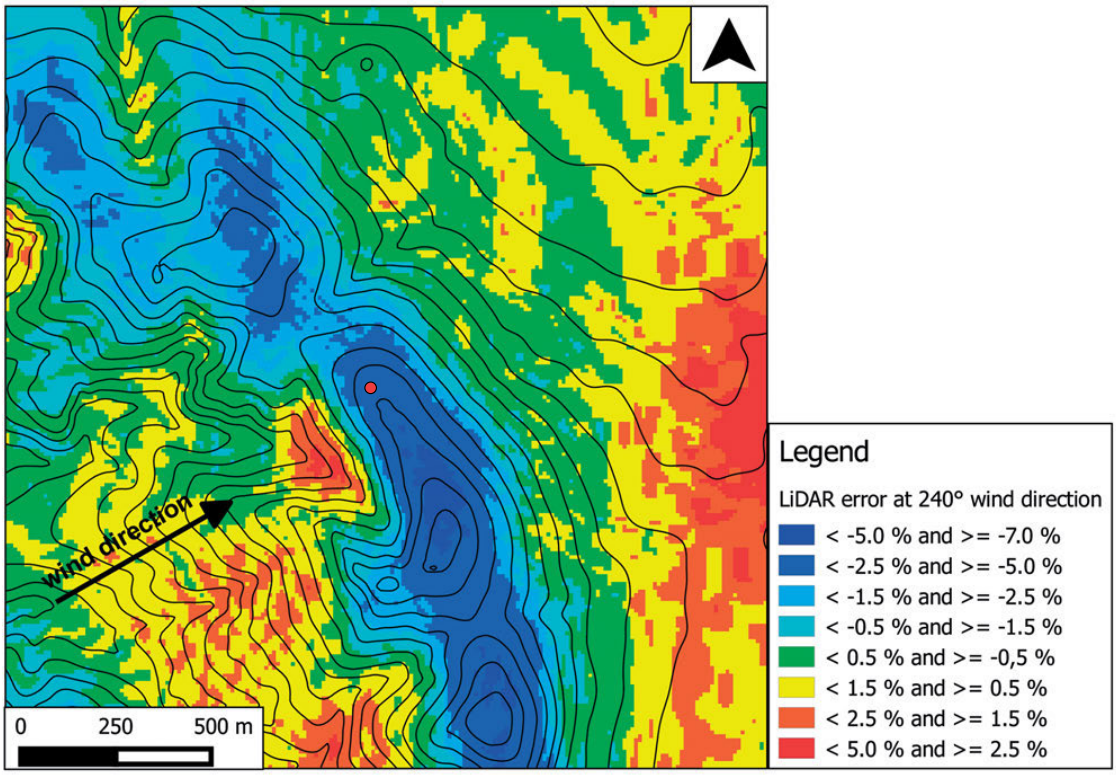

Figure 7: Map of estimated LiDAR errors around Rödeser Berg for 240 ° wind direction. The LiDAR errors are modelled with Meteodyn WT by using the above explained methodology. The map has a resolution of 10 m. Blue colour marks areas of underestimation, while yellow / red colour marks overestimation of the 'true' wind by a LiDAR measurement. Green areas are close to zero deviation. Black lines are 10 m height contour lines. The red dot marks the approximate LiDAR and mast location.

It is clearly visible that the ridge and hill top locations of Rödeser Berg show high underestimations of the horizontal wind speed by the LiDAR. The valleys upstream of the hill exhibit a positive LiDAR error. The overestimation at the right edge of the graph is caused by a small hill, which is located outside of the domain shown in this graph (compare Fig. 1).

To better understand the performance of the models, it is crucial to understand the sensitivity to their parameterisations. One of the biggest challenges in modelling atmospheric boundary layer flows is the representation of forests (e.g. Finnigan and Belcher, 2004). Therefore, the influence and parameterisation of the forest model of Meteodyn WT is more closely investigated here.

Table 3 and Fig. 6 (lower plot) depict the results of a series of Meteodyn WT runs using different forest parameterisations. It is obvious that the spread of the results is large – especially for flow with steep terrain inclination angles. Differences between the different model parameterisations reach up to 5 % in estimated LiDAR error.

It is also intriguing to note that a reduction of forest height and density results in larger deviations between the observed LiDAR-mast deviations and the estimated LiDAR error. The worst model performance is achieved when removing the forest model from the simulations. Note also that the modelling results can be slightly improved when the tree height is increased to an unrealistic value of 40 m. In general, the sensitivity of the modelling results to the parameterisation of the forest is in accordance to other studies investigating flow simulations in forested areas (e.g. Dellwik et al., 2006; Finnigan and Belcher, 2004; Crasto, 2007). Over forested hills Finnigan and Belcher (2004) concluded that including the forest canopy model had important effect on streamlines and profiles of the flow. It underlines the need for a careful choice and parameterisation of the forest model. Moreover, the importance of the forest parameterisation in the estimations of the LiDAR error indicates that the forest representation in the model is not only important for an accurate horizontal and vertical extrapolation of the wind speed, but also for the simulation of the flow angles in complex orography. As pointed out in Section 3.1 the flow angle in the LiDAR beams is expected to have the strongest influence on the LiDAR error.

For WEng the forest is modelled using a roughness length of z_0 = 1.0 m and a displacement height of d = 20 m (Table 4). There was no significant influence on

Table 4: Parameterization of the three different flow models and model runs for Meteodyn WT (MWT). At the given horizontal resolution it was not possible to run the WAsP Engineering (WEng) model with the same model extension as the two other models. Regardless of that, the modelled area is still of sufficient size. The main focus of the parameter variation was on the forest modelling in Meteodyn WT runs 1 to 11. To ensure comparability, a displacement height of 20 m was set for the two model runs without forest modelling (WAsP Engineering and Meteodyn WT run 11). The parameterization of WindSim was kept as close as possible to the Meteodyn WT run 1.

Model (run)	**Forest model**	**Forest height [m]**	**Forest porosity**	**Forest roughness**	**A**	**d [m]**	**Model extension**	**Direction sectors**	**Horizontal resolution**	**Vertical resolution**	**No. of cells**	**run time [h]**	**Software version**
WEng	none	-	-	1.0 m	-	20	$10 \times 10\,km^2$	36 (10 ° step)	10 m	not applicable	1000×1000 (1 MM)	~ 4	2.0
WindSim	standard	30	0.3	n/a	-	n/a	$20 \times 20\,km^2$		10 m, expanding factor 1.2	5 m (at the ground), expanding factor 1.1	$281 \times 286 \times 30$ (2,410,980)	~ 60	5.1.0
MWT (1)	dissipative	30	high		30	n/a	$20 \times 20\,km^2$		8 m (at the LiDAR), expanding factor 1.1	4 m (at the ground), expanding factor 1.2	$148 \times 148 \times 35$ (766,640)	~ 12	4.8.1
MWT (2)			low										
MWT (3)			normal										
MWT (4)		20	high		20								
MWT (5)		40			40								
MWT (6)	robust	30	high		30								
MWT (7)			low										
MWT (8)			normal										
MWT (9)		20	high		20								
MWT (10)		40			40								
MWT (11)	none	0	-	1.0 m	0	20							

the results regarding the LiDAR error estimation from WEng when increasing z_0 to 2.0 m. In contrast to the RANS models in WEng, there is no forest model implemented. This might partly explain some of the large deviations between the observed LiDAR-mast deviations and estimated LiDAR errors. However, the RANS simulation without a forest model achieved slightly better results than WEng indicating an improved performance to represent the complexity of the flow due to the orography (Table 3).

5 Conclusion and outlook

At Rödeser Berg a LiDAR-mast inter-comparison in complex terrain was carried out using high quality equipment. While the averaged LiDAR-mast deviations over all wind directions was relatively small, terrain induced errors in the LiDAR were significantly larger for individual sectors. The double sine wave curve of the LiDAR-mast deviations can be directly linked to the shape of the terrain. For the measurement location at Rödeser Berg the mean wind speed is underestimated by about 0.8 to 1.5 % for all relevant heights. Regardless of this very good result, it is important to point out that the shape and orientation of ridges and hills in relation to the wind direction distribution at the particular site do heavily influence the resulting mean deviation. In average, deviations in individual directions might cancel out. But for certain configurations, with wind mostly coming from sectors with highest LiDAR errors, the mean wind speed measurement could be considerably biased. This stresses that careful consideration needs to be given to the LiDAR error due to complex terrain – especially when high precision wind speed measurements are required.

The inter-comparison of the different flow models revealed large differences between individual models and parameterisations. The results emphasize the importance of an appropriate representation of the forest in the flow simulations to reproduce the LiDAR errors to a sufficient degree of accuracy. Also the results from the model runs without a forest model indicating that the RANS models perform slightly better compared to the linear model without a forest model.

Given the right parameterisation and model choice, flow simulations can be a valuable tool to post-process LiDAR-measurements in complex terrain.

If simulations are performed in advance of a measurement campaign the expected errors can be estimated a priori and the experiment design can be adapted to the local conditions. An important fact to bear in mind, here, is that the uncertainty in the estimated LiDAR error and, thus, the wind speeds derived from the LiDAR, will depend on the performance of the model. This is likely to decrease with the complexity of the terrain and, therefore, the magnitude of the estimated error. This is especially important when economic decisions are based on the outcome of the measurements – e.g. in wind resource assessments.

Acknowledgments

The work presented within this paper is part of the research project “Utilization of Inland Wind Power”, funded by the German Federal Ministry for Economic Affairs and Energy (BMWi).

References

Albers, A., A.-W. Janssen, 2008: Evaluation of Windcube. – Internal Project. – Deutsche WindGuard Consulting GmbH, Varel.

Antoniou, I., H.E. Jørgensen, T. Mikkelsen, T. Friis Pedersen, G. Warmbier, D. Smith, 2004: Comparison of wind speed and power curve measurements using a cup anemometer, a LIDAR and a SODAR. – In: European Wind Energy Association (Ed.), Scientific proceedings, London, 47–51.

Bingöl, F., J. Mann, D. Foussekis, 2009: Conically scanning lidar error in complex terrain. – Meteorol. Z. **18**, 189–195.

Bradley, S., 2008: Wind speed errors for LIDARs and SODARs in complex terrain. – IOP Conf. Ser.: Earth Environ. Sci. 1, 12061, DOI:10.1088/1755-1315/1/1/012061.

Bradley, S., Y. Perrott, P. Behrens, A. Oldroyd, 2012: Corrections for Wind-Speed Errors from Sodar and Lidar in Complex Terrain. – Bound.-Layer Meteor. **143**, 37–48.

Bradley, S., A. Strehz, S. Emeis, 2015: Remote sensing winds in complex terrain – a review. – Meteorol. Z., **25**, 547–555, DOI:10.1127/metz/2015/0640

Clive, P.J.M., 2008: Compensation of bias in Lidar wind resource assessment. – Wind Engineering **32**, 415–432.

Courtney, M.S., R. Wagner, P. Lindelöw, 2008: Testing and comparison of lidars for profile and turbulence measurements in wind energy. – IOP Conf. Ser.: Earth Environ. Sci. **1**, 14 pp.

Crasto, G., 2007: Numerical Simulations of the Atmospheric Boundary Layer. – Dissertation, Cagliari, 195 pp.

Dellwik, E., L. Landberg, N.O. Jensen, 2006: WAsP in the Forest. – Wind Energy **9**, 211–218.

Emeis, S., M. Harris, R.M. Banta, 2007: Boundary-layer anemometry by optical remote sensing for wind energy applications. – Meteorol. Z. **16**, 337–347.

Fikke, S., G. Ronsten, A. Heimo, S. Kunz, M. Ostrozlik, P.-E. Persson, 2007: COST 727: Atmospheric Icing on Structures, Measurements and Data Collection on Icing: State of the Art. – Bundesamt für Meteorologie und Klimatologie, MeteoSchweiz.

Finnigan, J.J., S.E. Belcher, 2004: Flow over a hill covered with plant canopy. – Quart. J. Roy. Meteor. Soc. **130**, 1–29.

Gottschall, J., M.S. Courtney, R. Wagner, H.E. Jørgensen, I. Antoniou, 2011: Lidar profilers in the context of wind energy – a verification procedure for traceable measurements. – Wind Energy **15**, 147–159.

Gravdahl, A.R., 1998: Meso Scale Modeling with a Reynolds Averaged Navier-Stokes Solver: Assessment of wind resources along the Norwegian cost. – 31th IEA Experts Meeting State of the Art on Wind Resource Estimation, Roskilde.

Hurley, P.J., 1997: An evaluation of several turbulence schemes for the predictio of mean and turbulent fields in complex terrain. – Bound.-Layer Meteor. **83**, 43–73.

HVBG, 2010: Digitales Landschaftsmodell / Digitales Geländemodell. – Hessische Verwaltung für Bodenmanagement und Geoinformationen, Wiesbaden.

IEC, 2013: Wind turbines - Part 12-1: Power performance measurements of electricity producing wind turbines (2nd Committee Draft), 2nd ed. 27.180. Wind turbine energy systems. – Aviable at http://www.iec.ch.

Jackson, P.S., J.C.R. Hunt, 1975: Turbulent wind flow over a low hill. – Quart. J. Roy. Meteor. Soc. **101**, 929–955, DOI:10.1002/qj.49710143015.

Kindler, D., A. Oldroyd, A. Macaskill, D. Finch, 2007: An eight month test campaign of the Qinetiq ZephIR system: Preliminary results. – Meteorol. Z. **16**, 479–489.

Landberg, L., L. Myllerup, O. Rathmann, E.L. Petersen, B.H. Jørgensen, J. Badger, N.G. Mortensen, 2003: Wind Resource Estimation: An Overview. – Wind Energy **6**, 261–271, DOI:10.1002/we.94.

Mann, J., P. Astrup, L. Kristensen, O. Rathmann, P.H. Madsen, D. Heathfield, 2000: WAsP Engineering DK. – Roskilde.

Mann, J., S. Ott, B.H. Jørgensen, H.P. Frank, 2002: WAsP Engineering 2000. – Roskilde, Denmark.

MEASNET, 2009: Anemometer Calibration Procedure: Version 2. – Measuring Network of Wind Energy Insitutes.

METEODYN, 2007: Technical Note. – meteodyn WT, Nantes.

METEODYN, 2014: Manual. – meteodyn WT, Nantes.

Palma, J., F.A. Castro, L.F. Ribeiro, A.H. Rodrigues, A.P. Pinto, 2008: Linear and nonlinear models in wind resource assessment and wind turbine micro-siting in complex terrain. – J. Wind Eng. Ind. Aerodyn. **96**, 2308–2326, DOI:10.1016/j.jweia.2008.03.012.

Pauliac, R., 2009: WINDCUBE. – User's Manual, Orsay.

Ronsten, G., T. Wallenius, M. Hulkkonen, I. Baring-Gould, R. Cattin, M. Durstewitz, et al., 2012: IEA Wind Task 19: State-of-the-Art of Wind Energy in Cold Climates. – IEA.

Ross, A.N., S.B. Vosper, 2005: Neutral turbulent flow over forested hills. Quart. J. Roy. Meteor. Soc. **131**, 1841–1862.

Smith, D.A., M. Harris, A.S. Coffey, 2006: Wind Lidar Evaluation at the Danish Wind Test Site in Høvsøre. –Wind Energy **9**, 87–93.

Troen, I., 1990: A spectral diagnositic model for wind flow simulations in complex terrain, in: American Meteorological Society (Ed.). – 9. Symposium on turbulence and diffusion, Vol. 9, Boston, MA, 243–249.

Wagner, R., J. Bejdic, 2014: Windcube + FCR test at Hrgud, Bosnia and Herzegovina. – DTU Wind Energy. 40 p.

Wilson, J.D., J.J. Finnigan, M.R. Raupach, 1998: A first-order closure for distrurbed plant-canopy flows, and its application to winds in a canopy on a ridge. – Quart. J. Roy. Meteor. Soc. **124**, 705–732.

C. Pauscher et al. (2016)

Pauscher, L., Vasiljevic, N., Callies, D., Lea, G., Mann, J., Klaas, T., Hieronimus, J., Gottschall, J., Schwesig, A., Kühn, M. and Courtney, M.: An inter-comparison study of multi- and DBS-lidar measurements in complex terrain, Remote Sensing, 8(9),782, doi:10.3390/rs8090782, 2016.

Pauscher, L., Vasiljevic, N., Callies, D., Lea, G., Mann, J., Klaas, T., Hieronimus, J., Gottschall, J., Schwesig, A., Kühn, M. and Courtney, M.: Erratum: An inter-comparison study of multi- and DBS-lidar measurements in complex terrain, Remote Sensing, 9(7),667, doi:10.3390/rs9070667, 2017.

remote sensing

MDPI

Article

An Inter-Comparison Study of Multi- and DBS Lidar Measurements in Complex Terrain

Lukas Pauscher [1,2,*], Nikola Vasiljevic [3], Doron Callies [1], Guillaume Lea [3], Jakob Mann [3], Tobias Klaas [1,4], Julian Hieronimus [5], Julia Gottschall [6], Annedore Schwesig [1], Martin Kühn [5] and Michael Courtney [3]

1 Fraunhofer Institute for Wind Energy and Energy System Technology (IWES), Fraunhofer IWES | Kassel, Königstor 59, 34119 Kassel, Germany; doron.callies@iwes.fraunhofer.de (D.C.); tobias.klaas@iwes.fraunhofer.de (T.K.); annedore@schwesig-schauenburg.de (A.S.)
2 Department of Micrometeorology, University of Bayreuth, 95447 Bayreuth, Germany
3 DTU Wind Energy, Risø Campus, Technical University of Denmark, 4000 Roskilde, Denmark; niva@dtu.dk (N.V.); gule@dtu.dk (G.L.); jmsq@dtu.dk (J.M.); mike@dtu.dk (M.C.)
4 Institute for Geophysics and Meteorology, University of Cologne, 50923 Köln, Germany
5 ForWind, Center for Wind Energy Research, Carl von Ossietzky Universität Oldenburg, Küpkersweg 70, 26129 Oldenburg, Germany; Julian.Hieronimus@uni-oldenburg.de (J.H.); Martin.Kuehn@forwind.de (M.K.)
6 Fraunhofer Institute for Wind Energy and Energy System Technology (IWES), Fraunhofer IWES | Northwest, 27572 Bremerhaven, Germany; julia.gottschall@iwes.fraunhofer.de
* Correspondence: lukas.pauscher@iwes.fraunhofer.de; Tel.: +49-561-7294-475

Academic Editors: Guoqing Zhou, Richard Müller and Prasad S. Thenkabail
Received: 1 July 2016; Accepted: 13 September 2016; Published: 21 September 2016

Abstract: Wind measurements using classical profiling lidars suffer from systematic measurement errors in complex terrain. Moreover, their ability to measure turbulence quantities is unsatisfactory for wind-energy applications. This paper presents results from a measurement campaign during which multiple WindScanners were focused on one point next to a reference mast in complex terrain. This multi-lidar (ML) technique is also compared to a profiling lidar using the Doppler beam swinging (DBS) method. First- and second-order statistics of the radial wind velocities from the individual instruments and the horizontal wind components of several ML combinations are analysed in comparison to sonic anemometry and DBS measurements. The results for the wind speed show significantly reduced scatter and directional error for the ML method in comparison to the DBS lidar. The analysis of the second-order statistics also reveals a significantly better correlation for the ML technique than for the DBS lidar, when compared to the sonic. However, the probe volume averaging of the lidars leads to an attenuation of the turbulence at high wave numbers. Also the configuration (i.e., angles) of the WindScanners in the ML method seems to be more important for turbulence measurements. In summary, the results clearly show the advantages of the ML technique in complex terrain and indicate that it has the potential to achieve significantly higher accuracy in measuring turbulence quantities for wind-energy applications than classical profiling lidars.

Keywords: multi-lidar; WindScanner; complex terrain; turbulence; wind energy

1. Introduction

Over recent years, lidar (light detection and ranging) technology has quickly penetrated wind-energy applications. Especially in resource assessment, Doppler lidars are now widely used for wind measurements to predict the annual energy production of windfarms. In flat and homogeneous terrain, classical profiling lidars using the Doppler beam swinging (DBS) or velocity azimuth display (VAD) techniques achieve high accuracy [1]. Therefore, in recent years, their use has been adopted into national and international standards and guidelines [2,3].

The application of Doppler lidars in complex terrain, however, remains difficult and is often associated with systematic errors in mean wind-speed estimations [4,5]. If the flow is complex, the homogeneity assumption underlying the DBS and VAD techniques is often violated. First comparison studies have shown promising results in the capabilities of flow models in correcting this complex terrain error at individual sites [4,6]. However, they also indicated a high sensitivity to model parameterisations [6] and remain limited to moderately complex terrain. Moreover, the application of corrections leads to an increased uncertainty.

Another disadvantage of profiling lidars compared to mast-based measurements is that the estimation of turbulence characteristics, which are, e.g., relevant for wind-turbine loads, is not possible with the desired accuracy [7–9]. Most prominently, the estimation of the variance of the wind-vector components and the respective spectra suffer from systematic errors due to the effects of cross-contamination and volume averaging [9,10]. Newman and co-workers showed that some of the cross-contamination effect can be mitigated by applying a correction based on the measurement of the vertical variance [11]. However, their experimental results indicated that even after the application of the correction, a large deviation between lidar and mast-based measurements can remain. In general, a turbulence correction is difficult since it depends not just on lidar technology and measurement configuration but also the three-dimensional structure of the turbulence itself and, as a consequence, on atmospheric conditions [8,9]. New scanning strategies thus need to be developed. A promising example is the six-beam method [12,13], where turbulence parameters are directly derived from the radial velocity variances. Although the first encouraging experimental results have been reported in [12], other experiments indicated mixed results [11]. In complex terrain, the six-beam method might also be affected by an inhomogeneous turbulence field.

Probably the most intuitive solution to reduce the potential errors in lidar measurements is to set up multiple lidars such that the various lidar beams intersect at a single point from different directions (muti-lidar technique or ML). This strongly reduces the need for flow homogeneity in lidar measurements. Moreover, intersecting lidar beams probably offer the best approach to derive highly resolved time series of the three-dimensional wind-vector and turbulence statistics [14].

In flat and homogeneous terrain, first experimental results intersecting three lidar beams next to a sonic anemometer showed encouraging results for mean wind speeds [15–17] and turbulence statistics [14,16]. Mann and co-authors showed good agreement between second-order turbulence statistics of the radial wind velocities from multiple lidar systems and a sonic anemometer measurement [14] which was corrected using the spectral tensor model of [18]. Fuertes and co-authors achieved good agreement in second-order turbulence statistics between three intersecting lidars and a sonic anemometer to which they applied a simpler, pseudo-spatial filtering approach [16]. However, both studies were performed under idealised conditions in flat and homogeneous terrain and only report on very limited sample sizes. Newman and co-workers have also used three lidar beams intersected in a single point to derive turbulence statistics [19], but no adequate reference was available to assess the accuracy of their measurements.

This paper presents measurements performed during the *Kassel 2014 Experiment*. The aim of the *Kassel 2014 Experiment* was to experimentally explore and demonstrate the advantages of ML measurements under conditions which are realistic for wind-energy applications in complex terrain. The experiment also served as a test bed for the complex terrain experiments in the New European Wind Atlas which will heavily rely on ML measurements [20]. Here, we present measurements and comparisons of four long-range WindScanners, which intersected at one point, a DBS lidar, and a sonic anemometer at a reference mast at a complex forested site. An analysis of the radial velocity statistics is used to examine the measurement accuracy of the individual instruments as well as the accuracy of the setup process. It is also used to provide insight into the path-averaging effect on turbulence measurements with the WindScanners. An analysis of the first- and second-order statistics of the horizontal wind speed contrasts error sources for the different lidar techniques.

The ML-DBS-mast inter-comparison is especially valuable to analyse and quantify the benefits of the ML technique over the standard DBS lidar and experimentally compare their measurement behaviour in complex terrain. The WindScanners were located at distances ranging from directly next to the mast to 3740 m from the reference mast; they reflect a measurement scenario which is "realistic" in windfarm development scenarios in complex terrain.

2. Materials and Methods

2.1. Wind Vector Reconstruction and Scanning Strategies

Doppler lidars provide an estimate of reflectivity-weighted, radial velocities of aerosol particles. This velocity was applied as a good approximation for the radial wind velocity. In the context of wind profilers, the difference between Doppler velocity and real-wind velocity has been addressed by [21]. For Doppler lidars, the assumption seems justified as most of the backscattering for optical wavelengths is from particles which are small enough to be advected with the wind (e.g., [22]). Moreover, a homogeneous aerosol concentration within the probe volume needs to be assumed at this point. The measured radial velocity ($v_{r\,i}$) is thus a projection of the three-dimensional wind vector ($\mathbf{v}$) onto the lidar beam

$$v_{r\,i} = \mathbf{v_i} \cdot \boldsymbol{n_i}, \tag{1}$$

where $\boldsymbol{n_i}$ is the unit vector in the direction of the lidar beam and i denotes the individual beam and its location. In meteorological applications, it is convenient to write this equation as:

$$v_{r\,i} = u_i \cos(\theta_i)\cos(\phi_i) + v_i \cos(\theta_i)\sin(\phi_i) + w_i \sin(\theta_i), \tag{2}$$

where u is directed into the mean wind direction during the averaging interval, v is perpendicular to u in the horizontal and w is the vertical component of the wind vector. The projection onto the radial is defined by the elevation angle θ in addition to the angle between the mean wind direction and the beam ϕ. The azimuth angle (ψ) or beam-pointing angle is often used instead of ϕ in the literature to define (2). However, in this paper, the use of ϕ makes the notation in the later chapters more consistent.

Assuming homogeneous flow (i.e., $\mathbf{v_i} = \mathbf{v}$) between the measurement locations or—as is the case for ML configurations—the intersection of the beams in a single location, multiple measurements can be combined to derive $\mathbf{v}$ using matrix inversion

$$\mathbf{v} = \boldsymbol{M}^{-\mathbf{1}} \cdot \boldsymbol{v_r}, \tag{3}$$

where $\boldsymbol{M} = \{\boldsymbol{n_1}, \boldsymbol{n_2}, \ldots\}$. For a reconstruction of all components of $\mathbf{v}$, at least three beams need to be combined.

The horizontal wind speed (V_h) is then defined as:

$$V_h = \sqrt{u^2 + v^2}. \tag{4}$$

Classical profiling wind lidars usually rely on a scanning strategy, which employs a conical scan above the instrument and measures $v_{r\,i}$ at a fixed height and at different azimuth angles. The wind profiler lidar (manufacturer Leosphere, type Windcube v2), which is used as a reference instrument in this study, scans in DBS mode and uses four beams (with $\theta = 62°$), which are arranged in two perpendicular planes (Figure 1). An additional vertical beam is used to measure w directly. The resulting separation between two opposing beams in this setup is roughly equal to the measurement height.

Especially in complex terrain, the assumption of homogeneous flow across the different beams of a profiling lidar is often violated; significant, direction-dependent errors in the estimation of the mean can be introduced [4,5]. The main reason for the observed errors is thought to be the difference in $\overline{w}$ (the overbar denotes the mean) across the different beam locations [4,5]. Differences in the other

components will of course also introduce an error. For the site of the current experiment, a deviation to mast-bound cup anemometer measurements of approx. −4% to +2% in $\overline{V_h}$ has previously been reported [6]. Also the scatter in the inter-comparison was higher than in comparable experiments in flat and homogeneous terrain [1].

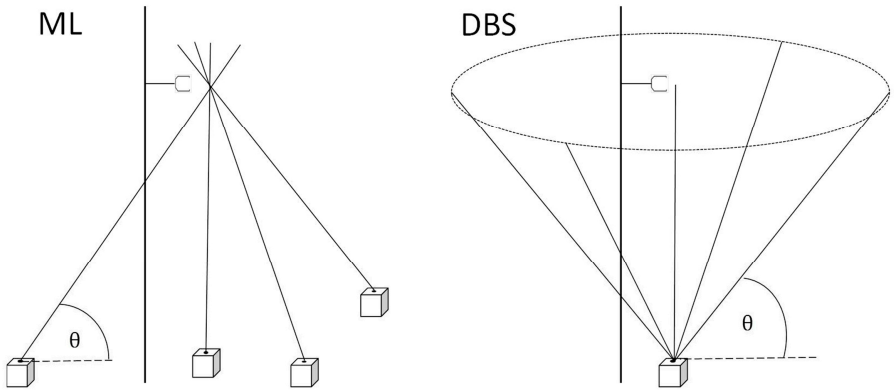

Figure 1. Sketch of the multi-lidar (ML) and Doppler beam swinging (DBS) strategies next to a reference mast with a sonic as used in this study. Note that the angles and positions of the lidars differ from the instrument setup for reasons of illustrative clarity.

In contrast to profiling lidars, the ML-technique uses a combination of multiple lidars, which are located around the measurement location and focus their laser beams to intersect in a single location (Figure 1). Since multiple independent measurements of the radial velocity are made at the point of interest, the assumption of horizontal homogeneity of the mean flow among the different beam locations is not needed. The effect of a potential inhomogeneity within the probe volume of the ML measurement is expected to be much smaller and the beam separation problem inherent in a profiling lidar measurement is potentially overcome.

2.2. Second-Order Statistics of v_r

One of the characteristics of wind-speed measurements from Doppler lidars is that, due to the measurement principle, v_r is retrieved from a measurement within a probe volume. The width of the laser beam is usually negligible compared to the length of the probe volume along the path. The effect of the measurement volume on $v_{r\ lidar}$ can thus be simplified to line averaging along the direction of the lidar beam. This can be expressed as

$$v_{r\ lidar} = \int_{-\infty}^{\infty} \varphi(s)\, \boldsymbol{n}\cdot\mathbf{V}(\mathbf{r}+\boldsymbol{n}\mathrm{s})\, ds, \tag{5}$$

where $\varphi(s)$ is the weighting function along the probe volume, $\mathbf{r}$ is the centre of the probe volume and $\mathbf{V}$ is the three-dimensional velocity field. Depending on the signal processing and shape of the emitted laser pulse, $\varphi(s)$ will vary and different forms have been suggested (e.g., [23,24]). Here we follow the concept that the weighting function can be estimated from a convolution of the form of the laser pulse $\varphi_p(s)$ and the gate-weighting function $\varphi_g(s)$, which results from the size and shape of the sampling gate—i.e., the internal signal processing [25]. Since the effects of line averaging depend on the scale of the turbulent eddies, it is convenient to express the problem in Fourier space. The Fourier transform of (5) can be written as [14,26]:

$$\hat{v}_{r\ lidar}(\boldsymbol{k}) = \hat{\varphi}(\boldsymbol{k}\cdot\boldsymbol{n})\, \boldsymbol{n}\cdot\hat{\mathbf{V}}(\boldsymbol{k}), \tag{6}$$

where $\boldsymbol{k}$ is the wave vector (k_1, k_2, k_3) and $\hat{}$ denotes the Fourier transform. For the WLS 200s (a scanning lidar manufactured by Leosphere) used in this study, both weighting functions can be approximated by a Gaussian function [27]. $\hat{\varphi}(\boldsymbol{k})$ can thus be approximated by

$$\hat{\varphi}(\boldsymbol{k}) = \hat{\varphi}_p(\boldsymbol{k})\,\hat{\varphi}_g(\boldsymbol{k}) = e^{-\boldsymbol{k}^2\sigma_p^2} e^{-\boldsymbol{k}^2\sigma_g^2}, \tag{7}$$

where σ_p is the standard deviation of $\varphi_p(s)$ and σ_g is the standard deviation of $\varphi_g(s)$.

In practice, pulsed lidars use an accumulation time to derive the radial wind speed. We thus need to account for the temporal averaging. This can be done by adding the additional term $\hat{\zeta}(k_1) = sinc(k_1 \cdot t \cdot u/2)$, where t is the averaging time [14]. Assuming a homogeneous turbulence field along the probe volume and Taylor's hypothesis of frozen turbulence, we can express the line averaging in (6) on the measured turbulence spectrum, $F_{v_r}(k_1)$, using the spectral density tensor $\Phi_{ij}(\boldsymbol{k}) = \hat{\mathbf{V}}(\boldsymbol{k})\,\hat{\mathbf{V}}^*(\boldsymbol{k})$ as [14,26]

$$F_{v_r}(k_1) = n_i n_j \left|\hat{\zeta}(k_1)\right|^2 \iint \hat{\varphi}(\boldsymbol{k}\cdot\boldsymbol{n})\,\hat{\varphi}^*(\boldsymbol{k}\cdot\boldsymbol{n})\,\Phi_{ij}(\boldsymbol{k})\,dk_2 dk_3\,, \tag{8}$$

where * denotes the complex conjugate. Summation over repeated indices is assumed. In analogy to what Kaimal and co-workers [26] suggested for sonic anemometers, we can now define a spectral transfer function between the spectrum measured by the lidar and a point measurement as

$$T_{v_r}(k_1) = \frac{F_{v_r\ lidar}(k_1)}{F_{v_r\ point}(k_1)} = \frac{n_i n_j \left|\hat{\zeta}(k_1)\right|^2 \iint \hat{\varphi}(\boldsymbol{k}\cdot\boldsymbol{n})\,\hat{\varphi}^*(\boldsymbol{k}\cdot\boldsymbol{n})\,\Phi_{ij}(\boldsymbol{k})\,dk_2 dk_3}{n_i n_j \iint \Phi_{ij}(\boldsymbol{k})\,dk_2 dk_3}. \tag{9}$$

The attenuation in $v_{r\ lidar}$ can then be calculated by integrating the spectra over k_1. One of the difficulties with (9) is that a model for $\Phi_{ij}(\boldsymbol{k})$ [18,26] is needed to estimate $T_{v_r}(k_1)$. If $\mathbf{n}$ is in the direction of x_1, $\hat{\varphi}(\boldsymbol{k}\cdot\mathbf{n})$ becomes independent of k_2 and k_3 and they can be removed from the integral [26]. In this case, the effect of line averaging can be expressed as

$$T_{v_r}(k_1) = \left|\hat{\varphi}(k_1)\right|^2 \left|\hat{\zeta}(k_1)\right|^2. \tag{10}$$

This special case has the advantage of removing the need for a model of $\Phi_{ij}(\boldsymbol{k})$. The line averaging effect can now be modelled by applying the theoretical formulation in (10) to a point measurement. If the centre of the lidar range gate and the point measurement are co-located, the only assumption that we have to make is Taylor's frozen turbulence hypothesis along the probe volume of the lidar and the form of $\hat{\varphi}(\boldsymbol{k})$. In field measurements, the lidar beam will rarely be exactly parallel to the streamlines. In fact, during the *Kassel Experiment 2014*, the beams of all WindScanner devices were pointed upwards into the atmosphere to some degree. Therefore, (9) would be the exact expression. However, in the later analysis, we assume that (10) is still a good approximation if the angle between the mean streamlines is small.

2.3. Second-Order Statistics from Multiple Lidar (ML) Beams

In wind-energy applications $\overline{{V'_h}^2}$ or $\overline{u'^2}$ and, in more complex terrain, also $\overline{v'^2}$ and $\overline{w'^2}$ are of key interest in a site suitability analysis [28]. The respective spectra are also important as they directly feed into models commonly used for load simulation in the design process of wind turbines [29,30].

In case the lidar beam is not pointing exactly in the direction of the wind component of interest, we need to use a combination of multiple beams (Section 2.1). In this situation, in addition to the line averaging, the location of the different lidar beams to each other becomes important. For a mathematical formulation of the effect of beam separation, it is convenient to define the distance of the lidar measurement from the point for which the measurement is assumed to be representative of

($\boldsymbol{x_0}$). In case of the conical scan of a profiling (DBS) lidar this would be the centre of the circle of the lidar scan:

$$\boldsymbol{d} = \boldsymbol{x} - \boldsymbol{x_0}, \tag{11}$$

where $\boldsymbol{x}$ is the location of the centre of the averaging path. Adding the measurement location to (6) and including the temporal averaging, $\hat{v}_{r\ lidar}$ can now be rewritten as [26]

$$\hat{v}_{r\ lidar}\left(\boldsymbol{k}, \boldsymbol{d}\right) = \hat{\zeta}\left(k_1\right) e^{i\boldsymbol{k}\cdot\boldsymbol{d}} \hat{\varphi}\left(\boldsymbol{k}\cdot\mathbf{n}\right) \mathbf{n}\cdot\hat{\mathbf{V}}\left(\boldsymbol{k}\right). \tag{12}$$

The term $e^{i\boldsymbol{k}\cdot\boldsymbol{d}}$ basically decorrelates the wind field which is sensed at the different measurement locations for high wavenumbers by introducing a phase shift. By combining (3) and (12), a matrix $\boldsymbol{N}$ can now be defined, which accounts for the effects of line averaging and path separation in the vector reconstruction. The entries of $\boldsymbol{N}$ are

$$N_{ab}\left(\boldsymbol{k}\right) = M_{ab}\hat{\zeta}\left(k_1\right)\ e^{i\boldsymbol{k}\cdot\boldsymbol{d_b}} \hat{\varphi}\left(\boldsymbol{k}\cdot\mathbf{n_b}\right) \tag{13}$$

and its inverse $\boldsymbol{J} = \boldsymbol{N}^{-1}$. The vector reconstruction in the Fourier domain then becomes

$$\hat{\mathbf{v}}\left(\boldsymbol{k}\right) = \mathbf{J}\left(\boldsymbol{k}\right)\cdot\hat{\mathbf{V}}\left(\boldsymbol{k}\right) \tag{14}$$

The spectrum of e.g., the u component derived from three lidar beams can be written as

$$F_u\left(k_1\right) = \iint \sum_{b=1}^{3} J_{1b}\left(\boldsymbol{k}\right) J_{1b}^{*}\left(\boldsymbol{k}\right) \Phi_{ij}\left(\boldsymbol{k}\right) dk_2 dk_3\,, \tag{15}$$

where again the summation for repeating indices i and j is assumed. Sathe and co-workers call $\boldsymbol{J}$ "weighting factors," because they define how $\Phi_{ij}\left(\boldsymbol{k}\right)$ is weighted in the vector reconstruction [9]. The effect of the beam separation on the time series-derived wind vector is twofold. The decorrelation leads to a damping of the contribution of the spectral tensor, $\Phi_{ij}\left(\boldsymbol{k}\right)$, in the direction of the desired component (e.g., $i = j = 1$ for u) for high wavenumbers. However, the decorrelation effect is also present for the other components of $\Phi_{ij}\left(\boldsymbol{k}\right)$. As a result, some of the spectral energy of these components is folded onto $F_u\left(k_1\right)$. This effect is often referred to as cross-contamination in the literature [9,26], because the desired spectrum is contaminated by the other terms of $\Phi_{ij}\left(\boldsymbol{k}\right)$. As explained in Section 2.2. the effect of the probe volume averaging is mainly attenuation at small wavenumbers.

Using the spectral tensor model of [18], this effect for two different conically scanning lidars was investigated [9,10]. It was shown that the combined effects of beam separation and line averaging strongly depend on the beam configuration and the probe volume, which define $\boldsymbol{J}$, but also the atmospheric conditions i.e., $\Phi_{ij}\left(\boldsymbol{k}\right)$. Experimental evidence confirms these results and an underestimation as well as an overestimation of $\overline{u'^2}$ and $\overline{v'^2}$ has been reported [8,9,11,12]. It should also be noted that, in complex terrain, the assumption of a statistically homogeneous turbulence field implicitly inherent in (15) is likely to be violated and additional errors might be introduced into the turbulence measurement.

If the range gates which are used for the wind-vector reconstruction intersect at the same location, $e^{i\boldsymbol{k}\cdot\boldsymbol{d}} = 1$ and the effect of beam separation vanishes. Also, the distance for which a homogeneous turbulence needs to be assumed is greatly reduced. It is interesting to note that the line averaging still introduces some cross-contamination. The effect is small compared to the spectral probe-volume averaging, but may be increased if the probe volume differs between the beams.

In general, the same principles concerning the line averaging and path separation apply for a sonic anemometer as well. However, the sonic anemometer used in this study uses intersecting measurement paths which are 2–3 orders of magnitude smaller than the path averaging of the lidars. Thus these effects are neglected and the sonic anemometer is treated as an approximation of a point measurement in the analysis in this study.

2.4. Experimental Setup: The Kassel 2014 Experiment

The data presented in this paper was collected during the *Kassel 2014 Experiment* at Rödeser Berg—a hill in central Germany close to Kassel—during summer 2014 (3 July–17 August 2014). Five long-range WindScanners (scanning lidars based on the Windcube WLS200s) were set up around the hill (EE, SE, SW, WW, NN in Figure 2). A sixth scanner (MA) was placed on the ridge of the hill directly next to a 200 m high meteorological mast. An additional Windcube v2 (DBS lidar) was operated at a few meters' distance from the mast. The measurements from a sonic anemometer mounted on the mast serve as a reference in this study.

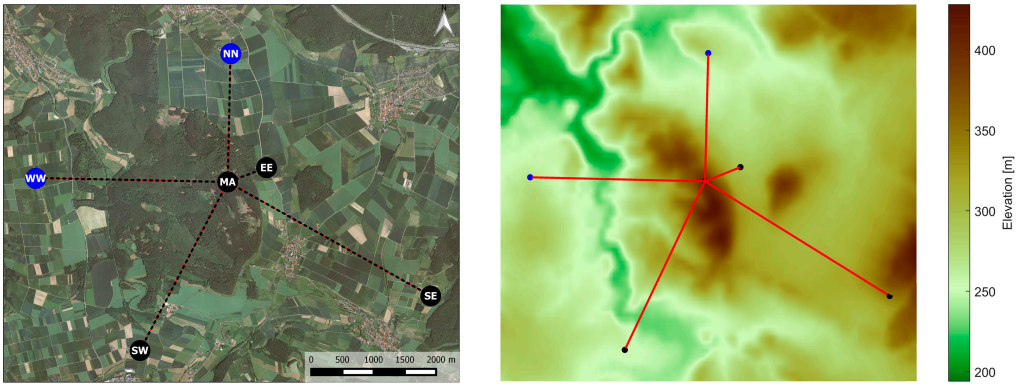

Figure 2. Instrumental setup during the measurement campaign. Left: aerial photograph (data source: published with kind permission of ©Hessische Verwaltung für Bodenmanagement und Geoinformation (HVBG)) with circles indicating the locations of the lidar and the met mast; the locations which are used in this study are indicated in black. Right: terrain (data source: Shuttle Radar Topography Mission [31] version 2.1) and trajectories of the intersecting lidar beams for the ML measurement. The windcube v2 (WC) is also located at the MA position.

The reference mast is erected on a small clearance within a forest which, depending on direction, stretches from 0.4 to 2.5 km around the mast. The wider surroundings are characterised by a patchy landscape of mainly agricultural land use, villages and forested hills (Figure 2). The height of the hill above the surrounding terrain is approx. 100–200 m depending on direction. More details about the measurement site can be found in [6].

During the deployment of the WindScanners the procedures for calibration of the home position, levelling, and sensing range as outlined in [15] were applied. For the purpose of these procedures around each WindScanner, with the exception of the MA WindScanner, at distances of approx. 100 m, three 2 cm thick surveying stakes were installed, separated by 120° in azimuth. The absolute positions of the WindScanners, stakes, and reference mast top were surveyed using a differential GPS and a theodolite. These positions were acquired with cm accuracy. The stakes were then mapped using the CNR-Mapper [15]. After the calibration, the reference mast top was mapped by each WindScanner to validate the setup procedure, and the static laser beam pointing accuracy and the sensing range accuracy were estimated to be 0.05° and 1 m, respectively.

Due to the terrain configuration, reference mast structure and surrounding vegetation, the deployment steps, which are described above, could not be applied completely to the MA WindScanner. Hence, a single surveying stake and the branch of a tree nearby were used for the CNR mapping. Both hard targets were located about 50 m from the WindScanner and separated by 180° in azimuth. However, since the MA system was located directly next to the reference mast, the static pointing accuracy and sensing range accuracy could not be validated by mapping the

mast top. The WindScanners were coordinated and synchronized by a remote master computer [15], which communicated with the WindScanners using a 3G network [32].

This paper analyses data from measurements when all WindScanners were staring at a single point close to a Gill HS50 sonic anemometer mounted on the reference mast at a height of 188 m (agl).

The reference anemometer is mounted on a foldable boom with a length of 5.4 m to minimise the effects of the mast structure. The wind sector 100°–160° is excluded from the analysis to remove data which is affected by the mast shadow. According to [2], the influence of the mast structure is estimated to be less than 0.5%. In a wind tunnel test the directional deviation of the Gill HS50 is well below ±1%. The inclinometer accuracy is given as ±0.15°. The direction-dependent error of the measurement of the horizontal wind speed is thus estimated to be below ±1%. The sampling frequency of the Gill HS50 was set to 50 Hz.

Although there is data from six available WindScanners, we restrict the analysis to four locations (EE, SW, SE and MA). These locations have the advantage that they have the longest time series in the analysed scanning mode. Details about the setup of the four scanners can be found in Table 1.

Table 1. Overview of the lidar devices and locations which were used in this study. Coordinates are given in UTM Zone 32U. Pulse length and gate length are given as full width at half maximum (FWHM).

	MA	EE	SE	SW	WC
Instrument type	**WLS 200S V2**	**WLS 200S**	**WLS 200S**	**WLS 200S V2**	**WINDCUBE WLS7 V2**
Altitude (m)	387.7	294.6	346.6	258.3	387.7
Latitude (m)	5,690,182.6	5,690,409.1	5,688,371.9	5,687,503.8	5,690,181.2
Longitude (m)	513,590.5	514,213.3	516,843.2	512,185.9	513,593.1
θ (°)	90	23.3	3.5	6.0	62, 90
ψ (°)	-	250.6	299.3	27.4	8, 98, 188, 278, -
Dist. to mast (m)	2	732	3740	3047	3
Pulse length FWHM (ns)	100	400	400	400	175
Gate length FWHM (ns)	74	150	150	150	58
σ_p (m)	6.4	25.5	25.5	25.5	11.1
σ_g (m)	9.5	19.1	19.1	19.1	7.4
Accumulation time (s)	2	2	2	2	~1.12 (~5.62 for full circle)

2.5. Data Treatment, Quality Control and Coordinate Systems

Quality control of lidar data is usually done by using a lower carrier-to-noise ratio (CNR) threshold to identify periods when not enough backscatter is received to derive a reliable wind-speed estimate. If a structure is present close to the measurement volume, returns from this hard target can also contaminate the signal. Often this leads to an increased CNR and/or to an increased scatter in the observed CNR values. Careful analysis of the WindScanner data, which was collected during the presented experiment, however, showed that also periods during which the CNR fell into the expected CNR range (here −27.5 and −5 dB were used) and had a "normal" variability sometimes exhibited spurious radial wind-speed statistics. Therefore, two additional filter criteria were imposed on the WindScanner data.

The first sorts the radial wind velocities of each averaging interval according to their magnitude. Outliers are then removed if the gap between them and the rest of the data exceeds 1 $m \cdot s^{-1}$. This method is useful in situations with a relatively high radial velocity which is contaminated with hard target returns, as these are often characterised by a radial wind speed close to zero. The filter, however, becomes ineffective if the mean radial wind speed is close to zero—i.e., winds perpendicular to the lidar beam or low wind speeds. The second filter criterion therefore checks the time series during the averaging interval for its temporal consistency. If the time series after the application of the first filter still exhibits a difference between two adjacent measurements which exceeds 1 $m \cdot s^{-1}$, the respective period is removed completely from further analysis. This threshold seems justified because of the relatively high sampling frequency (0.5 Hz) and the damping effect of the lidar probe volume on small-scale turbulence. The exact reason for the problems with the hard targets could not fully be clarified. At the beginning of the experiment, the WindScanners were focused within

approx. 1 m above the reference sonic. The following points may then have led to interference with the mast structure: instability of the WindScanner systems (sinking into soil after installation, vibration of the systems due to e.g., wind), switching of the staring mode to other patterns inducing pointing error due to backlash of the internal gearing, and/or movement of the mast structure. For future inter-comparison experiments, it is thus recommended to increase the distance to the reference instrument/mast. The problem with the hard targets was not present in the data of the Windcube v2 and only a CNR filter was applied. The values (-22 and -5 dB) slightly differ from the WindScanners as the system configuration is different.

The analysis in this paper is based on 10 min averaging intervals, which is the standard in wind-energy applications. Before the analysis of the wind-vector components, a rotation into the mean wind direction ($\overline{v} = 0$ m·s^{-1}) is performed. A second rotation forcing $\overline{w} = 0$ m·s^{-1} as done in many other micrometeorological studies (cf. [33]) is not carried out as the aim of the study is mainly a comparison of the different measurement techniques. For this same reason, corrections which are often applied to eddy-covariance measurements (cf. [34]), such as correcting for high- and low-frequency loss, are not applied to the sonic anemometer measurements. In a previous study, Mauder and co-authors reported deviations between a Gill HS and other sonic anemometers, which was attributed to the Gill HS [35]. However, in their study, the internal correction/calibration was turned off, which removes the sensor head correction and the instrument-dependent calibration. In the present study, the internal corrections were turned on and the problems reported in [35] are assumed to not to be present in the collected data.

3. Results and Discussion

3.1. Radial Velocity Components

In a first step, the radial components of the individual WindScanners ($v_{r\ lidar}$) are compared to the projection of the sonic measurement on the respective WindScanner beam ($v_{r\ sonic}$). This allows an evaluation of the performance of the individual instruments and the accuracy of the setup process. Moreover, some of the complexities in the inter-comparison of the second-order moments, which arise from the combination of multiple lidar beams in three-dimensional space, can be simplified when the radial components of the sonic and lidar wind speed are compared directly. In Section 3.2., we then turn to the wind statistics which are derived from the combination of multiple WindScanner devices.

3.1.1. First-Order Statistics

The inter-comparison of the mean radial components reveals an excellent agreement between the sonic and all WindScanner devices. A two-parametric linear regression between the WindScanners located around the mast and the reference sonic produces slopes (m) and intersects (b) which are very close to 1 and 0 m·s^{-1} (Table 2). The goodness of fit for the linear regression for these instruments is $R^2 \geq 0.998$. The linear-regression statistics for MA are slightly worse. However, this instrument is pointing vertically into the atmosphere and $\overline{w}$ is usually small in the atmospheric boundary layer. In fact, $\overline{v}_{r\ MA}$ only varied between approx. ± 1 m·s^{-1} and the root-mean-square deviation (RMSD) is comparable to the other WindScanners.

The availability of all WindScanners is affected by hard targeting (mast structure, boom or guying). As a result, the number of valid measurement periods, especially for the MA location, is relatively low. A conclusion on how the measurement range affects the data availability is therefore unfortunately not possible.

Table 2. Summary of the inter-comparison of the radial velocities of the WindScanners and the sonic anemometer at 188 m; RMSD indicates the root-mean-square deviation; R^2 is the goodness of the fit, m is the slope and b the intersect of the of the linear regression.

	MA	EE	SE	SW
No 10 min periods	503	2592	1419	1278
Mean $\overline{v_r}$				
m	1.045	0.992	1.005	0.993
b (m·s^{-1})	0.056	−0.036	0.018	0.055
R^2	0.858	0.999	0.998	1.000
$RMSD$ (m·s^{-1})	0.087	0.104	0.116	0.079
Variance $\overline{v'^2_r}$				
m	0.970	0.829	0.836	0.819
b (m·s^{-1})	0.017	−0.025	−0.018	0.001
R^2	0.969	0.968	0.952	0.970

3.1.2. Second-Order Statistics

For the locations SE, SW and EE, the linear-regression statistics between $\overline{v'^2_{r\,lidar}}$ (measured by the WindScanners) and the respective variance derived from the projection of the sonic measurement onto the direction of the respective WindScanner beam ($\overline{v'^2_{r\,sonic}}$) are very similar (Table 2). The slope indicates a significant underestimation of $\overline{v'^2_{r\,sonic}}$ by the WindScanner measurements. This is likely to be due to the relatively large probe volume. In contrast, the slope of the linear regression for the MA system is significantly closer to 1. Here, the smaller range gate size seems to more than compensate for the smaller turbulent length scales which are usually found for w. R^2 is similar for all systems. The values are slightly worse than for the first-order statistics, except for the MA location, where R^2 is slightly higher. The reduced values in R^2 are probably partly caused by the reduced range of the observed variances when compared to the mean values. Another reason for the increased scatter is due to the fact that line averaging does not necessarily scale linearly with the observed variance. It is rather direction dependent on and selective of small wavenumbers. This makes the attenuation dependent on the form of $\Phi_{ij}(\boldsymbol{k})$ (9), which varies with atmospheric conditions—i.e., under stable conditions, a larger portion of the variance will be contained in small eddies as opposed to under unstable conditions. Also, since a finite time interval is used (10 min), some scatter will be introduced by the stochastic distribution of the eddy sizes in the individual period. To further investigate the probe-volume averaging effect on $\overline{v'^2_{r\,lidar}}$ periods with wind directions close to parallel (±15°) to the azimuth angle of the individual WindScanner beams, SE, SW and EE were selected. The spectral filter function defined by (7) and (10) was applied to $v_{r\,sonic}$ (Figure 3). The application of the filter function to the sonic data brings the slope of the linear regression between $\overline{v'^2_{r\,sonic}}$ and $\overline{v'^2_{r\,lidar}}$ closer to unity and slightly improves R^2 for all systems. Interestingly, this improvement is also observed for the EE system, which has quite a large inclination angle into the atmosphere (θ = 22.3°).

A comparison of the average spectra of v_r of the sonic and WindScanner measurements reveals a clear spectral attenuation for SE, SW and EE spectra from approx. $k_1 > 10^{-2}\ m^{-1}$ (Figure 4a–c). This corresponds nicely to what we would expect for the spectral transfer function (T_{v_r}) from theoretical considerations using the parameters in Table 1 and Equations (7) and (10) (Figure 4e). In contrast to the other systems, the spectrum of MA does not exhibit a clear spectral attenuation, which again is likely to be due to the smaller probe volume. Instead, the spectral energy at the high wavenumber tail for MA is actually higher than for the reference sonic. This behaviour can also be observed for the SW system (Figure 4c). Also T_{v_r} starts to increase and deviate from its theoretical form at appox.

$k_1 > 10^{-1}$ m^{-1} for all systems (Figure 4d). This effect becomes worse if measurements with small variances are included (data not shown) and is likely to be attributed to instrumental noise.

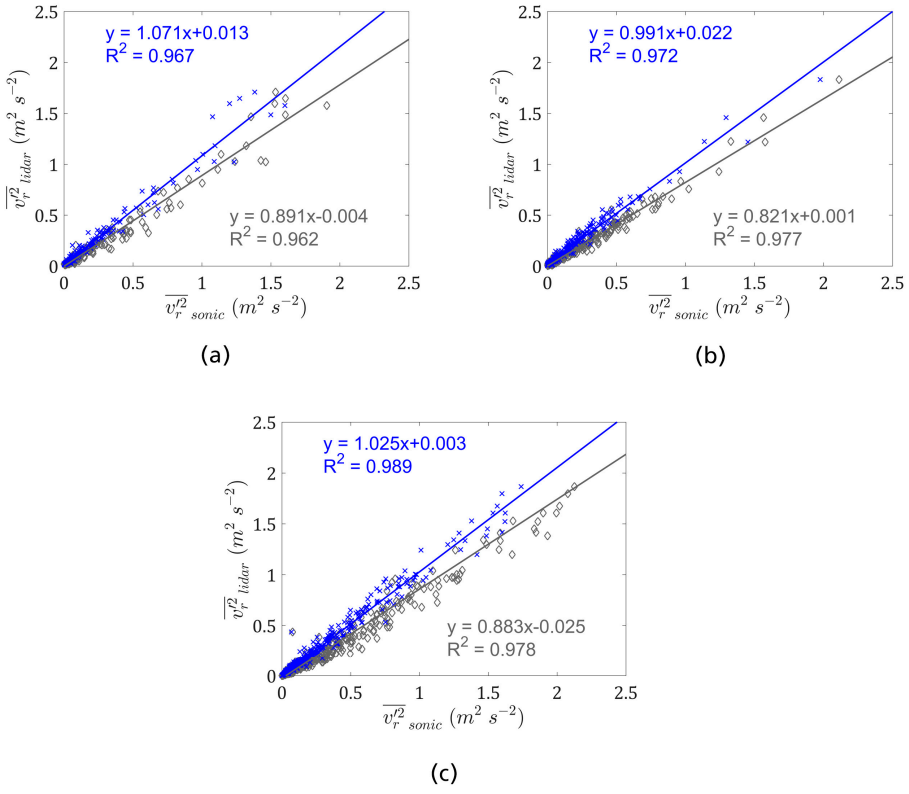

Figure 3. Variance of the radial velocity measurements of the WindScanners $\left(\overline{v'^2_{r\ lidar}}\right)$ against the respective variance in the direction of the beam derived from the sonic anemometer $\left(\overline{v'^2_{r\ sonic}}\right)$ when the wind direction was close to parallel ($\pm 15°$) to the azimuth angle of the WindScanner for (**a**) SE; (**b**) SW; (**c**) EE; grey diamonds indicate the unfiltered sonic measurements; blue crosses are the sonic data after the application of (10). The sonic data was filtered with $\left|\hat{\zeta}\left(k_1\right)\right|^2$ to separate out the effects of the temporal averaging.

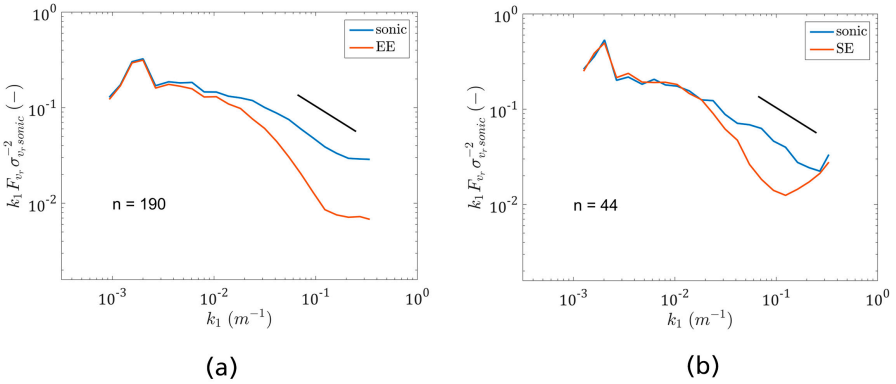

Figure 4. *Cont.*

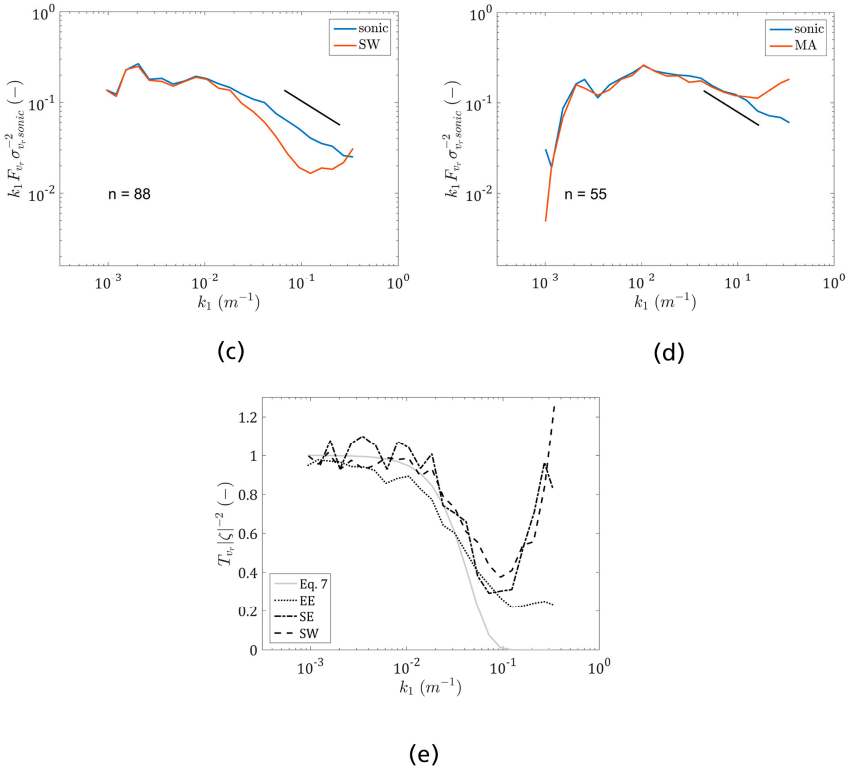

Figure 4. Spectra of v_r measured by different WindScanners and the sonic anemometer when the wind direction was close to parallel ($\pm 15°$) to the azimuth angle of the WindScanner (**a–c**); (**d**) spectra of the MA location and the w component of the sonic anemometer; sonic time series have been aggregated to 0.5 Hz before calculation of the spectra to account for the temporal averaging effect and the associated filter function $\hat{\zeta}(k_1)$; the black line indicates the theoretical $-2/3$-slope in the inertial subrange; (**e**) spectral transfer function $\left|\hat{\zeta}\right|^{-2} T_{v_r}$ derived from the average of the normalised spectra in (**a–c**); only periods with $\overline{u}_{sonic} > 4$ m·s^{-1} and $\overline{u'^2}_{sonic} > 0.2$ m^2·s^{-2} (SW, SE, EE), and $\overline{w'^2}_{sonic} > 0.1$ m^2·s^{-2} (MA) were used in the spectral averaging; n indicates the number of periods used for averaging.

Up until now, only a few experimental studies investigating $\overline{v'^2_r}_{lidar}$ and its spectrum against reference measurements have been undertaken. Most interesting in regards to pulsed lidars, Mann and co-authors reported a similar agreement between the observed and theoretical forms of T_{v_r}. However, in contrast to this study, they only used five selected periods and the lidars were set up in the direct vicinity of the reference mast. As this leads to large elevation angles, they had to use a spectral tensor model to derive T_{v_r}. Also, they used a simpler, triangular-shaped weighting function. The influence of measurement noise at the high-wave-number end of the spectra has also been reported for continuous wave lidars [36,37] and deserves further investigation for the WindScanner systems. Figure 4e indicates that the concept of line averaging (9 and 10) can be used to explain the majority of the differences in the observed second-order statistics between the sonic and the WindScanners.

3.2. Horizontal Wind-Speed Statistics from the ML and Doppler Beam Swinging (DBS) Technique

3.2.1. First-Order Statistics of the Horizontal Wind Speed

For resource estimation in the wind industry, it is standard to use the scalar horizontal velocity ($\overline{V_h}$). This approach is also followed here. Although in many remote sensing applications it is common practice to work with the vector average of the wind velocity, publications concerning the accuracy

of lidars in complex terrain often use the scalar mean [4,6]. While vector averaging produces slightly different numbers, the general patterns that can be observed remain the same and the differences are very small.

The comparison of $\overline{V_h}$ measurements of the ML combination using three lidars and the sonic reveals an excellent agreement between the two techniques as would be expected from the comparison of $\overline{v_r}$ (Figure 5a). Also, the ML technique using two lidars and neglecting the vertical component in the vector reconstruction only produces marginally different results for the scanner combination SE/SW (Figure 5b). For the SW/EE combination, the scatter slightly increases and we can see a few points which significantly deviate from the linear relationship (Figure 5d). The observed differences between the different dual-lidar configurations are likely to be at least partly caused by the setup of the instruments.

One characteristic which sets the different dual-lidar measurements apart is the difference in azimuth angle between the WindScanner beams. For SW/EE, the angle is smallest (43°) which causes the strongest error propagation from the radial wind speed onto the wind vector when solving Equation (3) (cf. [38]). The angle for SE/EE is slightly larger (49°) and the SE/SW combination has an angle difference of 88°, which is close to the ideal 90°.

The DBS measurement with the Windcube v2 exhibits more scatter and the linear regression significantly deviates from 1:1 when compared to the sonic (Figure 5e). Especially for low wind speeds, an overestimation of the $\overline{V_{h\,sonic}}$ by the DBS lidar can be observed.

In general, the linear-regression statistics for the DBS lidar are similar to what has been reported at Rödeser Berg in earlier measurement campaigns [6] and are similar to what has been reported from other lidar-mast inter-comparisons in complex terrain [39] albeit significantly worse than in flat terrain (e.g., [1]). In contrast, the statistics for the ML combinations are similar to the results which we regularly observe during DBS lidar calibrations in flat and homogeneous terrain. The "bump" in the DBS data at low wind speeds might be associated with turbulence effects which are more important for low wind speeds. Moreover, thermal effects on the flow might create increased vertical velocities (relative to the horizontal wind speed) which are likely to spatially vary in the complex surroundings at Rödeser Berg. In combination with the large scanning volume of the DBS lidar at 188 m this would introduce an increased complex terrain error.

To our knowledge no statistics from a comparably long-term data set for assessing the performance of ML measurements to derive the mean wind speeds have been published so far. Previously published results of mast-lidar inter-comparisons either focused on the evaluation of individual measurement periods [16] or employed scanning strategies that focused more on assessing the spatial heterogeneity of the wind field than on evaluating ML measurements against a reference [17,40]. The ML-mast inter-comparison in the latter two references is slightly worse, but due to the different focus of the scanning strategy, is likely to not be directly comparable. A recently published study by Newman only compares co-located DBS and ML measurements [19]. The sonic anemometer used in this study only measures at significantly lower altitudes than the lidars and is only used to give an indication of the wind field below the lidar measurements. This precludes a quantification of the advantages of either of the techniques over the other in their study or a comparison to the results presented.

One of the typical observations for profiling lidars in complex terrain is that the deviation in $\overline{V_h}$ between the lidar and the mast measurements varies with the shape of the terrain and thus wind direction [4,6]. This behaviour can also be observed for the DBS data collected during the *Kassel Experiment 2014* (Figure 6). The pattern clearly reflects the shape of the terrain and is very similar to what has been observed in earlier inter-comparisons between cup anemometers and a DBS lidar at Rödeser Berg [6]. If the flow is directed across the ridge of the hill (aprox. 50°–100° and 200°–270°), the DBS lidar underestimates $\overline{V_h}$. This is a typical observation for convex flow as observed over e.g., ridges or hilltops [4,5]. In contrast, the sectors showing an overestimation of $\overline{V_h}$ by the DBS lidar (approx. 290°–20° and 160°–180°) correspond to along the ridge flow. Here, the mast is located on the slope in front of/behind the highest point on the ridge and the terrain is slightly concave.

This might also cause a concave flow pattern which results in an overestimation of the horizontal wind speed by the DBS lidar. Some evidence for this can be found in the change of sign of the flow angle measured by the sonic between 290°–20° and 160°–180°. Whereas for the first sector (mast in front of the hill top) the median flow angle is 1.7° (directed upwards), it is −2.2° (directed downwards) for the second sector (mast behind the hill top). It should be noted, however, that the real flow might be more complex than this simplified explanation. A more detailed discussion and modelling results of directional errors of DBS lidar measurements at Rödeser Berg can be found in [6].

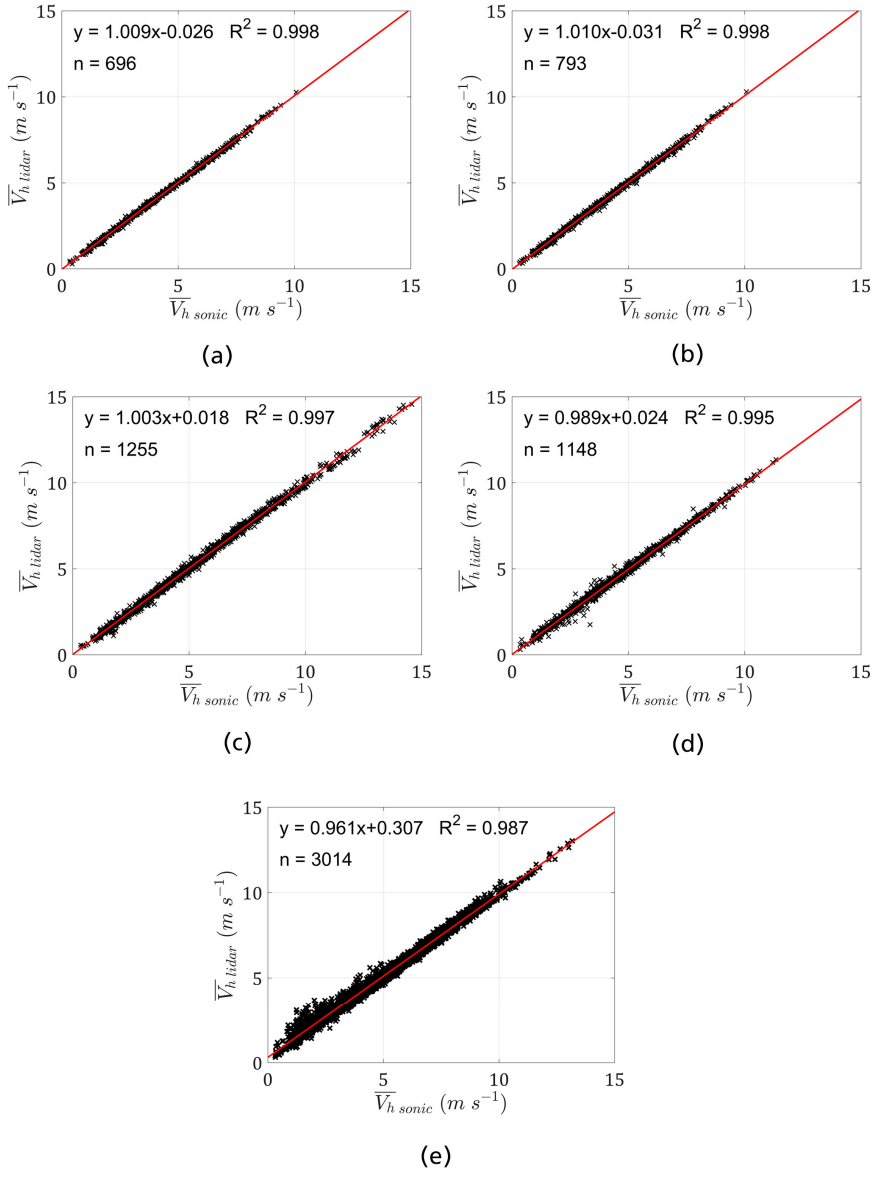

Figure 5. Scatter plots of $\overline{V_h}$ from different lidar configurations against the reference sonic at 188 m; (**a**) SE/SW/EE; (**b**) SE/SW; (**c**) SE/EE; (**d**) SW/EE; (**e**) Windcube v2 next to the mast; (**a**–**d**) are measurements from WindScanners in ML mode; the Windcube in (**e**) is operated in DBS mode. For ML combinations with only two beams, $w = 0$ m·s^{-1} is assumed in the wind-vector reconstruction; n indicates the number of value pairs displayed in the individual scatter plots.

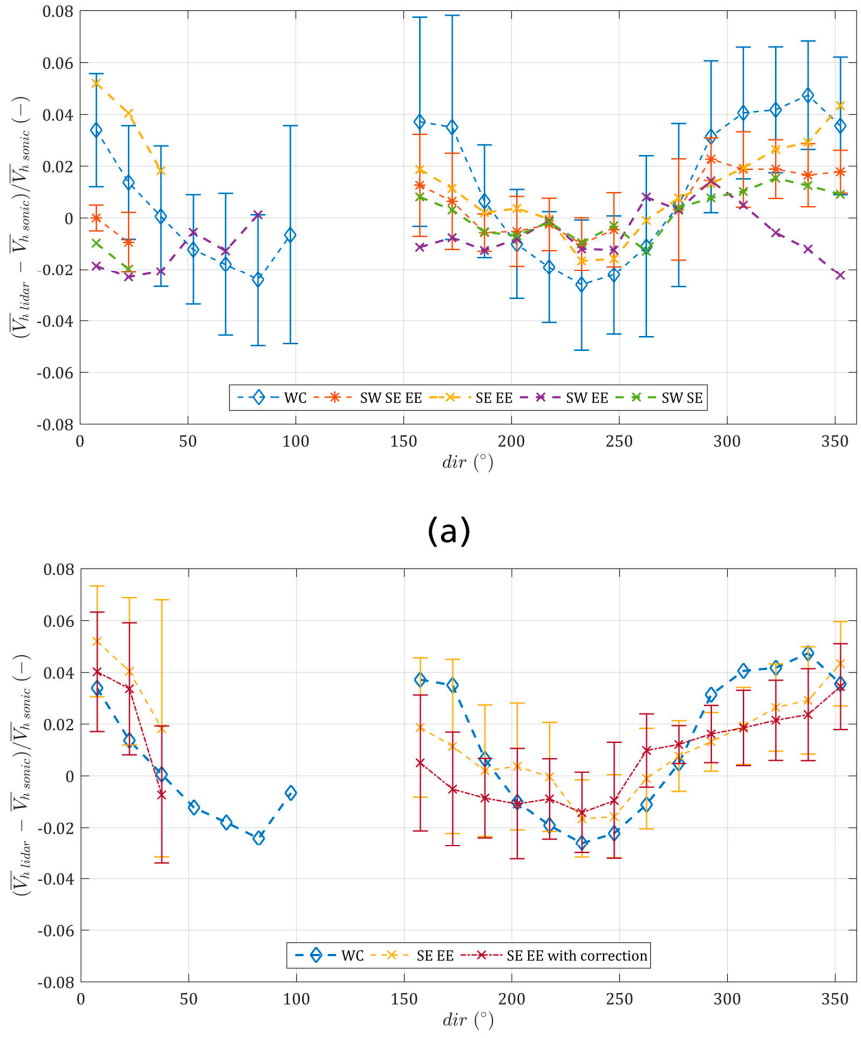

Figure 6. (**a**) mean of the directional deviation in $\overline{V_h}$ between the sonic and the different lidar configurations; (**b**) same as (**a**) but for the SE/EE combination with and without the correction for $\overline{w}$; see text for details; periods during which $\overline{V_{h\ sonic}} < 4$ m·s^{-1} were excluded from the comparison to increase the comparability to other complex terrain measurements reported in the literature. Also, bins with n < 5 are not displayed; error bars denote $\pm$ one standard deviation.

On average, the DBS-mast deviations are slightly shifted (1%–2%) towards an increased $\overline{V_{hlidar}}$ (relative to $\overline{V_{hsonic}}$) when compared to the earlier inter-comparison to cup anemometry. This might be caused by the different reference anemometers or the different DBS instruments used in the present study, although the reason could not be fully clarified.

The deviation between $\overline{V_{hlidar}}$ and $\overline{V_{hmast}}$ for the ML measurements is smaller than for the DBS system for most sectors and WindScanner combinations (Figure 6). Especially for the WindScanner combinations SW/SE/EE and SE/SW, the differences are small for all directions and only vary between approx. -2% and 2%. For the SE/EE combination, a relatively large positive deviation of

the ML system in comparison to the sonic wind speed can be observed between approx. 350 and 25°, which even exceeds the DBS-sonic deviations. This is likely due to the fact that within this range, the angle between the mean wind direction and the beam directions of SE and EE are large and the difference in beam directions is small (cf. [38]). This configuration leads to an increased error propagation in the estimation of u that largely dominates $\overline{V_{hlidar}}$—i.e., the azimuth angles and flow direction are unfavourable for the retrieval of $\overline{V_{hlidar}}$. For flow angles which are directed in a more parallel manner to the orientation of the lidar beams, the error propagation for v is expected to be large. The effect on $\overline{V_{hlidar}}$, however, is then much smaller.

A second effect which can affect the quality of the measurements of SE/EE combination is the relatively large elevation angle of the EE system compared to the other systems (Table 1). The assumption, $\overline{w} = 0$ m·s^{-1}, thus results in a contamination of $\overline{V_{hlidar}}$ by $\overline{w}$. Due to the low availability, an inclusion of the MA system which could correct for the influence of $\overline{w}$ in the directional analysis was not possible. Therefore, a direction-dependent correction factor was calculated using $\overline{w}_{sonic}$. Equation (3) is first solved using $\overline{v}_{r\ SE}$, $\overline{v}_{r\ EE}$ and $\overline{w}_{sonic}$. In a second step, (3) is solved only using $\overline{v}_{r\ SE}$ and $\overline{v}_{r\ EE}$. The ratio of the two results is then applied as a correction factor to $\overline{V_{hlidar}}$. The correction reduces the deviations in the 350°–25° sector. The effect is, however, relatively small. Therefore, the assumption $\overline{w} = 0$ m·s^{-1} does not seem to be the main cause of the observed deviations. Some of the deviations between the sonic and the lidar measurements might also be caused by the flow distortion of the mast. However, we estimate this effect to be small (c.f. Section 2.4.).

3.2.2. Second-Order Statistics of the Horizontal Wind Vector Components

This section presents the second-order statistics (variances and spectra) of the horizontal wind components u and v. The second-order statics for the w component can be found in Section 3.1.2. (MA WindScanner). Figure 7 displays the scatter plots and linear-regression statistics for the different ML combinations and the DBS lidar when compared to the sonic measurements. The differences between the DBS and ML, but also among the different ML combinations, are quite large. Almost identical linear-regression statistics can be observed for the SW/SE/EE and SW/SE combinations (Figure 7a,b). The R^2 values of the linear regression for $\overline{u'^2}$ and $\overline{v'^2}$ are similar to the statistics of $\overline{v_r'^2}$ (Table 2 and Figure 3). Also the slope indicates a similar underestimation of $\overline{u'^2}$ (and $\overline{v'^2}$) of about 20%. Looking at the spectra of SW/SE/EE and SW/SE, one can clearly see the effects of line averaging which causes the reduction in $\overline{u'^2}$ and $\overline{v'^2}$ (Figure 8a,b). As for v_r, an attenuation in the spectral density from approx. $k_1 = 10^{-2}$ m^{-1} for u and v can be observed. The line averaging effect thus also causes the reduced $\overline{u'^2}$ and $\overline{v'^2}$ in SW/SE/EE and SW/SE.

The scatter in the inter-comparison between the SW/EE and SE/EE is larger than for SW/SE/EE and SW/SE and the slope of the linear regression shifts close to 1. One of the reasons for the increased scatter in the ML combinations using two WindScanners including the EE system might be that the EE system has an inclination angle which is not close to 0°. In the wind-vector reconstruction for two scanners, the w component is assumed to be 0 m·s^{-1}. Some of $\overline{w'^2}$ will thus contaminate the measurement of $\overline{u'^2}$ and $\overline{v'^2}$. Moreover, as discussed earlier, the direction of the flow in relation to the beam directions will also influence the error propagation for the individual components, especially if the angle between the beams is small [38]. In the experimental setup it is, however, difficult to separate these effects as they are likely to be correlated.

This observation suggests that for the ML method, an adequate positioning of the lidar devices is even more important for measuring turbulence quantities than for the mean wind speed.

In general, random measurement errors in the time series will always lead to an increased variance. Therefore, both the contamination by the w component and the unfavourable angles in the lidar combination lead to increased $\overline{u'^2}$ and $\overline{v'^2}$ in the lidar measurement. The slope values close to the 1:1 line are thus likely a result of the combination of these measurement errors and the line averaging, which act in opposing directions.

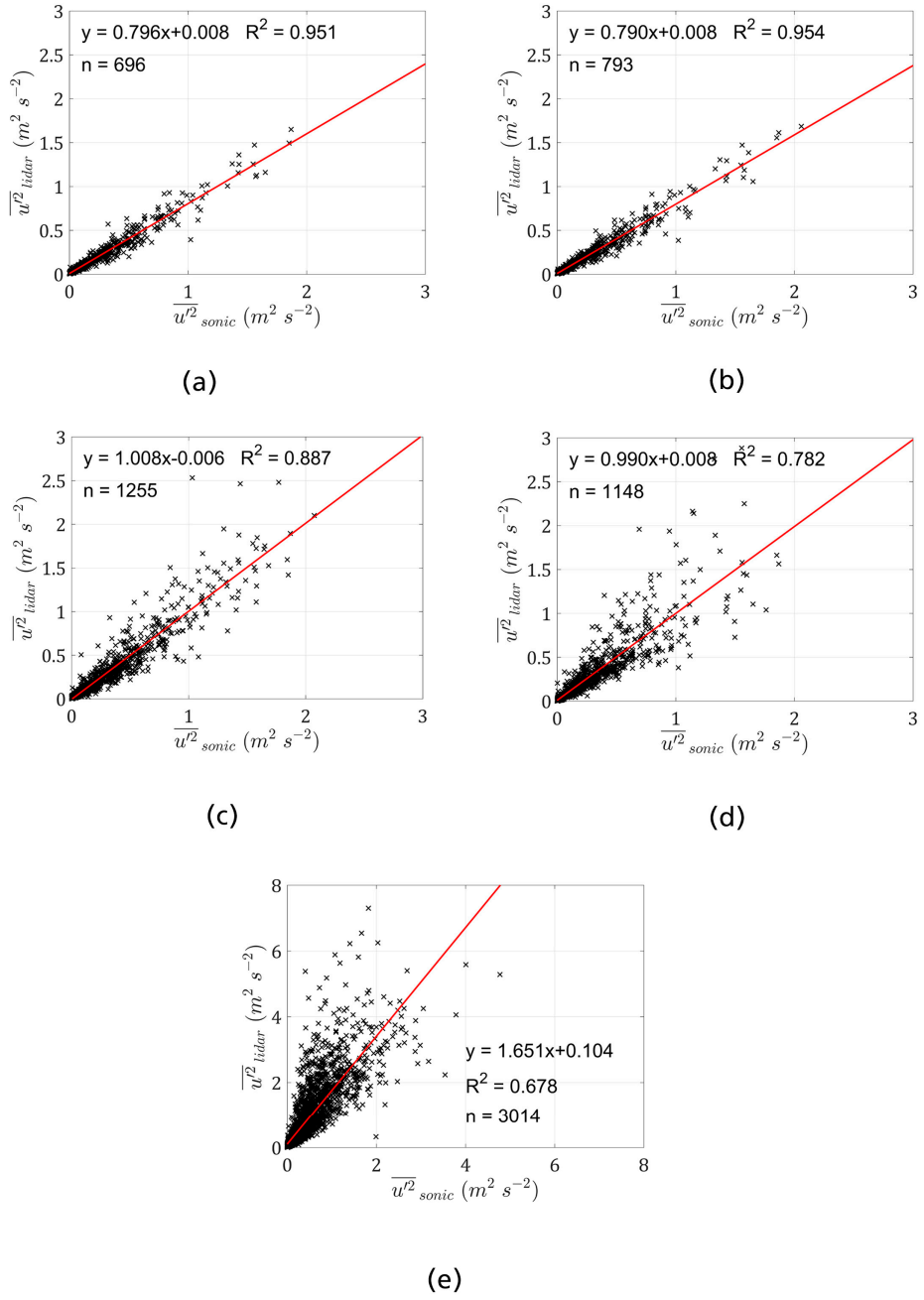

Figure 7. Scatter plots of $\overline{u'^2}$ from different lidar configurations against the reference sonic at 188 m; (**a**) SE, SW and EE; (**b**) SE and SW; (**c**) SE and EE; (**d**) SW and EE; (**e**) Windcube v2 next to the mast; (**a**–**d**) are measurements from WindScanners in ML mode; the Wincube is operated in DBS mode. For ML combinations with only two beams, $w = 0$ m·s^{-1} is assumed in the wind-vector reconstruction; n indicates the number of value pairs displayed in the individual scatter plots.

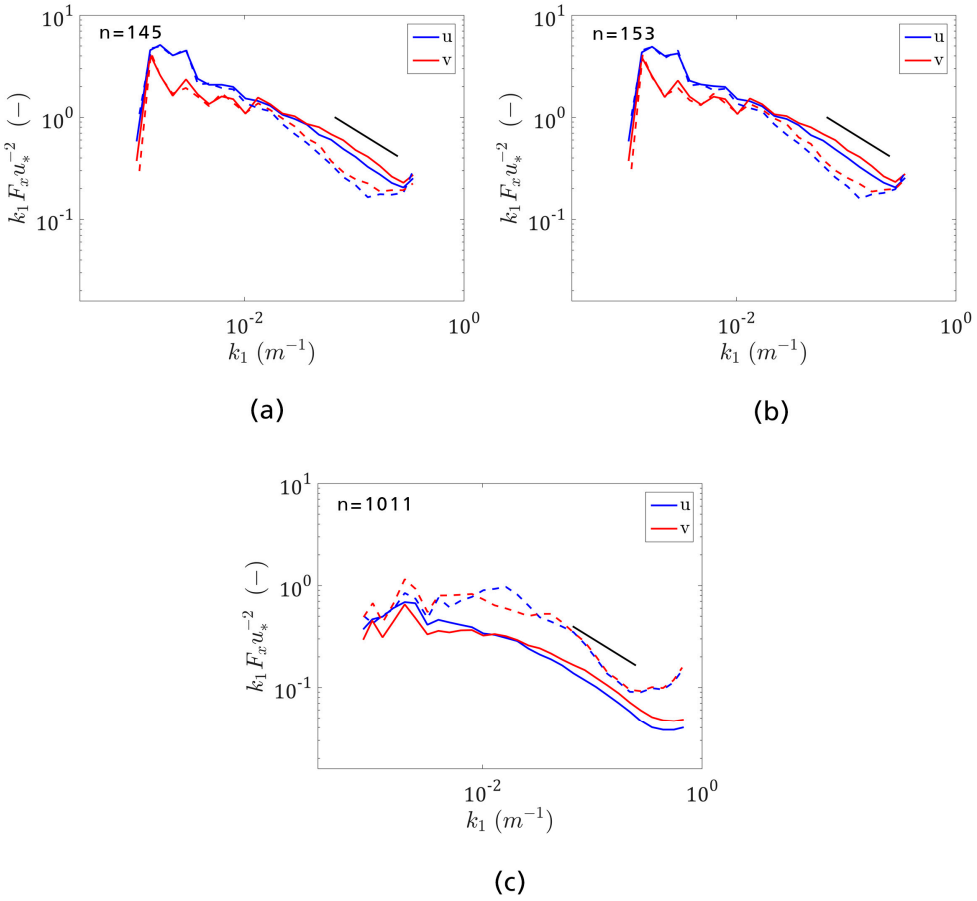

Figure 8. Normalised spectra of u and v . For (**a**) SW/SE/EE, (**b**) SW/SE and (**c**) Windcube v2 next to the mast; solid lines are the sonic spectra; dashed lines are the lidar spectra; sonic time series have been aggregated to 0.5 Hz (a and b) and 0.89 Hz before calculation of the spectra; only periods with $\overline{u}_{sonic} > 4$ m·s^{-1} and $\overline{u'^2}_{sonic} > 0.2$ m^2·s^{-2} were used in the spectral averaging; u_* is the friction velocity computed from the sonic anemometer measurements; the black line indicates the theoretical $-2/3$ slope in the inertial subrange; n indicates the number of periods used for averaging.

The comparison between the DBS system and the sonic indicates a clear overestimation of $\overline{u'^2}$ and $\overline{v'^2}$ by the DBS system (Figure 7e and Table 3). Also, the R^2 values are lower than for all ML combinations. The spectra of the DBS system show a significant contamination of the variance measurements across almost the whole wavenumber range. Only for very large k_1 are the spectra for the u component of the DBS lidar and the sonic close together. For the u component, a local maximum can be observed around approx. $k_1 = 10^{-1.8}$ m^{-1}. The v spectrum of the DBS lidar is higher than the sonic spectrum for the whole wave number range and a (smaller) second maximum can be observed around $k_1 = 10^{-1.4}$ m^{-1}. For higher wave numbers, the spectra then quickly drop off.

The exact shape of the measured spectra of a Windcube does not only depend on the atmospheric conditions and measurement heights, but will also vary with the flow direction towards the scanning geometry of the Windcube [10]. It is thus difficult to explain all features of the measured spectra.

The strong positive deviations from the sonic spectra in this range are likely to be caused by the cross-contamination effects between $\overline{u'^2}$, $\overline{v'^2}$ and especially by the contamination of the horizontal variances by $\overline{w'^2}$. The short region where the spectra are almost horizontal at the high wavenumber

end is likely to be caused by the algorithm which derives the wind vector from the measurements of v_r. In analogy with the internal software of the Windcube v2, in this paper the wind vector was calculated whenever a new measurement of v_r was available—i.e., at a frequency of approx. 0.89 Hz. One full rotation, however, takes five measurements of v_r and thus acts similarly to a moving average filter [41].

Table 3. Summary of the linear-regression statistics for $\overline{u'^2}$ and $\overline{v'^2}$ for different lidar configurations; values in brackets are statistics for which periods with $\overline{u}_{sonic} < 4$ m·s^{-1} have been excluded; R^2 is the goodness of the fit, m is the slope and b the intersect of the of the linear regression.

	SE SW EE	SW SE	SE EE	SW EE	WC
			$\overline{u'^2}$		
m	0.796 (0.829)	0.790 (0.816)	1.008 (1.026)	0.990 (0.916)	1.651 (1.531)
b (m·s^{-1})	0.008 (0.006)	0.008 (0.009)	−0.006 (-0.011)	0.008 (0.006)	0.104 (0.070)
R^2	0.951 (0.963)	0.954 (0.967)	0.887 (0.896)	0.782 (0.865)	0.678 (0.796)
			$\overline{v'^2}$		
m	0.825 (0.800)	0.822 (0.800)	0.884 (0.861)	0.883 (0.890)	1.822 (1.731)
b (m·s^{-1})	0.003 (0.008)	0.004 (0.009)	-0.006 (-0.007)	0.020 (0.018)	0.076 (0.038)
R^2	0.962 (0.963)	0.966 (0.966)	0.903 (0.930)	0.861 (0.901)	0.689 (0.737)

The relatively strong overestimation in the measured variances by the Windcube compared to some other studies using similar instruments (Windcube v1 and v2) [9,19] is likely to be related to the great measurement height (188 m) and thus the large distance between the different beams. In parts, it might also be caused by a dominance of unstable conditions which are more frequent during the summer season and the inhomogeneous flow caused by the terrain complexity.

In Table 3, we also provide the statistics for periods when $\overline{u}_{sonic} > 4$ m·s^{-1}, as this filter criterion is often used in applications and studies in the wind-energy sector, thereby allowing a more direct comparison to other experiments. For the ML combinations SW/SE/EE, SW/SE and SE/EE, there is only a small change in the linear-regression statistics. For the Windcube v2 and the SW/EE, which have lower R^2 values, R^2 significantly improves after the application of the $\overline{u}_{sonic} > 4$ m·s^{-1} criterion.

4. Conclusions

Two of the biggest challenges for ground-based remote sensing in wind energy are the systematic errors in the mean wind speed which can be introduced by complex flow in complex terrain and the inability of traditional profiling devices to accurately measure turbulence. This paper experimentally explores the improvements in these two areas which can be made using the multi-lidar (ML) technique. For this purpose, results from the *Kassel 2014 Experiment* are presented, during which multiple WindScanners and a Doppler beam swinging (DBS) lidar were operated surrounding a reference mast in complex terrain.

The comparison of the radial wind velocities between the WindScanner measurements and a reference sonic shows that, given an accurate setup, an excellent agreement with the reference sonic could be achieved for individual systems, even if they are positioned several kilometres from the mast. Combination of multiple lidars to an ML measurement demonstrate that this also holds true for the derivation of the horizontal wind speed. ML wind speeds were considerably closer to the mast reference than the DBS lidar at this complex terrain site. The significantly reduced scatter and the smaller directional deviation in comparison with the reference sonic clearly demonstrate the advantages of focusing multiple lidar beams at one point over the classical DBS-profiling method. Correction methods (based on e.g., flow models) can be avoided, which can significantly reduce the uncertainty in applications like wind resource assessments or site calibrations. Exploiting the flexibility of the WindScanner technology, the measurements presented here could be extended to a scan of multiple measurement locations within a planned windfarm site. Especially in complex

terrain this could significantly reduce the uncertainty associated with the horizontal extrapolation of the wind resource. For research applications like flow model validation, the ML technique removes the constraints of a mast measurement for an accurate measurement of the horizontal wind speed.

The ML measurements of $\overline{v'^2_r}$, $\overline{u'^2}$ and $\overline{v'^2}$ (for SW/SE/EE and SW/SE) showed a high correlation to the reference sonic. However, while larger scale turbulence was accurately captured, due to the relatively large measurement volume and the associated path averaging, attenuation for higher wave numbers could be observed. This results in an overall underestimation of the variances. An obvious way forward would be to reduce the measurement volume. With currently available lidar technology, however, this comes at the cost of a reduced measurement range and, therefore, reduces the flexibility of ML measurements. An alternative is to develop correction methods for the variance which is lost due to the line averaging. The good agreement between observed and theoretical spectral transfer functions is encouraging for this approach. First-order corrections could be based on model spectra as often done for eddy-covariance measurements (e.g., [42]). Alternatively, the correction could be based on an extrapolation of the spectra in the inertial sub-range [43,44]. This, however, requires that a part of the inertial sub-range is not affected by line averaging. More sophisticated approaches could exploit e.g., the spectral broadening of the received backscatter [25,45,46]. The results for the variance measurements of the DBS lidar clearly illustrate the errors introduced by cross-contamination in this technique and reiterate the unreliability of turbulence measurements from profiling lidars.

From a practical perspective, it is interesting that the good results of the ML method could also be maintained if only two lidars were used. This reduces the additional costs, which are one of the disadvantages of the ML method, when compared to the DBS lidar (or other profiling lidar). Differences between the different dual-lidar ML systems are likely to be mainly caused by the setup or, more precisely, the different angles between the WindScanners. While the mean wind speed is only slightly affected, the variances of the horizontal wind-speed components seem to be more sensitive to an unfavourable setup of the WindScanners. A detailed analysis of the effect of the setup on the accuracy of ML measurements is part of ongoing investigations.

Acknowledgments: The authors would like to acknowledge four anonymous referees for their valuable reviews. We would also like to thank Richard Döpfer and Klaus Otto for the support during the field work. The authors are grateful to Thomas Foken for fruitful discussions and valuable comments on the manuscript. The authors would like to thank Anna Krolczik who helped with editing the final figures. The work of this article was funded by the following projects: WindScanner.eu, Windenergie im Binnenland II (Förderkennzeichen 0325171A), and neweuropeanwindatlas.eu.

Author Contributions: D.C. and M.C. first initiated the experiment; D.C., M.C., J.M., N.V., J.G., L.P. and M.K. planned and designed the measurement campaign; N.V., G.L, M.C., D.C., T.K. and J.H. performed the experiments; L.P., G.L., N.V., T.K. and J.H. performed the quality control of the measurements/data; L.P., G.L. and A.S. carried out the data analysis; M.K. and M.C. were responsible for the provision of the WindScanners; J.G. and D.C. were responsible for the provision of the DBS lidars; L.P. wrote the manuscript; all authors read, reviewed and approved the final manuscript and provided valuable editorial and critical input and feedback for the final document.

Conflicts of Interest: The authors declare no conflict of interest.

Abbreviations

The following abbreviations are used in this manuscript:

CNR	Carrier-to-noise ratio
DBS	Doppler beam swinging
lidar	Light detection and ranging
ML	Multi-lidar
FWHM	Full width at half maximum
RMSD	Root-mean-square deviation
VAD	Velocity azimuth display

References

1. Gottschall, J.; Courtney, M.S.; Wagner, R.; Jørgensen, H.E.; Antoniou, I. Lidar profilers in the context of wind energy—A verification procedure for traceable measurements. *Wind Energy* **2012**, *15*, 147–159. [CrossRef]

2. International Electrotechnical Commission. *IEC 61400-12 Wind Turbines—Part 12-1: Power Performance Measurements of Electricity Producing Wind Turbines (2nd Committee Draft)*, 2nd ed.; International Electrotechnical Commission: Geneva, Switzerland, 2013.
3. Fördergesellschaft Windenergie und andere Erneuerbare Energien e.V. (FGW). TR6 Bestimmung von Windpotenzial und Energieerträgen. Available online: http://www.wind-fgw.de/TR.html (accessed on 20 September 2016).
4. Bingöl, F.; Mann, J.; Foussekis, D. Conically scanning lidar error in complex terrain. *Meteorol. Z.* **2009**, *18*, 189–195. [CrossRef]
5. Bradley, S.; Strehz, A.; Emeis, S. Remote sensing winds in complex terrain—A review. *Meteorol. Z.* **2015**, *24*, 547–555.
6. Klaas, T.; Pauscher, L.; Callies, D. Lidar-mast deviations in complex terrain and their simulation using CFD. *Meteorol. Z.* **2015**, *24*, 591–603.
7. Sathe, A.; Mann, J. A review of turbulence measurements using ground-based wind lidars. *Atmos. Meas. Tech.* **2013**, *6*, 3147–3167. [CrossRef]
8. Sathe, A.; Banta, R.; Pauscher, L.; Vogstad, K.; Schlipf, D.; Wylie, S. *Estimating Turbulence Statistics and Parameters from Ground- and Nacelle-Based Lidar Measurements; IEA Wind Expert Report*; DTU Wind Energy: Roskilde, Denmark, 2015.
9. Sathe, A.; Mann, J.; Gottschall, J.; Courtney, M.S. Can wind lidars measure turbulence? *J. Atmos. Ocean. Technol.* **2011**, *28*, 853–868. [CrossRef]
10. Sathe, A.; Mann, J. Measurement of turbulence spectra using scanning pulsed wind lidars. *J. Geophys. Res.* **2012**, *117*. [CrossRef]
11. Newman, J.F.; Klein, P.M.; Wharton, S.; Sathe, A.; Bonin, T.A.; Chilson, P.B.; Muschinski, A. Evaluation of three lidar scanning strategies for turbulence measurements. *Atmos. Meas. Tech.* **2016**, *9*, 1993–2013. [CrossRef]
12. Sathe, A.; Mann, J.; Vasiljevic, N.; Lea, G. A six-beam method to measure turbulence statistics using ground-based wind lidars. *Atmos. Meas. Tech.* **2015**, *8*, 729–740. [CrossRef]
13. Eberhard, W.L.; Cupp, R.E.; Healy, K.R. Doppler lidar measurement of profiles of turbulence and momentum flux. *J. Atmos. Ocean. Technol.* **1989**, *6*, 809–819. [CrossRef]
14. Mann, J.; Cariou, J.-P.; Courtney, M.S.; Parmentier, R.; Mikkelsen, T.; Wagner, R.; Lindelöw, P.; Sjöholm, M.; Enevoldsen, K. Comparison of 3D turbulence measurements using three staring wind lidars and a sonic anemometer. *Meteorol. Z.* **2009**, *18*, 135–140. [CrossRef]
15. Vasiljevic, N. A Time-Space Synchronization of Coherent Doppler Scanning Lidars for 3D Measurements of Wind Fields. Ph.D. Thesis, Technical University of Denmark, Roskilde, Denmark, 2014.
16. Fuertes, F.C.; Iungo, G.V.; Porté-Agel, F. 3D turbulence measurements using three synchronous wind lidars: Validation against Sonic Anemometry. *J. Atmos. Ocean. Technol.* **2014**, *31*, 1549–1556. [CrossRef]
17. Berg, J.; Vasiljevíc, N.; Kelly, M.; Lea, G.; Courtney, M. Addressing spatial variability of surface-layer wind with long-range WindScanners. *J. Atmos. Ocean. Technol.* **2015**, *32*, 518–527. [CrossRef]
18. Mann, J. The spatial structure of neutral atmospheric surface-layer turbulence. *J. Fluid Mech.* **1994**, *273*, 141–168. [CrossRef]
19. Newman, J.F.; Bonin, T.A.; Klein, P.M.; Wharton, S.; Newsom, R.K. Testing and validation of multi-lidar scanning strategies for wind energy applications. *Wind Energy* **2016**. [CrossRef]
20. Mann, J.; Angelou, N.; Arnqvist, J.; Callies, D.; Cantero, E.; Chávez Arroyo, R.; Courtney, M.; Cuxart, J.; Dellwik, E.; Gottschall, J.; et al. Complex terrain experiments in the New European Wind Atlas. *Philos. Trans. R. Soc. A* **2016**, in review.
21. Tatarskii, V.I.; Muschinski, A. The difference between Doppler velocity and real wind velocity in single scattering from refractive index fluctuations. *Radio Sci.* **2001**, *36*, 1405–1423. [CrossRef]
22. Huffaker, R.M.; Hardesty, R.M. Remote sensing of atmospheric wind velocities using solid-state and CO_2 coherent laser systems. *Proc. IEEE* **1996**, *84*, 181–204. [CrossRef]
23. Frehlich, R. Effects of wind turbulence on coherent Doppler lidar performance. *J. Atmos. Ocean. Technol.* **1997**, *14*, 54–75. [CrossRef]
24. Lindelöw, P.J.P.; Mohr, J.J.; Peucheret, C.; Feuchter, T.; Christensen, E.L. *Fiber Based Coherent Lidars for Remote Wind Sensing*; Technical University of Denmark, DTU: Kgs. Lyngby, Denmark, 2008.

25. Banakh, V.A.; Smalikho, I.N. Estimation of the turbulence energy dissipation rate from the pulsed Doppler lidar data. *Atmos. Ocean. Opt.* **1997**, *10*, 957–965.
26. Kaimal, J.C.; Wyngaard, J.C.; Haugen, D.A. Deriving power spectra from a three-component sonic anemometer. *J. Appl. Meteorol.* **1968**, *7*, 827–837. [CrossRef]
27. Cariou, J.-P.; Leopshere, Paris, France. Personal communication, 2016.
28. International Electrotechnical Commission. *IEC 61400-1 Wind Turbines—Part 1: Design Requirements*; International Electrotechnical Commission: Geneva, Switzerland, 2005.
29. Veers, P.S. *Three-Dimensional Wind Simulation*; Sandia National Laboratories: Albuquerque, NM, USA, 1988.
30. Mann, J. Wind field simulation. *Probab. Eng. Mech.* **1998**, *13*, 269–282. [CrossRef]
31. Farr, T.G.; Rosen, P.A.; Caro, E.; Crippen, R.; Duren, R.; Hensley, S.; Kobrick, M.; Paller, M.; Rodriguez, E.; Roth, L.; et al. The shuttle radar topography mission. *Rev. Geophys.* **2007**, *45*. [CrossRef]
32. Vasiljevic, N.; Lea, G.; Hansen, P.; Jensen, H.M. *Mobile Network Architecture of the Long-Range WindScanner System*; DTU Wind Energy: Roskilde, Denmark, 2016.
33. Kaimal, J.C.; Finnigan, J.J. *Atmospheric Boundary Layer Flows: Their Structure and Measurement*; Oxford University Press: New York, NY, USA, 1994.
34. Foken, T.; Leuning, R.; Oncley, S.R.; Mauder, M.; Aubinet, M. Corrections and data quality control. In *Eddy Covariance: A Practical Guide to Measurement and Data Analysis*; Aubinet, M., Vesala, T., Papale, D., Eds.; Springer Netherlands: Dordrecht, The Netherlands, 2012; pp. 85–131.
35. Mauder, M.; Oncley, S.P.; Vogt, R.; Weidinger, T.; Ribeiro, L.; Bernhofer, C.; Foken, T.; Kohsiek, W.; de Bruin, H.; Liu, H. The energy balance experiment EBEX-2000. Part II: Intercomparison of eddy-covariance sensors and post-field data processing methods. *Bound. Lay Meteorol.* **2007**, *123*, 29–54. [CrossRef]
36. Angelou, N.; Mann, J.; Sjöholm, M.; Courtney, M. Direct measurement of the spectral transfer function of a laser based anemometer. *Rev. Sci. Instrum.* **2012**, *83*, 033111. [CrossRef] [PubMed]
37. Sjöholm, M.; Mikkelsen, T.; Mann, J.; Enevoldsen, K.; Courtney, M. Spatial averaging-effects on turbulence measured by a continuous-wave coherent lidar. *Meteorol. Z.* **2009**, *18*, 281–287. [CrossRef]
38. Stawiarski, C.; Träumner, K.; Knigge, C.; Calhoun, R. Scopes and challenges of dual-Doppler lidar wind measurements — an error analysis. *J. Atmos. Ocean. Technol.* **2013**, *30*, 2044–2062. [CrossRef]
39. Bradley, S.; Perrott, Y.; Behrens, P.; Oldroyd, A. Corrections for wind-speed errors from sodar and lidar in complex terrain. *Bound. Lay. Meteorol.* **2012**, *143*, 37–48. [CrossRef]
40. Newsom, R.K.; Berg, L.K.; Shaw, W.J.; Fischer, M.L. Turbine-scale wind field measurements using dual-Doppler lidar. *Wind Energy* **2015**, *18*, 219–235. [CrossRef]
41. Canadillas, B.; Bégué, A.; Neumann, T. Comparison of turbulence spectra derived from Lidar and sonic measurements at the offshore platform FINO1. In Proceedings of the 10th German Wind Energy Conference (DEWEK 2010), Bremen, Germany, 17–18 November 2010.
42. Moore, C.J. Frequency response corrections for eddy correlation systems. *Bound. Lay. Meteorol.* **1986**, *37*, 17–35. [CrossRef]
43. Hogan, R.J.; Grant, A.L.M.; Illingworth, A.J.; Pearson, G.N.; O'Connor, E.J. Vertical velocity variance and skewness in clear and cloud-topped boundary layers as revealed by Doppler lidar. *Q. J. R. Meteorol. Soc.* **2009**, *135*, 635–643. [CrossRef]
44. Barlow, J.F.; Halios, C.H.; Lane, S.E.; Wood, C.R. Observations of urban boundary layer structure during a strong urban heat island event. *Environ. Fluid Mech.* **2015**, *15*, 373–398. [CrossRef]
45. Smalikho, I.; Köpp, F.; Rahm, S. Measurement of atmospheric turbulence by 2-μm Doppler lidar. *J. Atmos. Ocean. Technol.* **2005**, *22*, 1733–1747. [CrossRef]
46. Mann, J.; Peña, A.; Bingöl, F.; Wagner, R.; Courtney, M.S. Lidar scanning of momentum flux in and above the atmospheric surface layer. *J. Atmos. Ocean. Technol.* **2010**, *27*, 959–976. [CrossRef]

remote sensing

MDPI

Erratum

Erratum: Pauscher, L., et al. An Inter-Comparison Study of Multi- and DBS Lidar Measurements in Complex Terrain. *Remote Sens.* 2016, *8*, 782

Lukas Pauscher [1,2,*], Nikola Vasiljevic [3], Doron Callies [1], Guillaume Lea [3], Jakob Mann [3], Tobias Klaas [1,4], Julian Hieronimus [5], Julia Gottschall [6], Annedore Schwesig [1], Martin Kühn [5] and Michael Courtney [3]

1 Fraunhofer Institute for Wind Energy and Energy System Technology (IWES), Fraunhofer IWES | Kassel, Königstor 59, 34119 Kassel, Germany; doron.callies@iwes.fraunhofer.de (D.C.); tobias.klaas@iwes.fraunhofer.de (T.K.); annedore@schwesig-schauenburg.de (A.S.)
2 Department of Micrometeorology, University of Bayreuth, 95447 Bayreuth, Germany
3 DTU Wind Energy, Risø Campus, Technical University of Denmark, 4000 Roskilde, Denmark; niva@dtu.dk (N.V.); gule@dtu.dk (G.L.); jmsq@dtu.dk (J.M.); mike@dtu.dk (M.C.)
4 Institute for Geophysics and Meteorology, University of Cologne, 50923 Köln, Germany
5 ForWind, Center for Wind Energy Research, Carl von Ossietzky Universität Oldenburg, Küpkersweg 70, 26129 Oldenburg, Germany; Julian.Hieronimus@uni-oldenburg.de (J.H.); Martin.Kuehn@forwind.de (M.K.)
6 Fraunhofer Institute for Wind Energy and Energy System Technology (IWES), Fraunhofer IWES | Northwest, 27572 Bremerhaven, Germany; julia.gottschall@iwes.fraunhofer.de
* Correspondence: lukas.pauscher@iwes.fraunhofer.de; Tel.: +49-561-7294-475

Academic Editor: Prasad S. Thenkabail
Received: 13 June 2017; Accepted: 19 June 2017; Published: 28 June 2017

The authors would like to correct the following errors in [1]. In the original article [1], there is a typo in Equation (7) and the theoretical function in Figure 4e in the original publication is wrong. The correct form of Equation (7) should read:

$$\hat{\varphi}(k) = \hat{\varphi}_p(k)\hat{\varphi}_g(k) = e^{-k^2\sigma_p/2}e^{-k^2\sigma_g/2} \tag{7}$$

The corrected version of Figure 4e is displayed in the following:

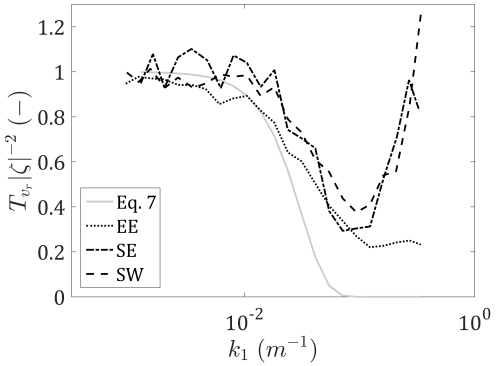

Figure 4. (**e**) Spectral transfer function $|\hat{\zeta}|^{-2} T_{v_r}$ derived from the average of the normalised spectra.

The correction to Figure 4e increases the deviations between the observations and theoretical considerations. The sentence "*The good agreement between observed and theoretical spectral transfer functions is encouraging for this approach.*" in the conclusion of [1] not longer seems appropriate in this context.

We apologise for any inconvenience this might have caused to the readers. The manuscript will be updated and the original will remain online on the article webpage.

Reference

1. Pauscher, L.; Vasiljevic, N.; Callies, D.; Lea, G.; Mann, J.; Klaas, T.; Hieronimus, J.; Gottschall, J.; Schwesig, A.; Kühn, M.; et al. An Inter-Comparison Study of Multi- and DBS Lidar Measurements in Complex Terrain. *Remote Sens.* **2016**, *8*, 782.

D. Pauscher et al. (2017b)

Pauscher, L., Mann, J., Vasiljevic and Lea, G.: Estimation of the dissipation rate of TKE from a single staring lidar, to be submitted to Journal of Atmospheric and Oceanic Technology.

Estimation of the dissipation rate of TKE from a single staring lidar

Lukas Pauscher* †

Fraunhofer IWES Kassel

Jakob Mann

Nikola Vasiljevic

Guillaume Lea

DTU

Corresponding author address: Lukas Pauscher, Fraunhofer Institute for Wind Energy and Energy System Technology, Königstor 59, 34119 Kassel, Germany

E-mail: lukas.pauscher@iwes.fraunhofer.de

†Department of Micrometeorology, University of Bayreuth, 95447 Bayreuth, Germany

ABSTRACT

Three different methods to derive the dissipation rate of turbulent kinetic energy ε from a staring lidar are evaluated by comparison to sonic anemometry. The first method uses the behaviour of the temporal power spectra of the radial velocity in the inertial sub-range. The second method is based on the calculation of short-term variances by chopping the lidar time series into smaller pieces. This method is a correction to an approach suggested earlier (Bouniol et al. 2003; O'Connor et al. 2010). The third approach exploits the spatial structure function along the lidar beam. All methods produce good results in estimating ε given the spectral transfer function of the lidar is known. Care needs to be taken here as the experimentally derived spectral transfer function from the lidar and sonic spectra showed discrepancies to the one obtained from theoretical considerations. For the method based on short-term variances it is important to apply the corrected version suggested in this paper, otherwise a gross overestimation of ε can result. While all methods yielded similar results, the range of experimental scenarios for which they can be used differs. The fact, that the structure-function method uses spatial statistics, makes it the most flexible. While the short-term variance and the spectral method are mainly applicable to staring configurations, the structure-function method can also be used in more complex scan patterns.

1. Introduction

Due to the needs of the growing wind energy sector the estimation of turbulence parameters using lidars has come into the focus of recent research efforts. Reviews can be found in Sathe and Mann (2013) and Sathe et al. (2015). One of the most difficult parameters to estimate is the dissipation rate of turbulent kinetic energy ε. Due to its well established relationship to the spectral density in the inertial sub-range, ε is readily suited to describe the spectral distribution of turbulent kinetic energy and is, thus, widely used in turbulence modelling (Wyngaard 2010). In wind engineering applications it can be used for e.g. modelling the turbulent inflow for load simulations of wind tubines (Mann 1994, 1998).

Several methods have been suggested and used to derive ε from lidar measurements. For a staring lidar they broadly fall into three categories:

I using the slope of the velocity spectrum in the inertial sub-range (e.g. Banakh et al. 1999; Davies et al. 2005; Lothon et al. 2009; O'Connor et al. 2010)

II exploiting the behaviour of the structure function in the inertial sub-range (e.g. Banakh et al. 1999; Smalikho et al. 2005; Davies et al. 2004; Kristensen et al. 2011) and

III utilizing the spectral broadening of the Doppler spectra (e.g. Banakh et al. 1995; Smalikho et al. 2005).

Moreover, based on the structure function approach ε can also be derived from scanning lidars using multiple beam locations (Banakh et al. 1999).

While the approach using the spectral broadening has successfully been tested for continuous-wave lidars, the spectral broadening of a pulsed lidar depends on the pulse characteristics and internal signal processing of the lidar and is, thus, not straight forward. O'Connor et al. (2010) suggested a simplified approach of (I), which relies on the variance of short-term measurements

using the variance of the wind velocity rather than the spectrum directly to avoid the need to calculate Fourier-transforms.

Despite the existence of multiple studies using lidars to estimate ε, experimental studies evaluating measurements of ε against reference measurements are rather scarce. If reference measurements are available they are either limited to a short time period (e.g. Banakh et al. 2010; Smalikho and Rahm 2010) or only compare individual profile measurements (Frehlich et al. 1998, 2006; O'Connor et al. 2010, e.g.)

In this study we compare three different methods to derive ε from a staring pulsed lidar against sonic anemometer measurements. Namely, we use the spatial structure function approach following Kristensen et al. (2011) and the spectral energy density. Moreover, a correction to the approach based on the short-term variances suggested by O'Connor et al. (2010) for contributions of larger scale turbulence is developed. Finally, the advantages and weaknesses of the different approaches are discussed.

2. Theory

a. Estimation of ε from the spectra

One of the most widespread approaches to estimate ε from high frequency wind speed measurements is to exploit the well defined behavior of the spectra in the inertial sub-range. In the inertial sub-range the velocity spectrum can be expressed as (e.g. Wyngaard 2010)

$$S(k_1) = \frac{9}{55}\alpha\left(1+\frac{1}{3}\sin^2\beta\right)\varepsilon^{2/3}k_1^{-5/3}, \tag{1}$$

where $\alpha \approx 1.7$ is the spectral Kolmogorov constant and k_1 is the wavenumber in the direction of the stream lines. The term in the brackets is introduced to account for the angle between the wind

direction and the beam or velocity component orientation β (e.g. Banakh et al. 1999; Kristensen et al. 2011). Exploiting this behaviour, ε can then be estimated from the spectrum of the wind velocity fluctuations (e.g. Champagne et al. 1977). This is done using the maximum likelihood method

$$\varepsilon = \left[\frac{9}{55}\alpha\left(1+\frac{1}{3}\sin^2\beta\right)\right]^{-3/2}\left(\frac{1}{n}\sum_{i=1}^{n}S(k_{1,i})k_{1,i}^{5/3}\right)^{3/2}. \tag{2}$$

The wave numbers k_i, $i = 1,...,n$ are all in the inertial sub-range. The relative statistical error can then be approximated by (Smalikho 1997)

$$E \equiv \frac{\sigma(\varepsilon)}{\langle\varepsilon\rangle} = \left(\frac{9}{4n}+\frac{c\left\langle u^2\right\rangle\tau}{\langle u\rangle^2 T}\right)^{1/2} \approx \frac{3}{2}n^{-1/2}, \tag{3}$$

where n is the number of spectral estimates used in the averaging, τ is the correlation time and T is the length of the measurement period. While the first term in Equation 3 describes the reduction of the error with increasing sample size, the second term is related to the uncertainty in the estimate of the mean wind speed. Equation 2 is only valid for a continuous point measurement. Due to its short sampling path and high sampling frequency this is usually a valid assumption for sonic anemometers. In case of a lidar measurement, the wind velocity is often averaged over a larger probe volume. Also sampling/accumulation times are usually longer. The spectra therefore become (e.g. Mann et al. 2009)

$$S(k_1) = n_i n_j \iint |\varphi(\boldsymbol{k}\cdot\boldsymbol{n})|^2|\zeta(k_1)|^2\Phi_{ij}(\boldsymbol{k})dk_2dk_3 \tag{4}$$

where $\boldsymbol{n}$ is the unit vector in the beam direction, φ and ζ are the spectral transfer functions for the probe volume averaging and temporal averaging, respectively, and Φ_{ij} is the spectral velocity tensor of turbulence. The temporal averaging can be described by

$$\zeta(k_1) = \operatorname{sinc} \frac{k_1 \langle u \rangle t}{2}, \tag{5}$$

where $\langle u \rangle$ is the mean wind speed in the direction of the stream lines and t is the accumulation time. Within the inertial sub-range, turbulence can be assumed to be isotropic and Φ_{ij} can be written as

$$\Phi_{ij} = \frac{E(k)}{4\pi k^4} \left(\delta_{ij} k^2 - k_i k_j \right), \tag{6}$$

with

$$E(k) = \alpha \varepsilon^{2/3} k^{-5/3}. \tag{7}$$

where $k = \sqrt{k_1^2 + k_2^2 + k_3^2}$ is the length of the wave vector. In several studies in the literature the volume averaging effect is neglected (e.g. Lothon et al. 2009; Lenschow et al. 2012; Pruis et al. 2013; Borque et al. 2016). The implications of the choice of φ or neglecting the volume averaging will be discussed in Section 4 .

b. Estimation of ε from short-term variances

The estimation of ε from short-term variances is basically a variation of the spectral method. For this method the time series of the radial wind velocity of the lidar is broken up into shorter pieces. This approach was first developed by Bouniol et al. (2003) for radar measurements and later applied to lidar data. O'Connor et al. (2010) suggested that if the short-term period is short enough to only be affected by turbulence in the inertial sub-range, the variance within the short-term period σ_{vl}^2 can be approximated by the integral

$$\sigma_{vl}^2 = \int_{k_a}^{k_b} S(k_1) = \int_{k_a}^{k_b} \frac{18}{55} \alpha \varepsilon^{2/3} k_1^{-5/3} dk_1, \tag{8}$$

where $k_a = 2\pi/L_a$ and $k_b = 2\pi/L_b$ and the length scales are $L_a = \langle u \rangle T$ and $L_b = \langle u \rangle \Delta t$. Here Δt is the accumulation time (which corresponds to the sampling frequency) and T is the length of each individual short-term period. The path averaging effect of the lidar is again neglected in Equation 8. From this O'Connor et al. (2010) derive

$$\varepsilon = 2\pi \left(\frac{110}{54\alpha} \right) \sigma_{vl}^3 \left(L_a^{2/3} - L_b^{2/3} \right)^{-3/2}. \tag{9}$$

Note that unlike in the original formulation (Bouniol et al. 2003; O'Connor et al. 2010) the three-dimensional value of the Kolmogorov constant α is used here. However, the formulation in Equation 8 neglects the probe volume averaging of the lidar and the contribution of turbulence with scales larger than k_a. More correctly Equation 8 should read

$$\sigma_{vl}^2 = \iiint_{-\infty}^{\infty} \left[1 - \mathrm{sinc}^2 \left(\frac{k_1 L_a}{2} \right) \right] |\varphi(\boldsymbol{k} \cdot \boldsymbol{n})|^2 |\zeta(k_1)|^2 n_i n_j \Phi_{ij}(\boldsymbol{k}) dk_1 dk_2 dk_3. \tag{10}$$

This means that also scales larger than L_a contribute to σ_{vl}^2. Figure 1 illustrates this effect. In fact, assuming Equation 1 to be valid for the whole wave number range contributing to the short-term variance, the contribution from scales larger than L_a are slightly larger than for scales smaller than L_a. The difference between Equation 8 and 10 depends on the averaging time, the wind speed, wind direction, accumulation time and φ. The effects of the spatial and temporal averaging will counteract the overestimation in Equation 8 to some degree. In this paper we use the mean short-term variances within the measurement period (e.g. 30 min) $\left\langle \sigma_{vl}^2 \right\rangle$ to estimate ε_{lidar}.

The statistical error in this estimation of ε_{lidar} depends on the choice of the short-term interval. The random error also depends on the relation between T and τ. Using the framework of Lenschow

et al. (1993, 1994) the expected error can be estimated. Here, first Equation A5 in Lenschow et al. (1993) is used to to derive the relative random error $\sigma_2^2(T/\tau)/\mu_2^2$. σ_2^2 is the variance of the second moment of the short-term period and μ_2 is the expected value of the long-term interval. Then Equation A1 in Lenschow et al. (1993) is used to estimate the ratio $\mu_2(T/\tau)/\mu_2$, where $\mu_2(T/\tau)$ is the expected value for the short-term variance. The relative random error then can be esimated as

$$E_{vl}^2 = \frac{\sigma_2^2(T/\tau)}{\mu_2^2(T/\tau)}. \tag{11}$$

If the individual estimates of σ_{vl}^2 are assumed to be independent and follow a Gaussian distribution the uncertainty for ε follows as

$$E_\varepsilon = \frac{3}{2}\sqrt{\frac{\langle E_{vl}^2 \rangle}{N}}, \tag{12}$$

where N is the number of the short-term periods used in the estimation of $\left\langle \sigma_{vl}^2 \right\rangle$.

O'Connor et al. (2010) also suggest a method to remove the noise contribution from the variance measurements based on the instrument characteristics. However, the necessary parameters were not available to the authors. Therefore, the noise contribution is estimated from the measurement statistics. Extrapolation of the auto-covariance function to zero lag is used (Mayor et al. 1997; Lenschow et al. 2000). The noise is determined using the first two lags to extrapolate to zero lag (Frehlich 2001).

c. Estimation of ε from the structure function

As pulsed lidars are capable of probing the atmosphere at several locations along the beam synchronously, the spatial structure of turbulence can be exploited to measure ε without the need to invoke Taylors hypothesis. If turbulence is assumed to be isotropic and homogeneous along

multiple locations along the beam, the structure function of the wind velocity D can be used for the estimation of ε. In the inertial sub-range (Tatarski 1961)

$$D(r) \equiv \left\langle [\boldsymbol{n} \cdot (\boldsymbol{u}(\boldsymbol{x}) - \boldsymbol{u}(\boldsymbol{x}+\boldsymbol{r}))]^2 \right\rangle = C_v \varepsilon^{2/3} r^{2/3} \tag{13}$$

where $C_v = 1.32\alpha$ is the structure function constant and r is the distance between the measurements. Notice no dependence on β because the separation vector $\boldsymbol{r}$ is always parallel with the velocity component being measured. If the distances are chosen small enough this behavior can be exploited and ε can be estimated without the need of an estimation of the outer length scale (Kristensen et al. 2011).

The field underlying the structure function along the lidar beam can be defined as

$$\Delta v_l(\boldsymbol{x}, \boldsymbol{r}) = v_l(\boldsymbol{x}) - v_l(\boldsymbol{x}+\boldsymbol{r}), \tag{14}$$

where $v_l \equiv \boldsymbol{n} \cdot \boldsymbol{u}$ is the velocity component along the beam. In Fourier space this becomes

$$\Delta \hat{v}_l(\boldsymbol{k}, \boldsymbol{r}) = \varphi(\boldsymbol{k} \cdot \boldsymbol{n}) \zeta(k_1) \hat{\boldsymbol{u}}(\boldsymbol{k}) \left(1 - e^{-i\boldsymbol{k}\cdot\boldsymbol{r}}\right), \tag{15}$$

where $\hat{\boldsymbol{u}}$ is the Fourier transform of the velocity field. To simplify the further notation, it is convenient to define

$$a(\boldsymbol{r}, \boldsymbol{k}) = \varphi(\boldsymbol{k} \cdot \boldsymbol{n}) \zeta(k_1) \left(1 - e^{-i\boldsymbol{k}\cdot\boldsymbol{r}}\right). \tag{16}$$

The structure function measured by the lidar $\overline{D}$ can then be expressed as

$$\overline{D}(\boldsymbol{r}) = \int a(\boldsymbol{r}, \boldsymbol{k}) a^*(\boldsymbol{r}, \boldsymbol{k}) n_i n_j \Phi_{ij}(\boldsymbol{k}) d^3k. \tag{17}$$

If r is small enough to lie within the inertial sub-range, the temporal averaging is neglected and $\varphi(k)$ is assumed to be Gaussian, i.e. $\varphi^2(k) = e^{-k^2\sigma_l^2}$, Equation 17 can be simplified to

$$\overline{D}(r, \sigma_l) = \frac{18}{55} \alpha \varepsilon^{2/3} \int e^{-k^2\sigma_l^2} (1 - \cos kr) k^{-5/3} dk. \tag{18}$$

Scaling with the length scale of the lidar probe volume it becomes obvious that the integral in Equation 18 is only dependent on the ratio r/σ_l (Kristensen et al. 2011)

$$\overline{D}(r,\sigma_l) = \frac{18}{55}\alpha\varepsilon^{2/3}\sigma_l^{2/3}\int e^{-\kappa^2}\left(1-\cos(\kappa r/\sigma_l)\right)\kappa^{-5/3}d\kappa. \tag{19}$$

The integral in Equation 17 can be solved analytically to give

$$\overline{D}(r,\sigma_l) = \frac{54}{55}\alpha\varepsilon^{2/3}\sigma_l^{2/3}\Gamma\left(\frac{2}{3}\right)\left\{{}_1F_1\left(-\frac{1}{3};\frac{1}{2};-\frac{r^2}{4\sigma_l^2}\right)-1\right\}, \tag{20}$$

where ${}_1F_1$ is the confluent hypergeometric function of the first kind and Γ is the gamma function. ε can then be estimated from the lidar measurements by fitting the measured structure function to the theoretical formulation. To remove the influence of the measurement noise the extrapolation of the auto-covariance function to zero lag is used (Mayor et al. 1997; Lenschow et al. 2000). $\overline{D}$ is estimated using the first two lags to extrapolate to zero lag (Frehlich 2001).

To derive a statistical uncertainty for the structure function approach, first the length scale of the process in Equation 14 using the spectrum of the structure function (term in the integral in Equation 18) is estimated. For this purpose the wave number with the maximum contribution to $\overline{D}$ is calulated and then converted to the corresponding length scale

$$\mathscr{L} = \frac{2\pi}{\arg\max_k e^{-k^2\sigma_l^2}\left(1-\cos kr\right)k^{-2/3}}. \tag{21}$$

Equation 21 is somewhat inconvenient as the integral length scale depends on r as well as on σ_l. However, for $r \gg \sigma_l$ r will dominate and vice versa (Figure 2).

To derive the statistical uncertainty from $\mathscr{L}$, again we use the framework of Lenschow et al. (1993, 1994). The statistical uncertainty in the estimate in $\overline{D}(r,\sigma)$ from a single measurement along the lidar beam can then be estimated using Equations A1 and A5 in Lenschow et al. (1993) as described for the short-term variance but using $\mathscr{L}$ and the length along the beam over which $\overline{D}$ is estimated L_D instead of τ and T. This is useful for horizontally staring lidars which sample

over a very long distance (e.g. a few km) over homogeneous terrain as it allows an uncertainty estimate of quasi-instantaneous measurements of ε. Comparing $\mathscr{L}$ with the expected integral length scales of turbulence can also serve as an indication if the Equations 18 and 19 are suitable for the estimation of ε in the experimental setup.

If these instantaneous estimates are averaged over a longer time period, the statistical uncertainty can be further reduced. In this study the scales corresponding to the temporal averaging over 30 min $L_T = \langle u \rangle T$ will be dominant in the uncertainty estimation when compared to L_D.

d. Measurement of the spectral transfer function

Since the understanding of the spectral transfer function $\varphi^2(k)$ is essential to interpreting the results of the measurements of ε, $\varphi^2(k)$ is is also investigated experimentally in this paper. If co-located measurements of the lidar and the sonic anemometer exist, there are generally two approaches to estimate the $\varphi^2(k)$ (Angelou et al. 2012). Probably the most intuitive way is to use the individual auto-spectra of the sonic and lidar measurement. If the wind is parallel to the beam direction the following relationship can be derived assuming Taylor's frozen turbulence hypothesis (Kaimal et al. 1968; Mann et al. 2009):

$$\varphi^2(k_1) = S_{u,l}(k_1) S_{u,s}^{-1}(k_1), \tag{22}$$

where $S_{u,s}$ is the velocity spectrum of the sonic measurements and $S_{u,l}$ is the velocity spectrum of the lidar measurements. Alternatively $\varphi(k)$ can also be measured using the real part of the cross-spectrum $\chi_{l,s}$ of lidar and the sonic velocities (Angelou et al. 2012):

$$\varphi^2(k_1) = \Re(\chi_{l,s}(k_1))^2 S_{u,s}^{-2}(k_1). \tag{23}$$

This assumes the real part of the spectrum to be positive. If the noise in the two measurements is uncorrelated, Equation 23 has the advantage that the noise will cancel out (Angelou et al. 2012).

3. Description of the measurements and data treatment

Measurement Setup

The measurement campaign was performed at the wind turbine test station at Høvsøre, Denmark (Peña et al. 2016). A scanning lidar of the type WindScanner (Vasiljevic et al. 2016) was placed approximately 1.6 km from a reference mast and the beam was oriented in such a way that the laser was pointed next to a sonic anemometer at a height of 100 m mounted on a 116 m mast, see Figure 3. The elevation angle of the laser beam was 3.58° and thus very close to horizontal. In the further analysis the elevation angle is neglected and the beam is assumed to be horizontal. The instrument was operated at a pulse repetition rate of 20 kHz and the accumulation time was set to 0.5 s. The pulse length was 200 ns. Data was sampled at 100 range gates centered around the reference anemometer and with 1 m between them. Data was collected during summer 2014 (22 August - 6 October).

The reference anemometer is a Metek USA1 F2901A sonic which is mounted at a height of 100 m on a triangular lattice tower. At the height of measurement the tower has a width of 1.1 m and the measurement boom has a length of 1.9 m (Peña et al. 2016). High frequency data from the sonic is collected at a sampling frequency of 20 Hz.

Data treatment

All statistics in this study are based on 30 minute intervals. Sonic data was despiked and gap-filled. Periods during which the wind direction was between 150 and 210° were excluded from the analysis to avoid effects of the mast structure on the sonic measurements.

Higher order statistics are more sensitive to measurement noise or random outliers in measurement data than mean wind speeds. Therefore, a two step quality control process to the lidar measurements is performed. Both steps are based on the carrier-to-noise-ratio (CNR). The CNR has the advantage to be independent of the wind statistics themselves. First, a CNR-threshold is applied to the data. Measurements with CNR values < -25 dB are excluded from further analysis. After that, the median CNR is calculated for each individual 30 minute period. Within this period all measurements with an absolute difference of > 5 dB from the median are removed. This approach has proven to be useful to remove effects of hitting hard targets with the lidar beam in an earlier study (Pauscher et al. 2016). It can also potentially help to detect problems with the pulse emission or signal processing.

The effect of the second CNR-filter is given in Figure 4. A comparison of the variances measured by the lidar and the sonic reveals a very high correlation between the two instruments if the second CNR-filter is applied to the lidar data. Several outliers can be removed. Still, a clear underestimation of the sonic by the lidar can be observed. This is likely to stem from the effects of the spatial and to a lesser extend also the temporal averaging of the lidar measurement. For the mean wind, velocity differences between the sonic and the WindScanner are small. Also, the effect of the second CNR-Filter on the mean values is very small.

4. Results and Discussion

THE SPATIAL TRANSFER FUNCTION

The assumption of a Gaussian shape of the lidar pulse is often used for simplicity in the literature (e.g. Frehlich and Cornman 2002; Banakh et al. 2010; Kristensen et al. 2011). The manufacturer gives the full-width-half-maximum of the pulse as 200 ns resulting in a standard deviation of the pulse length of σ_p = 12.7 m. The internal signal processing of the lidar device employed in this

study uses a Gaussian tapering window with σ_g = 9.5 m. The convolution of the two results in σ_l = 15.9 m.

In addition to the simplified Gaussian shape of the pulse, the pulse intensity emitted by the lidar was also measured. The measured shape is clearly non-Gaussian and significantly skewed (Figure 5a). This effect gets smoothed to some degree by the convolution with the gating function (Figure 5b). However, also the theoretical weighting function using the measured pulse intensity remains skewed. Measurements using two other WindCube 200s devices brought very similar pulse shapes for all instruments.

As outlined in Section 2, the spectral transfer function of the lidar using co-located sonic measurements can be obtained by either using the temporal spectra of the lidar and the sonic measurement or the temporal cross-spectrum of the two. Figure 5c shows the comparison of the measurements using the two methods with the theoretically derived transfer functions. The measurements using the cross-spectral method show a good agreement with the theoretical formulations in wavenumber space. The difference between the weighting function using the measured pulse and assuming a Gaussian pulse is rather small.

In contrast to the cross-spectral method, the spectral transfer function based on the individual spectra of the two instruments shows an attenuation only at significantly higher wave numbers. For illustration purposes the theoretical transfer function for σ_l = 9 m is also shown in Figure 5c. This gives a much better fit than the theoretical weighting functions derived from the instrument properties. In the following analysis, therefore, σ_l = 9 m will be used in addition to σ_l = 15.9 m to estimate the effects of the spatial averaging.

A faster drop-off of the spectral transfer function derived from the cross-spectrum has been observed by Angelou et al. (2012) for a continuous wave lidar. In their investigation the spectral method also showed a worse agreement to the theoretical considerations than the cross-spectral

method. Some of the differences can probably be explained by measurement noise, which is also visible in the increase for the spectra-based approach at the high wave number end. For pulsed lidars Pauscher et al. (2016) reported a similar observation for the spectral methods. At this point the reason for the difference between the spectral and cross-spectral method cannot fully be clarified.

ε FROM LIDAR SPECTRA

The first method under investigation in this paper to derive ε uses the spectral density in the inertial sub-range (Equation 2). This is also the method which is used to derive the dissipation rate from the sonic measurements ε_{sonic} which serves as the reference in this paper. To ensure an appropriate determination of ε_{sonic}, the wave number range which is used must be high enough to lie in the inertial sub-range. On the other side, measurement noise might contaminate the measurements at high frequencies.

Figure 6a shows the median dissipation rate $\tilde{\varepsilon}$ as derived from different wave number intervals. For the sonic measurements a plateau can be observed between approximately 0.1 and 0.5 m^{-1}. This is a good indication for the spectra showing the -5/3-slope in this range. Therefore, this interval to derive ε_{sonic} is an appropriate choice in this experimental setup. The u-component of the wind vector is chosen to derive ε_{sonic} as it usually shows inertial sub-range behaviour already at lower wave numbers than v and especially w.

Unlike the sonic measurements ε_{lidar} does not show a clear plateau. It rather increases up to $k_1 \approx 0.03m^{-1}$ and then starts to drop again (Figure 6). Here, the effects of the spatial averaging are clearly visible. For higher wave numbers the values increase again. This is likely to be the effect of measurement noise, which was also reported from other lidar measurements (e.g. Angelou et al. 2012; Pauscher et al. 2016). For all wave number intervals ε_{lidar} is lower than ε_{sonic}. This

fits well to the observation that $\sigma^2_{vr,l}$ is smaller than $\sigma^2_{vr,s}$ (Figure 4). Figure 6b also highlights some of the difficulties associated with an estimation of ε from the raw lidar spectra. On the one hand, estimates of ε should be made within the inertial sub-range. On the other hand the spatial averaging effects can bias the estimated value of ε towards a significant underestimation at higher wave numbers.

Figure 6b displays the comparison of $\tilde{\varepsilon}$ by wave number interval only for flow along the lidar beam. This has the advantage that $\varphi^2(k_1)$ is simply multiplied onto the sonic spectrum to get the lidar spectrum and therfore, in theory, the spectral attenuation can be annihilated by dividing the lidar spectrum with $\varphi^2(k)$, if this is known. However, for high wave numbers the effects of measurement noise quickly become dominant. This is also associated with the quick drop-off of $\varphi^2(k)$ at high wave numbers (Figure 5c), which makes the expected turbulent signal very small and the measurement prone to noise. In Figure 6b the onset of the plateau of $\tilde{\varepsilon}$ derived from the sonic measurements and the start of the noise dominated region of the lidar measurements fall very closely together.

If $\varphi(k)$ is unknown the first maximum of the lidar measurements in Figure 6a seems to be the natural choice to make an estimate of ε from the lidar data. Here, one can get as close to the inertial sub-range as possible while the effect of the spatial averaging by the lidar still is comparatively low. Also, the dip for higher wave numbers is reassuring that the measurements are not dominated by noise in this wave number range. However, in the current setup this point (0.0215 - 0.0464 m^{-1}) lies only at the edge of -5/3-slope. This induces a systematic underestimation of $\tilde{\varepsilon}$ by the lidar. For a more vertically pointing beam direction the onset of the inertial sub-range is expected to be at higher wave numbers. Thus, the underestimation is likely to be stronger.

Figure 7 shows the direct comparison of ε_{sonic} and ε_{lidar} derived from the wave number range 0.0215 - 0.0464 m^{-1}. Also shown is the comparison for the wave number range 0.0464 - 0.1

m^{-1} corrected with $|\varphi(k_1)|^3$. In general there is a good correlation between dissipation estimates from the sonic and the lidar for both comparisons across several orders of magnitude. As would be expected from Figure 6, for the uncorrected ε_{lidar} from the wave number interval (0.0215 - 0.0464 m^{-1}) there is an average (median) underestimation of ε_{sonic} by ε_{lidar} (apporx. 39%). For the corrected ε_{lidar} in the wave number interval 0.0464 - 0.1 m^{-1} this changes to a small overestimation (2 %).

As outlined in Section 2 the spectral attenuation also depends on the angle between wind direction and the lidar beam direction. To make an estimate of its influence on ε_{lidar} numerical integration of Equation 4 using Equation 6 can be used. Due to relatively fast sampling of the lidar the effect of the temporal averaging is relatively small. For $u = 18$ m s^{-1} neglecting $\zeta(k_1)$ leads to a theoretical underestimation of approximately 5 % in ε.

In the absence of a reference measurement it might be difficult to identify the appropriate wave number intervals and transfer functions. Thus, choosing the first peak as shown in Figure 6 and acknowledging the systematic underestimation of ε might be the only practical approach method in some situations.

Another consideration that should be taken into account when selecting the wave number interval is that the statistical random error in the estimate of $S(k_1)$ is of the order of $S(k_1)$ if no frequency bin averaging is applied. This is an issue, especially, if short measurement periods and/or low wave numbers are used for the estimation of ε. For the two wave number intervals shown in Figure 7 the statistical random error is between approximately 13 % - 33 % and 9 % - 22 % depending on the wind speed.

In practical applications the spectral method requires a relatively high sampling frequency. Otherwise an estimation of $S(k_1)$ inside the inertial sub-range is not possible. Moreover, for a disjunct sampling with a short integration time, aliasing effects can contaminate the spectral estimates. Due

to the principles of a pulsed lidar, relatively long accumulation times are needed (usually at least 0.5 - 1 s). Moreover, the currently available scanning technology for pulsed lidars has a moving speed in the order of 30° s^{-1}. Complex scan patterns, therefore, take too long to revisit the same point and the method is mainly restricted to staring configurations.

ε from short-term variances of the lidar time series

If ε is to be estimated from short-term variances, the length of the short-term interval has to be chosen. O'Connor et al. (2010) used an interval length of 40 s which corresponds to a length scale L_a= 400 m at a wind speed of 10 m s^{-1} but varies with wind speed. From theoretical considerations, however, it seems more appropriate to base the choice of the averaging interval on spatial scales and, thus, use a varying time period. This has the advantage that it is also easier to compare to the spectral method, where also a fixed spatial scale was chosen.

In this context a compromise needs to be made. On the one hand, scales need to be large enough to include enough points in the short-term interval to allow for a reasonable calculation of the standard deviation. On the other hand, scales should be small enough so that all wave numbers contributing significantly to the variance in Equation 10 should be contained within the inertial sub-range. Based on the analysis in Figure 6a, L_a = 100 m (k_a = 0.0628 m^{-1}) is chosen in this paper.

Figure 8 shows a comparison between ε_{lidar} estimated using L_a = 100 m and ε_{sonic}. In general, a good correlation between the lidar and the sonic measurements can be observed. However, there is a bias towards an underestimation of the sonic measurements by the lidar measurements. A likely cause for this is, that the scales contributing to σ_{vl} are not fully contained within the wave number range within which the -5/3-slope applies. At this point it should also be reiterated that the original formulation of Bouniol et al. (2003) and O'Connor et al. (2010) should not be used

as this can produce a significant overestimation of ε. For the setup in this study the systematic overestimation of ε using Equation 9 compared to Equation 10 is between approximately a factor of 1.6 - 3.7 depending on wind speed and direction.

Especially at lower values of ε a significant difference between the ε_{lidar} estimated with and without accounting for the measurement noise can be observed. While the values for directly using σ_{vl} flatten out for low ε_{sonic}, the auto-covariance method shows a much better correlation with the sonic measurements and seems to effectively remove the measurement noise.

Similar to the spectral method a high frequency sampling is important for a successful application of the method. Longer time periods between the individual samples require larger time/spatial scales L_a and L_b which conflicts with the requirement that all contributing wave numbers lie within the inertial sub-range. The statistical random error of the method is dependent on wind speed. Assuming $\tau = 20$ s and $T = 10$ s ($u = 10$ m s^{-1}) the $E_{epsilon} = 10$ %. For $u = 5$ m s^{-1} and ($u = 15$ m s^{-1}) this value is 13 % and 8 %, respectively.

As lined out in Section 2 the estimation of ε_{lidar} form the short-term variances can bee seen as a simplification/special case of the spectral method. However, it also has similarities to the structure function method as it 'integrates' the variations over a certain wave number interval.

ε from the spatial structure function

Figure 9 shows the influence of the form of the spatial averaging window, which is used in the calculation of ε_{lidar} from $\overline{D}$. The ratio between $\varphi(k)$ from the measured pulse and the Gaussian form with $\sigma_l =$ 15.9 m only slightly differs by distance. This indicates that for the calculation of ε_{lidar} the differences between the two shapes are small. The ratio between the larger ($\sigma_l = 15.9$ m) and smaller ($\sigma_l = 9$ m) Gaussian window is strongly dependent on r. Here, the effects of range-

gate overlapping between the two points and the effect of small scale turbulence attenuation which varies with σ_l can be seen.

Motivated by the considerations about the theoretical and measured form of $\varphi(k)$ (Figure 5) and their influence on the values derived for ε_{lidar} (Figure 9) two Gaussians with σ_l = 9 m and σ_l = 15.9 m were used to derive ε_{lidar} from the structure-function method. For σ_l = 9 m the median value of ε_{lidar} is slightly lower than the reference but relatively constant over the investigated range of r. In contrast, for σ_l = 15.9 m ε_{lidar} strongly decreases with increasing r The ratio for the two follows the theoretical pattern shown in Figure 9 a. This behaviour again supports that σ_l = 9 m is more appropriate than σ_l = 15.9 m for the investigated measurements.

The pattern in the blue lines in Figures 9 and 10a also shows that the sensitivity of the estimates of ε_{lidar} to $\varphi(k)$ decreases with increasing r. Thus, as for the method based on the short-term variances, there is a trade-off between small distances to ensure inertial sub-range behaviour of the turbulence and large distances to decrease the uncertainty due to $\varphi(k_1)$. In contrast to the method relying on short-term variances small separation distances can also be applied for high wind speeds. Especially for low measurement heights this can be advantageous. However, if there is uncertainty in $\varphi(k)$ or relatively high noise levels it might be advantageous to use larger r.

As discussed in Section 2 the statistical uncertainty for the structure function method depends on wind speed, σ_l, r and also on wind direction. Flow parallel to the lidar beam can be seen as a worst case scenario for the statistical uncertainty. This case is shown in Figure 10b for different σ_l, r and u. From a statistical point of view it is advantageous to use settings with a small σ_l. There is also a dependency on r, however, at small separation distances (roughly $\sigma_l > 3r$) the effect is limited as σ_l dominates in Equation 21. As for the short-term variance method and the spectral method, there is a strong dependency of E_ε on the wind speed.

An interesting property of the spatial structure-function method is that the requirement for high frequency sampling is strongly relaxed. Indeed, applying Taylor's concept of frozen turbulence and assuming u parallel to the beam, probing the same beam direction with a frequency higher than u/L_D will not reduce the statistical uncertainty. For the current experiment with a typical u = 10 m/s and L_D = 100 m a return time to the same point $\leq$ 10 s would not increase E_ε. One thing that needs to be kept in mind is that the estimation of the measurement noise from the temporal auto-correlation function is not adequate in this situation and other noise removal techniques such as from instrument characteristics (O'Connor et al. 2010) or e.g. using the odd and even pulse accumulation technique suggested by Frehlich (2001) need to be applied.

The spatial structure function method is also the only method which does not require knowledge of the mean horizontal wind speed. This is a strong advantage in staring configuration, as in many cases staring configurations do not provide a measurement of the mean wind speed. For the spectral and short-term-variance methods additional measurements or modelled values of the mean wind speed are required in these cases.

The direct comparison of the individual measurements of ε_{lidar} and ε_{sonic} shows a good correlation between the two over several orders of magnitude. This is similar to what Banakh et al. (2010) observed for a few selected hours using a pulsed lidar and the structure function approach, but also including the outer length scale in the model for the structure function. Other studies using the structure function approach only show the comparison of individual vertical profiles between lidar and a thethered system were reported by Frehlich et al. (2006) or lack a reliable reference measurement (Frehlich et al. 1998; Smalikho et al. 2005; Smalikho and Rahm 2010).

5. Conclusion

Three methods were investigated to estimate the dissipation rate of turbulent kinetic energy from a staring lidar. In general, if the appropriate $\varphi(k)$ is applied to account for the spatial averaging along the beam and the noise is accounted for, all three methods yielded good results. However, care needs to be taken in this context, as $\varphi(k)$ determined from measurements of the auto-spectra significantly differed from the theoretical considerations. The method based on the short-term variances should only be applied in the corrected form to account for the large scales contributing to the short-term variances. The corrected formulation of the method is more complex. As its simplicity is one of its biggest advantages, the method becomes less attractive in the corrected form. The advantage of the spectral method is, that the analysis of the spectra also provides insight into the noise in the measurement and to some degree into the spatial averaging along the beam.

In many situations the method based on the structure function will be a good choice. It is at least as accurate as the other methods. Moreover, in contrast to the other two methods, it relies on spatial instead of temporal statistics. This provides a great advantage, if multiple beam directions are scanned by a single lidar and the sampling rate in one beam direction becomes low. Another advantage of the structure-function method is its independence from the mean wind speed. This is useful for staring configurations where no reliable estimates of the mean wind speed are available. Finally, pulsed lidar technology allows for the use of relative small separation distances in the structure function method, which is useful in case of small turbulent scales and/or high wind speeds.

Acknowledgments. The work in this publication was funded by the projects windscanner.eu and New European Wind Atlas. Lukas Pauscher received funding from the IRPWIND mobility programme to perform the work presented in this article.

References

Angelou, N., J. Mann, M. Sjöholm, and M. Courtney, 2012: Direct measurement of the spectral transfer function of a laser based anemometer. *Review of Scientific Instruments*, **83 (3)**, 033 111, doi:10.1063/1.3697728.

Banakh, V. A., I. Smalikho, F. Köpp, and C. Werner, 1999: Measurements of turbulent energy dissipation rate with a cw Doppler lidar in the atmospheric boundary layer. *Journal of Atmospheric and Oceanic Technology*, **16 (8)**, 1044–1061, doi:10.1175/1520-0426(1999)016⟨1044:MOTEDR⟩2.0.CO;2.

Banakh, V. A., I. N. Smalikho, F. Köpp, and C. Werner, 1995: Representativeness of wind measurements with a cw Doppler lidar in the atmospheric boundary layer. *Appl. Opt.*, **34 (12)**, 2055–2067, doi:10.1364/AO.34.002055.

Banakh, V. A., I. N. Smalikho, E. L. Pichugina, and W. A. Brewer, 2010: Representativeness of measurements of the dissipation rate of turbulence energy by scanning doppler lidar. *Atmospheric and Oceanic Optics*, **23 (1)**, 48–54, doi:10.1134/S1024856010010100.

Borque, P., E. Luke, and P. Kollias, 2016: On the unified estimation of turbulence eddy dissipation rate using Doppler cloud radars and lidars. *Journal of Geophysical Research: Atmospheres*, **121 (10)**, 5972–5989, doi:10.1002/2015JD024543.

463 Bouniol, D., A. J. Illingworth, and R. J. Hogan, 2003: Deriving turbulent kinetic energy dissi-
464 pation rate within clouds using ground based 94 GHz radar. *Preprints 31st Conf. on Radar*
465 *Meteorology*, 193–196.

466 Champagne, F. H., C. A. Friehe, J. C. LaRue, and J. C. Wyngaard, 1977: Flux measurements,
467 flux estimation techniques, and fine-scale turbulence measurements in the unstable surface layer
468 over land. *Journal of the Atmospheric Sciences*, **34 (3)**, 515–530, doi:10.1175/1520-0469(1977)
469 034⟨0515:FMFETA⟩2.0.CO;2.

470 Davies, F., C. G. Collier, and K. E. Bozier, 2005: Errors associated with dual-Doppler-lidar
471 turbulence measurements. *Journal of Optics A: Pure and Applied Optics*, **7 (6)**, S280, doi:
472 10.1088/1464-4258/7/6/005.

473 Davies, F., C. G. Collier, G. N. Pearson, and K. E. Bozier, 2004: Doppler lidar measurements of
474 turbulent structure function over an urban area. *Journal of Atmospheric and Oceanic Technol-*
475 *ogy*, **21 (5)**, 753–761, doi:10.1175/1520-0426(2004)021⟨0753:DLMOTS⟩2.0.CO;2.

476 Frehlich, R., 2001: Estimation of velocity error for Doppler lidar measurements. *Journal of Atmo-*
477 *spheric and Oceanic Technology*, **18 (10)**, 1628–1639, doi:10.1175/1520-0426(2001)018⟨1628:
478 EOVEFD⟩2.0.CO;2.

479 Frehlich, R., and L. Cornman, 2002: Estimating spatial velocity statistics with coherent
480 Doppler lidar. *Journal of Atmospheric and Oceanic Technology*, **19 (3)**, 355–366, doi:10.1175/
481 1520-0426-19.3.355.

482 Frehlich, R., S. M. Hannon, and S. W. Henderson, 1998: Coherent Doppler lidar measure-
483 ments of wind field statistics. *Boundary-Layer Meteorology*, **86 (2)**, 233–256, doi:10.1023/A:
484 1000676021745.

Frehlich, R., Y. Meillier, M. L. Jensen, B. Balsley, and R. Sharman, 2006: Measurements of boundary layer profiles in an urban environment. *Journal of Applied Meteorology and Climatology*, **45 (6)**, 821–837, doi:10.1175/JAM2368.1.

Kaimal, J. C., J. C. Wyngaard, and D. A. Haugen, 1968: Deriving power spectra from a three-component sonic anemometer. *Journal of Applied Meteorology*, **7 (5)**, 827–837, doi:10.1175/1520-0450(1968)007⟨0827:DPSFAT⟩2.0.CO;2.

Kristensen, L., P. Kirkegaard, and T. Mikkelsen, 2011: *Determining the Velocity Fine Structure by a Laser Anemometer with Fixed Orientation*. Danmarks Tekniske Universitet, Risø Nationallaboratoriet for Bæredygtig Energi, Risø-R-1762(EN).

Lenschow, D. H., M. Lothon, S. D. Mayor, P. P. Sullivan, and G. Canut, 2012: A comparison of higher-order vertical velocity moments in the convective boundary layer from lidar with in situ measurements and large-eddy simulation. *Boundary-Layer Meteorology*, **143 (1)**, 107–123, doi:10.1007/s10546-011-9615-3.

Lenschow, D. H., J. Mann, and L. Kristensen, 1993: 3. How long is long enough when measuring fluxes and other turbulence statistics? NCAR, 53 pp.

Lenschow, D. H., J. Mann, and L. Kristensen, 1994: How long is long enough when measuring fluxes and other turbulence statistics? *Journal of Atmospheric and Oceanic Technology*, **11 (3)**, 661–673, doi:10.1175/1520-0426(1994)011⟨0661:HLILEW⟩2.0.CO;2.

Lenschow, D. H., V. Wulfmeyer, and C. Senff, 2000: Measuring second- through fourth-order moments in noisy data. *Journal of Atmospheric and Oceanic Technology*, **17 (10)**, 1330–1347, doi:10.1175/1520-0426(2000)017⟨1330:MSTFOM⟩2.0.CO;2.

Lothon, M., D. H. Lenschow, and S. D. Mayor, 2009: Doppler lidar measurements of vertical velocity spectra in the convective planetary boundary layer. *Boundary-Layer Meteorology*, **132 (2)**, 205–226, doi:10.1007/s10546-009-9398-y.

Mann, J., 1994: The spatial structure of neutral atmospheric surface-layer turbulence. *Journal of Fluid Mechanics*, **273 (-1)**, 141, doi:10.1017/S0022112094001886.

Mann, J., 1998: Wind field simulation. *Probabilistic Engineering Mechanics*, **13 (4)**, 269 – 282, doi:http://dx.doi.org/10.1016/S0266-8920(97)00036-2.

Mann, J., J.-P. C. Cariou, R. M. Parmentier, R. Wagner, P. Lindelöw, M. Sjöholm, and K. Enevoldsen, 2009: Comparison of 3d turbulence measurements using three staring wind lidars and a sonic anemometer. *Meteorologische Zeitschrift*, **18 (2)**, 135–140, doi:10.1127/0941-2948/2009/0370.

Mayor, S. D., D. H. Lenschow, R. L. Schwiesow, J. Mann, C. L. Frush, and M. K. Simon, 1997: Validation of NCAR 10.6-μm CO_2 Doppler lidar radial velocity measurements and comparison with a 915-MHz profiler. *Journal of Atmospheric and Oceanic Technology*, **14 (5)**, 1110–1126, doi:10.1175/1520-0426(1997)014⟨1110:VONMCD⟩2.0.CO;2.

O'Connor, E. J., A. J. Illingworth, I. M. Brooks, C. D. Westbrook, R. J. Hogan, F. Davies, and B. J. Brooks, 2010: A method for estimating the turbulent kinetic energy dissipation rate from a vertically pointing Doppler lidar, and independent evaluation from balloon-borne in situ measurements. *Journal of Atmospheric and Oceanic Technology*, **27 (10)**, 1652–1664, doi:10.1175/2010JTECHA1455.1.

Pauscher, L., and Coauthors, 2016: An inter-comparison study of multi- and dbs lidar measurements in complex terrain. *Remote Sensing*, **8 (9)**, 782, doi:10.3390/rs8090782.

Peña, A., and Coauthors, 2016: Ten years of boundary-layer and wind-power meteorology at Høvsøre, Denmark. *Boundary-Layer Meteorology*, **158 (1)**, 1–26, doi:10.1007/s10546-015-0079-8.

Pruis, M., N. Ahmad, D. Delisi, and F. Proctor, 2013: Atmospheric turbulence estimates from a pulsed lidar. *51st AIAA Aerospace Sciences Meeting including the New Horizons Forum and Aerospace Exposition*, 512.

Sathe, A., R. Banta, L. Pauscher, K. Vogstad, D. Schlipf, and S. Wylie, 2015: Estimating turbulence statistics and parameters from ground- and nacelle-based lidar measurements: IEA Wind Expert Report. Roskilde, Denmark.

Sathe, A., and J. Mann, 2013: A review of turbulence measurements using ground-based wind lidars. *Atmospheric Measurement Techniques*, **6 (11)**, 3147–3167.

Smalikho, I., F. Kpp, and S. Rahm, 2005: Measurement of atmospheric turbulence by 2-μm Doppler lidar. *Journal of Atmospheric and Oceanic Technology*, **22 (11)**, 1733–1747, doi:10.1175/JTECH1815.1.

Smalikho, I. N., and S. Rahm, 2010: Lidar investigations of the effects of wind and atmospheric turbulence on an aircraft wake vortex. *Atmospheric and Oceanic Optics*, **23 (2)**, 137–146, doi:10.1134/S1024856010020107, URL http://dx.doi.org/10.1134/S1024856010020107.

Smalikho, J., 1997: Accuracy of the turbulent energy dissipation rate estimation from the temporal spectrum of wind velocity fluctuations. *Atmospheric and Oceanic Optics C/C of Optika Atmosphery i Okeana*, **10**, 559–563.

Tatarski, V. I., 1961: *Wave propagation in a turbulent medium*. McGraw-Hill, New York.

549 Vasiljevic, N., G. Lea, M. Courtney, J.-P. Cariou, J. Mann, and T. Mikkelsen, 2016: Long-range
550 windscanner system. *Remote Sensing*, **8 (11)**, 896, doi:10.3390/rs8110896.

551 Wyngaard, J. C., 2010: *Turbulence in the Atmosphere*. Cambridge University Press.

LIST OF FIGURES

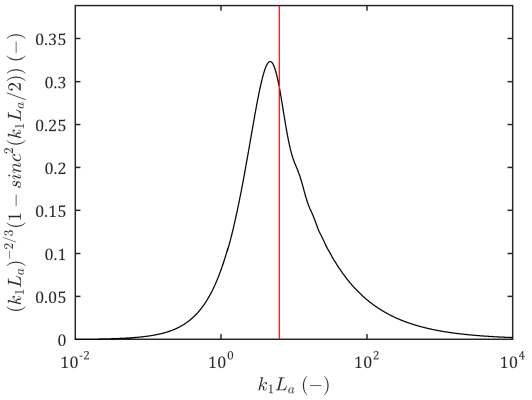

592 FIG. 1. Relative contribution to the variance for a short-term sample (σ_{vl}^2) in relation to the normalised wave
593 number in the direction of the mean flow (k_1L_a). The red line indicates the normalised wave number corresonding
594 to the scale L_a; the formulation assumes a -5/3-slope in the spectrum for the whole wave number space shown
595 here.

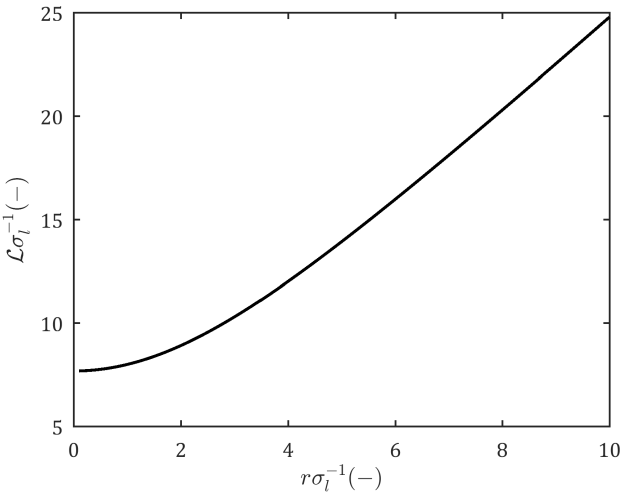

FIG. 2. Normalised length scale of the structure function $\mathscr{L}\sigma_l^{-1}$ as a function of the normalised separation distance $r\sigma_l^{-1}$.

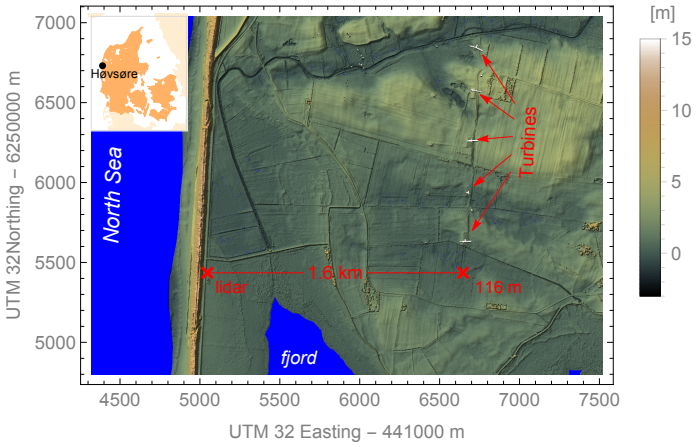

FIG. 3. Satellite image of the measurement site; red crosses indicate the positions of the lidar and the position of the mast; the distance between the two is approx 1.6 km.

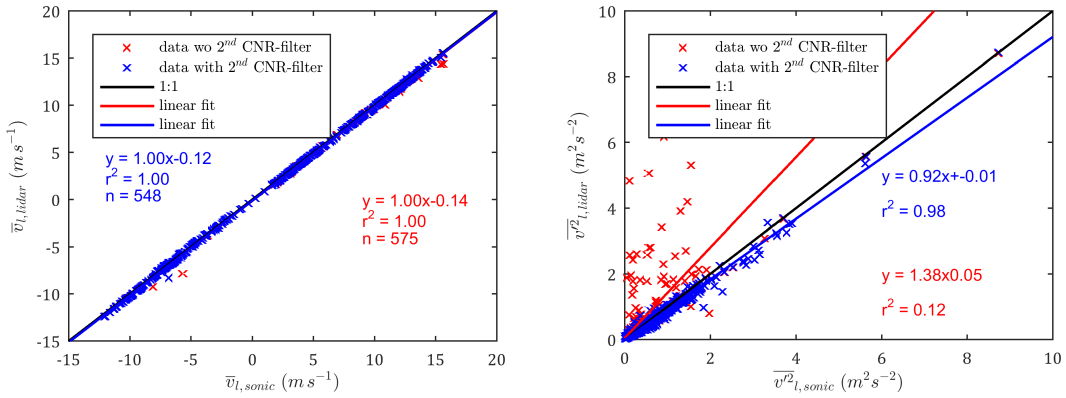

FIG. 4. Comparison of wind velocity statistics in the direction of the lidar beam as measured by the sonic anemometer and the lidar; **(a)** mean wind velocity and **(b)** variance of wind velocity; note that for clarity reasons not all points without 2nd CNR-filter are shown.

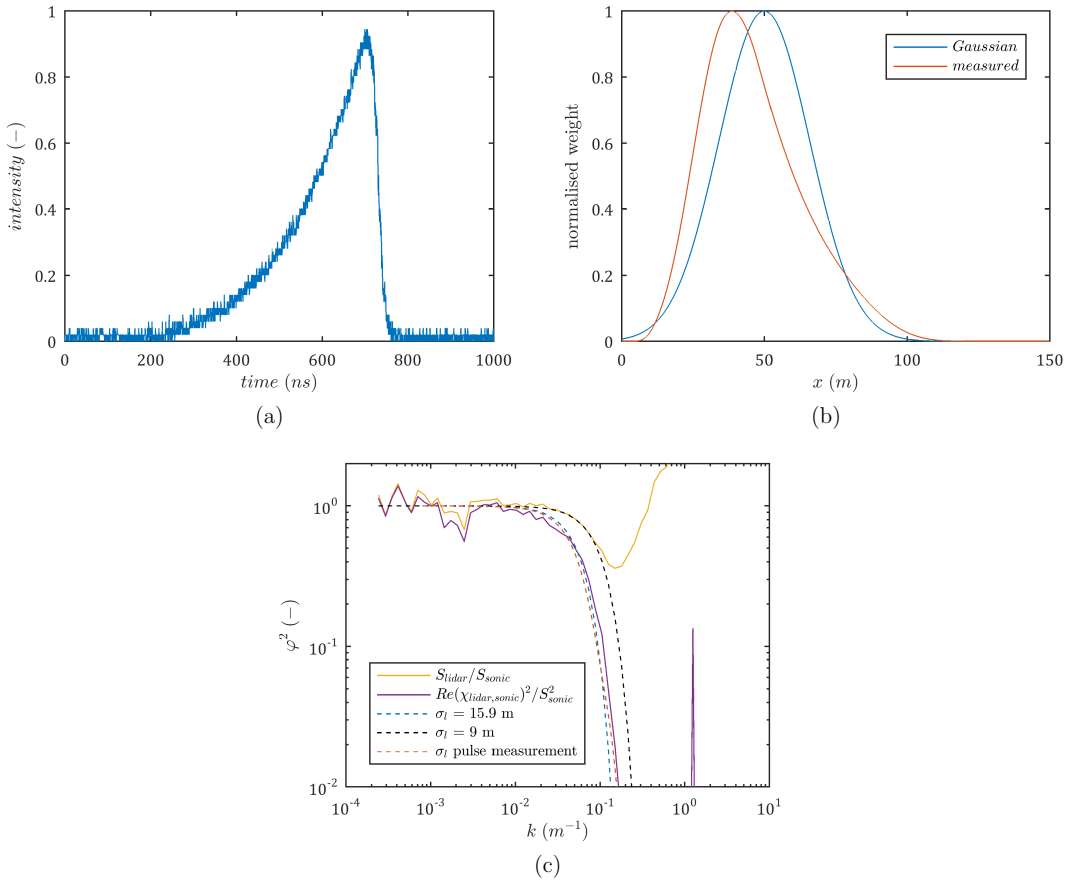

603 FIG. 5. **(a)** measured pulse intensity of the WindScanner (windcube 200s); **(b)** spatial weighting functions
604 of a Gaussian with σ_l = 15.9 m (blue line) and the measured pulse intensity (orange line); **(c)** comparison of
605 the theoretically derived spectral transfer functions with the measurements using the spectral and cross-spectral
606 method; wind directions $\pm 5^\circ$ from the beam direction were used.

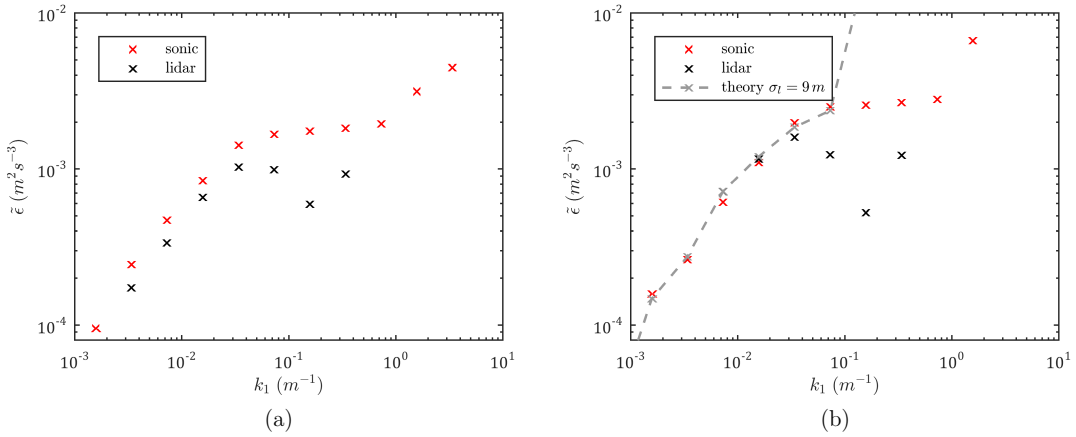

FIG. 6. **(a)** Dissipation rate (ε) as derived from varying wave-number intervals from the sonic and the lidar measurements using Equation 2; ˜ denotes the median in the respective wave number interval over all measurement periods passing the quality control; the sonic values were obtained from the u-component of the wind vector i.e. $\beta = 0°$ in Equation 2; **(b)** same as (a) but for wind directions parallel ($\pm 5°$) to the beam; the grey line indicates the ε derived from the lidar corrected with $|\varphi(k_1)|^3$ - i.e. the individual spectra were corrected using $|\varphi(k_1)|^2$ before calculating ε.

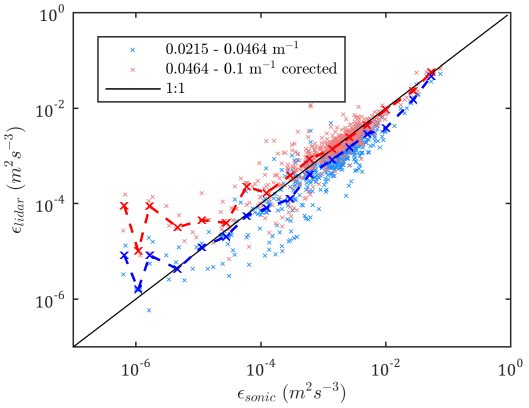

FIG. 7. Comparison of ε_{lidar} as derived from the spectral method using two different wave number intervals (0.0215 m^{-1} $< k_1 <$ 0.0464 m^{-1} and 0.0464 m^{-1} $< k_1 <$ 0.1 m^{-1}) of the lidar spectra and ε_{sonic}; the spectral density in the second interval has been corrected with $|\varphi(k_1)|^3$ (compare also Figure 6).

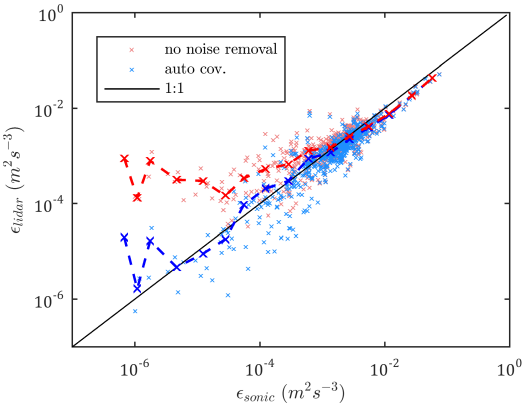

FIG. 8. Comparison of ε_{lidar} using the short-term-variance method (Equation 10); L_a = 100 m was used; the temporal averaging is neglected; red: without noise removal, blue: auto-covariance method has been applied.

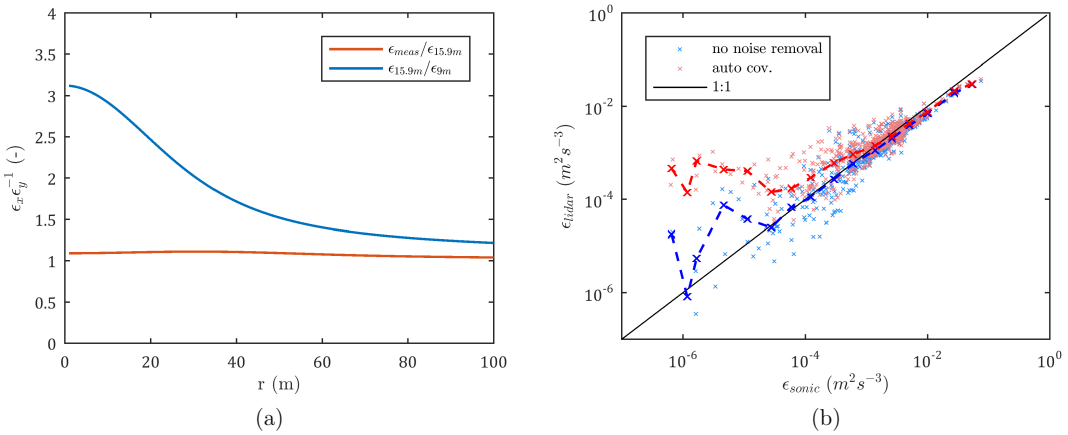

FIG. 9. **(a)** Influence of $\varphi(k)$ on ε_{lidar} as derived from $\overline{D}$ for different separation distances r; the effect of the temporal averaging is neglected; **(b)** scatter plot of ε_{sonic} vs ε_{lidar} derived from $\overline{D}$ using σ_l = 9 m and r = 25 m; the darker lines indicate the bin-averaged (median) values; blue: noise was removed using the autocorrelation method; red: no noise removal.

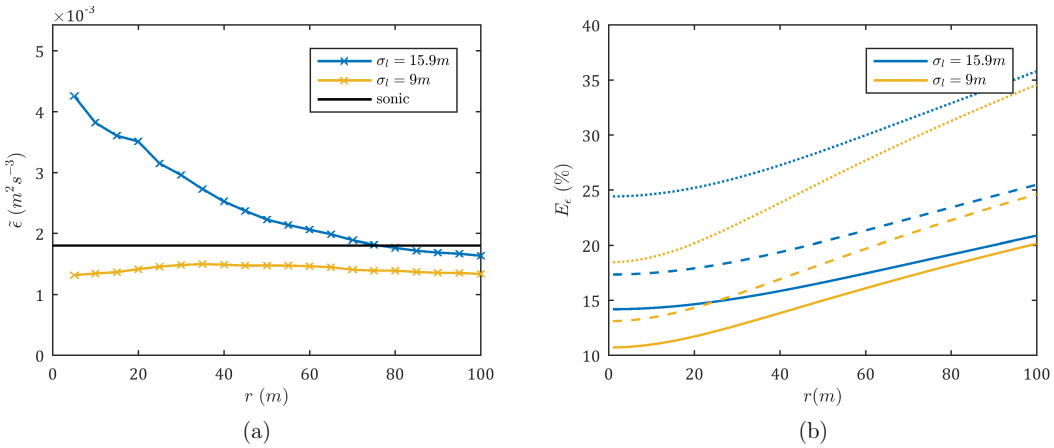

FIG. 10. **(a)** ε_{lidar} as derived from $\overline{D}$ for different r using a Gaussian form of $\varphi(k)$ with σ_l = 9 m and σ_l = 15.9 m; ε_{sonic} from the spectral method is also shown as a reference; **(b)** relative error of the estimates of ε_{lidar} from the lidar data estimated using the structure function method as a function of r for different wind speeds; solid lines u = 15 m/s, dashed lines u = 10 m/s, dotted lines u = 5 m/s; stream lines parallel to the lidar beam were assumed.

E. Pauscher et al. (2017a)

Pauscher, L., Callies, D., Klaas T. and Foken, T.: Wind obsevations from a forested hill: Relating turbulence statistics to surface characteristics in hilly and patchy terrain, Meteorologische Zeitschrift, accepted for publication.

Meteorologische Zeitschrift, PrePub DOI 10.1127/metz/20xx/xxxx

Wind observations from a forested hill: Relating turbulence statistics to surface characteristics in hilly and patchy terrain

LUKAS PAUSCHER[1,2*], DORON CALLIES[1], TOBIAS KLAAS[1], THOMAS FOKEN[2]

[1]Fraunhofer Institute for Wind Energy and Energy System Technology IWES, Kassel, Germany
[2]Department of Micrometeorology University of Bayreuth, Bayreuth Center of Ecology and Environmental Research, Bayreuth, Germany

(Manuscript received xx 0xx, xxxx; in revised form xx 0xx, xxxx; accepted xx 0xx, xxxx)

Abstract

This study investigates turbulence characteristics as observed at a 200 m tall mast at a hilly and complex site. It thereby concentrates on turbulence statistics, which are important for the site suitability analysis of a wind turbine. The directional variations in terrain are clearly reflected in the observed turbulence intensities and drag. Integral turbulence statistics showed some variations from their typical flat terrain values. Footprint modelling was used to model the area of effect and to relate the observed turbulence characteristics to the ruggedness and roughness within the estimated fetch area. Among the investigated turbulence quantities, the normalised standard deviation of the wind velocity along the streamlines showed the highest correlation with the effective roughness and ruggedness within the footprint followed by the normalised friction velocity and normalised standard deviation of the vertical wind speed. A differentiation between the effects of roughness and ruggedness was not possible, as forest cover and complex orography are highly correlated at the investigated site. An analysis of turbulence intensity by wind speed indicated a strong influence of atmospheric stability. Stable conditions lead to an overall reduction in turbulence intensity for a wind speed range between approx. 6-12 m s^{-1} when compared to neutral stratification. The variance of the horizontal wind speed strongly varied over the height range which is typical for a modern wind turbine and was in the order of the differences between different standard turbulence classes for wind turbines.

Keywords: wind energy, turbulence intensity, footprint, complex terrain, ruggedness, design wind conditions

1 Introduction

Today a significant part of the wind energy development in, e.g., Germany takes place at inland sites located relatively far from the coast (BERKHOUT et al., 2015). New turbine technology has made sites with relatively low wind speeds and/or forest cover technically and economically viable. Due to the increased wind resource, hilltop locations in lower mountain ranges are attractive for turbine siting in this context. This results in a significant increase in complexity of orography of the terrain when compared to many coastal sites, where a lot of the wind energy development has taken place in the past. Also, a lot of the unused wind energy potential of e.g. Germany and Scandinavia is located in complex and/or forested terrain (CALLIES, 2015; SIYAL et al., 2015). Many of these potential sites exhibit a significant amount of heterogeneity in surface cover and orography.

To avoid the increased turbulence induced by forest canopies and to make use of the larger wind resources at greater heights, modern wind turbines at inland sites now reach hub heights of 160 m and more. The tip heights of modern wind turbines can reach well above 200 m. Despite this development there is very little published experimental wind and turbulence data from forested areas covering the height range relevant for wind energy applications. This is especially true when the effects of complex orography and patchy forested landscape are combined. As a consequence, there is a lack of validation of models used in wind resource estimation and site assessment in complex and patchy terrain. Therefore, the estimation of the wind resource and especially the turbulence parameters, which are required for the site suitability analysis of a wind turbine, are associated with high uncertainties.

The interest in ecosystem-atmosphere exchange of trace gases such as carbon dioxide has led to an extensive body of experimental studies of flows within and directly above plant canopies including complex and heterogeneous sites (e.g. BALDOCCHI, 2014). The vertical extension of measurements in these studies is often limited to twice of the canopy height. Therefore, most of these experimental results only have limited value in the context of wind energy applications. One of the few sites with published experimental results from a tall tower (135 m) stems from a boreal forest in Sweden (ARNQVIST et al., 2015). The analysis showed a general applicability of Monin-Obukhov similarity theory (MOST) with a slight deviation for upper heights, but also indicated the influence of a limited boundary layer height on the wind profile. Additionally, a detailed analysis of turbulence statistics was presented. For the same

*Corresponding author: Lukas Pauscher, Fraunhofer Institute for Wind Energy and Energy System Technology IWES, Koenigstor 59, Kassel, Germany, e-mail: lukas.pauscher@iwes.fraunhofer.de

site, CHOUGULE et al. (2015) investigated the turbulence spectra in the frame work of the spectral tensor model of MANN (1994) in near neutral conditions. As expected, they found strongly increased turbulence levels but could not observe significant differences in the length scales or anisotropy of the turbulence when compared to flat terrain. Both studies focused on a homogeneous wind sector.

If we turn our attention to the combination of orography and forested landscape, the lack of experimental data is even more severe and only a handful of published experimental field campaigns exist. As for forest in flat terrain, many studies in complex terrain only employ relatively short masts and thus are not suitable to investigate wind and turbulence statistics at elevated heights (e.g. ZERI et al., 2010; GRANT et al., 2015). BRADLEY (1980) published measured wind and turbulence profiles for neutral conditions from of a measurement tower up to 124 m over a 10 m tall eucalyptus forest and heterogeneous fetch conditions. A limited number of experimental results on the effects of orography covered by plant canopies is also available from wind tunnel experiments (e.g. KAIMAL and FINNIGAN, 1994; NEFF and MERONEY, 1998; RUCK and ADAMS, 1991) and flume experiments (POGGI and KATUL, 2007, 2008). Besides the experimental evidence gathered, theoretical modelling studies have had a strong contribution to our current knowledge of flow over forested hills (e.g. FINNIGAN and BELCHER, 2004; ALLEN and BROWN, 2002; BROWN et al., 2001; ROSS and VOSPER, 2005; PATTON and KATUL, 2009).

Although modelling studies have started to turn on more complex inhomogeneous forests (e.g. SOGACHEV et al., 2009; BOUDREAULT, 2015), it is still very difficult for the experimentalist or practitioner from the wind energy community to relate the observed wind and turbulence statistics to the surface characteristics surrounding the site in heterogeneous landscapes. Detailed models often require large computer resources as well as detailed expert knowledge and are thus not a feasible option in many situations. Recently, remotely-piloted aircraft have been used to experimentally explore small scale variations in the turbulent flow over complex orography in a wind energy context (WILDMANN et al., 2017).

In this paper we present turbulence and wind speed measurements from a 200 m tall tower located on a forested hill surrounded by a patchy and hilly landscape in central Germany. To analyse the link between the upstream surface characteristics and turbulence quantities, we borrow from the surface flux community and use footprint modelling (for an overview see e.g. VESALA et al. (2008) or LECLERC and FOKEN (2014)) to identify the area influencing the measurement. We thus follow an idea which was recently suggested by FOKEN (2013) and experimentally investigate the transferability of the footprint approach to wind energy applications. Thereby, this analysis mainly focuses on turbulence quantities which are relevant for the site suitability assessment of a wind turbine. The influence of surface cover is described using the classical concept of surface roughness, while the effects of orography are conceptualised using a ruggedness index. Also, the paper discusses some of the observations made at Rödeser Berg in relation to standards for the description of the turbulence environment (IEC, 2005a).

2 Methods

2.1 Experimental site and instrumentation

The data analysed in this paper was collected at a 200 m tall mast at Rödeser Berg in northern Hesse in Germany ($51°21'46''N, 9°11'43''E$). A brief description of the site can also be found in KLAAS et al. (2015) and PAUSCHER et al. (2016). The mast is located at the south-western edge of a clearing (approx. 280 m north to south and 200 m east to west) on the ridge of a forested hill which stretches from approx. SSE to NNW (Figure 1).

The closer surroundings of the mast are characterised by forest of varying heights and several clearings. The distance, up to which the forests stretches, strongly varies with direction. In the direction NNW the forest extends approx. 5.8 km, while in ENE the forest edge is already reached within approx. 400 m from the mast. The orography of the hill also varies strongly with direction. In general, the terrain is hilly and undulated. Towards the NNW-direction a hilly ridge extends for about 5.8 km.

The wider surroundings consist of a patchy landscape of mainly agricultural land use, forest and some settlements. The immediate surroundings of the forested hill are mainly characterised by open agricultural areas. In the east and the west these are bordered by forested hills. In general, the terrain surrounding Rödeser Berg is very heterogeneous, which makes a definition of sectors with a consistent fetch as done in many other studies difficult if not impossible.

The mast consists of a rectangular lattice structure with a side length of 1.05 m. The solidity of the mast structure is 0.220 m^2 m^{-2} for the lower section (below 100 m) and 0.204 m^2 m^{-2} for the upper section (above 100 m). Here, solidity is defined according to IEC (2005b) as the projected area of all structural members divided by the exposed area of the mast. The mast is equipped with a dense array of sensors. An overview of the sensors used for the analysis is given in Table 1. Although the mast has opposing boom pairs, sonic anemometers are only mounted on the side facing $315-322°$. The analysis in this paper thus focuses on the analysis of sensors mounted on this side. Since the mast structure is slightly twisting with height, boom directions vary with height. To minimise the effects of the mast structure, the wind sensors are mounted on booms with a length of 5.4 m and meet the recommendations given in (IEC, 2005b). The sector $100-180°$ is removed

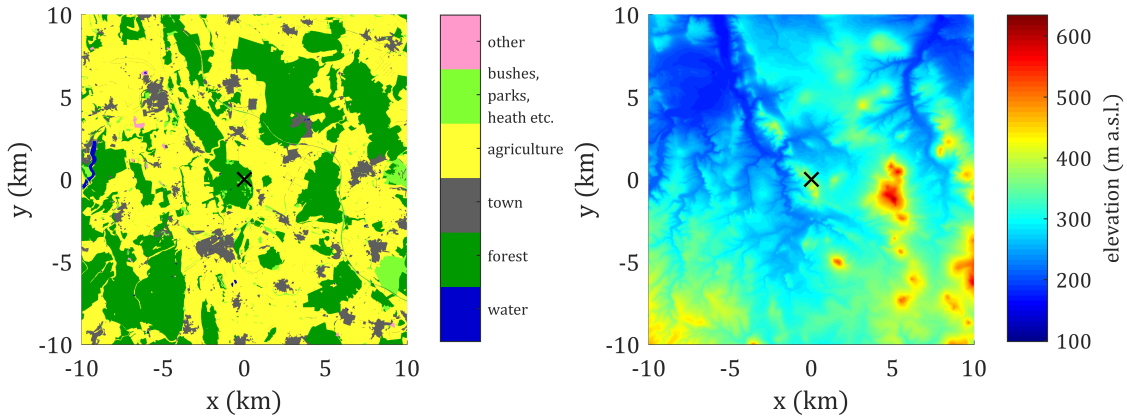

Figure 1: Left: Landuse map of the area around Rödeser Berg (data source ©GeoBasis-DE / Bundesamt für Kartographie und Geodäsie (2013) and www.openstreetmap.org); **right:** map of the terrain elevation around Rödeser Berg (data source ©GeoBasis-DE / Bundesamt für Kartographie und Geodäsie (2013)). The coordinate system for both maps is centered at the mast location - i.e. the location of the mast is (0,0).

from the analysis to avoid mast shadow effects. This choice was made by looking at the wind speed ratio between two opposing cup anemometers at the height of 191 m. The interval was then chosen conservatively and a 'safety band' of 20° was put around the sector where the mast shadow effect was visible.

2.2 Data preparation and quality control

The data analysed in this study comprises a period between 01.07.2012 and 01.12.2014. After that, several wind turbines were installed on site and large sectors are now influenced by wind turbine wakes. The data was filtered for physically unreasonable values and spiky periods in the sonic anemometer measurements were removed from the analysis. All analysis is based on 10-minute intervals, as these are most commonly used in wind energy applications.

The wind speed measurements from the sonic anemometer are rotated into the mean stream lines for each individual period (KAIMAL and FINNIGAN, 1994) before calculation of turbulence statistics from the sonic data. Compared to the often used planar-fit method (WILCZAK et al., 2001), the double rotation has been suggested to be superior at complex sites with varying slopes (STIPERSKI and ROTACH, 2016). Due to multiple instrument defects of the sonic anemometers, however, the number of valid measurements and the periods for which the instruments were functional vary with height. Only averaging periods, when no data was missing during the averaging interval, were used. Complete profiles with measurements at all levels are indicated in the text or the caption of the figure/table.

In Section 3, three different normalisations are used to present the measured turbulence statistics. First results are presented in the classical micro-meteorological framework (Section 3.1). Here, the turbulence statistics are normalised by the local (measured at the same height) wind speed and friction velocity. This facilitates the comparison to other measurements in the literature. A normalisation with the surface value, i.e. the friction velocity at the lowest measurement height, does not seem to be reasonable due to the strong variations in the fetch area with height.

In Section 3.2, the presented turbulence statistics are normalised by the wind speed measured by the cup anemometer at 191 m. The aim of this section is the investigation of the relationship between the surface characteristics and the turbulence statistics. To avoid speed-up effects in the wind profile to bias this analysis a common wind speed for the normalisation is necessary here. Ideally, the normalisation would be done with a wind speed which is independent of the local surface characteristics (e.g. the geostrophic wind speed). However, this would involve additional modelling which introduces additional uncertainties. The wind speed measured by the cup at 191 m was chosen as it is furthest from the surface and speed-up effects due to the terrain are expected to be weaker than at the lower heights.

In Section 3.3, the turbulence statistics are investigated from the 'perspective' of a wind turbine. Therefore, the normalisation is made using the wind speed at 120 m (U_{120}), a typical current hub height. This also allows the evaluation of the variation of the variance in the wind field across the rotor area of a turbine - i.e. how much the variance of the wind field changes with height. The top (191 m) and bottom (60 m) heights in this analysis roughly correspond to these upper and lower tip height. This means that turbulence intensities in Sections 3.1/3.2 and 3.3 are collected using different instruments and are expected to differ because of the different measurement principles of sonic and cup anemome-

Table 1: Overview of the anemometers used in this study; heights marked with * are bearing heated; heights marked with † are fully heated.

Sensor Type	height (m)	sampling frequency (Hz)	wind components
Thies First Class Advanced Cup Anemometer	$60^\star, 120^\star, 191$	1	U
Thies Ultrasonic Anemometer 3D	$80^\dagger$	20	u, v, w
Gill HS50 Ultrasonic Anemometer	40, 135, 188	50	u, v, w

ters. This is also reflected in the taxonomy used in this article. The turbulence intensity derived from the cup anemometers is denoted by I_U to indicate that there is no directional information available. In contrast, the turbulence intensity of the sonics is denoted by I_u to indicate the vector component along the mean stream lines. In general, the cup anemometers are expected to yield slightly lower values for the turbulence intensities of the horizontal component because of their distance constant of 3 - 3.9 m and their averaging time of 1 s. The data from the cup anemometers in Section 3.3 is chosen for two reasons. Firstly, they had a higher availability than the sonic anemometers. Secondly, cup measurements at a sampling frequency of 1 Hz still provide the standard for the wind energy community, which is important if the measured data is compared to existing standards.

The focus of Sections 3.1 and 3.2 is put on the influence of the terrain on the variations in turbulence statistics. Therefore, only neutral conditions are considered in these sections.

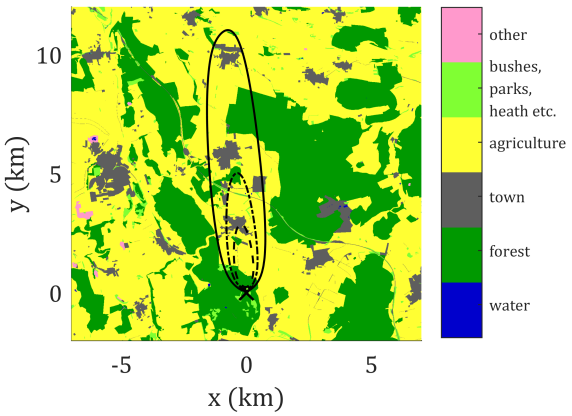

Figure 2: Example for a footprint climatology calculated for 135 m for neutral conditions and wind directions between $350-360°$; the dashed, dash-dotted and solid lines indicate the 40-, 60- and 80-%-effect levels of the flux footprint (data source ©GeoBasis-DE / Bundesamt für Kartographie und Geodäsie (2013) and www.openstreetmap.org).

2.3 Footprint analysis

Interpretation and understanding of observed wind and turbulence characteristics in a complex and heterogeneous environment like the current site pose a particular challenge to experimentalists. If the observations are to be linked to the surrounding surface/terrain, two major challenges need to be addressed. The surface area influencing the measurement (i.e. the area of effect) must be identified and appropriate measures for the characterisation of the surface/terrain within this area need to be found.

For the first problem in this study, a footprint modelling approach is used. Within the flux measurement community this method is widely used to relate observed scalar fluxes to source areas, which are seen by the sensor (RANNIK et al., 2012). Here, the footprint model of KLJUN et al. (2015), which is parametrised based on a more complex Langrian backward footprint model (KLJUN et al., 2002), is used to identify the surface area which is seen by the measurements at the different heights. The analysis then concentrates on the surface cover and the orography within the modelled foot print. The KLJUN et al. (2015) model is probably nowadays the best easy-to-use model on a good theoretical basis. This model compared well with a LES footprint model (STEINFELD et al., 2008). It thus provides a good compromise between simplicity and functionality. While the input parameters are easily derived from sonic anemometer measurements it is still valid for a wide range of atmospheric conditions and elevated measurement heights. MARKKANEN et al. (2009) found that at heights of 100-200 m there is a good agreement between the KLJUN et al. (2002) model and a large eddy simulation for idealised conditions. A sample footprint climatology for a $10°$ sector is shown in Figure 2.

The analysis in this study is confined to neutral conditions. Therefore, the boundary layer height z_i in the footprint model can be approximated as

$$z_i = c_n \frac{u_*}{|f|}, \tag{2.1}$$

as recommended in the appendix by KLJUN et al. (2015). In Equation 2.1 u_* is the friction velocity, f is the Coriolis parameter and $c_n = 0.3$ (HANNA and CHANG, 1993). Periods where the estimate z_i was smaller than the measurement height (i.e. very small local friction velocities) were not considered in the footprint analysis. According to MARKKANEN et al. (2009), for z_i of about 500 m the footprint can be well determined for heights of about 200 m and less without a significant influence of the boundary layer height. Due to the wind speed limit (4 m s^{-1}), which was used, this applies to

about 94 % of all measurement periods for the highest sonic anemometer. The influence of z_i on the footprint modelling results is, thus, expected to be small.

While strictly only valid for scalar fluxes, in this analysis the footprint approach is also used to identify the area which influences the measured turbulence statistics. The argument for the appropriateness of this approach is derived from the fact that the vertical length scales of the footprint concept and the blending height concept as well as the internal boundary-layer concept are very similar (HORST, 2000). Moreover, following PHILIP (1997), a convection-diffusion equation for shear stress in analogy to passive scalars can be derived. If the eddy diffusivity and eddy viscosity are assumed to be equal, the blending height of scalar fluxes and shear stress are very similar.

In practical applications, FOKEN and LECLERC (2004) have suggested to use roughness changes and isolated obstacles as natural tracers to validate footprint models. Footprint models have also been used to estimate the averaged roughness representative of the footprint area of a measurement (GÖCKEDE et al., 2004, 2006). More recently, the footprint approach has also been suggested to be used to estimate the area and, hence, the surface roughness influencing the wind conditions experienced by a wind turbine (FOKEN, 2013).

It should be noted, that the applied footprint model assumes homogeneous conditions and is thus not suited for heterogeneous terrain/flow. This is somewhat in contrast to the idea of identifying the relevant features in a heterogeneous environment, but is inherent in most footprint models. One of the purposes of this paper is to experimentally explore the applicability and limitations of the simplified footprint-modelling approach. Therefore, the footprint approach used in this study can only serve as a first approximation of the area of effect for a measurement/wind turbine. More sophisticated footprint models based on e.g. large eddy simulations (e.g. STEINFELD et al., 2008) might lead to more realistic results. However, this strongly increases the complexity of the model and therefore removes one of the main advantages of the footprint approach.

2.4 Terrain classification

For wind energy applications mainly the aerodynamic properties of the surface are of interest. These are strongly influenced by the surface cover and the drag which is exerted by the surface form or ruggedness of the terrain. The first aspect can be addressed by aggregating the roughness of the different land cover types into a roughness which is representative of the area of effect - i.e. the effective roughness length $z_{0,eff}$.

Here, the logarithmic average (TAYLOR, 1987) of the footprint weighted roughness length within the 80-%-effect level of the footprint is used to determine $z_{0,\mathrm{eff}}$:

$$\log(z_{0,\mathrm{eff}}) = \sum_{i=1}^{n} p_i \log(z_{0,i}), \qquad (2.2)$$

Table 2: Roughness lengths (z_0) for different surface cover types as used in this study (slightly modified after FOKEN, 2017).

Land cover	z_0 (m)
forest	1
settlements	1
agriculture, sports and recreational	0.03
bushes, clearings, swamps	0.2
gravel pit, waste disposal site	0.3
water	0.0005

where p_i and $z_{0,i}$ are the footprint weighting and and the roughness length assigned to each individual pixel; n is the number of pixels within the footprint.

It is acknowledged that there are more sophisticated averaging schemes available which also take the spatial arrangement of the different surface types within the averaging area into account (e.g. HASAGER and JENSEN, 1999; HASAGER et al., 2003). However, for simplicity reasons the simple logarithmic approch is chosen here. Also, it can often be used as a good first approximation (TAYLOR, 1987).

The surface cover and, thus, the underlying roughness map is based on a digital land-use model with a resolution of 10 m (Figure 1) and dimensions of 60x60 km^2. The roughness lengths used in this study are displayed in Table 2. Other possibilities to characterise the surface cover include e.g. the enhanced vegetation index (STOY et al., 2013). This index also captures the effects of seasonality in vegetation structure (e.g. agriculture or forest) and they could be accounted for in the estimation of $z_{0,\mathrm{eff}}$. Again, for simplicity reasons this is not done here.

The influence of the surface ruggedness on the drag is difficult to quantify on the scale of the footprint of a wind turbine. Tables which directly specify roughness length for different terrain shapes as in the case of surface cover (e.g. TROEN and LUNDTANG PETERSEN, 1989; WIERINGA, 1992) are not available and existing classifications are very coarse. In meso-scale modelling the effects of sub-grid orography are sometimes parametrised using the standard deviation of the elevation σ_s (e.g. DOMS et al., 2011). However, this measure is sometimes misleading, as e.g. constantly sloping terrain has a high σ_s but exhibits very little ruggedness.

In this study, an index based on the steepness of the slopes is used to define the ruggedness (r_s) within the footprint. The index is based on the concept of the ruggedness index (RIX) which is often used in wind resource assessment applications to classify sites according to their ruggedness and to estimate errors in modelled wind speeds (BOWEN and MORTENSEN, 1996; MORTENSEN and PETERSEN, 1997). The basic idea of this index is to identify slopes upstream of the wind measurement or turbine which exceed a critical value (Θ_{crit}).

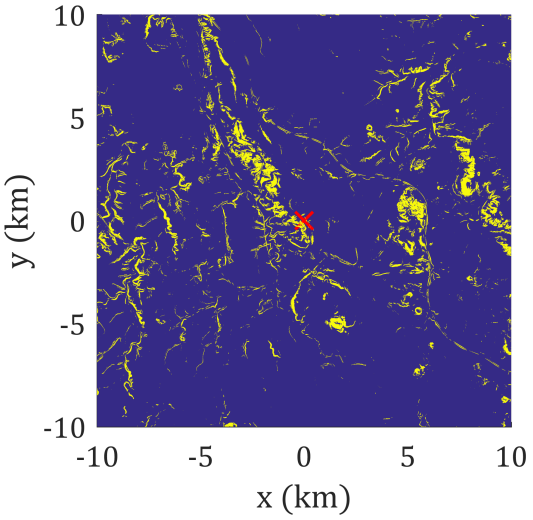

Figure 3: Ruggedness around the mast at Rödeser Berg. Yellow indicates areas exceeding the critical slope $\Theta_{crit} = 0.3$. The coordinate system is centered at the mast location denoted by the red cross.

r_s is then defined as:

$$r_s = \frac{A_{r_s}}{A_{80}}, \tag{2.3}$$

where A_{r_s} is the area inside the 80-%-effect level of the footprint exceeding the critical slope and A_{80} is the total area of the 80-%-effect level of the footprint. As for the RIX index, the critical slope is defined as $\Theta_{crit} = 0.3$ in this study. This roughly corresponds to the onset of flow separation (WOOD, 1995).

While the RIX-Index only considers the slope of the terrain in the direction of the flow, here, the slope of the terrain is calculated for all directions within a semicircle (0 to 180°) in 1°-steps by shifting the terrain elevation map by 10 m in the respective direction. Linear interpolation is applied to derive the shifted map. Pixels which exceed the critical slope are flagged as 'rugged'. Using this procedure a ruggedness map of the terrain surrounding the measurement site is created (Figure 3). For each sector r_s is then calculated as the percentage of pixels which are flagged as 'rugged' within the 80-%-effect area of the footprint climatology. A digital elevation model with a 10 m resolution (BUNDESAMT FÜR KARTOGRAPHIE UND GEODÄSIE, 2015) is used in this analysis.

The procedure described above differs from the RIX defined by BOWEN and MORTENSEN (1996) and MORTENSEN and PETERSEN (1997) in two main points. Firstly, the distance within which the index for the ruggedness is calculated dynamically varies with the extend of the footprint. Secondly, the ruggedness is defined by slopes in all directions rather than just the flow direction and positive an negative slopes both add to the ruggedness rather than cancelling out.

3 Results and discussion

3.1 Turbulence statistics at Rödeser Berg

To investigate the directional behaviour of the turbulence quantities at the measurement site the data was binned in 10°-sectors and the average values were calculated. Since the analysis in this paper is mainly motivated by wind energy applications, periods with $U_{120} < 4$ m s^{-1} were excluded from the directional analysis. The significance of smaller wind speeds for wind energy applications - e.g. for the loads exerted on the turbine - is expected to be small and the threshold is typical for investigations in the wind energy community. The cup anemometer at 120 m was chosen as it is close to the hub height of a modern wind turbine and was available during the entire measurement period (unlike the sonic anemometers which suffered multiple failures).

Figure 4 displays the directional dependence of turbulence statistics as measured by the sonic anemometers at the different heights for locally neutral conditions ($|L| > 500m$; where L is the Obukhov length). Also, local normalisation (i.e. with $u*$ at the individual heights) is used in Figure 4. The approach of using local scaling is motivated by the fact that we expect the characteristics of the footprint for the different heights to differ significantly. Later a common height for the normalisation is used to compare the turbulence statistics among different heights (Sections 3.2 and 3.3).

A clear directional pattern is visible for all heights (Figure 4) for the turbulence intensity of the stream-wise component of the wind vector $I_u = \sigma_u/\overline{u}$. For all heights a peak in I_u can be observed at roughly 300 to 320°. Within this direction the upstream area is characterised by the forested ridge extending for approx. 5.8 km (Figure 1). This terrain exhibits high roughness as well as high ruggedness. I_u for wind directions between approx. 350 and 60° is relatively low. Here, the terrain is more open and shows less variations in elevation. Between 180 and 300° the two elevated sonic anemometers (135 and 188 m) show a very similar pattern with a constantly increasing I_u. The measurement at 80 m shows a decline between 180 and 210°. Also, I_u at 80 m is significantly higher than at the top two levels for $180 - 360°$. In this sector the vicinity of the mast is forested and orographically complex, while the wider surroundings are more open. Values are similar at all levels between $0 - 90°$. Here, open agricultural areas are located much closer to the mast and forested hills are located in a distance of several km. A similar pattern as for I_u can be observed for the surface drag ($u_* u^{-1}$), although the variation between the top two measurement heights (135 m and 188 m) appears somewhat smaller.

The integral turbulence statistics for the u component ($\sigma_u u_*^{-1}$) vary between 1.67 and 2.18 for the measurements at 135 m and 188 m, and between 1.90 and

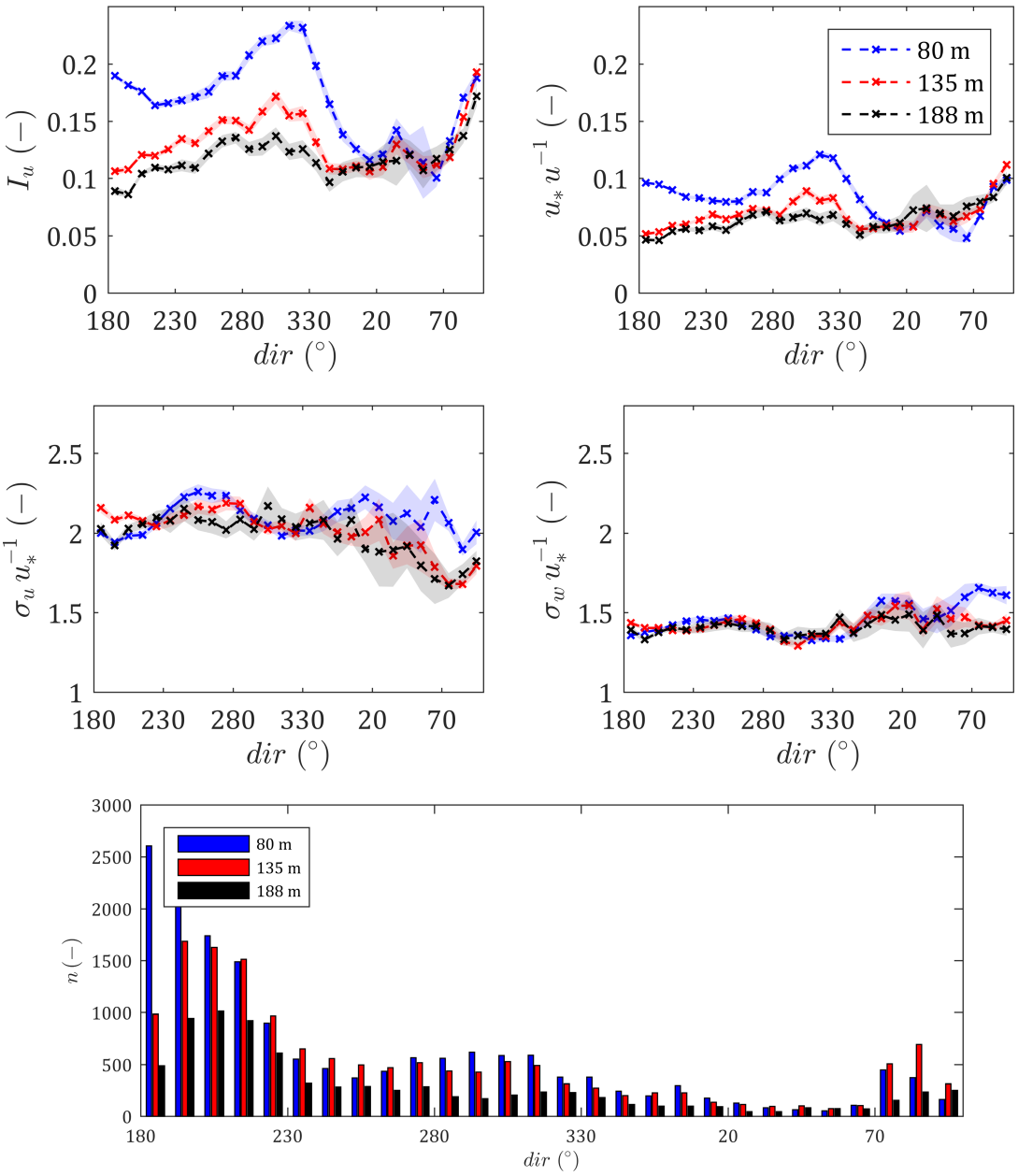

Figure 4: Directional variation of mean turbulence statistics calculated from 10° bins for neutral conditions ($|L| > 500$ m); **top left:** I_u, **top right:** $u_* u^{-1}$, **middle left:** $\sigma_u u_*^{-1}$, **middle right:** $\sigma_w u_*^{-1}$, **bottom:** data availability (n); L was determined locally from the individual sonic anemometer; only periods when $U_{120} > 4$ m s^{-1} are included in the analysis; the shaded areas indicate the 95-%-confidence intervals derived using student's t statistics.

2.26 at 80 m. This is lower than the value that is often given for neutral conditions in flat and homogeneous terrain $\sigma_u u_*^{-1} = 2.4$ (e.g. PANOFSKY and DUTTON, 1984) but slightly higher than roughness sub-layer flows above canopies given by RAUPACH et al. (1996) (1.7) and the values reported by ARNQVIST et al. (2015) (approx. 1.7-1.9) for neutral conditions at a tall profile with a long and homogeneous forest fetch for most sectors. For a site with complex orography FRAGOULIS (1997) reported values of 2.1 - 2.4. The directional variation especially at 80 m is to some degree anti-cyclic to the variations in drag and I_u.

$\sigma_w u_*^{-1}$ is in general slightly higher than 1.25 usually assumed over homogeneous terrain. Values range from 1.33 to 1.66 for 80 m and from 1.29 to 1.55 for the upper two heights. Increased values for $\sigma_w u_*^{-1}$ have also been observed at other sites with complex orography (e.g. FRAGOULIS, 1997). $\sigma_w u_*^{-1}$ also shows a similar anti-cyclic pattern for 80 m as $\sigma_u u_*^{-1}$ between 180° and 360°. For the $0-100°$-sector $\sigma_w u_*^{-1}$ exhibits relatively strong variations for 80 m and is larger than the observed values for 135 and 188 m. Interestingly, this is also the case for $\sigma_u u_*^{-1}$. As a note of caution it should be said here that especially for 80 m the data availability is quite low for some of the bins in this sector (the minimum is $n = 25$).

At this point it should be reiterated, that the turbulence statistics were calculated using averaging intervals of 10 minutes, because this is common practice in wind energy applications - e.g. FRAGOULIS (1997) also used 10-minute intervals. Many other micrometeorological studies (including ARNQVIST et al., 2015) use averaging intervals of 30 minutes (e.g. AUBINET et al., 2012). Depending on the integral scales of the different turbulent quantities the choice of the averaging interval will lead to differences in the observed turbulence statistics (for a detailed discussion see LENSCHOW et al., 1994). We therefore also derived the turbulence characteristics based on 30-minute intervals. If the mean turbulence statistics are compared over all valid sectors, there is very little difference (approx. -1 to 3 %) for $\sigma_w u_*^{-1}$ and $u_* u^{-1}$. I_u and $\sigma_u u_*^{-1}$ are increased by approx 7 to 13 % for the 30-minute intervals with increasing gain for increasing height. Some of the deviation from the typically reported values for $\sigma_u u_*^{-1}$ are, thus, likely to be caused by the 10-minute averaging interval used in this study. This might to some extend be related to the larger turbulent length scales of u. However, also the increasing contribution of meso-scale variations might become visible. At elevated heights the micro-scale turbulence and the meso-scale variations tend to blend into one another and the spectral gap separating the two can disappear (LARSÉN et al., 2016). As for wind turbine loads only the micro-scale turbulence is considered (and important), the choice of a 10-minute averaging interval is more appropriate here.

3.2 The relation between surface characteristics within the footprint and the observed turbulence statistics

The results for the surface characteristics ($z_{0,\mathrm{eff}}$ and r_s) derived from the footprint analysis are displayed in Figure 5. For comparison, also a roughness length which corresponds to the measured turbulence statistics ($z_{0,m}$) is derived using the log-law relationship:

$$z_{0,m} = \exp(\ln(z-d) - \kappa u u_*^{-1}), \tag{3.1}$$

where κ is the von Kármán constant and d is the displacement height. d was estimated from the tree height and density in the direct vicinity of the met mast. It varies by direction with a maximum value of 25 m (for southerly directions with tall and densely spaced trees) and a minimum value of 5 m (for the direction of the clearing). Due to the high measurement heights the sensitivity to the value of d is rather small. As only neutral conditions are analysed, no stability correction of Equation 3.1 is necessary.

At this point it should be noted that the values of $z_{0,m}$, which are displayed in Figure 5 are intended to facilitate a direct comparison to $z_{0,\mathrm{eff}}$ derived from the surface characteristics of the footprint area. $z_{0,m}$ is also influenced by orography related effects such as e.g. local speed-up effects and should not directly be interpreted as a roughness length. Despite this restriction, $z_{0,m}$ and $z_{0,\mathrm{eff}}$ show similarity in their pattern and magnitudes for all heights between 180° and 360°. However, between 0° and 100° the correlation gets worse and especially for 135 and 188 m, $z_{0,m}$ is significantly higher than $z_{0,\mathrm{eff}}$.

The directional variation of r_s is somewhat similar to $z_{0,\mathrm{eff}}$ with relatively low values for wind directions between 0 and 100°.

Figure 6 displays scatter plots of the relation between different turbulence statistics and surface charcteristics. In contrast to Figure 4, turbulence quantities are normalised using the wind speed at a common height (191 m) in Figure 6. A direct comparison of the turbulence statistics across different heights might be misleading as in neutral conditions we expect the wind speed to generally increase with increasing height. On the other hand, the highest values for r_s and $z_{0,\mathrm{eff}}$ are observed at the lowest heights. This fact might introduce some artificial correlation if local scaling is used. The height of 191 m is chosen as it is far away from the surface and thus expected to be less affected by surface effects than lower measurements. It should be noted, however, that the wind speed at 191 m is still influenced by the surface and will, thus, introduce some de-correlation for the turbulence statistics at 135 m and especially at 80 m.

A trend of increasing values of $\sigma_u u_{191}^{-1}$ with increasing r_s and $\ln(z_{0,\mathrm{eff}})$ can be observed for all heights and most values cluster around a more or less linear relationship. Several outliers can be observed, which ex-

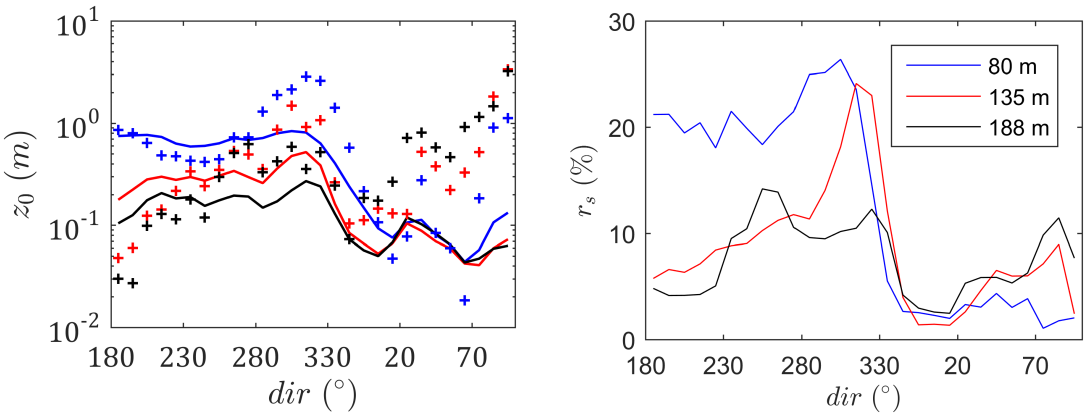

Figure 5: Directional variation of **left:** lines $z_{0,\mathrm{eff}}$ calculated from the footprint climatology (see text) of the 10° bins for neutral conditions ($|L| > 500$ m); the crosses are $z_{0,m}$ calculated from Equation 2.3; **right:** r_s; note that the left scale is logarithmic, while the right is linear.

hibit high values for $\sigma_u u_{191}^{-1}$ but low r_s and $\ln(z_{0,\mathrm{eff}})$. The outliers for 135 and 188 m are associated with the $60-100^\circ$-bin where a sharp increase in $\sigma_u u_{191}^{-1}$ but only a moderate increase in r_s can be observed (diamonds in Figure 6) . For 80 m another group of outliers can be observed for wind directions between $310-340^\circ$ where r_s for 80 m starts to drop off but the turbulence intensity remains at a high level (compare also Figure 4). For $\ln(z_{0,\mathrm{eff}})$ no outliers are visible within this sector. However, the scatter for low $\ln(z_{0,\mathrm{eff}})$ is generally slightly higher. The correlation between $\sigma_u u_{191}^{-1}$ and r_s and $\ln(z_{0,\mathrm{eff}})$ is similar (Pearson's r is 0.62 for r_s and 0.60 for $\ln(z_{0,\mathrm{eff}})$).

The correlation for $u_* u^{-1}$ is weaker than for $\sigma_u u_{191}^{-1}$ and the scatter increases. r is 0.43 and 0.26 for r_s and $\ln(z_{0,\mathrm{eff}})$, respectively. The weakest correlation is observed for $\sigma_w u_{191}^{-1}$ (r is 0.28 and 0.12). The distribution of the points in the scatter plot also suggests that the relationship between r_s and $\sigma_w u_{191}^{-1}$ and $u_* u^{-1}$ is somewhat stronger than for $\ln(z_{0,\mathrm{eff}})$ when the outliers are excluded.

It is difficult to draw conclusions concerning the relative importance of the terrain ruggedness vs the forest cover within the footprint for the observed turbulence levels, as r_s and $z_{0,\mathrm{eff}}$ are highly correlated in the area around Rödeser Berg. Both properties show a high correlation with especially $\sigma_u u_{191}^{-1}$. Nevertheless, some interesting patterns can be observed when the two are compared.

The 'outliers' in the $\sigma_u u_{191}^{-1}$ vs r_s relationship are directed towards a turbulence level but low r_s. Points with high r_s and low $\sigma_u u_{191}^{-1}$ are not observed. This is also true to some extend for the $\sigma_w u_{191}^{-1}$ and $u_* u^{-1}$. This suggests that the ruggedness is an important factor in turbulence production but r_s does not capture all effects responsible for turbulence production. For $\ln(z_{0,\mathrm{eff}})$ the outliers are also directed towards high turbulence and low $\ln(z_{0,\mathrm{eff}})$, however, the lower boundary is less clear.

Much of the increased scatter which is found in the relationship between the turbulence quantities and r_s and $\ln(z_{0,\mathrm{eff}})$, respectively, is related to wind sectors between $60-100^\circ$. It is interesting to note that within this sector also the turbulence statistics show some differences when compared to the other wind directions. $\sigma_u u_*^{-1}$ is reduced for the 135 and 188 m measurements and $\sigma_w u_*^{-1}$ is increased for 80 m. For these directions the Schreckenberg and the Gudenberg start to move into the footprint of the measurements at Rödeser Berg (Figure 1). With a maximum elevation of 568 m it is significantly higher than Rödeser Berg. The presence of this relatively large orographical obstacle is probably not well represented in the definition of r_s, as it only accounts for the slope and not the height of the ruggedness elements.

Summarising the observations, especially r_s inside the footprint area seems to be a promising way to explain the directional variations in $\sigma_u U_{191}^{-1}$ induced by the orography. It should, however, be noted that r_s is only an approximation for the surface ruggedness. The results will depend to some degree on the choice of Θ_{crit}, which here is motivated by the onset of flow separation. The critical slope for flow separation will vary with surface cover i.e. be smaller for forested hills than for bare soil (FINNIGAN and BELCHER, 2004).

Also due to the categorical nature of r_s the calculation of a footprint-weighted ruggedness is not as straight forward as for $z_{0,\mathrm{eff}}$ and is not attempted here. Nevertheless, it is intuitive that the effect of orographic features will vary according to their location within the footprint area.

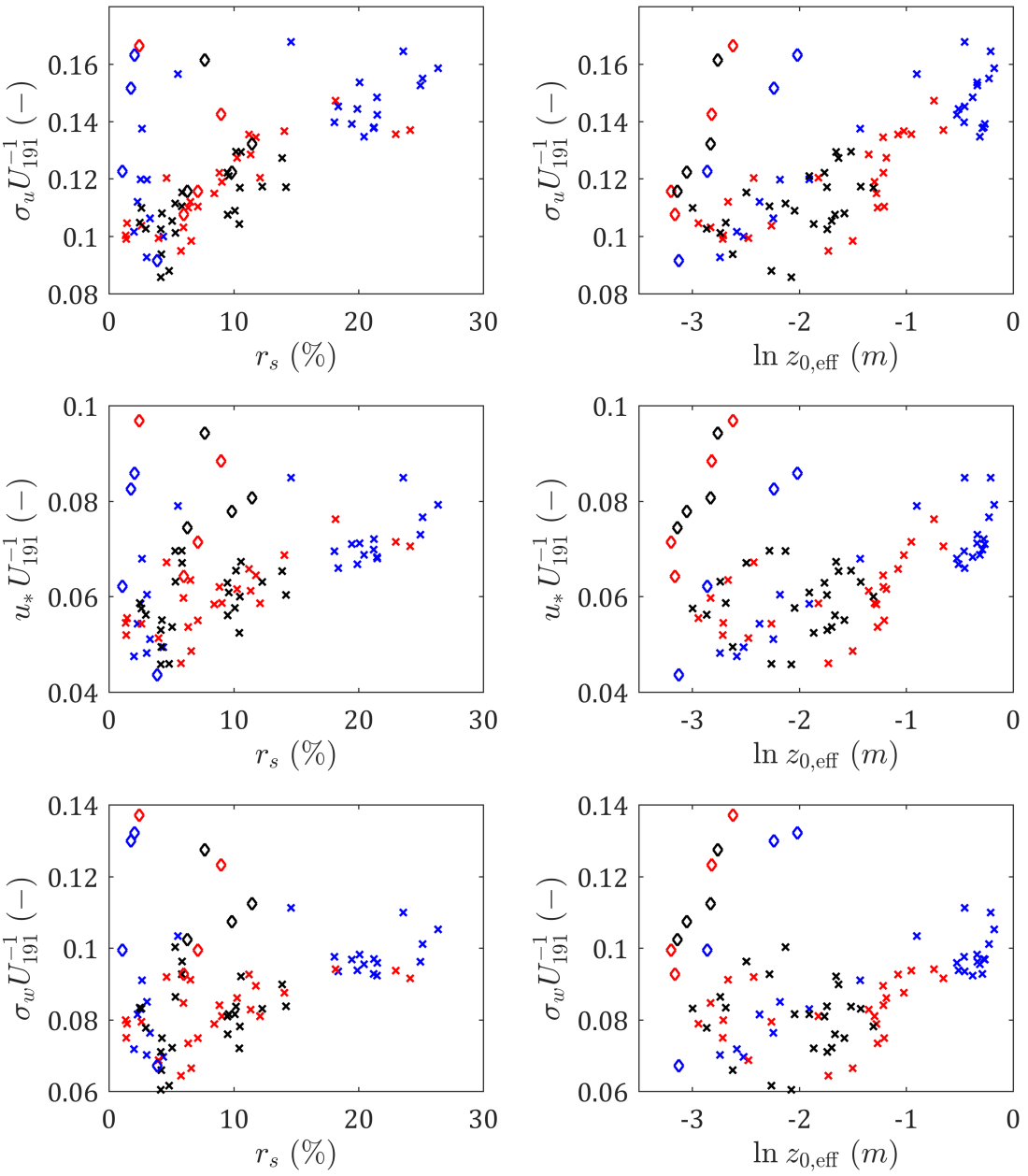

Figure 6: Scatter plots of different turbulence statistics in relation to surface properties within the simulated footprint climatologies; **left column:** normalised turbulence quantities vs the index for ruggedness r_s within the footprint; **right column:** normalised turbulence quantities vs the effective roughness $z_{0,\mathrm{eff}}$ within the footprint; **top:** $\sigma_u U_{191}^{-1}$ **middle:** $u_* U_{191}^{-1}$ and **bottom:** $\sigma_w U_{191}^{-1}$; only periods with neutral conditions ($|L| > 500$ m) have been used; calculations are based on 10°-bins; diamonds indicate bins which lie within $60 - 100°$; periods when $U_{120} > 4$ m s^{-1} are excluded from the analysis; for colour coding see Figure 4.

3.3 Turbulence intensity in comparison to existing design guidelines and the influence of atmospheric stability

Turbulence intensity of the horizontal wind speed is one of the key parameters used in the site suitability analysis for wind turbines (IEC, 2005a). To model the expected loads during the life time of a wind turbine the turbulence intensity as a function of wind speed is required. This section therefore focuses on the analysis of this quantity.

In standard load modelling applications the representative turbulence intensity $I_{rep} = \sigma_{rep}/U$ is often described by the 'normal turbulence model' (NTM) according to IEC (2005a):

$$\sigma_{rep} = I_{ref}(0.75U + 5.6\ m\ s^{-1}), \tag{3.2}$$

where I_{ref} is a dimensionless constant which depends on the turbine class (for the different turbine classes see also Figure 7). In site assessment applications I_{rep} is compared to the 90%-percentile of the measured turbulence intensity of the horizontal wind speed to see if a turbine is suitable for a specific site. From measurements this is usually approximated as $I_{U90} = I_U + 1.28\sigma_{I_U}$, where I_U is the mean turbulence intensity and σ_{I_U} is the standard deviation of the turbulence intensity. Stability effects are not parametrised in this formulation. For the analysis in this paper I_{U90} and I_U are calculated using wind-speed bins with a width of 1 m s^{-1}.

As shown in Section 3.2 turbulence statistics strongly vary with wind direction. To allow for the exploration of other effects on the turbulence intensity the analysis in this section is therefore confined to a narrow sector including the main wind direction ($180 - 220°$).

Also, unlike in the previous sections cup anemometers are used to derive the turbulence intensity. This is mainly motivated by two facts. Firstly, as mentioned in Section 2.2, there were multiple instrument failures on the sonic anemometers. The set of concurrent measurements over the wide height range is rather limited for the sonics. Using cup anemometers the data base for the analysis in this section is significantly enhanced. Secondly, it is common practice in the wind energy community to use cup rather than sonic to measure turbulence intensity. It should be noted again that the standard deviation of the horizontal wind speed between a sonic and a cup measurement is expected to differ. As the sonic is able to resolve smaller turbulent scales, it will usually measure slightly higher turbulence intensities.

Figure 7 displays the standard deviation of the wind speed measured by cup anemometers (σ_U) at 60, 120 and 191 m height normalised by the wind speed at 120 m (U_{120}) as a function of U_{120}. The heights roughly reflect the lower tip, hub and upper tip heights of a modern wind turbine. The somewhat unusual normalisation is motivated by a better direct comparability of the variance within the wind field at the different heights. In load simulations it is common practice to specify a target variance of the wind field and keep this constant across the whole modelling domain. This stems from classical surface layer theory in homogeneous terrain, which is, however, questionable for heterogeneous surfaces like in the current setup.

The first striking observation is that there is a relatively strong variation of the turbulence levels at the different heights with strongly decreasing turbulence with height. Especially the difference between the 60 m and 120 m measurements is large and in the order or even exceeding the differences between the different standard turbulence classes for wind turbine design (Figure 7). The behaviour of σ_u with height from other experiments is not entirely clear. While GARRATT (1994) suggests an almost constant σ_u throughout most of the atmospheric boundary layer, ARYA (2001) suggest an exponential reduction which is equal to the reduction in σ_w. Profiles reported in a high roughness environment over a homogeneous forest in Sweden (ARNQVIST et al., 2015) indicate a reduction of σ_u between comparable heights (60 and 135 m) which is smaller than the reduction in Figure 7. As demonstrated in Section 3.2, one of the main reasons for this observation is the variation of the surface characteristics within the footprint of the different measurement heights (Figure 5).

As the IEC standard (IEC, 2005a) only defines three different turbulence classes, it is unlikely that the absolute turbulence levels will match one of the defined classes. It is thus more interesting to compare the shape of the observed to the empirically derived curve in IEC (2005a). A prominent feature of I_u as well as I_{U90} is that they show a minimum between approx. 8 - 10 m s^{-1} (Figure 7). For higher wind speeds the turbulence intensities are increasing again. This behaviour is contrary to the shape of the NTM, which is monotonically decreasing. The pattern of the observed atmospheric stability at 135 m shows an interesting correlation with the mean turbulence intensity and I_{U90}. At low wind speeds, where turbulence intensities are high, unstable conditions are dominant. With increasing wind speed the percentage of stable conditions increases and reaches a maximum at about the same wind speeds as where the minimum of the turbulence intensities is observed. For the classification according to the observed Obukhov length see caption of Figure 7.

If only neutral conditions are considered, no clear minimum is visible for neither I_{U90} nor I_U. In fact, within the wind speed range where the maximum number of stable conditions is found, also the maximum difference between the overall and neutral statistics can be observed. For wind energy applications this observation is highly relevant, as the wind speed range between 6 - 12 m s^{-1} is very important for fatigue loads on onshore turbines.

There are different possible mechanisms which might be responsible for the observation of this correlation between atmospheric stability and wind speed. The first is that the influence of the stable stratification dampens the frictional forces which can lead to an increased

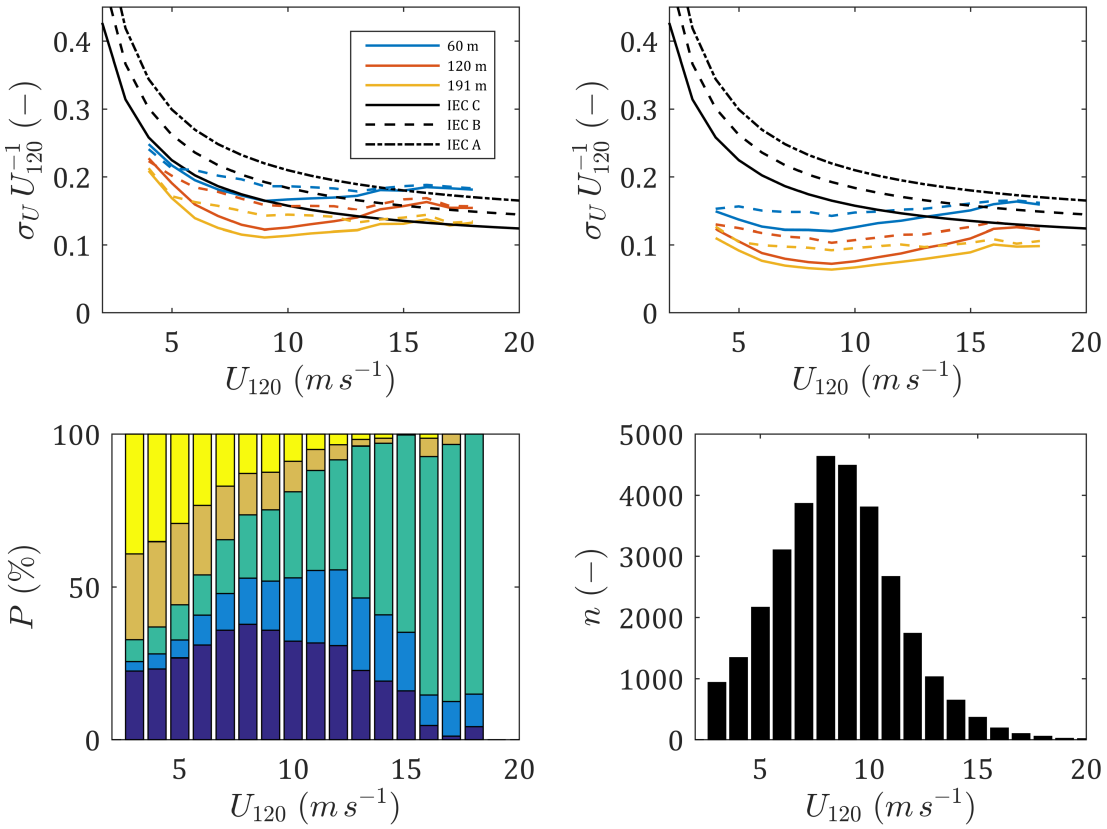

Figure 7: Top left: σ_U/U_{120} by wind speed for $180-220°$; the solid lines indicate I_{U90} as defined by equation 3.2 for all measurements, dashed lines are only neutral conditions ($|L| > 500$ m); the black lines show the normal turbulence model; turbulence class A ($I_{ref} = 0.16$); turbulence class B ($I_{ref} = 0.14$); turbulence class C ($I_{ref} = 0.12$); **top right:** same as the left panel but the bin-wise mean (rather than the 90-%-percentile) of the observed turbulence intensities is displayed. **bottom left:** occurrence of atmospheric stability classes for different wind speeds as observed at 135 m; dark blue denotes stable (0 m $< L <$ 200 m), light blue slightly stable (200 m $< L <$ 500 m), green neutral ($|L| > 500$ m), orange slightly unstable (-200 m $> L >$ -500 m) and yellow unstable (0 m $> L >$ -200 m) conditions; **bottom right:** data availability for the different wind-speed bins; only bins with more than 20 observations are included.

flow at higher levels and the formation of a low level jet (LLJ). The LLJ is usually defined by a wind speed maximum in the first few hundred meters above ground. It has been studied over several decades (BLACKADAR, 1957; STENSRUD, 1996). More recently, its importance for resource estimation in wind energy applications in northern Germany has been suggested (EMEIS, 2014; LAMPERT et al., 2016). Also in forested low mountain ranges in Germany the frequent occurrence of LLJs has been reported (SERAFIMOVICH et al., 2017).

An often used definition of the LLJ is a wind maximum which is at least 2 m s^{-1} higher than the minimum aloft (STULL, 1988). However, only very few profiles fulfill this criterion within the first 200 m above ground at Rödeser Berg. Although there are more profiles where the wind speed is decreasing with height at the top measurement height(s), a clear identification of LLJ-events with the mast data is difficult. In fact, the reported typical heights of LLJ reported from other sites vary from between 100 - 200 m (e.g. BANTA et al., 2002; BAAS et al., 2009) up to several hundred meters (e.g. BONNER, 1968; ZHANG et al., 2006). EMEIS (2014) found that the persistence of a LLJ is limited by a critical shear below the jet, which is dependent of the Richardson number (EMEIS, 2017). This can also set a lower limit to the height of the jet core. The typical height of the LLJs at Rödeser Berg might thus be too high to be reliably detected by the mast measurement.

The second possible reason for increased wind speeds in stable conditions at Rödeser Berg is the interaction between stability and orographic effects. The speed-up over hills and ridges can be significantly in-

creased in stable conditions (e.g. CARRUTHERS and CHOULARTON, 1982; BRADLEY, 1983; COPPIN et al., 1994). Moreover, if the boundary layer is very shallow, the flow might be forced around the hill in diverging flow lines (SNYDER et al., 1985). In a shallow boundary layer the mast measurements might even be above the turbulent boundary layer. A more detailed investigation of the flow over the hill and speed-up effects is currently done using a spatial network of profiling and scanning lidars in the framework of the New European Wind Atlas Project (MANN et al., 2017).

There are only few studies reporting explicitly on the distribution of atmospheric stability and σ_u as a function of wind speed. SATHE et al. (2013) investigated the influence of atmospheric stability on wind turbine loads. Their analysis also showed a clear reduction of σ_u with increasing stability (they used the Obukhov length) for a homogeneous site.. The stability conditions over several different coastal sites generally indicated a decreasing occurrence of stable conditions with increasing wind speed. However, the stability distributions were derived from either eddy co-variance measurements close to the ground or profile measurements.

For a mildly complex site in the western USA WHARTON and LUNDQUIST (2012) reported similar observations as found at Rödeser Berg. The lowest wind speeds and highest turbulence intensities were found in unstable conditions. Their observations even indicated the highest wind speeds for stable conditions at their site. At Rödeser Berg for wind speeds above approx. 12 m s^{-1} neutral conditions begin to dominate and the mean wind speed during neutral conditions is larger than during stable conditions. This is in line with the fact that for high wind speeds in stable conditions the formation of low level jets is limited to greater heights as mechanical mixing will be induced if the shear exceeds a critical value (EMEIS, 2014) and the stable stratification will not longer persist. Also, the occurrence of the diverging flow lines is dependent on the wind speed and is more likely to be observed in lower wind speed conditions (SNYDER et al., 1985).

4 Conclusion and outlook

Linking surface properties to observed turbulence statistics provides a difficult task in complex and patchy terrain. At Rödeser Berg a directional analysis of turbulence statistics in relation to the surface characteristics within the modelled footprint was carried out. Especially the normalised standard deviation of the wind velocity in the direction of the flow lines ($\sigma_u U_{191}^{-1}$) showed a high correlation with the ruggedness and the effective roughness for all heights and most wind-direction sectors.

These results indicate that, despite the simplicity of the approach, footprint modelling, as frequently used in the flux community, can provide a valuable tool for relating measured turbulence statistics to observations. In wind energy applications footprint modelling can be used to e.g. identifying wind sectors for which high turbulence levels are to be expected. In combination with simple surface metrics its main benefit lies in the simple evaluation and possible classification of wind turbine sites.

The conclusion regarding the effects of terrain ruggedness vs high roughness areas within the footprint on turbulence quantities are less conclusive as ruggedness and roughness are strongly correlated in the area surrounding the measurement site.

Effective roughness length ($z_{0,\mathrm{eff}}$) and the ruggedness index (r_s) as used in this study are simplifications and the limit of the explanatory power for the variation of the turbulence levels was visible in the wind direction sector where a large orographical obstacle is present. Besides experimental campaigns, further validation studies of footprint tools for wind energy applications should include comparison with more complex models such as large eddy simulations. Within the simulation environment the range of the validity of simple analytical footprint approaches can be evaluated by switching certain terrain features in the modelling environment 'on' and 'off'.

The observed behaviour of the turbulence intensity showed significant deviations from the normal turbulence model suggested in IEC (2005a) for the investigated sector. The reason for this is likely to be the distribution of atmospheric stability. The differences between the normalised standard deviation of the horizontal wind speed for all stability conditions and only neutral cases are significant compared to design guidelines of wind turbines. They exceed the difference between the different turbulence classes specified in the current standard for wind turbine design (IEC, 2005a). From an applied point of view it is interesting to note that this effect occurs within a wind speed range which is highly relevant for the fatigue loads experienced by a wind turbine. Unfortunately, at higher wind speeds this effect vanishes and periods with high wind speeds and high turbulence result. This suggests that in the next generation wind farm design tools and models for estimating the site specific turbulence conditions should include the effect of atmospheric stability in addition to the terrain effects. While some first progress to include atmospheric stability in load simulations (e.g. SATHE et al., 2011; PARK et al., 2014) and wake modelling (e.g. ÖZDEMIR et al., 2013) has been made, the inclusion of atmospheric stability in site assessment still remains a difficult issue.

The strong variation of the standard deviation of the horizontal wind speed (σ_U) with height suggests that the assumption of a turbulence field with a constant variance across the modelling domain might not be adequate for wind turbines with large rotors in heterogeneous terrain.

Acknowledgments

The authors would like to acknowledge the technical support of Richard Döpfer, Klaus Otto and Zouhair

Khadiri and many others at IWES during the measurements. We would also like to thank the two anonymous reviewers who greatly helped to improve the quality of this manuscript with their critical comments and suggestions. The work for this publication was founded by the following project: Windenergie im Binnenland II (Förderkennzeichen 0325171A) funded by the German Federal Ministry of Economics.

References

ALLEN, T., A.R. BROWN, 2002: Large-eddy simulation of turbulent separated flow over rough hills. – Boundary-Layer Meteorology **102**, 177–198, DOI: 10.1023/A:1013155712154.

ARNQVIST, J., A. SEGALINI, E. DELLWIK, H. BERGSTRÖM, 2015: Wind statistics from a forested landscape. – Boundary-Layer Meteorology 1–19, DOI: 10.1007/s10546-015-0016-x.

ARYA, S.P., 2001: Introduction to micrometeorology, volume v. 79 of *International geophysics series* – Academic Press, San Diego, California and London.

AUBINET, M., T. VESALA, D. PAPALE, editors, 2012: Eddy Covariance – Springer, Dordrecht.

BAAS, P., F.C. BOSVELD, H. KLEIN BALTINK, A.A.M. HOLTSLAG, 2009: A climatology of nocturnal low-level jets at cabauw. – Journal of Applied Meteorology and Climatology **48**, 1627–1642, DOI: 10.1175/2009JAMC1965.1.

BALDOCCHI, D., 2014: Measuring fluxes of trace gases and energy between ecosystems and the atmosphere - the state and future of the eddy covariance method. – Global Change Biology **20**, 3600–3609, DOI: 10.1111/gcb.12649.

BANTA, R., R.K. NEWSOM, J.K. LUNDQUIST, Y.L. PICHUGINA, R.L. COULTER, L. MAHRT, 2002: Nocturnal low-level jet characteristics over Kansas during CASES-99. – Boundary-Layer Meteorology **105**, 221–252, DOI: 10.1023/A:1019992330866.

BERKHOUT, V., S. FAULSTICH, B. HAHN, J. HIRSCH, K. LINKE, M. NEUSCHÄFER, S. PFAFFEL, K. RAFIK, K. ROHRIG, SACK, ANDRE, STARK, ELISABETH, L. SCHULDT, M. ZIESSE, 2015: Wind energy report Germany 2014. Kassel.

BLACKADAR, A.K., 1957: Boundary layer wind maxima and their significance for the growth of nocturnal inversions. – Bulletin of the American Meteorological Society **38**, 283–290.

BONNER, W.D., 1968: Climatology of the low level jet. – Monthly Weather Review **96**, 833–850, DOI: 10.1175/1520-0493(1968)096<0833:COTLLJ>2.0.CO;2.

BOUDREAULT, L.E., 2015: Reynolds-averaged Navier-Stokes and large-eddy simulation over and inside inhomogeneous forests Ph.D. thesis, DTU Wind Energy, Denmark DTU Wind Energy PhD-0042.

BOWEN, A.J., N.G. MORTENSEN, 1996: Exploring the limits of wasp the wind atlas analysis and application program. – In: 1996 European Wind Energy Conference and Exhibition, 584–587.

BRADLEY, E., 1983: The influence of thermal stability and angle of incidence on the acceleration of wind up a slope. – Journal of Wind Engineering and Industrial Aerodynamics **15**, 231 – 242, DOI: http://dx.doi.org/10.1016/0167-6105(83)90193-9.

BRADLEY, E.F., 1980: An experimental study of the profiles of wind speed, shearing stress and turbulence at the crest of a large hill. – Quarterly Journal of the Royal Meteorological Society **106**, 101–123, DOI: 10.1002/qj.49710644708.

BROWN, A.R., J.M. HOBSON, N. WOOD, 2001: Large-eddy simulation of neutral turbulent flow over rough sinusoidal ridges. – Boundary-Layer Meteorology **98**, 411–441, DOI: 10.1023/A:1018703209408.

BUNDESAMT FÜR KARTOGRAPHIE UND GEODÄSIE, 2015: Digitales Geländemodell Gitterweite 10 m DGM10. http://www.geodatenzentrum.de/docpdf/dgm10.pdf (accessed at 03.08.2016).

CALLIES, D., 2015: Analyse des Potenzials der Onshore-Windenergie in Deutschland unter Berücksichtigung von technischen und planerischen Randbedingungen Ph.D. thesis, Universität Kassel, Hess.

CARRUTHERS, D.J., T.W. CHOULARTON, 1982: Airflow over hills of moderate slope. – Quarterly Journal of the Royal Meteorological Society **108**, 603–624, DOI: 10.1002/qj.49710845708.

CHOUGULE, A., J. MANN, A. SEGALINI, E. DELLWIK, 2015: Spectral tensor parameters for wind turbine load modeling from forested and agricultural landscapes. – Wind Energy **18**, 469–481, DOI: 10.1002/we.1709.

COPPIN, P.A., E.F. BRADLEY, J.J. FINNIGAN, 1994: Measurements of flow over an elongated ridge and its thermal stability dependence: The mean field. – Boundary-Layer Meteorology **69**, 173–199, DOI: 10.1007/BF00713302.

DOMS, G., J. FÖRSTNER, E. HEISE, H.J. HERZOG, M.R. MIRONOV, 2011: A description of the nonhydrostatic regional COSMO model: Part II : Physical Parameterization – Deutscher Wetterdienst, Offenbach, Germany.

EMEIS, S., 2014: Wind speed and shear associated with low-level jets over Northern Germany. – Meteorologische Zeitschrift **23**, 295–304, DOI: 10.1127/0941-2948/2014/0551.

EMEIS, S., 2017: Upper limit for wind shear in stably stratified conditions expressed in terms of a bulk richardson number. – Meteorologische Zeitschrift –, DOI: 10.1127/metz/2017/0828.

FINNIGAN, J.J., S.E. BELCHER, 2004: Flow over a hill covered with a plant canopy. – Quarterly Journal of the Royal Meteorological Society **130**, 1–29, DOI: 10.1256/qj.02.177.

FOKEN, T., 2013: Application of footprint models for wind turbine locations. – Meteorologische Zeitschrift **22**, 111–115, DOI: 10.1127/0941-2948/2012/0390.

FOKEN, T., 2017: Micrometeorology.

FOKEN, T., M.Y. LECLERC, 2004: Methods and limitations in validation of footprint models. – Agricultural and Forest Meteorology **127**, 223–234, DOI: 10.1016/j.agrformet.2004.07.015.

FRAGOULIS, A., 1997: The complex terrain wind environment and its effects on the power output and loading of wind turbines. – In: 35th Aerospace Sciences Meeting and Exhibit.

GARRATT, J.R., 1994: The atmospheric boundary layer Cambridge atmospheric and space science series. – Univ. Press, Cambridge.

GÖCKEDE, M., C. REBMANN, T. FOKEN, 2004: A combination of quality assessment tools for eddy covariance measurements with footprint modelling for the characterisation of complex sites. – Agricultural and Forest Meteorology **127**, 175–188, DOI: 10.1016/j.agrformet.2004.07.012.

GÖCKEDE, M., T. MARKKANEN, C.B. HASAGER, T. FOKEN, 2006: Update of a footprint-based approach for the characterisation of complex measurement sites. – Boundary-Layer Meteorology **118**, 635–655, DOI: 10.1007/s10546-005-6435-3.

GRANT, E.R., A.N. ROSS, B.A. GARDINER, S.D. MOBBS, 2015: Field observations of canopy flows over complex terrain. – Boundary-Layer Meteorology **156**, 231–251, DOI: 10.1007/s10546-015-0015-y.

HANNA, S.R., J.C. CHANG, 1993: Hybrid plume dispersion model (hpdm) improvements and testing at three field sites. – Atmospheric Environment. Part A. General Topics **27**, 1491–1508, DOI: 10.1016/0960-1686(93)90135-L.

HASAGER, C.B., N.O. JENSEN, 1999: Surface-flux aggre-

gation in heterogeneous terrain. – Quarterly Journal of the Royal Meteorological Society **125**, 2075–2102, DOI: 10.1002/qj.49712555808.

HASAGER, C.B., N.W. NIELSEN, N.O. JENSEN, E. BOEGH, J.H. CHRISTENSEN, E. DELLWIK, H. SOEGAARD, 2003: Effective roughness calculated from satellite-derived land covermaps and hedge-information used in a weather forecasting model. – Boundary-Layer Meteorology **109**, 227–254, DOI: 10.1023/A:1025841424078.

HORST, T., 2000: An intercomparison of measures of special inhomogeneity for surface fluxes of passive scalars. – In: Proceedings of the 14th Symposium on Boundary Layer and Turbulence, Aspen, CO. American Meteorological Society, Boston, MA, 11–14.

IEC, 2005a: IEC 61400-1 wind turbines – part 1: Design requirements.

IEC, 2005b: IEC 61400-12-1 wind turbines – part 12-1: Power performance measurements of electricity producing wind turbines..

KAIMAL, J.C., J.J. FINNIGAN, 1994: Atmospheric boundary layer flows: Their structure and measurement – Oxford University Press, New York.

KLAAS, T., L. PAUSCHER, D. CALLIES, 2015: Lidar-mast deviations in complex terrain and their simulation using cfd. – Meteorologische Zeitschrift **24**, 591–603, DOI: 10.1127/metz/2015/0637.

KLJUN, N., M.W. ROTACH, H.P. SCHMID, 2002: A three-dimensional backward lagrangian footprint model for a wide range of boundary-layer stratifications. – Boundary-Layer Meteorology **103**, 205–226, DOI: 10.1023/A:1014556300021.

KLJUN, N., P. CALANCA, M.W. ROTACH, H.P. SCHMID, 2015: A simple two-dimensional parameterisation for flux footprint prediction (ffp). – Geoscientific Model Development **8**, 3695–3713, DOI: 10.5194/gmd-8-3695-2015.

LAMPERT, A., B. BERNALTE JIMENEZ, G. GROSS, D. WULFF, T. KENULL, 2016: One-year observations of the wind distribution and low-level jet occurrence at Braunschweig, North German Plain. – Wind Energy **19**, 1807–1817, DOI: 10.1002/we.1951.

LARSÉN, X.G., S.E. LARSEN, E.L. PETERSEN, 2016: Full-scale spectrum of boundary-layer winds. – Boundary-Layer Meteorology **159**, 349–371, DOI: 10.1007/s10546-016-0129-x.

LECLERC, M.Y., T. FOKEN, 2014: Footprints in Micrometeorology and Ecology – Springer Berlin Heidelberg.

LENSCHOW, D.H., J. MANN, L. KRISTENSEN, 1994: How long is long enough when measuring fluxes and other turbulence statistics?. – Journal of Atmospheric and Oceanic Technology **11**, 661–673, DOI: 10.1175/1520-0426(1994)011<0661:HLILEW>2.0.CO;2.

MANN, J., 1994: The spatial structure of neutral atmospheric surface-layer turbulence. – Journal of Fluid Mechanics **273**, 141, DOI: 10.1017/S0022112094001886.

MANN, J., N. ANGELOU, J. ARNQVIST, D. CALLIES, E. CANTERO, R.C. ARROYO, M. COURTNEY, J. CUXART, E. DELLWIK, J. GOTTSCHALL, S. IVANELL, P. KÜHN, G. LEA, J.C. MATOS, J.M.L.M. PALMA, L. PAUSCHER, A. PEÑA, J.S. RODRIGO, S. SÖDERBERG, N. VASILJEVIC, C.V. RODRIGUES, 2017: Complex terrain experiments in the new european wind atlas. – Philosophical Transactions of the Royal Society of London A: Mathematical, Physical and Engineering Sciences **375**, DOI: 10.1098/rsta.2016.0101.

MARKKANEN, T., G. STEINFELD, N. KLJUN, S. RAASCH, T. FOKEN, 2009: Comparison of conventional lagrangian stochastic footprint models against LES driven footprint estimates. – Atmospheric Chemistry and Physics **9**, 5575–5586, DOI: 10.5194/acp-9-5575-2009.

MORTENSEN, N.G., E.L. PETERSEN, 1997: Influence of topographical input data on the accuracy of wind flow modelling in complex terrain. – In: 1997 European Wind Energy Conference, 317–320.

NEFF, D.E., R.N. MERONEY, 1998: Wind-tunnel modeling of hill and vegetation influence on wind power availability. – Journal of Wind Engineering and Industrial Aerodynamics **74-76**, 335–343, DOI: 10.1016/S0167-6105(98)00030-0.

ÖZDEMIR, H., M. VERSTEEG, A. BRAND, 2013: Improvements in ecn wake model. – In: International Conference on Aerodynamics of Offshore Wind Energy Systems and Wakes (ICOWES2013), volume 1.

PANOFSKY, H.A., J.A. DUTTON, 1984: Atmospheric turbulence: Models and methods for engineering applications – Wiley, New York and Chichester.

PARK, J., S. BASU, L. MANUEL, 2014: Large-eddy simulation of stable boundary layer turbulence and estimation of associated wind turbineâĂŹloads. – Wind Energy **17**, 359–384, DOI: 10.1002/we.1580.

PATTON, E.G., G.G. KATUL, 2009: Turbulent pressure and velocity perturbations induced by gentle hills covered with sparse and dense canopies. – Boundary-Layer Meteorology **133**, 189–217, DOI: 10.1007/s10546-009-9427-x.

PAUSCHER, L., N. VASILJEVIC, D. CALLIES, G. LEA, J. MANN, T. KLAAS, J. HIERONIMUS, J. GOTTSCHALL, A. SCHWESIG, M. KÃIJHN, M. COURTNEY, 2016: An inter-comparison study of multi- and dbs lidar measurements in complex terrain. – Remote Sensing **8**, 782, DOI: 10.3390/rs8090782.

PHILIP, J., 1997: Blending and internal boundary-layer heights, and shear stress. – Boundary-Layer Meteorology **84**, 85–98, DOI: 10.1023/A:1000345015838.

POGGI, D., G.G. KATUL, 2007: An experimental investigation of the mean momentum budget inside dense canopies on narrow gentle hilly terrain. – Agricultural and Forest Meteorology **144**, 1–13, DOI: 10.1016/j.agrformet.2007.01.009.

POGGI, D., G.G. KATUL, 2008: Turbulent intensities and velocity spectra for bare and forested gentle hills: Flume experiments. – Boundary-Layer Meteorology **129**, 25–46, DOI: 10.1007/s10546-008-9308-8.

RANNIK, Ü., A. SOGACHEV, T. FOKEN, M. GÖCKEDE, N. KLJUN, M.Y. LECLERC, T. VESALA, 2012: Footprint analysis. – In: M. AUBINET, T. VESALA, and D. PAPALE (Eds.), Eddy Covariance, Springer Netherlands, Dordrecht, 211–261, DOI: 10.1007/978-94-007-2351-1_8.

RAUPACH, M., J. FINNIGAN, Y. BRUNEI, 1996: Coherent eddies and turbulence in vegetation canopies: The mixing-layer analogy. – Boundary-Layer Meteorology **78**, 351–382, DOI: 10.1007/BF00120941.

ROSS, A.N., S.B. VOSPER, 2005: Neutral turbulent flow over forested hills. – Quarterly Journal of the Royal Meteorological Society **131**, 1841–1862, DOI: 10.1256/qj.04.129.

RUCK, B., E. ADAMS, 1991: Fluid mechanical aspects of the pollutant transport to coniferous trees. – Boundary-Layer Meteorology **56**, 163–195, DOI: 10.1007/BF00119966.

SATHE, A., J. MANN, J. GOTTSCHALL, M.S. COURTNEY, 2011: Can wind lidars measure turbulence?. – Journal of Atmospheric and Oceanic Technology **28**, 853–868, DOI: 10.1175/JTECH-D-10-05004.1.

SATHE, A., J. MANN, T. BARLAS, W. BIERBOOMS, VAN G. BUSSEL, 2013: Influence of atmospheric stability on wind turbine loads. – Wind Energy **16**, 1013–1032, DOI: 10.1002/we.1528.

SERAFIMOVICH, A., J. HÜBNER, M.Y. LECLERC, H.F. DUARTE, T. FOKEN, 2017: Influence of Low-Level Jets and Gravity Waves on Turbulent Fluxes, 247–276 Springer Inter-

national Publishing, Cham, DOI: 10.1007/978-3-319-49389-3_1.

SIYAL, S.H., U. MÃŰRTBERG, D. MENTIS, M. WELSCH, I. BABELON, M. HOWELLS, 2015: Wind energy assessment considering geographic and environmental restrictions in Sweden: A GIS-based approach. – Energy **83**, 447 – 461, DOI: http://dx.doi.org/10.1016/j.energy.2015.02.044.

SNYDER, W.H., R.S. THOMPSON, R.E. ESKRIDGE, R.E. LAWSON, I.P. CASTRO, J.T. LEE, J.C.R. HUNT, Y. OGAWA, 1985: The structure of strongly stratified flow over hills: dividing-streamline concept. – Journal of Fluid Mechanics **152**, 249–288.

SOGACHEV, A., J. MANN, E. DELLWIK, F. BINGÖL, O. RATHMANN, H. EJSING JØRGENSEN, O. PANFEROV, 2009: Wind energy availability above gaps in a forest. – In: EWEC 2009 Proceedings, volume 6, EWEC, 4198–4206.

STEINFELD, G., S. RAASCH, T. MARKKANEN, 2008: Footprints in homogeneously and heterogeneously driven boundary layers derived from a lagrangian stochastic particle model embedded into large-eddy simulation. – Boundary-Layer Meteorology **129**, 225–248, DOI: 10.1007/s10546-008-9317-7.

STENSRUD, D., 1996: Importance of low-level jets to climate: A review. – Journal of Climate **9**, 1698–1711, DOI: 10.1175/1520-0442(1996)009<1698:IOLLJT>2.0.CO;2.

STIPERSKI, I., M.W. ROTACH, 2016: On the measurement of turbulence over complex mountainous terrain. – Boundary-Layer Meteorology **159**, 97–121, DOI: 10.1007/s10546-015-0103-z.

STOY, P.C., M. MAUDER, T. FOKEN, B. MARCOLLA, E. BOEGH, A. IBROM, M.A. ARAIN, A. ARNETH, M. AURELA, C. BERNHOFER, A. CESCATTI, E. DELLWIK, P. DUCE, D. GIANELLE, E. VAN GORSEL, G. KIELY, A. KNOHL, H. MARGOLIS, H. MCCAUGHEY, L. MERBOLD, L. MONTAGNANI, D. PAPALE, M. REICHSTEIN, M. SAUNDERS, P. SERRANO-ORTIZ, M. SOTTOCORNOLA, D. SPANO, F. VACCARI, A. VARLAGIN, 2013: A data-driven analysis of energy balance closure across fluxnet research sites: The role of landscape scale heterogeneity. – Agricultural and Forest Meteorology **171-172**, 137–152, DOI: 10.1016/j.agrformet.2012.11.004.

STULL, R.B., 1988: An Introduction to Boundary Layer Meteorology – Springer Netherlands, Dordrecht.

TAYLOR, P.A., 1987: Comments and further analysis on effective roughness lengths for use in numerical three-dimensional models. – Boundary-Layer Meteorology **39**, 403–418, DOI: 10.1007/BF00125144.

TROEN, I., E. LUNDTANG PETERSEN, 1989: European Wind Atlas – Risø National Laboratory.

VESALA, T., N. KLJUN, U. RANNIK, J. RINNE, A. SOGACHEV, T. MARKKANEN, K. SABELFELD, T. FOKEN, M.Y. LECLERC, 2008: Flux and concentration footprint modelling: state of the art. – Environmental pollution (Barking, Essex : 1987) **152**, 653–666, DOI: 10.1016/j.envpol.2007.06.070.

WHARTON, S., J.K. LUNDQUIST, 2012: Assessing atmospheric stability and its impacts on rotor-disk wind characteristics at an onshore wind-farm. – Wind Energy **15**, 525–546, DOI: 10.1002/we.483.

WIERINGA, J., 1992: Updating the Davenport roughness classification. – Journal of Wind Engineering and Industrial Aerodynamics **41**, 357–368.

WILCZAK, J.M., S.P. ONCLEY, S.A. STAGE, 2001: Sonic anemometer tilt correction algorithms. – Boundary-Layer Meteorology **99**, 127–150, DOI: 10.1023/A:1018966204465.

WILDMANN, N., S. BERNARD, J. BANGE, 2017: Measuring the local wind field at an escarpment using small remotely-piloted aircraft. – Renewable Energy **103**, 613 – 619, DOI: http://dx.doi.org/10.1016/j.renene.2016.10.073.

WOOD, N., 1995: The onset of separation in neutral, turbulent flow over hills. – Boundary-Layer Meteorology **76**, 137–164, DOI: 10.1007/BF00710894.

ZERI, M., C. REBMANN, C. FEIGENWINTER, P. SEDLAK, 2010: Analysis of periods with strong and coherent CO_2 advection over a forested hill. – Agricultural and Forest Meteorology **150**, 674–683, DOI: 10.1016/j.agrformet.2009.12.003.

ZHANG, D.L., S. ZHANG, S.J. WEAVER, 2006: Low-level jets over the Mid-Atlantic States: Warm-season climatology and a case study. – Journal of Applied Meteorology and Climatology **45**, 194–209, DOI: 10.1175/JAM2313.1.

(Eidesstattliche) Versicherungen und Erklärungen

(§ 5 Nr. 4 PromO)
Hiermit erkläre ich, dass keine Tatsachen vorliegen, die mich nach den gesetzlichen Bestimmungen über die Führung akademischer Grade zur Führung eines Doktorgrades unwürdig erscheinen lassen.

(§ 8 S. 2 Nr. 5 PromO)
Hiermit erkläre ich mich damit einverstanden, dass die elektronische Fassung meiner Dissertation unter Wahrung meiner Urheberrechte und des Datenschutzes einer gesonderten Überprüfung hinsichtlich der eigenständigen Anfertigung der Dissertation unterzogen werden kann.

(§ 8 S. 2 Nr. 7 PromO)
Hiermit erkläre ich eidesstattlich, dass ich die Dissertation selbständig verfasst und keine anderen als die von mir angegebenen Quellen und Hilfsmittel benutzt habe.

(§ 8 S. 2 Nr. 8 PromO)
Ich habe die Dissertation nicht bereits zur Erlangung eines akademischen Grades anderweitig eingereicht und habe auch nicht bereits diese oder eine gleichartige Doktorprüfung endgültig nicht bestanden.

(§ 8 S. 2 Nr. 9 PromO)
Hiermit erkläre ich, dass ich keine Hilfe von gewerblichen Promotionsberatern bzw. -vermittlern in Anspruch genommen habe und auch künftig nicht nehmen werde.

Bayreuth, den _____ _____

Lukas Pauscher